Combustion synthesis of NiAl and NiAl based composites by Induction heating

by

Xiaomeng Zhu

Kingston University London

Submitted in Partial Fulfilment

of the requirements for the Degree

Doctor of Philosophy

Supervised by: Professor Tao Zhang

Faculty of Engineering

Kingston University, London

June 2010

Acknowledgement

I would like to give my special thanks to my supervisor Professor Tao Zhang for his supports all the time. His guidance and encouragement made this thesis possible. Professor Zhang's influence in building my professional career has been immeasurable. My sincere gratitude to him can hardly be addressed here.

My other supervisors Mr. Denis Marchant and Mrs. Valerie Morris are also acknowledged for their precious suggestion and expertises in various aspects. They support this project throughout the whole progress.

I would show my gratitude to all technicians in the machine laboratory, materials laboratory and auto laboratory. They offered great help in the experimental setting.

The Faculty of Science in Kingston University provides the access to microscopy for which I am very grateful. Also, Professor Peter Foot's help in the X-ray diffraction testing is appreciated.

The Faculty of Computing, Information Systems and Mathematics in Kingston University offers the usage of high revolution thermal image camera for which I am also grateful.

I would like to acknowledge Mr. Wei Xie and Dr. Feng Liu at University of Sheffield for their help in X-ray diffraction testing.

I am also grateful to Dr. Jiming Gao at South Bank University for his assistance in micro-hardness testing.

Particularly I want to thank my parents. Thanks for their love, understanding and encouragement.

The financial support comes from faculty of engineering, Kingston University, is highly appreciated.

Abstract

Intermetallic NiAl has the potential to be used for elevated temperature applications. Self-propagating high-temperature synthesis (SHS) has been developed as a relatively simple route to obtain intermetallics. To date different ignition techniques have attempted to synthesize NiAl and produce coatings. Induction heating has been used to produce coatings and differs from conventional heating techniques in which the material is heated from the inside. This paper considers the use of induction heating to preheat and ignite the synthesis directly and investigates the effect of induction parameters on the phase transformation, microstructures and properties of Ni/Al compacts synthesized by SHS. During synthesis the temperature profiles were measured with infrared thermometers and a high resolution thermal image camera to monitor the reaction process. Scanning electron microscopy (SEM), Energy Dispersive X-ray test (EDX) and X-ray Diffraction (XRD) were used to characterize products. The mechanical properties of the products were evaluated by measuring hardness. The results show that single phase NiAl can be produced by induction heating whilst processing parameters such as heating rates and green densities have a significant effect on the properties and structures of the sintered products. To further improve the mechanical properties and control the deformation of NiAl during combustion reaction caused by the formation of liquid, Al_2O_3 was used as an additive and dilution agent. The results show that single phase NiAl can be produced by this process regardless of the addition of Al_2O_3. However, the addition of Al_2O_3 is found to have a significant effect on heating rates, combustion behaviour and properties of the synthesized products. Additionally, there is a critical concentration for Al_2O_3 above which the compacts cannot be ignited by induction

heating. Tests showed that the addition of Al_2O_3 can significantly improve the mechanical properties of NiAl.

The synthesis of TiC and NiAl/TiC composites using induction heating via SHS process was also studied in this project. High density NiAl/TiC composites and two-layer TiC-NiAl structures were successfully produced using this process. The results show that the reaction was complete and that stoichiometric products of NiAl and TiC were produced. The properties of the NiAl/TiC composites were found to be functions of composition and processing parameters. The reaction mechanism was analyzed using temperature monitoring, thermodynamic analysis and microstructure investigation.

A computer simulation using ANSYS was carried out to investigate the effects of processing parameters on the temperature distribution in induction heating. Experimental work has shown that the simulation results had a good agreement with experimental tests and the simulation can be applied to explain the heating behaviour during induction heating. The simulation was also used to investigate the solidification process to understand the cooling process during SHS.

Contents

ACKNOWLEDGEMENT i

ABSTRACT iii

LIST OF FIGURES ix

LIST OF TABLES xii

CHAPTER 1 INTRODUCTION 1

1.1 BACKGROUND 1

1.2 OBJECTIVES OF THE PRESENT STUDY 3

CHAPTER 2 LITERATURE REVIEW 6

2.1 LITERATURE REVIEW OF SELF-PROPAGATING HIGH-TEMPERATURE SYNTHESIS 6

2.1.1 Introduction 6

2.1.2 SHS Applications 7

2.1.3 Advantage and limitation 9

2.1.4 SHS reaction 11

2.1.5 Study on the mechanism of combustion 20

2.2 INDUCTION HEATING TECHNIQUE 25

2.2.1 Introduction 25

2.2.2 Theoretical background 26

2.2.3 Current and Power density 28

2.2.4 New applications in materials engineering 30

2.3 INDUCTION HEATING WITH SHS 31

2.4 SUMMARY 32

CHAPTER 3 EXPERIMENTAL DETAILS 34

3.1 INTRODUCTION 34

3.2 MATERIALS PREPARATION 34

3.2.1 Particle selection 34

3.2.2 Sample pellet preparation *38*

3.3 THE INDUCTION HEATING SYSTEM 41

3.4 THE ATMOSPHERIC CONTROL SYSTEM 42

3.5 TEMPERATURE MONITORING AND CALIBRATION 44

3.6 CHARACTERISATION OF THE PRODUCTS 51

CHAPTER 4 THE STRUCTURE AND PROPERTIES OF NIAL FORMED BY SHS USING INDUCTION HEATING **53**

4.1 INTRODUCTION 53

4.2 EXPERIMENTAL PROCEDURE 57

4.3 RESULTS AND DISCUSSION 57

4.3.1 Phase characteristics *57*

4.3.2 Combustion reaction under induction heating *61*

4.4 MICROSTRUCTURE OF THE SYNTHESISED PRODUCTS 71

4.4.1 The crystalline structure of synthesized product *71*

4.4.2 The effect of green density *74*

4.4.3 The effect of heating rates *76*

4.4.4 Mechanical properties of synthesized products *78*

4.5 SUMMARY 80

CHAPTER 5 COMBUSTION SYNTHESIS OF NIAL/AL_2O_3 COMPOSITES BY INDUCTION HEATING **82**

5.1 INTRODUCTION 82

5.2 EXPERIMENTAL PROCEDURES 83

5.3 RESULTS AND DISCUSSION 83

5.3.1 Chemical phase characteristics *83*

5.3.2 The effect Al_2O_3 content on the combustion temperature *84*

5.3.3 Heating behaviour *85*

5.3.4 Ignition process *87*

5.3.5 Combustion and solidification *92*

5.3.6 Microstructure and properties *95*

5.3.7 Formation of Ni_2Al_3 ..... *97*

5.4 SUMMARY 99

CHAPTER 6 COMBUSTION SYNTHESIS OF TIC-NIAL COMPOSITE BY INDUCTION HEATING **101**

6.1 INTRODUCTION 101

6.2 EXPERIMENTAL DETAILS 102

6.3 RESULTS AND DISCUSSION 103

6.3.1 Synthesis of NiAl and TiC composites *103*

6.3.2 Combustion reaction under induction heating *104*

6.3.3 Microstructure and synthesis mechanism for TiC *108*

6.3.4 Synthesis of two-layer composite *112*

6.3.5 Thermal dynamics analysis for the NiAl/TiC system *116*

6.3.6 Reaction mechanism of the combustion synthesis *119*

6.4 CONCLUSION 121

CHAPTER 7 COMPUTER SIMULATION FOR INDUCTION HEATING **123**

7.1 INTRODUCTION 123

7.2 SIMULATION MODEL SETUP FOR INDUCTION HEATING 124

7.2.1 Procedure and setting *124*

7.2.2 Model build *126*

7.2.3 Attributes assignment *127*

7.2.4 Validation with experimental work *130*

7.3 THE EFFECT OF AIR-GAP IN AXIS DIRECTION 132

7.4 THE EFFECT OF AIR-GAP IN RADIAL DIRECTION ON INDUCTION HEATING 142

7.5 THE SIMULATION OF PRODUCT SOLIDIFICATION 151

7.5.1 Assumptions and settings *152*

7.5.2 Validation of the mode *156*

7.5.3 NiAl solidification with preheating *157*

7.5.4 The effect of Al_2O_3 as additive *159*

7.6 SUMMARY 161

CHAPTER 8 CONCLUSION AND FURTHER WORK 162

8.1 CONCLUSIONS 162

8.1.1 SHS of NiAl and its composites using induction heating *162*

8.1.2 The temperature recording and combustion monitoring *163*

8.1.3 Synthesis mechanism of NiAl and NiAl based composite *164*

8.2 RECOMMEND FUTURE WORK 164

APPENDIX A SIMULATION CODES 166

APPENDIX B ELEMENT USED IN INDUCTION HEATING SIMULATION 183

APPENDIX C ANIMATION OF SIMULATION FOR INDUCTION AND SOLIDIFICATION 185

APPENDIX D (DATA SOURCE: ANSYS 12.0 HELP FILE) 186

List of Figures

Figure 2-1 The process of SHS technique 7

Figure 2-2 Schematic representation of two different approaches to describe combustion wave propagation: (a) quasihomogenous ;(b)heterogeneous (relay-race type) [115] 19

Figure 2-3 Illustration of the module quenching design by Guoqing Xiao 20

Figure 2-4 Schematic drawing of a model to the dissolution-precipitation mechanism 21

Figure 2-5 General view of the time-resolved X-ray diffraction and infrared camera device (1) Synchrotron radiation λ = 0.15406 nm, (2) fast X-ray detector, (3) sample holder, (4) infrared camera, (5) carbon ribbon electrode, (6) reacting chamber under nitrogen atmosphere and (7) sample. 24

Figure 3-1 The morphologies of raw materials used in this study 36

Figure 3-2 The steel model for powder compressing 39

Figure 3-3 Compressed pellets (a) Ni/Al; (b) Ni/Al with 20 wt% of Ti/C 40

Figure 3-4 Sketch of acrylic panel and setting of panel 44

Figure 3-5 Calibration of Raynger MX infra-red thermometer; a) 10 K/s and b) 20 K/s 49

Figure 3-6 Calibration of Marathon MM1MH thermometer 50

Figure 3-7 Schematic diagram of experimental set up 50

Figure 4-1 The phase diagram of Ni-Al system [9] 55

Figure 4-2 X-ray diffraction patterns; a) sintered compact and b) compact before sintering. 59

Figure 4-3 X-ray diffraction pattern for sintered samples with different green densities 61

Figure 4-4 Thermal image before ignition heated at 300A 63

Figure 4-5 The effect of currents on the heating rates and ignition of Ni/Al compacts 63

Figure 4-6 Thermal image during combustion synthesis using (a) 300A; (b) 200A 65

Figure 4-7 The flow chart of reaction temperature calculation 67

Figure 4-8 Preheating effect on the combustion temperature for the synthesis NiAl 68

Figure 4-9 The effect of green density on the heating rates and ignition of Ni/Al compacts 69

Figure 4-10 Microstructure of synthesized NiAl using 300A. (a)non-etched; (b)etched 15s; (c) individual faceted crystal in a large grain; (d) faceted crystal at grain boundary 72

Figure 4-11 EDX analysis result; a) the facetted crystal; b)the matrix of sample 73

Figure 4-12 Fracture surface of green compacts: (a) 49.4%TD; (b) 64.4%TD 75

Figure 4-13 Microstructure of synthesised products with different green densities: (a) 56.3%TD; (b) 58.6%TD; (c) 61.2%TD; (d) 64.4%TD 76

Figure 4-14 Microstructure of synthesised products with different heating power: (a) 200A; (b) 225A; (c) 250A ;(d) 275A; (e) 300A 78

Figure 4-15 The effects to heating current on the hardness of synthesised products 79

Figure 4-16 The effect of green density on the hardness of synthesised products 80

Figure 5-1 X-ray diffraction pattern for 10% and 12% Al_2O_3 addition products 84

Figure 5-2 Measured temperature during process for the samples with different Al_2O_3 contents 85

Figure 5-3 Ignition and combustion propagation (a)3wt%; (b)7wt%; (c)10wt%; (d)12wt% 89

Figure 5-4 Monitoring of combustion behaviour for reacted samples (a) 3wt%; (b)7wt%; (c)10wt%; (d)12wt%. P1 to P5 represent the positions given in Figure 5-3 90

Figure 5-5 Fracture surface of compressed sample with 12wt% Al_2O_3. 92

Figure 5-6 The effects of preheating and Al_2O_3 wt% on the liquid content of NiAl 94

Figure 5-7 Microstructure with varies Al_2O_3 content (a) 3wt %; (b) 12wt% 95

Figure 5-8 Effect of Al_2O_3 addition to hardness of product 96

Figure 5-9 Fracture surface of product with Al_2O_3 addition (a) 3wt%; (b) 12wt% 97

Figure 6-1 The X-ray pattern of synthesized products 104

Figure 6-2 Temperature profile of samples during synthesis 105

Figure 6-3 Thermal images and temperature profiles during synthesis. (a) 5wt% TiC ; (b) 10wt% TiC;(c) 15wt% TiC 107

Figure 6-4 Microstructure of NiAl/TiC samples 109

Figure 6-5 Fracture surface of 5wt%TiC and 15wt%TiC specimen 110

Figure 6-6 Effect of TiC on NiAl hardness 112

Figure 6-7 Thermal images of two layers sample during combustion reaction 113

Figure 6-8 XRD pattern of two layer products 114

Figure 6-9 Microstructure of two layer product (a)two layer product;(b)TiC rich area; (c) NiAl rich area;(d) EDX results 116

Figure 6-10 Calculated combustion temperature as a function of Ti/C content and preheating temperature..... 119

Figure 7-1 Flow diagram for induction heating simulation 125

Figure 7-2 Model setting induction heating simulation 128

Figure 7-3 Mesh results for the induction heating simulation 130

Figure 7-4 Measured steel temperature via induction heating 131

Figure 7-5 The effect of air-gaps in axis direction on the temperature distribution at the end of heating of 4 s. 135

Figure 7-6 Heating of samples with various air-gap (a) nodes position ; (b) 2mm; (c) 3mm; (d) 4mm; (e) 5mm; (f) 6mm 138

Figure 7-7 Magnetic field distribution at different air-gap: (a) 2mm; (b) 3mm; (c) 4mm; (d) 5mm; (e) 6mm . 141

Figure 7-8 Temperature distribution at the end of heating for samples heated at different air-gaps (=10- the radius of sample) in radial direction 144

Figure 7-9 Temperature profile during induction heating for the samples with different radius; a) node positions; b) radius 5mm; c) radius 6mm; d) radius 7mm; e) radius 8mm; f) radius 9mm 148

Figure 7-10 Magnetic field distribution in radius group a) radius 5mm; b) radius 6mm; c) radius 7mm; d) radius 8mm; e) radius 9mm 151

Figure 7-11 Model of product cooling cases 154

Figure 7-12 Meshing for the solidification simulation 155

Figure 7-13 Temperature profile of 300A sample 157

Figure 7-14 Nodes' position of product 158

Figure 7-15 Simulation results of product solidification with preheating condition 159

Figure 7-16 Simulation results for synthesized NiAl with 10wt% Al_2O_3 during solidification..... 160

Figure 7-17 Temperature profile of 10wt% Al_2O_3 sample 161

List of Tables

Table 3-1 Raw materials' properties 37

Table 3-2 Electrical technical information of induction heating system 41

Table 3-3 Technical information of infra-red thermometers 45

Table 3-4 Technical data for thermal image camera 48

Table 4-1 Heating rate at different induction current 58

Table 4-2 Heating rate of green density group specimen 61

Table 5-1 Average heating rate as a function of Al_2O_3 content 85

Table 5-2 Thermal capacity of materials (date reference [149]) 87

Table 6-1 Thermal properties of elements (Data reference [149]) 118

Table 7-1 Relative permeability of Steel at different temperature 127

Table 7-2 Resistivity of Steel at different temperature 127

Table 7-3 Attributes setting for environments and modelling 128

Table 7-4 Attributes setting for modelling in product solidification case 154

Table 7-5 Materials properties in solidification simulation 155

Chapter 1 Introduction

1.1 Background

In the last two decades, intermetallic NiAl has been brought up to front stage as a candidate for high temperature applications. The excellent properties of this material include great oxidation resistance, high melting point, high thermal conductivity, low density (compare with Ni-based alloys) and relatively low cost. Therefore it has been widely investigated throughout aviation and new energy industries as a bulk material and protective coatings.

Significant work has been done related to NiAl and NiAl-based alloys. To summarize recent researches related to NiAl and NiAl-based alloys, there are four major research interests as listed below:

- The superplasticity and its mechanisms.
- The nanocrystalline NiAl and its composites.
- Effect of alloying elements and development NiAl eutectic alloys
- In-situ particle reinforced composites and mechanisms.

The first research direction, the superplasticity of NiAl and NiAl alloys, simplifies the manufacture process for thermal structural applications. It's been proved that NiAl, NiAl-25Cr, NiAl-Fe-Y etc. alloys have superplasticity behaviour [1-4]. The nanocrystalline microstructure enhances the yield stress and thermal resistance [5-9]. The NiAl eutectic alloys have decent mechanical properties compared to other

commercialize high temperature alloys, besides it does not require precious element such as Co, W, Nb, Ta etc.

The in-situ particle composites synthesis attracted researchers' interests due to the improvement of reinforced strength, plasticity along with ordinary manufacturing route. For example, by using thermal explosion synthesis, the yield stress of NiAl-20%TiB_2 (atom percentage) can reach to 1365 MPa, compare with 632 MPa of NiAl. The simple synthesis process also suggests future applications in thermal barrier coating.

As stated above the thermal explosion synthesis had been employed for in-situ particle composites synthesis. Technically the thermal explosion synthesis is an extreme condition of the "Self-Propagating High-temperature Synthesis" (SHS), which has been industrialized for the production of ceramics, intermetallics and composites since 1990s. It is also named as "Combustion Synthesis" (CS) in many occasions. Recently it has been introduced to synthesis shape memory alloy [10-13] and hydrogen storage alloys [14-18]. The synthesis method relies on energy releases from exothermic reactions to sustain the combustion. It is considered as an economic and energy efficient route with fewer requirements on equipment. Based on SHS, other applications including sintering, joining, casting, coating fabrication etc. were developed.

Abundant heating and ignition systems have been employed for SHS, including induction heating. The induction heating technique provides characteristics of fast heating rate and is friendly to the environment. In addition, it can be easily combined with other forming techniques such as Hot Isostatic Pressing (HIP) to achieve in-situ

synthesis and densification. Previously there are a few researches attempting to study the synthesis progress within an induction furnace. But the reaction was not fully monitored due to the restriction of the furnace. As a result, the heating behaviour and reaction mechanism under induction were not well investigated and the advantages of induction heating were not utilized.

1.2 Objectives of the present study

The objectives of this study were set up as below:

1. To develop a synthesis system for SHS of NiAl and its composites with induction heating. This work includes raw materials selection and equipment design. To avoid oxidation during SHS reaction, a reaction chamber with atmosphere control is needed.
2. To study the induction heating behaviour Ni/Al during SHS synthesis. The heating progress will be monitored. The heating rate effect and the influence of sample green density will be investigated.
3. To study the whole synthesis progress with complete temperature monitoring. The complete temperature profile including heating, combustion and cooling will be monitored with high speed thermal imaging and fast response infra-red (IR) thermometer.
4. To study the thermodynamics of NiAl synthesis. The maximum reaction temperature will be computed with various heating conditions and raw materials compositions.

5. To investigate the effects of Al_2O_3 on the synthesis of $NiAl/Al_2O_3$ composites and their mechanical properties. The synthesis progress of $NiAl/Al_2O_3$ will be monitored and synthesis mechanism will be analysized.
6. To synthesize NiAl/TiC composites using SHS with induction heating. Researches on NiAl/TiC composite will be implemented. The synthesis mechanism, microstructure of synthesized products and their mechanical properties will be studied.
7. To carry out finite element analysis for induction heating on steel and synthesised product. This work will enhance the understanding of the induction heating process, and will provide information for the analysis of sample solidification and crystallization after SHS reaction.

This thesis provides a systematic study to develop a new methodology for conventional "Self-Propagating High-temperature Synthesis" (SHS). Progressing in this direction, this thesis pioneers and studies the synthesis of NiAl and NiAl-based composites via induction heating.

The motivation, objectives and methodology are described in Chapter 2, along with a summary of contributions made in this study. Chapter 2 is an overview of recent research work in this field.

Chapter 3 addresses the requirements and techniques employed for this study. A complete manufacturing and progress monitoring system was developed. The sample preparation, reaction chamber and the calibrations of measurement devices are

discussed in this chapter. At the end of this chapter the sample characteristics methods are listed.

Chapter 4 presents the study on SHS of NiAl by induction heating. The complete synthesis process: ignition, combustion propagation and product cooling were recorded and analysized. The effects of heating rate and sample's green density were summarized. The crystallization of NiAl under this experimental setting was compared with other works.

The researches on $NiAl/Al_2O_3$ composites are presented in Chapter 5. The addition of Al_2O_3 affects the heating behaviour, combustion propagation and the cooling of products, consequently influences the properties of synthesized products. In addition, the critical concentration of Al_2O_3 with this ignition system was discussed.

Chapter 6 furthers the interests to NiAl/TiC composites. The NiAl/TiC was successfully fabricated and the fabrication of two-layer composites was attempted. Along with the property testing the reaction mechanisms for NiAl and TiC synthesis are proposed.

The finite element simulation results for induction heating on steel are shown in Chapter 7. Apart from this, the solidification and cooling of synthesized products were also investigated via finite element computation and validated with experimental data. The results provided more details helping to understand the ignition by induction heating and the solidification and cooling after synthesis reaction, which will be useful for process control for industry applications.

The last chapter summarizes the results of this study and provides suggestions for further research.

Chapter 2 Literature review

2.1 Literature review of Self-Propagating High-temperature Synthesis

2.1.1 Introduction

Along with the fast development in technology, the importance of energy-saving in manufacturing has been gradually recognized. Particularly, for the synthesis of materials, the development of efficient and energy-saving processes has attracted great attention to scientists. Compared with conventional synthesis using furnaces, the Self-Propagating High-temperature Synthesis (SHS) attracts researchers' interests owing to its economic advantage in fabricating certain ceramics, intermetallics and composites. Generally, the SHS is based on exothermic reactions and contains five stages as schematically presented in Figure 2-1. Reactants are weighted based on the chemical reaction and final products then mixed and prepared to form green compact. After ignition, the reaction is self-sustainable and propagates until all the reactants are consumed, as it's termed "Self-Propagating". Temperature of combustion is normally between 1800-3500K, which is designated as "High temperature". In most cases reactions are extremely intensive and propagate in the form of combustion waves, so this technique is also termed as "Combustion Synthesis" (CS).

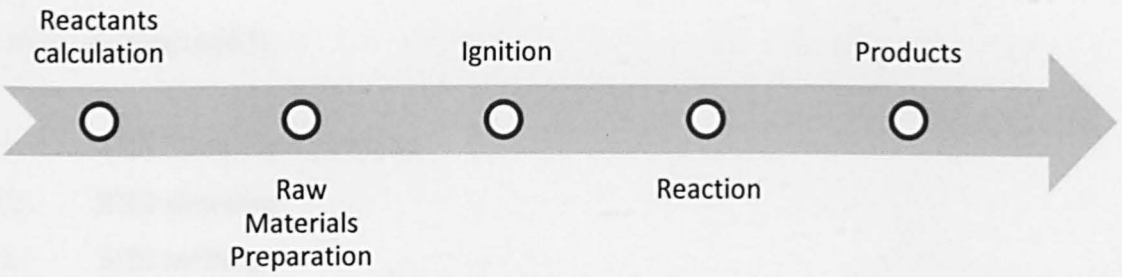

Figure 2-1 The process of SHS technique

2.1.2 SHS Applications

For SHS process, the reactants are normally in the form of fine powders which are mixed and compacted to the size required. The mixture is placed in a refractory container and ignited in a vacuum or inert atmosphere. The exothermic reaction of SHS is able to maintain the reaction after ignition and generates a combustion wave until the reaction is completed. Report has shown that the temperature of the combustion wave could reach to 3500k while velocity of the propagation wave can be as high as 250mm/s [19].

Previously, researchers have classified the SHS reactions in three types based on the reactants involved, namely [20]:

- Simple SHS reaction systems
- Thermite-type reaction systems
- Combustion synthesis of complex oxides

There are over 500 compounds that have been synthesizing by the SHS method [19]. The synthesis of carbides [21-36], borides [37-43], silicides [44-55] and

intermetallics [56-66] have been studied recently. The application of these materials was classified as[67]:

1. SHS fabrication powders
2. SHS sintering
3. SHS melting
4. SHS jointing
5. SHS coating

In general, two approaches were used in the application of SHS process. The first one combined the SHS process with other techniques by using the product obtained from SHS as raw materials. For example, since the SHS process can yield compounds with good chemical control, recently the SHS products were used for thermal spray. Celilia Bartuli et al. [68] have discussed the feasibility of using SHS powders for thermal spray. The SHS process was introduced after a Low-pressure Injection Moulding process in preparing AlN-TiB_2 ceramic slender tubes [69] to produce a densified product. After the success of utilizing SHS to synthesis powders as raw materials for advanced coating such as plasma deposition, attention recently are moved to the one-step coating process using SHS. Several attempts have been reported in cutting tool coatings and low friction coatings. But the porosity in coatings, weak bonding strength and microcracks reveal that great efforts on coating quality improvement are still required.

The second one takes the synthesis, structuring and shaping in one stage such as SHS coating. In the last decade researchers had shown great interest in SHS in-situ coating [70-82]. Various techniques were employed for SHS coating fabrication including laser, solar energy assistant, microwave, casting and thermal spray etc. The laser cladding of SHS coatings were successfully produced in Man's research [74].

Sierra et al. investigated the NiAl coating with solar assisted SHS process and managed to obtain metallic bonding [70, 79]. He also suggested that a thin Ni intermediate gradient layer can be used to achieve better bonding [80]. In these solar-assisted researches, the solar energy was not only used for ignition but also for enhancing the bonding strength. Although good bonding was received, the coating quality was not satisfied due to high porosity. The inherent limitation of solar energy technique restricted pressure assistance in coating synthesis since no pressure can be applied on the components. Ni_3Al and $MoSi_2$-MoS_2 coatings on steel were fabricated by SHS casting [76-77]. The casting route was designed to utilize the energy released in the casting process to ignite SHS subsequently to form the coating. The poor control in coating fabrication resulted in poor quality and reliability.

Other applications of SHS have also been investigated, for example, Zhang Ruizhu attempted using SHS for radioactive waste immobilization. In this research $CaTiO_3$ and $SrTiO_3$ were synthesis for final disposal of the nuclear wastes [83].

2.1.3 Advantage and limitation

One noticeable advantage of SHS is low cost compared to conventional synthesis processes. SHS relies on exothermally reactions and requires less complicated equipments and facilities to handle the entire processes. Therefore this simple process can reduce the initial costs. Meanwhile, the high velocity of combustion synthesis results in a high production rate.

Another advantage for the SHS is its high combustion temperature that can volatilize low boiling point impurities during the synthesis so that high purity products can be obtained. For example, researches showed that in the case of MoSi and TiC SHS

synthesis for thermal spray, no impurities or residual non-reacted compounds were detected [68].

In addition, the SHS technology provides the convenience to combine the synthesise process and consolidating process in one step, by utilizing the energy of exothermic reaction. Several researches focused on this field have been published [84-87] .

There are also some limitations in SHS technology. The limitation of exothermic reactions is one of them. If the reaction is not self-sustainable, the synthesis may require extra energy to active, or may not be able to react.

In relation to conventional ceramic or intermetallic synthesis, SHS has difficulties in controlling the microstructure of final products. Since the combustion reaction velocity and cooling rate are very high it is difficult to achieve thermal equilibrium in synthesis. Besides, the difficulty in controlling the grain size of SHS products remains as a shortcoming.

The products of SHS are normally porous, which could be considered as a limitation for some applications such shape memory alloy fabrication. Densification processes associated with SHS were introduced to achieve the expected mechanical properties. Nevertheless, the porosity of SHS products can be utilized for some industrial applications such as synthesis sponge products.

2.1.4 SHS reaction

Selection of raw materials

The particle size and shape of reactants have been widely investigated in past decades, and it is known that these affect the SHS process in several aspects: the degree of the reaction, the temporal sequence of the reaction, the temperature profile of the combustion zone and the velocity of the combustion wave [88]. Several studies focus on the relationship between particle size and the degree of reaction were conducted [19-20, 89]. Also, the effects of particle size distribution were considered by other authors [88].

Particularly, for the synthesis of NiAl, the particle size effects were studied in some literature [90-93]. Concerning the Al particle, Dong used nano size Al raw materials and produced single phase dense NiAl via SHS [90]. However, in Hunt's investigation, due to the high oxidation composition in nano size Al particle, residual Al_2O_3 was detected in the products [91]. For the Ni particle, in Fan's research the coarse Ni particle (100 micron) resulted in incomplete reaction which suggests that fine Ni particle should be used in combustion synthesis[92]. Biswas studied the effects of Ni particles at various heating rates and concluded that to synthesize single phase of NiAl the heating rate must be over 35℃/min for 130 micron and 110 micron Ni particles [93-94].

Particle shape effects have been analyzed in various aspects. In general, in compression the more slippery of particles' surface, the less inter friction between particles. Also the particle shape related to the thermal conductivity and other perspectives. For example, the carbonyl Ni particle has unique powder morphology

as spiky dendritic structure which broaden its application in electromagnetic wave absorption.

The effect of particle shape depends on its manufacture process and on the mixing process. The dry mixing process could result in inhomogeneous structures in the SHS synthesized products; therefore the wet process was recommended [19].

Preheating

Before the SHS process is ignited, in some cases, a preheating step was employed. Not only for the purification purpose, the preheating can also eliminate the rapid and large volume expansion of adsorbed gases in the sample which could lead to exfoliation of final product [88]. It is clear that another effect of preheating is that it will increase the initial temperature of the powder mixture, and eventually contributes to the highest temperature as well as the final products.

In the literature [20] it explains the preheating effect with the thermodynamics estimation. The combustion can be considered as an adiabatic condition due to its fast reaction velocity. Considering the energy conservation, the energy balance before and after synthesis can be expressed as:

$$\sum H\,(n_i R_i) = \sum H(m_j P_j) \qquad \textbf{2-1}$$

where H is the enthalpy, n_i and m_j are the numbers of reactants and synthesized products respectively, and R_i stands for reactance, P_j stands for products.

Given the initial temperature T_0, the ignition temperature T_{ig}, the highest temperature in adiabatic condition T_{ad}, the change of enthalpy for the reactants $H(R)$ can be expressed as:

$$H(R) = \int_{T_0}^{T_{ig}} \sum n_i C_p(R_i) dT + L(R_i) \quad \text{2-2}$$

where $C_p(R_i)$, $L(R_i)$ are the heat capacity and the phase transformation (if there is a phase transformation happening in the heating process) enthalpy of reactants, respectively. Accordingly, for the product, the change of enthalpy $H(P)$ can be expressed as:

$$H(P) = \int_{T_o}^{T_{ad}} \sum m_j C_p(P_j) dT + L(P_j) \quad \text{2-3}$$

where $C_p(P_j)$ and $L(P_j)$ are the heat capacity and phase transformation enthalpy (if there is a phase transformation during the heating) of the products respectively.

Therefore, given the $\Delta H\ (T_{ig})$ is the heat used to heat the adjacent reactant layer from T_0 to T_{ig}, the $\Delta H(T_{ig})$ can be considered as

$$\Delta H(T_{ig}) = -[H(P) + H(R)] \quad \text{2-4}$$

For every particular reaction system, once the parameters for the reaction have been fixed, the $\Delta H(T_{ig})$ will be a constant. So when the initial or preheating temperature (T_o) for the reaction system is increased, higher T_{ad} will be achieved.

It has also been reported that the preheating step can also affect the combustion front velocity significantly [95] . Despite the difference in the particle size and the porosity of green compact, each group of samples showed a tendency that the flame-front velocity increased along with raising the preheating temperature.

In the case of TiAl-TiB_2 researches, preheating step turned out to be a prerequisite to ignite the SHS process and varying the preheating temperatures affected the composition of final product [95]. In comparison with samples preheated at 200 °C,

the sample preheated at 300 °C contains no $TiAl_3$ phase which is considered as the first intermediate phase formed in the combustion synthesis [96].

However, the higher preheating temperature sometimes is not desirable for microstructure control of the final product. In the case of Al_2O_3-TiC composite powder fabrication, study showed that higher preheating temperature could result in bigger TiC particle size [96]. The author deduced that the most important factor in determining particle growth was the cooling time, but the Al_2O_3 produced wasn't influenced by the preheating temperature. The answer to why Al_2O_3 had not been affected by the cooling time was not explained in this study.

Ignition

The ignition mechanism for SHS depends on the ignition method and reactants. Previously researchers proposed the Frank-Kamenetskii's thermal ignition theory. Several mathematical models have been developed to describe the ignition mechanism, as summarized in literature [67]. In this literature it is concluded that so far no solid experimental work were reported to support these theoretical studies.

Various ignition methods for SHS reactions have been investigated since 1960s which are listed below:

- Radiation
- Combustion wave
- Laser
- Microwave
- Electric spark
- Solar
- Hot-blast
- Chemical

- Mechanical alloying

Radiation is one popular ignition method which has been used for decade[67]. There are various types of radiation heating and heating using tungsten wire is the popular one. The combustion wave process is designed to use one reaction's flame to ignite another reaction. For example, the Ti+C reaction is used to ignite the W+C reaction [67]. After synthesis, the TiC can be easily peeled off from WC product.

The laser ignition has recently revealed a fast developing process for SHS ignition recently [73-74, 91, 97-101]. This ignition technique provides a possibility to produce very high heat flux density, up to 10^{11} Wm^{-2}. Various types of laser have been employed, such as CO_2, neodymium-doped glass laser, ruby laser and cesium bromide laser. The convenience of high heat flux also brought the possibility of melting and vaporizing reactants and products.

Microwave ignition of SHS also attracted interests for many researchers, although the mechanism of heating up powders is complex to understand [44-45, 102-104]. Ignited by microwave, the combustion process starts at the centre of a green compact, and propagates outwards until finished. One limitation of the microwave ignition process is the heating is not controllable. This is because the coupling effect of compacted particles with the microwave was so complicated and so far no predicable models can be applied. The heating behaviour of microwave systems varies case by case. With the measured experimental data, in the literature [103] simulation work has been reported for optimizing the heating parameters.

Also, igniting the SHS mixture by solar energy was researched in the NiAl intermetallic coatings synthesis [70, 79-80, 86, 105]. Concentrated solar energy

(CSE) not only provided the necessary heat to initiate the reaction but also permitted the propagation of reaction through a reactant mixture of powders. This process has the advantage of energy efficiency and environmental safety, however, can be affected significantly by climate change which makes it unsuitable for industrial application.

In addition, for some particular chemical reactions, mechanical alloying (MA) which also is referred as high energy ball milling, is used to ignite the SHS as well [39, 106-113]. As Soni pointed out, the MA technique has advantages in homogeneity of products and fine particle sizes[114]. The combination of MA and combustion synthesis has successfully produced nano-scale products[111, 113].

Some researchers added chemicals to raw powders to achieve the chemical ignition [2]. Reactive gaseous or a liquid reagent was carefully calculated to ensure to expose the energy required for ignition.

During ignition the heating rate has been proved to have an influence on the SHS mechanism, but this is almost certainly reaction specific, and dependent on the possible intermediate reactions that can take place. For the case of Ni_3Al synthesis, the velocity of the reaction front decreased with an increase in ignition power. Using a high ignition power, namely a high heating rate, more energy is lost by conduction to the cold unreacted part, leading to an incompletely developed non-equilibrium microstructure which is similar to that achieved at low green density.

Heat transfer in SHS

It is desirable to study the heat transfer in SHS mixtures before discussing the SHS fabrication reaction. Debates upon the heat transfer models have shown the difficulty

of explaining the SHS reaction using thermal dynamic theory. Thus in this report only the mainstream point of view will be presented.

Based on high-speed digital video technology, Mukasyan et al. analyzed a model for the reactant medium [115]. With the assumption that the reactant medium was homogeneous and reaction happened in a narrow zone, they suggested that the combustion velocity can be expressed as:

$$V_{ad}^2 = f(n)\alpha C p T_{ad}^2 K_0 exp(-E/RT_{ad})/QE \qquad \textbf{2-5}$$

Where the $f(n)$ is a kinetic function of the reaction, n *and* k_0 are constants, E is the activation energy; R is gas constant; T is the temperature; Cp is the thermal capacity of product and α is the thermal conductivity. There is no relationship between the reaction velocity and particle size in the equation, since the "homogeneous" assumption didn't count the particle size effect.

For the model that one reactant melts and surrounds the spherical particles of other reactant, the mechanisms were considered as the diffusion of liquid phase through solid surface and reaction kinetics at the surface of solid reactant. Both of these two mechanisms are dependent to the particle size. Particularly in the two elements reaction, two combustion models were proposed as: diffusion and capillary. For diffusion mode there is an expression to descript the relationship of particles size:

$$r_0^2 \ll \sigma \lambda r_r \mu V^2 ln\left[\frac{(T_c - T_0)}{(T_m - T_0)}\right] \qquad \textbf{2-6}$$

where r_0 is the particle size of the starting metal component, r_r is the particle size of the refractory non molten component, l is the thermal diffusivity, σ is the surface tension of the liquid, μ is the viscosity of the liquid, V is the velocity of the

combustion front, T_c is the combustion temperature, T_m is the melting point of the molten component and T_0 is the pre-heating temperature or the initial temperature.

For the capillary mode:

$$r_0 \gg \frac{\sigma r_r}{\mu D} \qquad \text{2-7}$$

where D is the diffusion coefficient.

Mukasyan et al. have discussed the principle of this issue and described two approaches to understand the process [115].

If the temperature gradients ΔT in the green mixture could be considered as follow:

$$\Delta T_d \ll \Delta T_L \qquad \text{2-8}$$

Where ΔT_d refers to the temperature gradients of scale of particles

ΔT_L refers to the temperature gradients of system dimension L

and therefore in terms of analyzing the heat flow through the heterogeneous medium, the effect properties of the sample, such as heat capacity, thermal conductivity and radiation scattering coefficient, were used in a *quasihomogeneous* calculation, as shown in Figure 2-2a. In condensed systems, the characteristic time of chemical reaction ($t_{cr} \sim d^2/D$, where d is particle dimension and D is diffusion coefficient) is much smaller than time scale of heat transfer ($t_{ht} \sim L^2/\alpha$, where α is thermal diffusivity), hence the heterogeneous systems could be replaced to a homogeneous medium with the assumption that (Figure 2-2a)

$$t_{cr} \ll t_{ht} \qquad \text{2-9}$$

However, the SHS mixture system is essentially nonconsolidated heterogeneous media and normally the particles are randomly arranged with irregularly shape. In

some practical experiments, the t_{ht} is much larger (10^{-3}-10^{-4}s) than in bulk metals (10^{-5}-10^{-7}s), and t_{cr} in SHS mixture may rise to 10^{-4}-10^{-5}s. Thus the requirements of $\Delta T_d << \Delta T_L$ cannot be satisfied, and the analysis based on heterogeneous medium is required.

The mechanism of heat transfer in combustion synthesis involves conduction through the solid phase, conduction through the gas phase, convection through the pores and radiation. Generally the conduction through the solid phase can be considered as the fastest step mechanism, though the others can also affect the temperature profile of the combustion propagation to some extent.

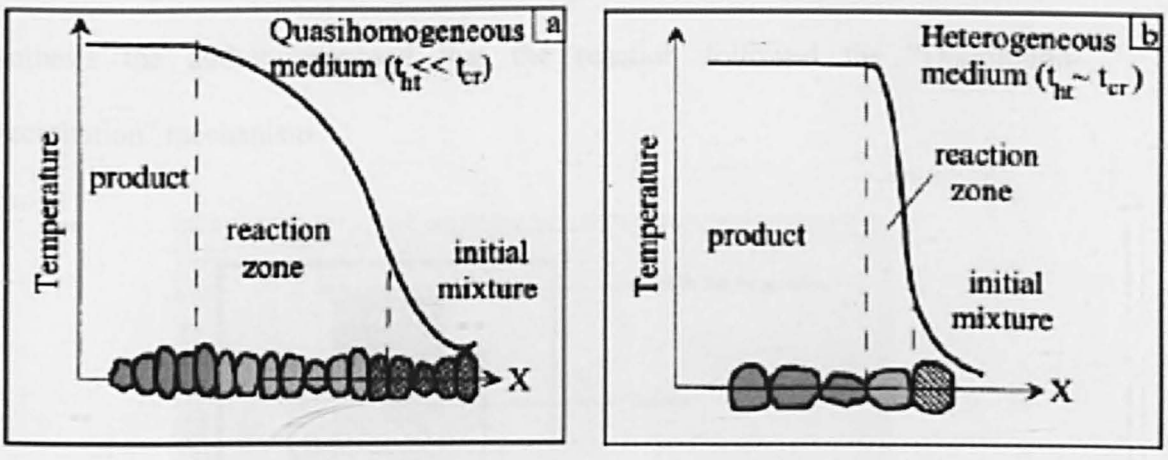

Figure 2-2 Schematic representation of two different approaches to describe combustion wave propagation: (a) quasihomogenous ;(b)heterogeneous (relay-race type) [115]

For more detailed description about the heterogeneous module introduced to combustion synthesis, Makino presented a comprehensive review in his study [116].

2.1.5 Study on the mechanism of combustion

To understand the mechanism of the combustion synthesis is the current research trend in SHS research. Since it is difficult to monitor the high temperature and high velocity reaction in-situ, the "quenching" method was widely employed to investigate the reaction [61, 92-93, 108, 117-119].

The quenching method was researched in a wide range with the purpose of analyzing the microstructure of the reaction zone, preheated zone and product respectively. Concerning the Ti-Ni the system, Xiao et al. studied the mechanism of the combustion reaction with quenching method [120]. The device they adopted was shown in Figure 2-3. In his device steel is employed for cooling. For Ti-Ni-C synthesis the author proposed that the reaction followed the "Dissolution-precipitation" mechanism.

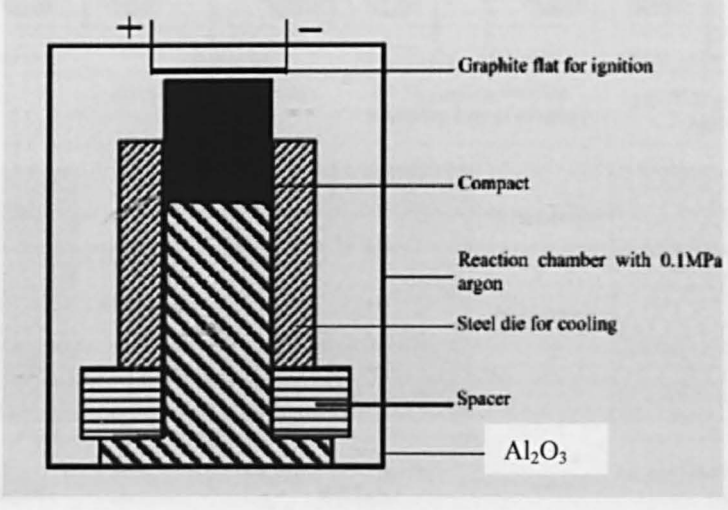

Figure 2-3 Illustration of the module quenching design by Guoqing Xiao

Quesheng has systematically studied the combustion mechanism of Ti/C reactions [121]. In his investigation the quenching device design was similar to Xiao's with differences in dimensions. For the product morphology research, Fan proposed that

the SEM scan should be conducted after etching. Fan extended the research of Ti+C reaction with the addition of Fe powder and the mechanism of the reaction for Ti+C+Ni system was presented [122].

There were several investigations on NiAl synthesis mechanism via quenching method. Fan proposed a schematic drawing of Figure 2-4[92]. As shown in Figure 2-4, the Al powder starts melting first, then the dissolving of Ni reactants indicates the beginning of synthesis. Ni particles keep dissolving into liquid, and the emergence of NiAl grain is shown in Figure 2-4 (d), which is termed as precipitation. Finally, the process of this dissolve-precipitation ends up with NiAl products.

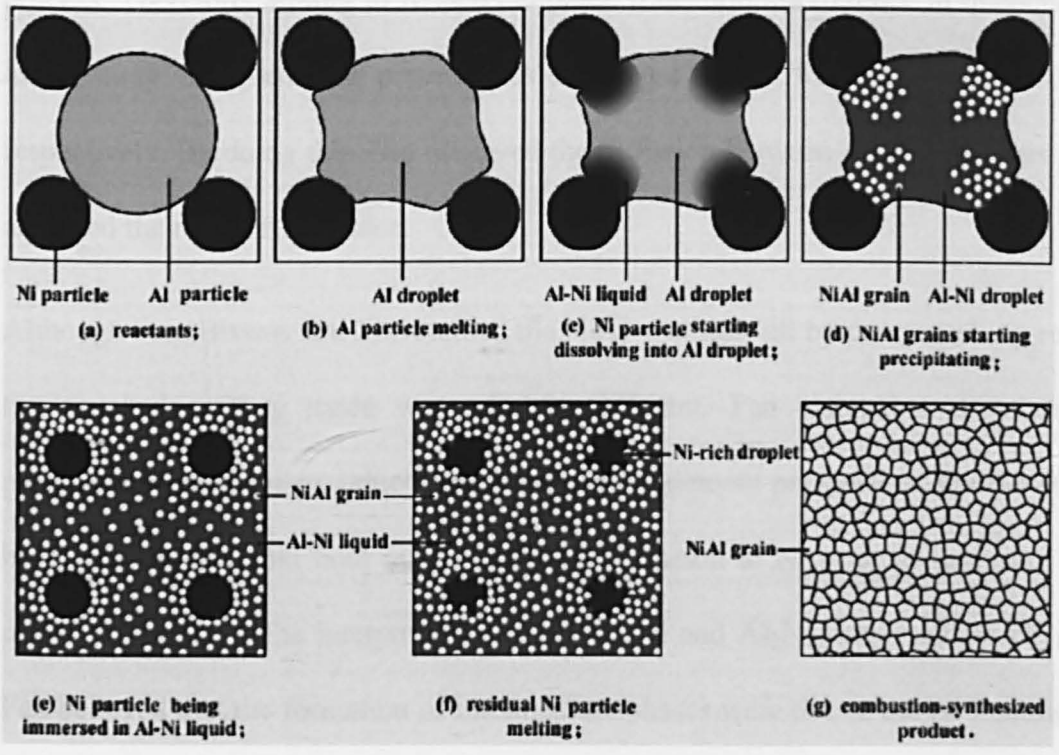

Figure 2-4 Schematic drawing of a model to the dissolution-precipitation mechanism

For the NiAl synthesis, Biswas et al. also conducted extensive researches by quenching the combustion front [93, 117]. Supported by the microstructure along

with combustion front, the author proposed that the reaction synthesis starts from the melting of Al and is followed by the formation of Al_3Ni films at the particle interface. The melting of Al continues with the formation of Al_3Ni_2 and NiAl crystals appear with Ni diffusion into the liquid phase. Finally the product of NiAl crystallization complete.

Still with NiAl synthesis, Zhu proposed a quench investigation with metal films [123]. Zhu believed that conventional particle reactants limited the research of reaction mechanism, so he conducted the study with alternative Ni and Al film for SHS NiAl. He also pointed out the possibility of phase transition in the quenching process. Therefore, aiming to reduce the phase transition interference in quenching, in his study, the quenching process was conducted at 700, 820, 1180 and 1280 °C respectively. By doing this Zhu observed the diffusion between Ni and Al films and analyzed the reaction sequence.

Although Fan, Biswas and Zhu studied the NiAl synthesis all by the quenching route, the conclusions they made were slightly different. Fan claimed a dissolution-precipitation mechanism, which was based on Ni element perspective. On the other hand, Biswas and Zhu both observed the Al diffusion to Ni prior to ignition. The major difference is the interpretation of the Al_3Ni and Al_2Ni_3 intermediate phases. Fan believed that the formation of intermediate phases were due to the Al melting at the interface. In comparison with Fan work, Zhu's quenching process was conducted below the Al melting point which minimized the quenching effect for phase analysis. The usage of thin films made the clear diffusion between layers become very convincing. Besides, the appearance of Al_3Ni and Al_3Ni_2 at an early

stage was in accordance with Biswas' work. Therefore the diffusion of Al to Ni particles should be the main reason for intermediate phases' formation.

The fast cooling rate provides a chance to detect phase transfer and chemical composition at the middle stage throughout the combustion. As mentioned above the liquid nitrogen was employed to quench the reaction so that metaphase products could be obtained [124].

As stated above, though the quenching method enables one to analyze the microstructure as well as the chemical phase in the combustion zone, it is valueable for the phase transition during the quenching process. Researchers have also employed other techniques to study the combustion synthesis mechanism, such as the "digital high-speed microscopic video recording" (DHSMVR) and time-resolved diffraction.

The DHSMVR technology used by Mukasyan [115] could record 12,000 frames per second, which enabled him to study the combustion reaction in a time scale of 10^{-4}s. In that study, the author observed that on the time scale of 10^{-2}-10^{-3}s the reaction front propagation consists of hesitations and rapid jumps, while on the time scale of 10^{-4}s the front propagation appears a scintillating reaction wave mechanism.

The DHSMVR technique gives detailed information for ignition and combustion propagation analysis, but limited data with the chemical reaction process. Another in-suit examining technique, the in-situ time-resolved diffraction, was developed to help researchers to understand the phase transitions throughout combustion, and it could be combined with other technologies such as infrared thermography and differential scanning calorimetry (DSC) to obtain more comprehensive data.

Recently the SHS reaction mechanism for the synthesis of TiN was investigated with the assistance of time-resolved diffraction and infrared thermography [125]. The devices setup is schematically shown in Figure 2-5. The X-ray diffractograms recorded evolutions of crystalline structure every 320 ms, which demonstrated the emergence of α-β-Ti transition both in with and without dilute conditions. Meanwhile, the infrared recording camera is placed with the X-ray diffractograms to detect the temperature changes during synthesis. The authors concluded the data and proposed the reaction model is the surface model that contacts between particles plays a vital role in the synthesis.

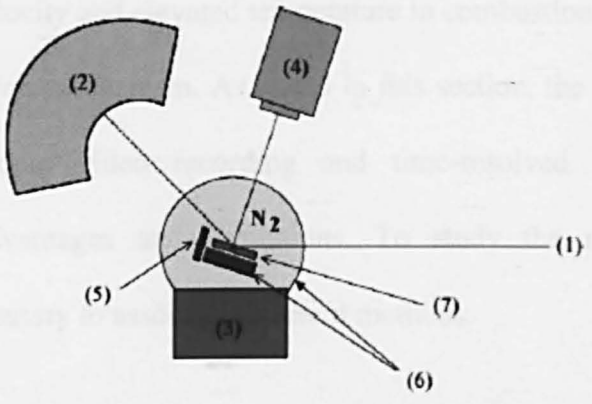

Figure 2-5 General view of the time-resolved X-ray diffraction and infrared camera device (1) Synchrotron radiation λ = 0.15406 nm, (2) fast X-ray detector, (3) sample holder, (4) infrared camera, (5) carbon ribbon electrode, (6) reacting chamber under nitrogen atmosphere and (7) sample.

In the NiAl intermetallic SHS synthesis a time-resolved X-ray diffraction study was reported [126]. Associated with DSC data, the author claimed that the Ni-Al SHS reaction starts at the melting of Al powder and ends up with $AlNi_3$, Al_3Ni_5 etc impurities.

The principal limitation of time-resolved X-ray diffraction technique is the incapability of detecting non-crystal phase, so it can't detect the liquid phase during the NiAl synthesis. The intermediate phase $AlNi_3$ and Al_2Ni_3 has a lower melting point compared with combustion temperature and it couldn't be detected via time-resolved X-ray diffraction. Another drawback of this technique is the response time. Curfs et al. had reduced scanning interval to 110 ms and speeded data process interval to 25 ms, still not be able to match the reaction velocity [108]. Thus the study results for NiAl synthesis by time-resolved X-ray diffraction technique need to be carefully used.

The high reaction velocity and elevated temperature in combustion synthesis restricts the analysis of reaction mechanism. As stated in this section, the quenching, digital high-speed microscopic video recording and time-resolved X-ray diffraction techniques have advantages and limitations. To study the reaction synthesis mechanism, it is necessary to associate different methods.

2.2 Induction heating technique

2.2.1 Introduction

The induction heating technology is considered as a highly efficient and economical process in metal heating and has been adopting for industrial heating for several decades. Conventionally its applications for engineering include:

- Metal forming
- Surface treatment
- Joining

- Heating vessels, vats and pipes
- Drying, curing and bonding

There are three basic principles for induction heating: electromagnetic induction, "skin effect", and heat transfer. Considering this research involves numerical simulation, it is desirable to go through some basic electromagnetic theory briefly.

2.2.2 Theoretical background

Fundamental electromagnetism principles

Based o n observation that in magnetic field, **B** always follows the rules that:

$$\nabla \cdot \mathbf{B} = 0 \qquad \textbf{2-10}$$

which implies that there are no isolated magnetic poles.

Maxwell's equations in differential form:

$$\begin{cases} \nabla \cdot \mathbf{D} = \rho & \text{(Gauss's Law)} \\ \nabla \times \mathbf{H} = \mathbf{J} + \frac{\partial \mathbf{D}}{\partial t} & \text{(Ampere's Law)} \\ \nabla \times \mathbf{E} = -\frac{\partial \mathbf{B}}{\partial t} & \text{(Law of electromagnetic induction)} \\ \nabla \cdot \mathbf{B} = 0 & \text{(Observation)} \end{cases}$$

In order to use Maxwell's equations, one must also know the applicable constitutive equations. For electromagnetic isotropic materials, there are

$$\begin{cases} \mathbf{D} = \varepsilon \varepsilon_0 \boldsymbol{E} \\ \mathbf{B} = \mu \mu_0 \mathbf{H} \\ \boldsymbol{j_0} = \sigma(\mathbf{E} + \mathbf{K}) \end{cases}$$

To couple with the Lorentz force equation,

$$\mathbf{F} = \boldsymbol{q}(\mathbf{E} + \mathbf{v} \times \mathbf{B}) \qquad \textbf{2-11}$$

Which describes the action of the fields on charged particles, this set of laws gives the complete classical description of the electromagnetic interaction of particles.

Skin effect

From the Maxwell's equations a diffusion equation for the magnetic field can be derived as:

$$\nabla^2 \mathbf{H} = \frac{\mu}{\rho}\frac{\partial \mathbf{H}}{\partial t}, \nabla^2 \mathbf{E} = \frac{\mu}{\rho}\frac{\partial \mathbf{E}}{\partial t}, \nabla^2 \mathbf{J} = \frac{\mu}{\rho}\frac{\partial \mathbf{J}}{\partial t} \qquad \textbf{2-12}$$

Then solution for the differential equation can be derived as:

$$H_x(y) = H_{0m}\exp(-\alpha y)\cos(\omega t - \sigma y) \qquad \textbf{2-13}$$

where α is define as $\sqrt{\frac{\mu\omega}{2\rho}}$, μ is the permeability, ω is the frequency and the ρ is the resistivity of material.

The Equation 2-13 implies that at the depth of $y=1/\alpha$, the magnitude falls to e^{-1} times its surface value and the phase has changed by a radian (57.3°). Thus the skin depth is defined as:

$$\delta = \sqrt{\frac{2\rho}{\mu_0 \mu_r \omega}} \qquad \textbf{2-14}$$

where: ρ = resistivity
μ_0 = permeability of free space
μ_r = permeability of the materials relative to free space
ω = frequency

The Equation 2-14 implies that once the frequency is selected, the skin depth is a function of the permeability and resistivity of the material. However, both these properties can be significantly affected by several factors such as temperature and packing conditions. The effects of frequency on the skin depth could be calculated when the properties of materials are available.

Resistivity dependence

During the heating process the resistivity of materials varies accordingly which should be taken into consideration. For the coil, since it is cooled by water, its temperature could be maintained in a narrow region. For the heated work piece, the change of resistivity occurs in a very short time so that in practice a representative value of resistivity, namely "integrated resistivity", was introduced in power calculation. Normally for pure metals, the resistivity can be presented as:

$$\rho(T) = \rho_0[1 + \alpha(T - T_0)] \qquad \textbf{2-15}$$

where α is the temperature coefficient.

2.2.3 Current and Power density

The power P in the coil or work piece can be expressed as:

$$P = IR^2 \qquad \textbf{2-16}$$

where $R=\frac{\rho\pi D}{\delta l}$

For the experiment design, the applied current in the coil refers to the applied power. To determine the applied current it is necessary to calculate the required power in work piece, which can be derived from Equation 2-16. For the cylinder heating and helical coil, the applied current I_c can be expressed as

$$I_c = \frac{I_w}{N} \qquad \textbf{2-17}$$

where N refers the turns of coil.

It is important to notice that the equation 2-17 is based on a design when the coil is close to the work piece (considering the tolerance and the thermal expansion the gaps between coil and work piece are normally in the ranges of several mm depending on the sizes of coil and work piece).

Conductivity and Heat transfer

The thermal conductivity of the substrate has a significant impact on the temperature distribution. Regarding the "skin effect", a non uniform temperature distribution in the heated part is inevitable. In this study the skin effect is desirable for many industrial applications when fast surface heating is needed. In this study this behaviour is an advantage since the heating will be used for the ignition not heating the entire work piece.

The relationship between time and mean temperature can be described with differential equations in simple geometries. For example, the relationship in a slab can be expressed as: [127] :

$$\frac{1}{b(c\gamma)}dt = \frac{d\theta}{P-P_R} \qquad \textbf{2-18}$$

where b=thickness of slab (m); c=specific heat (J kg^{-1} K^{-1}); γ= density (kg m^{-3}) and the radiation loss $P_R = \frac{5.67}{10^8}\varepsilon\theta_s^4$

For cylinder where R=radius of cylinder, the relation can be expressed as:

$$\frac{2}{R(c\gamma)}dt = \frac{d\theta}{P-P_R} \qquad \textbf{2-19}$$

These two equations simply illustrate the relationship between mean temperature and material proprieties. However the material properties are changing with temperature so it's hard to precisely predict the temperature. In practice the temperature distribution in a conductor is usually based on measurement. However, recently the numerical simulation provides a chance to predict the temperature distribution in a work piece during heating.

2.2.4 New applications in materials engineering

Recently researches have enlarged the scope of induction heating technology application. Some attempts were conducted to use this technology in polymer materials. Large amount of research work has been reported on the welding of thermoplastic composites. In this application induction heating provides a controllable, non-contact way to weld similar or dissimilar thermoplastics, or even thermoplastic to non-thermoplastic [128]. The induction heating was also introduced to the resin transfer moulding (RTM) to localize the heating for the resin in order to achieve an accurate control of the resin flow [129]. Because induction heating is a non-contact and fast heating process, in RTM application it is used to provide local heating to reduce resin viscosity and compensate for flow restriction in high resistance areas. Several researches have been done in this field and numerical simulations were computed as well. Induction heating was also used for coating application, for example, using this technique to produce nickel particulate films on polymer [130].

Another important application of induction heating is to produce Ni/WC alloy coating on metal [131]. In the application Ni based alloy powder (melting points range 900-1100°C) was mixed with WC or other refractory powders to produce slurry and then be placed on the tool steel or ordinary mild steel surface. After drying, the thickness of the dried mixture is generally in the range of 0.5mm to 2mm. The inductor heats the steel as well as the Ni based powder over 1000 °C, thereby a composite coating is fabricated.

Comparing with the laser sintering for Ni/WC alloy coating, the induction heating technology has several advantages. One advantage of this technology is the WC will not be carbonized during the heating process. This is fundamentally because of the induction heating is generating heat from the internal region of materials so the heating gradient is higher. Another advantage is that the coatings fabricated by this route are normally dense. This is due to the heating temperature is over 1000 ℃ and Ni alloy powder turn to liquid phase at that stage. When cooled down to room temperature, pores were filled by Ni alloy and refractory elements (as WC) were wrapped by the Ni alloy, resulted in a dense coating. The third advantage of this technology is it has little impact to the substrate. When using radio frequency, the heated zone is narrow therefore there is little influence to the mechanical properties. The heating temperature is controllable to a certain degree which also considered as an advantage. By adjusting the current and heating time, the highest temperature is predictable accordingly.

2.3 Induction heating with SHS

Recently a few researches on utilizing induction heating technique for combustion synthesis were reported. M.Shibuya et al. had conducted several investigations on using induction heating to active combustion synthesis (IFACS) of TiB_2-WB_2 system [40, 132]. In this IFACS process, a carbon heating sheet was used to pack compacted samples. Each compact was placed in a porous crucible inside a combustion chamber and then ignited by passing a current through the carbon ribbon. Outside the crucible another induction coil was employed for the "induction active" purpose. Apparently this IFACS process ignition is mainly because of the current applied in the carbon sheet, the induction field played only an assistance role.

Lee et al. studied the heating rate effect on NiAl synthesis in a induction heating furnace [133]. In Lee's experimental setting, a piece of casting steel was placed under the compact pellet as the substrate. A constant pressure was applied on the top to compress product to be bonded with steel substrate. In this setting, since the steel can be heated by induction heating, it remained unclear whether the compact pellet was ignited by induction or by the heat from the substrate. Also, the induction heating furnace increased the difficulty for temperature monitoring.

2.4 Summary

In past three decades numerous researches were devoted into the study of SHS synthesis of intermetalics, high temperature ceramics and their composites. The studies for the SHS process can be categorised in the following three areas:

1. Phenomenology
2. Zone structure of combustion wave
3. Mechanism and dynamics of phase/structure transformations behind the combustion front.

The reaction mechanism is important for the material selection, process control and property improvement and it has been widely investigated but with limited success. The research results showed the mechanism depends on the reaction system and on-line monitoring is necessary to provide a better understanding on the reaction mechanism. This will be a focus in this study.

In this section three basic principles of induction heating were reviewed. The unique heating behaviour of induction heating now has been adopted in other fields, and more and more applications are being explored.

The instinct complexity of electromagnetic waves limited the accurate control for induction heating, but along with development in computing technology, such as finite element simulation and computer assistant design provides a platform to achieving more precise induction heating controlling. With appropriate boundary conditions as well as measured data numerical simulation can be employed for process optimization in future.

The skin effect of induction heating provides a way for fast surface heating which has lead to many successful industrial applications. This advantage shows this technology has the potential to be used for SHS, but very limited research work has been carried out to date and the experimental setting restricted the investigation for the heating process. This study will explore the feasibility of using induction heating for SHS synthesis of Ni/Al based composites and investigate the synthesis mechanism.

Chapter 3 Experimental details

3.1 Introduction

The combustion synthesis of NiAl and NiAl-based composite with induction heating requires a completely new design for the experimental setting, as no previous experience can be referenced. The design of the experimental setting is to fulfil the requirements for manufacturing procedures and process monitoring to achieve the objectives described in Chapter 1. In this chapter, the experimental setting process will be addressed from the raw materials selection to product characterization.

3.2 Materials preparation

3.2.1 Particle selection

In this project, atomized Al manufactured by AlPOCO® and spherical carbonyl Ni by INCO® powder were used. The morphology of the powder is shown in Figure 3-1. The atomized Al particle has a relatively smooth surface as well as high purity. On the other hand, the selection of carbonyl Ni has three considerations. The small particle size of carbonyl Ni was the first consideration, since the coarseness of the Ni particle affects the degree of reaction. Commercially available carbonyl Ni particle sizes are 4-7 micron and 0.8-1.5 micron. The second consideration was the excellent magnetic properties of carbonyl powder. Its ability to absorb electromagnet wave will be beneficial for induction heating. Finally, compared with other manufacturing process, carbonyl Ni powder can achieve high purity (99.8%) without compromising the mechanical properties.

The selection of particle size was another consideration. In this study, based on preliminary test results, a combination of 15 micron Al and 4-7 micron Ni was selected since a previous investigation on the tribological properties of combustion synthesised NiAl has shown that synthesized produced using the combination of 15 micron Al and 4-7 micron Ni had excellent wear resistance[134].

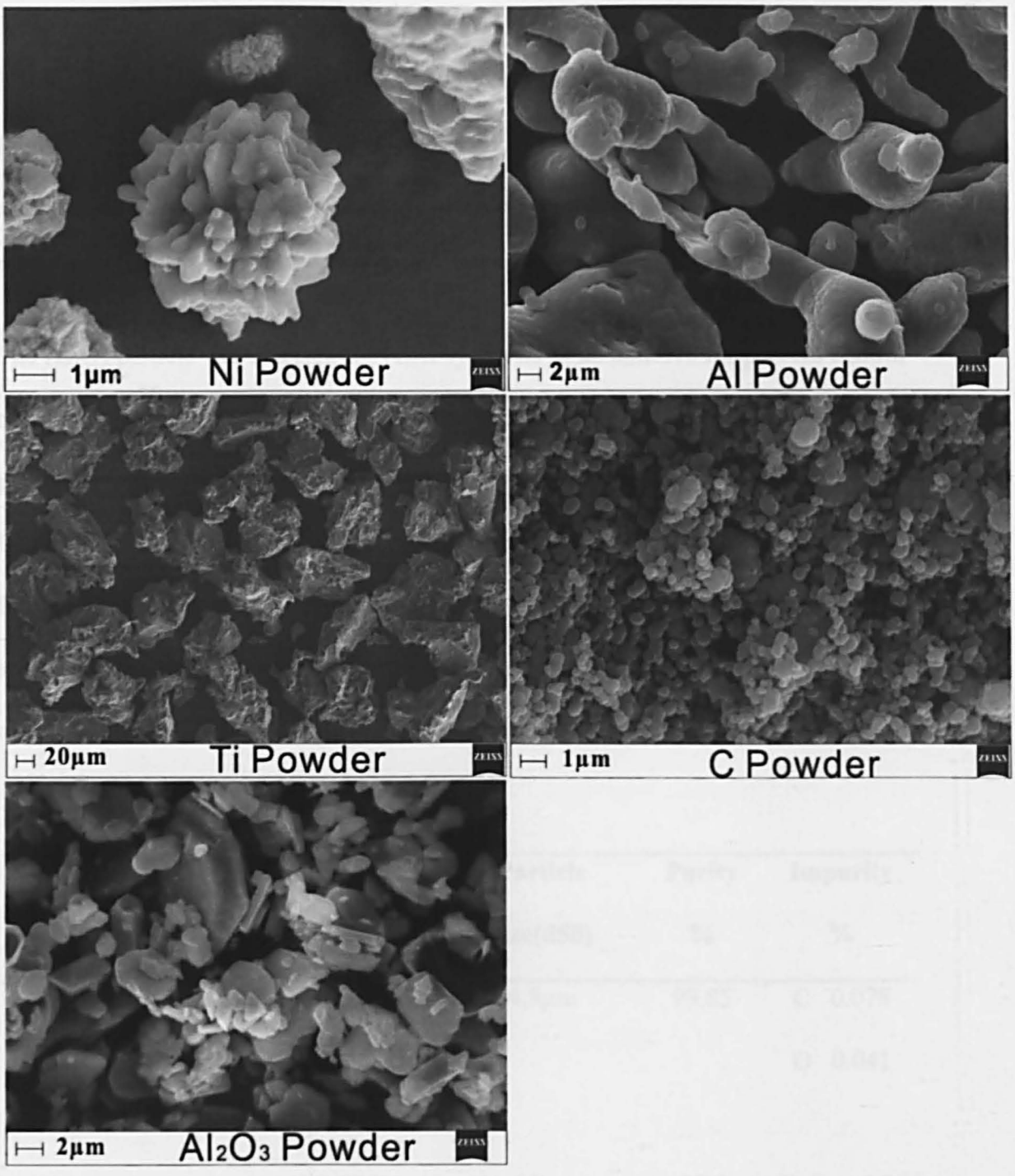

Figure 3-1 The morphologies of raw materials used in this study

The TiC combustion synthesis process starts with the melting of Ti particle, as stated in previous study [135]. This liquid-solid synthesis mechanism relies on the Ti

solid-liquid phase transition so the size of Ti is irrelevant to synthesis. In this study, Ti and C raw materials were provided by William Rowland Ltd. at Sheffield, England. The particle size of Ti powder is 300 mesh, approximately equal to 45 micron. The C powder was in the physical form of carbon black, as shown in Figure 3-1.

The Al_2O_3 particle was selected for NiAl synthesis as an additive for process control and to improve the properties of the synthesized products. Since the Ni and Al particles are fine powders, it was desirable to use finer particles for NiAl addition. In literature [136] a dense composite of $NiAl/Al_2O_3$ was successfully fabricated with the 3 micron Al_2O_3 particle addition. Based on this 3 micron size Al_2O_3 particle was selected from Alcan Chemical for this study. The details of all the raw materials used are listed in Table 3-1.

Table 3-1 Raw materials' properties

Material	Manufacturer	Particle size(d50)	Purity %	Impurity %
Nickel Powder	INCO® Carbonyl Ni Type 123	4.5μm	99.85	C 0.078 O 0.041
Aluminium Powder	AlPOCO®	15μm	99.7	Fe(max0.2) Si(max0.1)
Titanium Powder	William Rowland	48 μm	98	Fe 0.1
Carbon black	William Rowland	<1 μm	99.9	
Al_2O_3 Powder	Alcan Chemical	1 μm	99.8	

3.2.2 Sample pellet preparation

The Ni and Al powders with mole ratio 1:1 in acetone were mixed using an ultrasonic mixing machine for 5 minutes. The wet mixture was then transferred to an oven at 90 ℃ to evaporate the solvent acetone. After drying, the mixture was placed into a porcelain mortar for manually mixing. This procedure was repeated for Ti/C 1:1 molecular ratio mixture. All mixed powders were stored in sealed flasks and placed in a fume cupboard.

For Ni/Al with other particles mixtures, the dry mixture was weighed and placed in a mortar for a second mixing process. This second mixing process was to hand mix with acetone for 30 minutes. After drying, the mixtures were compressed to form compact pellets. Considering the sample shape a simple steel mould was designed as shown in Figure 3-2. The steel die was made in accordance with powder metallurgy model manufacturing reference[137]. The hardness of the die was above 60HRC after heat treatment and due to the fine powders that were used in the project, the tolerance grade of the mould was set as IT4-IT6 (5-18micron).

In traditional powder metallurgy theory, for axial cold compress, the ratio of diameter to height for pellet compacts should be above an index of 10 to achieve uniform density distribution within pellet. Otherwise due to the friction between powder and die the pellet's density distribution may vary considerably. In this study, for 1 g pellet with 100MPa pressure, the diameter of the pellet was 16mm and the thickness was approximately 1.4mm. The ratio of diameter to height was above the index of 10, thus the pellet density could be considered as uniformly distributed.

The fracture surfaces of compressed Ni/Al mixture and Ni/Al pellet with 20 weight percent (WT%) Ti/C are shown in Figure 3-3. Both samples were cold compressed at 100MPa, and the particle distribution within these two samples was uniform.

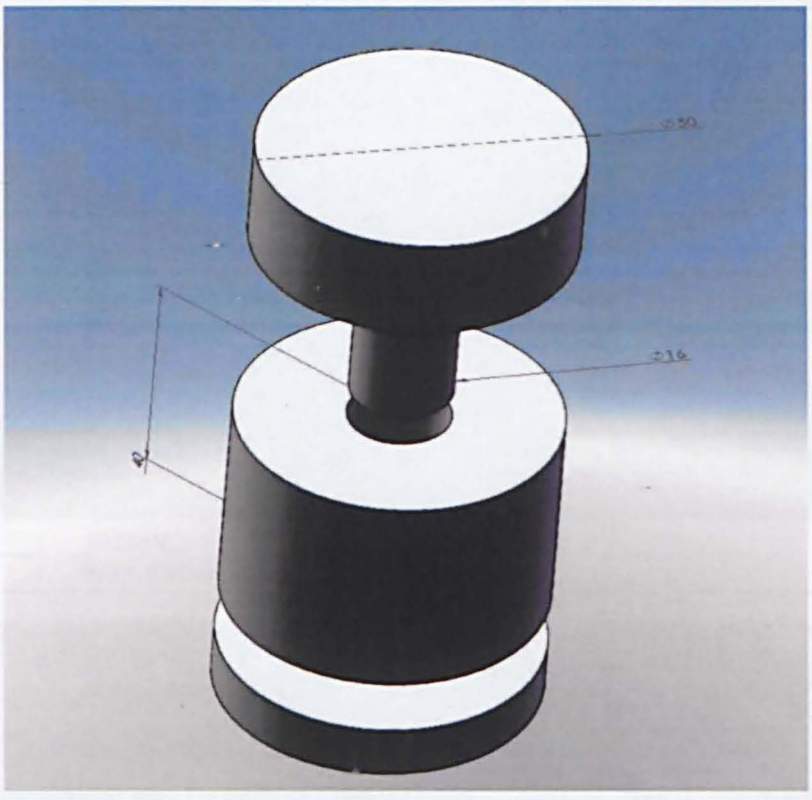

Figure 3-2 The steel model for powder compressing

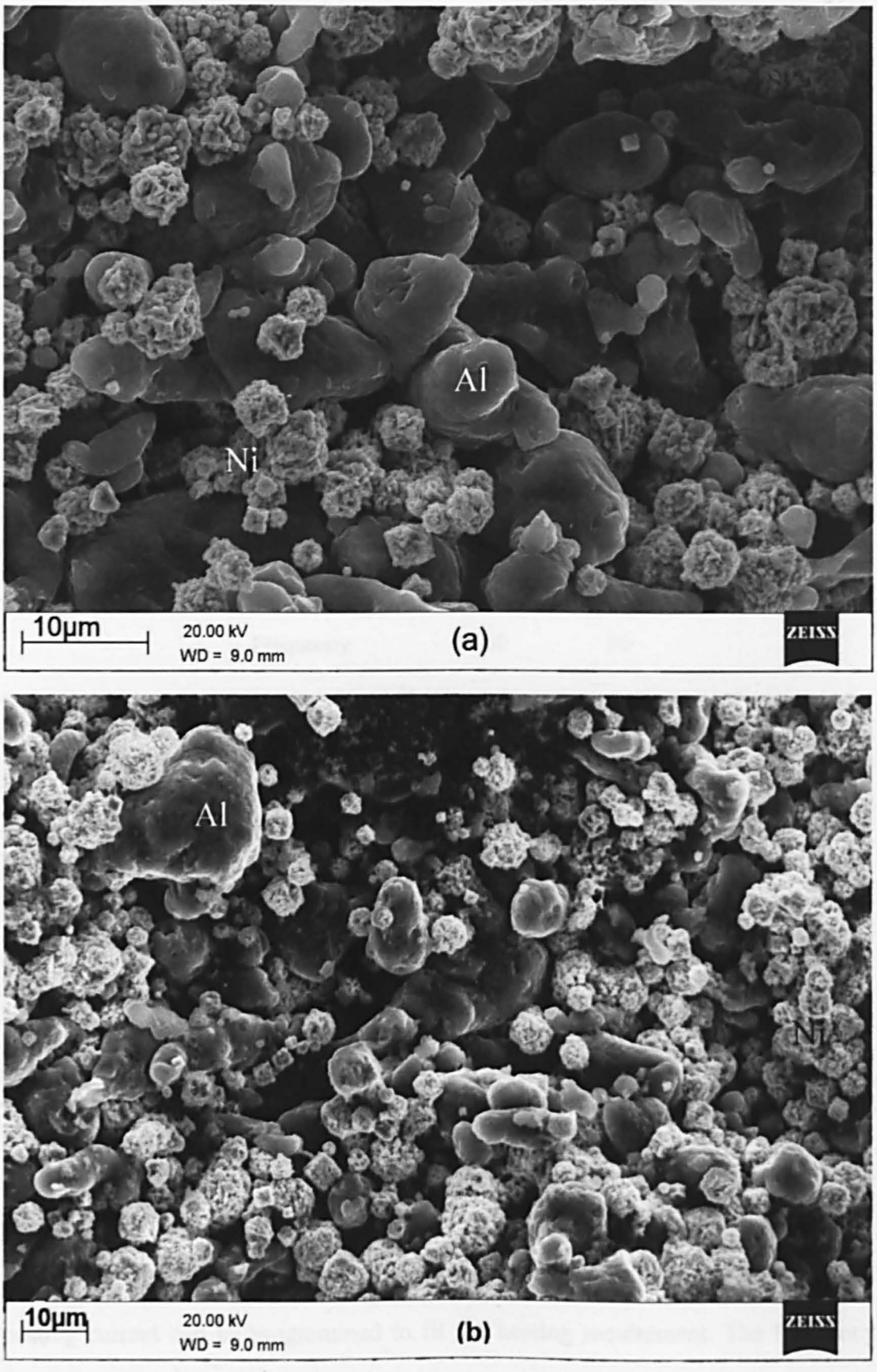

Figure 3-3 Compressed pellets (a) Ni/Al; (b) Ni/Al with 20 wt% of Ti/C

3.3 The induction heating system

The induction heating device used in this study was model EH-2.0 with maximum power 2kW manufactured by Cheltenham Induction Heating Limited (UK). Cooling for the coil is provided by cycling water using a pump. The electrical information for the equipment is listed in Table 3-2.

Table 3-2 Electrical technical information of induction heating system

	Description	Value	Units
Input	AC voltage	200-250	V
	Current(full load)	14.5	A
	Frequency	50-60	Hz
	Internal breaker	15	A
	Real power	2.0	kW max
	Apparent power	2.7	kVA max
	Power factor	0.78	
Output	Frequency	150-400	kHz
	RF current	90-400	A

In the front control panel of the induction heating device, the heating time and heating current can be programmed to fit the heating requirement. The frequency depends on the coil and varies from 100 kHz to 400 kHz. In this study, in order to obtain adequately fast heating for the combustion synthesis, a helix shape coil with

inner diameter of 20mm was selected. The frequency responses of this coil were in the range of 310-320 kHz, depending on the applied current in the coil.

3.4 The atmospheric control system

Concerning the reactants' physical states, the SHS reactions can be divided into two catalogues, the solid-solid reaction and the solid-gas reaction. To induce the solid-solid reactions, argon gas is popularly used. The reasons for selecting argon or vacuum atmospheres during the $MoSi_2$ SHS fabrication has been carefully studied [138]. Under an argon atmosphere, the maximum temperature and heating rate were relatively higher than those in a vacuum. Compared with products produced in a vacuum, the products obtained in argon have narrower particle size distributions and fewer impurities. The author explained that under an argon atmosphere extra convective heat transfer could be achieved compared to that in a vacuum so that lower temperature gradients were achieved. The lower temperature gradients therefore contributed to a faster flame-front velocity as well as a higher maximum temperature.

Martin et al. conducted research on the effect of gas pressure on NiAl fabrication [139-140]. These researches indicated that pressure has relatively little influence on heat capacity or on the enthalpy of the reaction. But the variation in gas pressure had caused changes in thermal conductivity and consequently affected the combustion velocity.

Another important aspect that needs to be carefully considered is the evaporation of materials when a vacuum condition is used for SHS process. This is because very high temperatures (> 3000 K) can be generated during combustion synthesis. The

vapour produced in a low melting point material may be significant and play an important role in the synthesis process when coupled with elements with high reaction enthalpy such as the Ti/C system used in this study.

Taking this into consideration, in this study it is desirable to complete the synthesis process within an atmospherically controlled environment since the Al element used in this study is sensitive to oxygen in the air. A glove box (Manufactured by Fisher Scientific®) was introduced for atmospheric control. The two doors glove box was made from clear acrylic with strong stainless steel fittings. The glove ports are made from solid blocks of 20mm acrylic for strength and 6 machined holes 4mm deep allow beaded gauntlets to be held securely. The internal dimensions of the glove box are 660x410x385mm (manipulator), and the loading hatch is 215x410x385mm.

The difficulty in adjusting the glove box for the project was to install the induction coil into the glove box without compromising its air-tight property. To overcome this difficulty an acrylic panel with identical dimensions to those of the glove box was produced. The panel was modelled using a probe system for the co-ordinate measuring machine (CMMs) and manufactured by computer numerical control (CNC) machining. Via this reverse engineering (RE) process the accuracy and tolerance could be guaranteed, consequently ensuring the air-tight property. Two holes were drilled in the panel for the coil installation and O-rings were applied for air-tight purpose. The sketch and setting of the panel are shown in Figure 3-4. The air-tight property of the setting was tested with soapy water and no air bubbles were found.

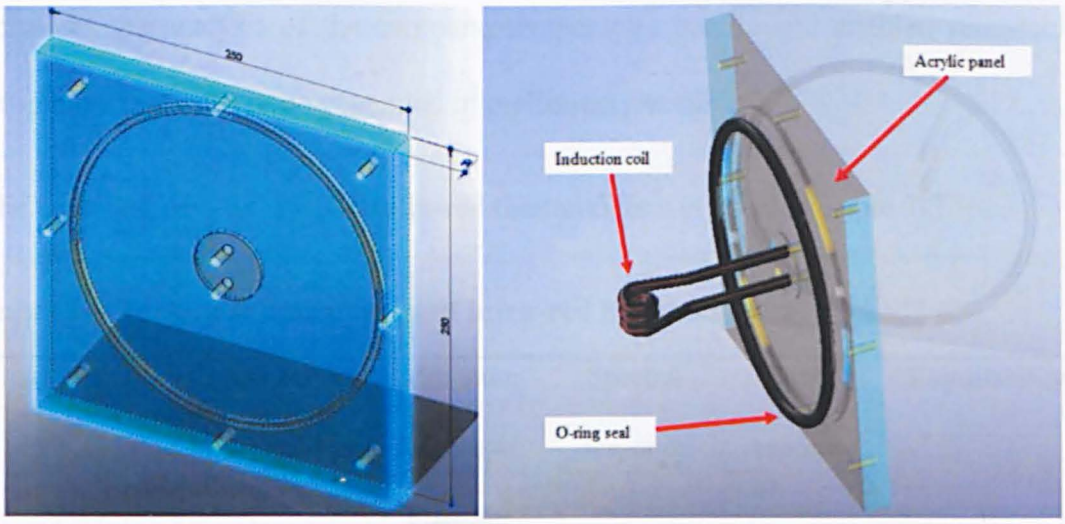

Figure 3-4 Sketch of acrylic panel and setting of panel

3.5 Temperature monitoring and calibration

To apply the induction heating technique for SHS ignition was a novel investigation. No previous work has been reported on analyzing the heating behaviour and ignition process by induction heating. The complete temperature profile of the whole synthesis process can provide sufficient data for the analysis of heating and combustion behaviour and help to understand both microstructure development and the reaction mechanism. But the high reaction velocity and elevated temperature can restrict the temperature measurement. In this study, aiming to monitor the heating and combustion process, a helical shape induction coil was selected. A combination of two infra-red thermometers and a high resolution thermal image camera was adopted for temperature measurement. The infra-red thermometers have short response times and a broad temperature range but are limited to point measurements. On the other hand, the thermal image camera can generate a complete temperature profile of combustion but with reduced accuracy of temperature. The combination

enhances the analysis of the complete temperature profile and enabled repeatable temperature profiles to be generated in preliminary tests.

The technical data for the two infra-red thermometers is listed in Table 3-3.

Table 3-3 Technical information of infra-red thermometers

Model	Temperature range	Minimum focus spot diameter	Spectral response	Time response	Repeatability
Raytek® Marathon MM1MH	480-3000 °C	1mm	1 μm	1ms (95% of reading)	±(0.1% of reading +1°C)
Raytek® Raynger MX	-30 to 900°C	6mm	8 μm to 14 μm	250 ms (95% of reading)	±(0.5% of reading or ±1°C)

Unlike thermocouples, calibration for infra-red thermometers is crucial for the setup configurations before they can be used for measurements. For the purpose of quantifying the temperature, this non-contact measurement relies on the emissivity of the target to be measured which depends on the measured reflectivity of the surface emissivity (or absorption rate), ambient temperature, air temperature, measuring distance, atmospheric attenuation and other factors. Thus, the manufacturer of infra-red thermometers suggested that the calibration should be carried out in the practical working environment.

Since the detectable temperature ranges of the two infra-red thermometers were different, the calibration had to be carried out separately. A type K thermal couple was embedded in the compressed pellet. A Pico ® TC-8 device was used for data acquisition and all the temperature readings were recorded with a computer. For the Raynger MX thermometer, within 300K to 1200K the calibration was done by adjusting the emissivity value setting of the thermometer to receive an identical or close reading to that received by the thermocouple. The results are shown in Figure 3-5. The blue curves were recorded by infra-red thermometer and the brown curves were thermocouple results. Various heating rates (10-30 K/s) were applied by changing the induction current in order to achieve a more feasible calibration result. For a slow heating rate (less than 10K/s), the result is shown in the Figure 3-5a. It can be seen that the measured temperatures from the two devices were very close, but the infra-red one had less fluctuation than the one measured with the thermocouple. The maximum temperature difference within the measured temperature range (30 to 900 K) was only 7K. The shorter response time of the thermocouple could be a reason for this difference. However, compared with the thermocouple which detected the temperature of a point, the infra-red thermometer recorded the average temperature of a surface and should present less fluctuation. With the same setting of emissivity the temperature difference was reduced for a quick heating (above 20K/s) process, as shown in Figure 3-5b. Less than 5K difference between the two readings was observed till combustion. At the combustion point, the infra-red thermometer reached the peak value while the Type K couple curve collapsed as it was melted. Since in both case the readings were very close, the emissivity setting for Raynger MX was fixed at 0.72 in this case.

The calibration for the other high temperature range thermometer, the Raytek® Marathon MM1MH one, was more complicated. Due to the different response spectrum, the emissivity setting of Raytek® Raynger MX one is not applicable to the Marathon MM1MH. Also, the phase transition in combustion varies the reflectivity of a surface which increases the difficulty in measurement. In the theoretical estimation, for NiAl SHS at the combustion point the product is a mixture of liquid and solid NiAl. Thus after combustion there will be a short period of solidification at the melting point of NiAl. This temperature is less sensitive to other experimental parameters such as heating rate and compact pressure, therefore it can be used for calibration. After hundreds of attempts, the emissivity of Marathon MM1MH was finally set at 0.820 and the result is shown in the Figure 3-6. The temperature profile in Figure 3-6 was recorded by both thermometers. The maximum temperature in the curve was 1894K, which is 17K lower than the theoretical estimation. Taking the undercooling effect during solidification into account, this measurement was quite acceptable for high temperature measurement.

Thermal imaging provides the temperature distribution during heating which together with the thermometers readings provides adequate data for further analysis. The thermal images were taken using VarioCAM® high resolution camera. The technical details are listed in Table 3-4. The data analysis for the thermal images was carried out using the IRBIS®3 professional developed by InfraTec. The relevant spectral range of the thermo-camera is 7.5-14μm, which indicates that it has low accuracy for high temperature measurement. As stated, the advantage of thermal image technique is to visualize the temperature distribution on the surface. In this

case, the thermal camera was only used for heating behaviour and ignition monitoring.

Table 3-4 Technical data for thermal image camera

Spectral range	(7.5-14)μm
Detector format (pixel)	(640x480) enhancement to 1280x960
Temperature measuring range	(-40-2000)°C
Digital colour video camera	1.3 megapixels
Measurement accuracy	±1.5K(0-100) °C;±2%(>100) °C
IR-frame rate	50/60Hz

To combine with the heating system, the atmosphere control and the temperature monitoring the whole experimental setting is schematically showing in Figure 3-7.

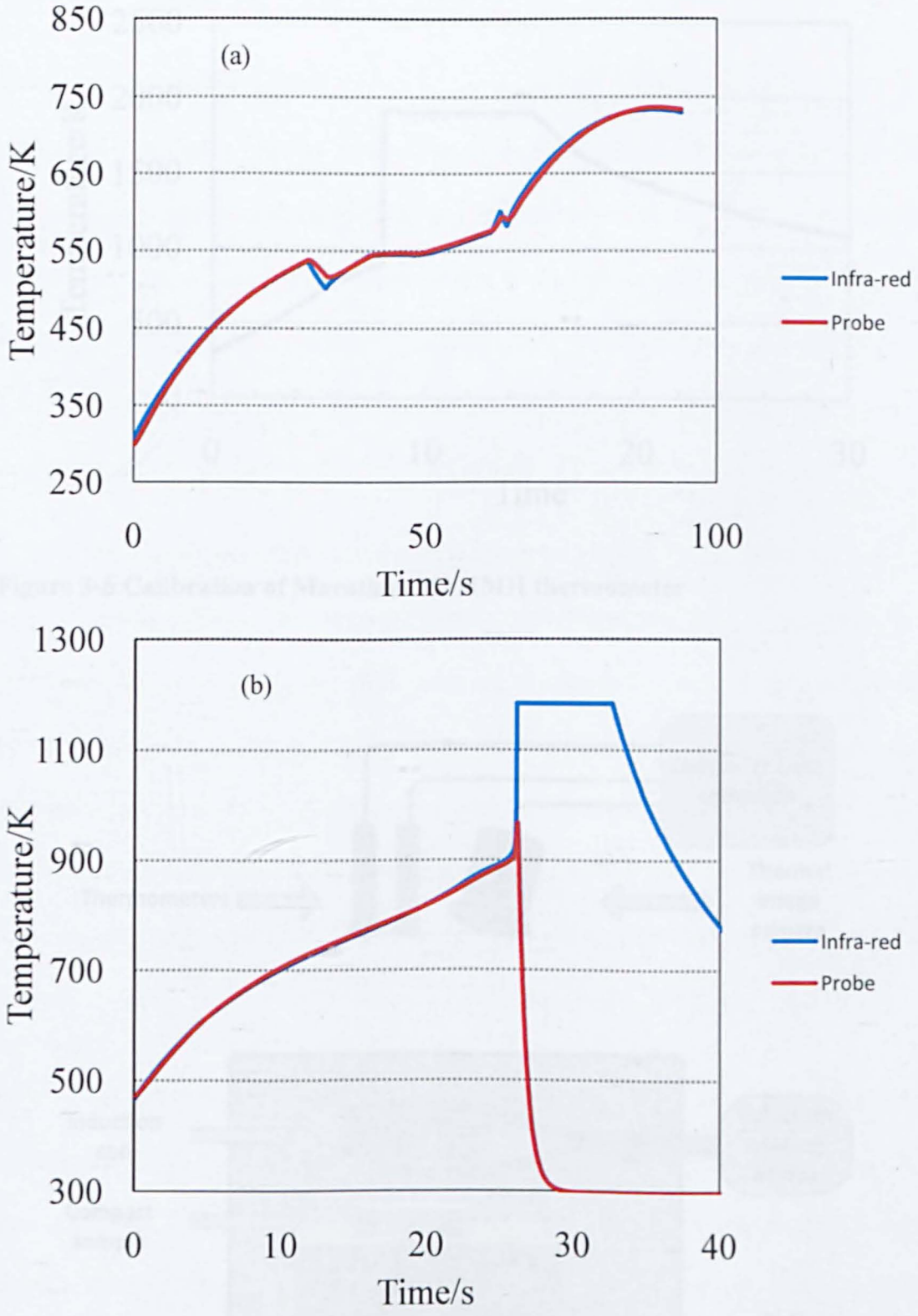

Figure 3-5 Calibration of Raynger MX infra-red thermometer; a) 10 K/s and b) 20 K/s

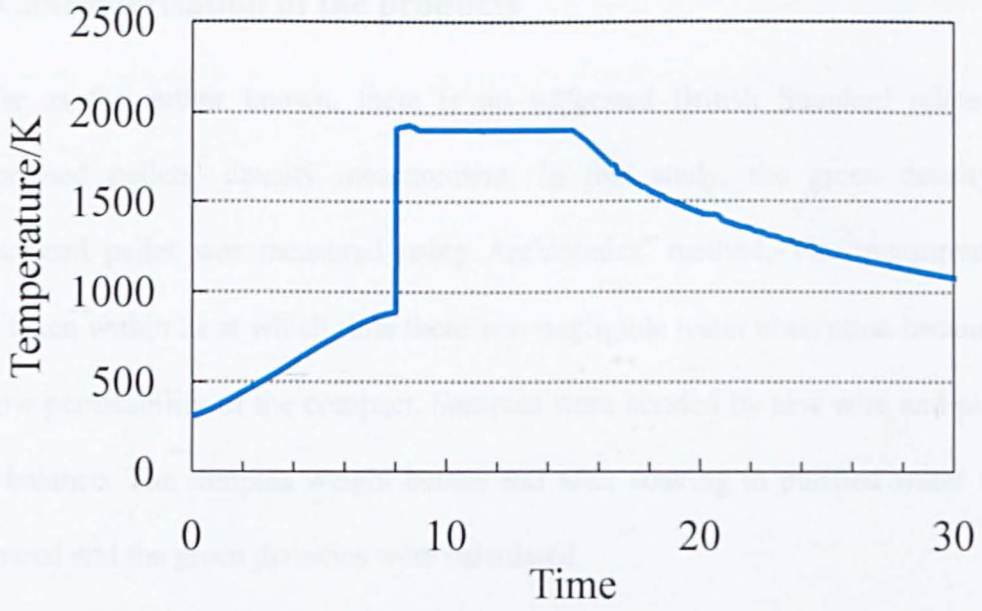

Figure 3-6 Calibration of Marathon MM1MH thermometer

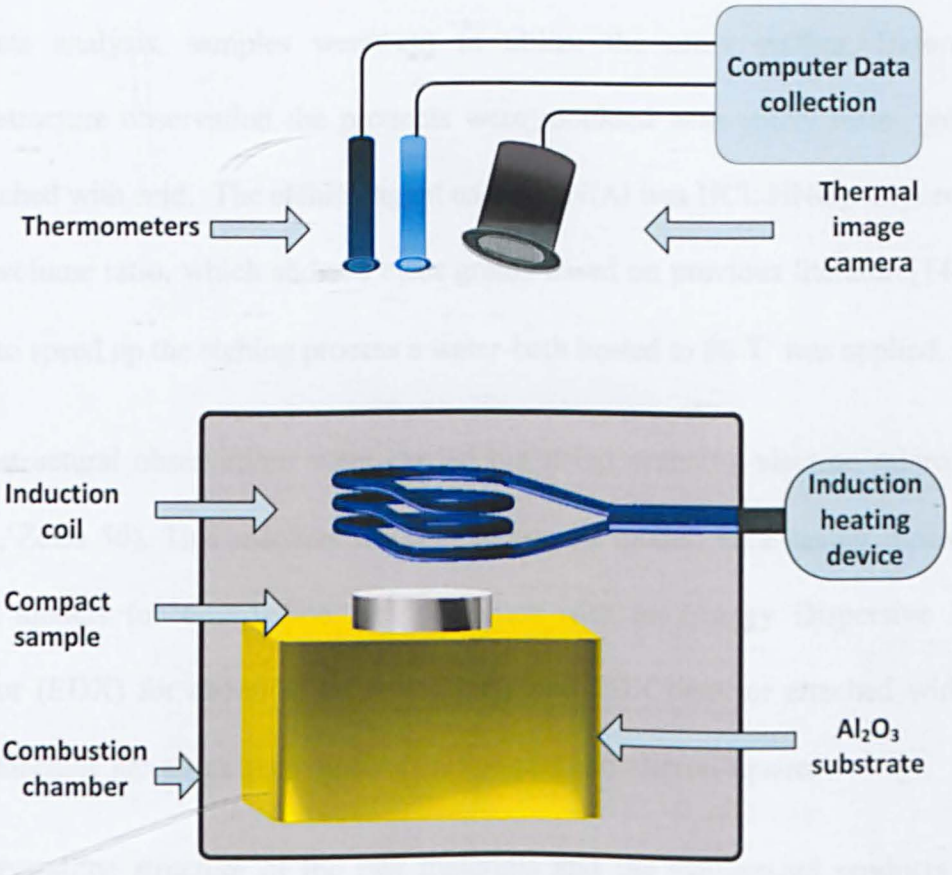

Figure 3-7 Schematic diagram of experimental set up

3.6 Characterisation of the products

As far as the author known, there is no suggested British Standard related to compressed pellets' density measurement. In this study, the green density of compressed pellet was measured using Archimedes' method. The measurements were taken within 2s at which time there was negligible water absorption because of the low permeability of the compact. Samples were bonded by sew wire and placed on a balance. The samples weight before and after soaking in purified water were compared and the green densities were calculated.

After synthesis the products were in the physical form of solid bulk materials. For X-ray diffraction analysis, 600 mesh silicon carbide paper was used to polish a flat surface on the products, followed by cleaning in ultrasonic machine. For two-layer products analysis, samples were cut to utilize the cross section. Before the microstructure observation the products were moulded with epoxy resin, polished and etched with acid. The etching agent used for NiAl was HCl: HNO_3: Glycerine at 2:1:1 volume ratio, which showed clear grains based on previous literature[141]. In order to speed up the etching process a water-bath heated to 80 ℃ was applied.

Microstructural observations were carried out using scanning electron microscopy (SEM, Zeiss 50). This machine features secondary model, back-scatter model and stereo models for observation and combines with an Energy Dispersive X-ray detector (EDX) for chemical atom analysis. The EDX detector attached with this SEM machine has a minimum analysis range of a 5x5 micron square.

The crystalline structure of the raw materials and the synthesized products were characterized with a SIEMENS D500 X-ray diffractometer (XRD) using Cu K_{α}. The

NiAl samples were polished and cleaned before XRD testing. The two-layer composites were cut into pieces and the cross sections were used for XRD analysis.

The micro-hardness test was performed by using a 0.1N load for 10s.

Chapter 4 The structure and properties of NiAl formed by SHS using induction heating

Intermetallic NiAl has the potential to be used for elevated temperature applications. To date different ignition techniques have been attempted to synthesize NiAl and produce coatings. Self-propagating high-temperature synthesis has been developed as a relatively simple route to obtain intermetallics. This research considers using induction heating to preheat and ignite the synthesis directly and investigates the effect of processing parameters on the phase transformation, microstructures and properties of Ni/Al compacts synthesized by SHS. The results show that single phase NiAl can be produced by induction heating whilst processing parameters such as heating rates and green densities have a significant effect on the properties and structures of sintered products.

4.1 Introduction

The unique properties of intermetallic NiAl, including its high melting point (1911K), low density (5830kg/m^3) and good thermal conductivity (75W/mK), have attracted wide attention and motivated extensive industrial studies. Owing to its high anti-oxidation properties it has the potential to be used as a coating material for elevated temperature applications. Among the processing techniques for the production of high temperature coatings, thermal spray is the most popular process and it has been used to deposit NiAl and doped-NiAl thermal barrier coatings (TBCs) [142-144]. For example nanostructured NiAl coating was produced using

high velocity oxy-fuel (HVOF) thermal spraying by Hu et al [72]. However industrial applications require the coating properties of intermetallic NiAl to be improved and research work is ongoing to achieve better performance. The properties of coatings are strongly dependant on the quality of the coating materials and processing parameters. The synthesis of high quality intermetallic NiAl is critical for the development of NiAl based coatings. Numerous experimental techniques have been attempted to improve the properties of Ni/Al by adding different elements. For example, Wang et al studied the effect of iron on the creep properties of NiAl [145-146] and Jiang et al. investigated the effect of Pt on its elastic properties[147]. A significant difficulty arises when using thermal spray in that the time for particle heating and solidification is very short. As a result, the material structure developed by conventional alloy synthesis may differ from the structure of a thermal sprayed coating. Therefore new synthesis and coating processes are needed to produce NiAl based coatings.

Regarding the thermodynamics of reaction, particularly for the two metallic elements synthesis, the phase diagram is a principal tool. Although the combustion synthesis has fast reaction velocity, the products are normally in accordance of the phase diagram prediction [67]. Figure 4-1 shows the latest phase diagram composed via experimental means [148]. The solid line in Figure 4-1 shows the Al-Ni phase diagram modified by Okamoto in 1993, which has agreement with latest data. The melting point of NiAl is 1638 ℃ (1911K). The peritectic decomposition point of NiAl to Ni_3Al is 1360 ℃ (1633K) and to Ni_2Al_3 is 1133 ℃ (1406K). At Al 42 atom percentage the AlNi will cross to Al_3Ni_2. The major discrepancy is the NiAl+Ni_3Al and Ni_3Al+ (Ni) phase boundary, as presented in dash and dot lines. The dot line,

originally from Nash at ASM International, has been replaced with Okamoto's result by ASM International in 2009. For the dash line, the author claimed that further investigation is needed with Ni_3Al peritectic decomposition point. So far no further publications on this debate were reported.

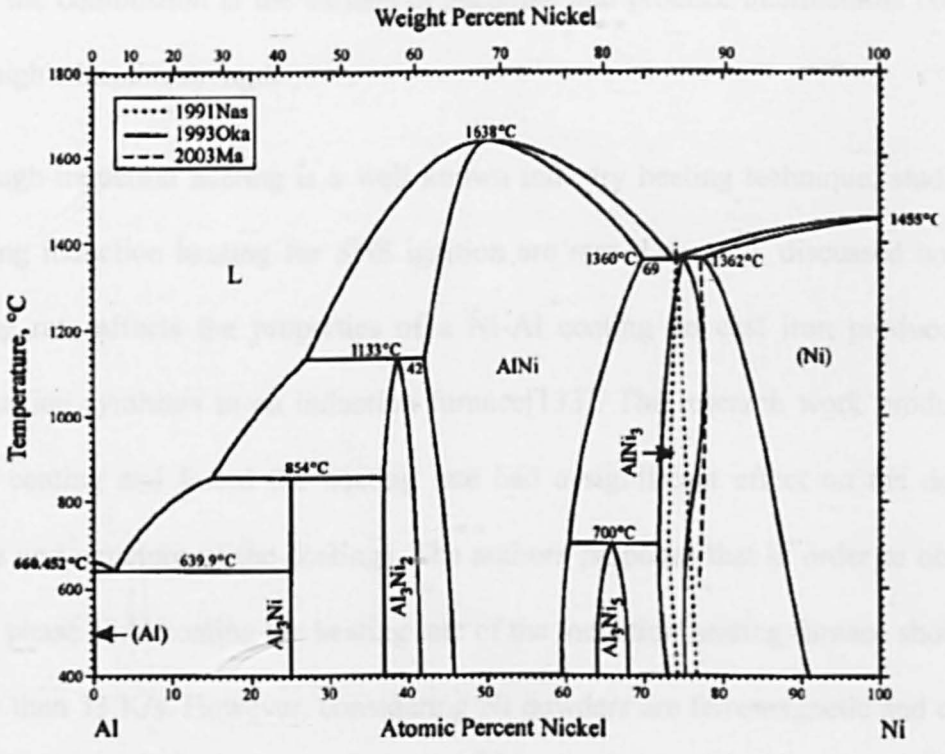

Figure 4-1 The phase diagram of Ni-Al system [9]

Induction heating differs from other heating techniques and is considered to be a fast and clean process. It generates heat directly in the coating materials and the substrate. It is possible to ignite the combustion reaction from the interface between coating and substrate. In induction heating, electromagnetic energy is converted into heat energy which is concentrated within a thin layer termed the penetration depth δ whose thickness can be described using Equation 2-14. The equation illustrates the response of bulk metallic material in an electromagnetic field, but for powder

mixture compact the conversion is more complicated since the properties of compacts strongly depend on the properties of powders and the packing density [103]. If a substrate with high permeability such as steel is used as substrate, the high temperature zone will be at the surface of the substrate. Therefore, it is practical to ignite the combustion at the surface of substrate and produce intermetallic coatings with high adhesion strength.

Although induction heating is a well known industry heating technique, studies on utilizing induction heating for SHS ignition are rare. Lee et al. discussed how the heating rate affects the properties of a Ni-Al coating on cast iron produced via combustion synthesis in an induction furnace[133]. The research work produced a dense coating and found the heating rate had a significant effect on the density, phases and structure of the coatings. The authors proposed that in order to obtain a single phase NiAl coating the heating rate of the induction heating furnace should be higher than 33 K/s. However, considering Ni powders are ferromagnetic and can be heated in electromagnetic fields, it remains unclear whether the compressed pallet of Ni/Al was ignited by the electromagnetic field induced in the compact or the heat transferred from the steel substrate. Since the reaction rate is very high (>100 mm/s), it is difficult to measure and control the reaction in a furnace. Due to these complexities this chapter will investigate the synthesis process utilising induction heating to directly preheat and ignite the Ni/Al compacts. The effects of processing parameters on the phase transformation, microstructures and properties of SHS synthesised NiAl compacts will be investigated and the results can be used for process control to produce high quality NiAl material and coatings.

4.2 Experimental procedure

In order to investigate the effects of heating rate and green density, two groups of samples were prepared. In the first group, Ni and Al powders were mixed and compressed in a steel die of 16mm diameter at a constant pressure of 100MPa to investigate the effect of heating rate. For the second group, compression pressures were varied from 35MPa to 100MPa so that the effect of green density could be studied. The green densities of the compacted samples were measured by Archimedes principle. The induction heating frequency was set at 317 kHz and a helix shape coil was selected.

The thermal image was taken using VarioCAM® high resolution camera. The temperature monitoring for a fixed point was carried out using two infrared thermometers, Raytek® Raynger MX (temperature range 0-910°C) and Raytek® Marathon MM (temperature range 540-3000 °C, response time 2ms). The data analysis for the thermal image was carried out using the IRBIS®3 professional developed by InfraTec.

The product characteristics process was conducted as chapter 3 describes. The samples were potted with epoxy resin, polished and etched with acid prior to microstructural observation. The micro-hardness test was performed using a 0.1N load for 10s.

4.3 Results and discussion

4.3.1 Phase characteristics

To investigate the effect of heating rate, the compacted samples (fixed pressure at 100 MPa) were heated with different applied currents as shown in Table 4-1. The

measured temperatures at the surface showed that there was an intensive combustion in each sample. The X-ray diffraction pattern for the sintered and the green compacts are shown in Figure 4-2. Comparison of the pattern for the sintered and green compacts indicated that no raw Nickel and Aluminium material existed in the sintered products thus showing that the reaction was complete. In all five sintered samples (Figure 4-2a), NiAl was detected as the dominate phase and no other Ni-Al compounds were observed. These results are in agreement with literature [133] which suggests that when the heating rate is higher than 33.2K/s single phase NiAl can be obtained. In this investigation, the heating rates were between 50 to 150K/s. However, the orientation of crystalline structures varies under different heating rates. At a low heating rate (50 K/s, 200 A), the (110) plane was parallel to the surface but at a high hearing rate (152 K/s, 300 A), the (100) plane was parallel to the surface.

Table 4-1 Heating rate at different induction current

Current(A)	300	275	250	225	200
Average Heating rate(K/s)	152	99	80	66	50

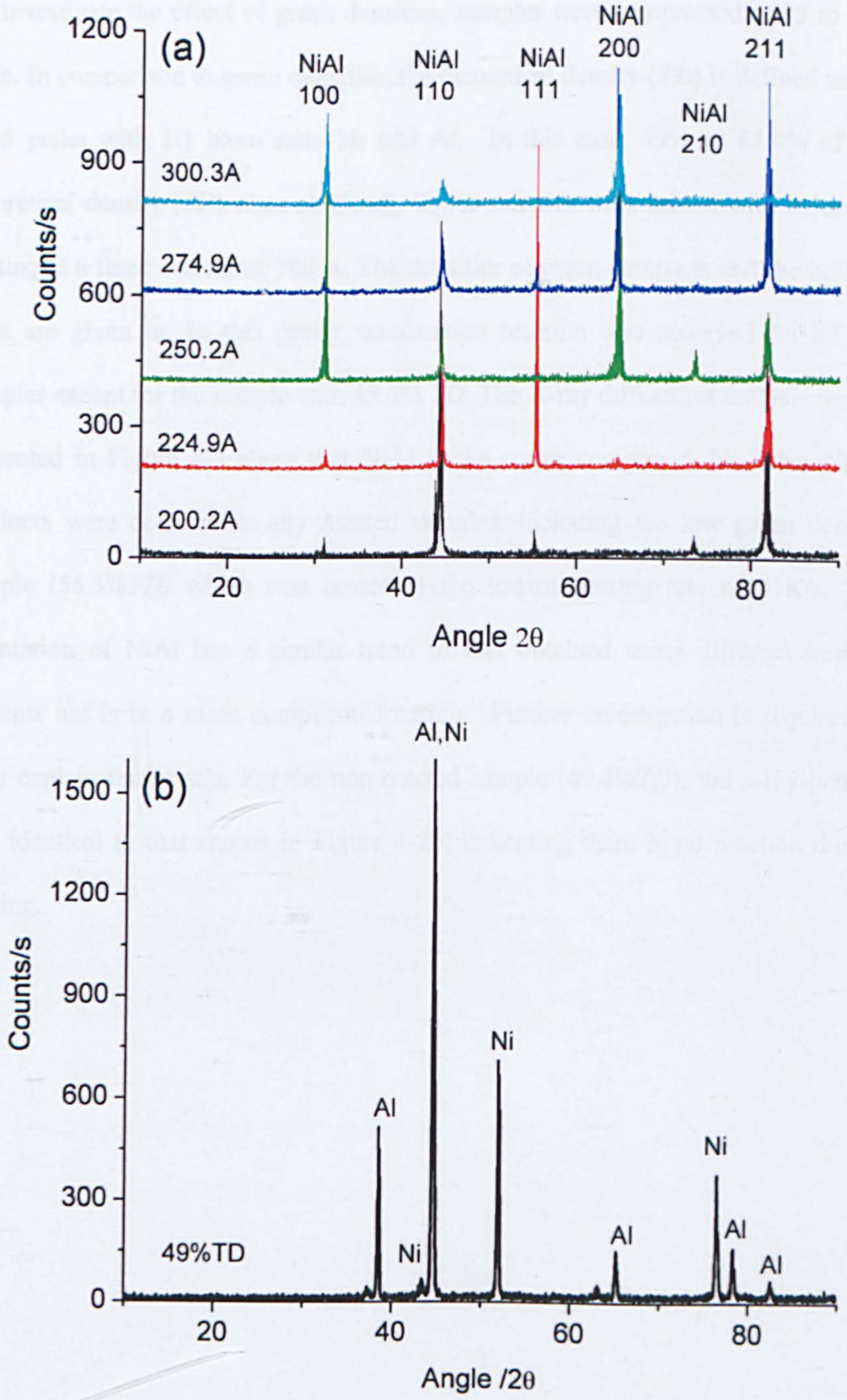

Figure 4-2 X-ray diffraction patterns; a) sintered compact and b) compact before sintering.

To investigate the effect of green densities, samples were compressed at 35 to 100 MPa. In comparison to green densities, the theoretical density (***TD***) is defined as the solid pellet with 1:1 atom ratio Ni and Al. In this case, 49% to 64.4% of the theoretical density (*TD*) were obtained. These samples were heated with induction heating at a fixed current of 300 A. The densities of green compacts and the heating rates are given in. In this group, combustion reaction was observed for all the samples except for the sample with 49.4% *TD*. The X-ray diffraction analysis results presented in Figure 4-3 show that NiAl is the major compound. No other Ni-Al products were detected in any reacted samples, including the low green density sample (56.3%*TD)* which was heated at the lowest heating rate of 41K/s. The orientation of NiAl has a similar trend to that obtained using different heating currents but is in a more complicated nature. Further investigation is required to fully explain the reason. For the non-reacted sample (49.4%*TD*), the x-ray pattern was identical to that shown in Figure 4-2b, indicating there is no reaction during heating.

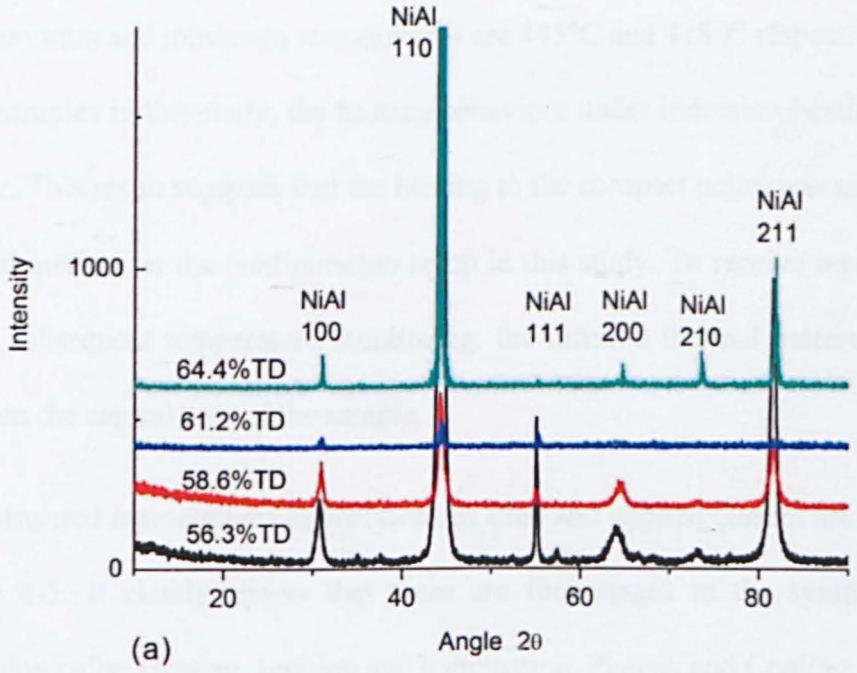

Figure 4-3 X-ray diffraction pattern for sintered samples with different green densities

Table 4-2 Heating rate of green density group specimen

Compression pressure (MPa)	100	85	70	50	35
Green density (TD %)	64.4	61.2	58.6	56.3	49.4
Average heating rate(K/s)	95.8	84.2	64.0	41.0	unreacted

4.3.2 Combustion reaction under induction heating

Figure 4-4 shows the temperature distribution of a sample which was heated under constant current of 300A. The thermal image presented was just before reach to ignition temperature. Generally the temperature at near the out ring is higher than that at the internal area. This is the nature of induction heating as described in Chapter 2. Close to the coil, there is a higher induced current, which results in higher heating rate at the out ring area. However, the temperature difference inside the

sample is not significant. For example, within the circled area shown in Figure 4-4, the maximum and minimum temperatures are 445°C and 418°C respectively. For the other samples in this study, the heating behaviour under induction heating was quite similar. This result suggests that the heating to the compact pellet was uniform to the internal area under the configuration setup in this study. To receive repeatable data, in the subsequent temperature monitoring, the infrared thermal meters were set to focus on the central area of the sample.

The measured temperatures as functions of time and applied current are presented in Figure 4-5. It clearly shows that there are four stages in the synthesis process chronologically: Heating, Ignition and combustion, Plateau and Cooling.

In the heating stage, these curves show that the increase of the applied current results in a corresponding increase to the heating rate. As shown in Table 4-1, the specimen heated under 300A has the highest heating rate of approximately 152K/s, while the specimen heated at 200A has the lowest heating rate of approximately 51K/s.

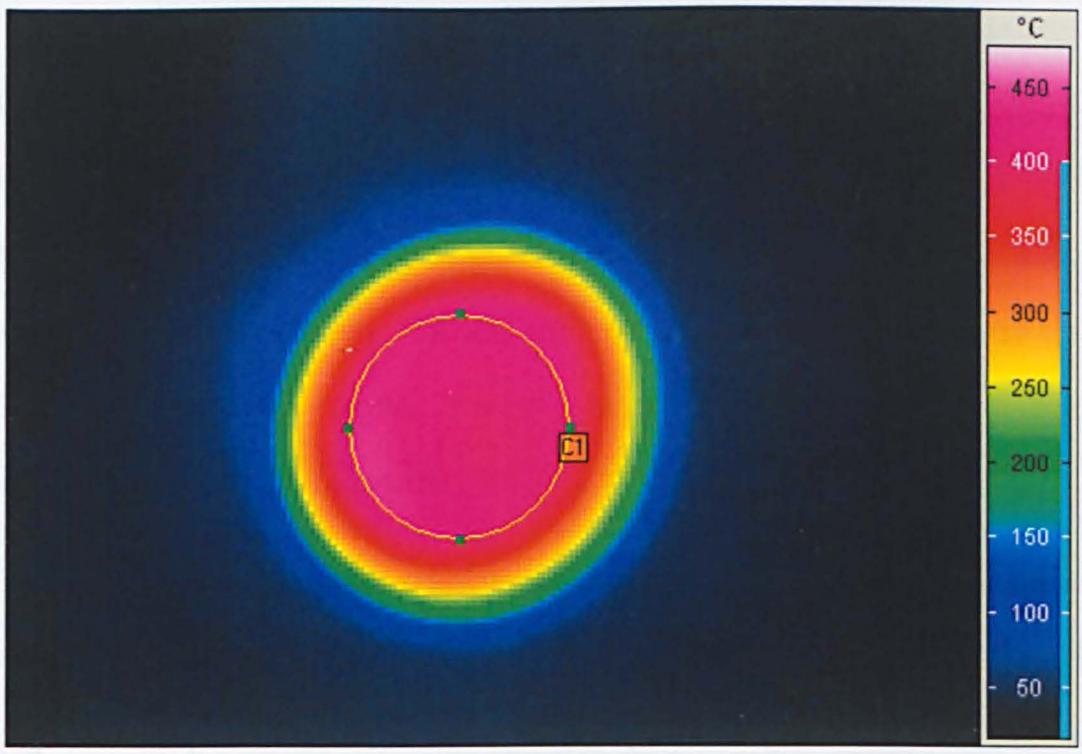

Figure 4-4 Thermal image before ignition heated at 300A

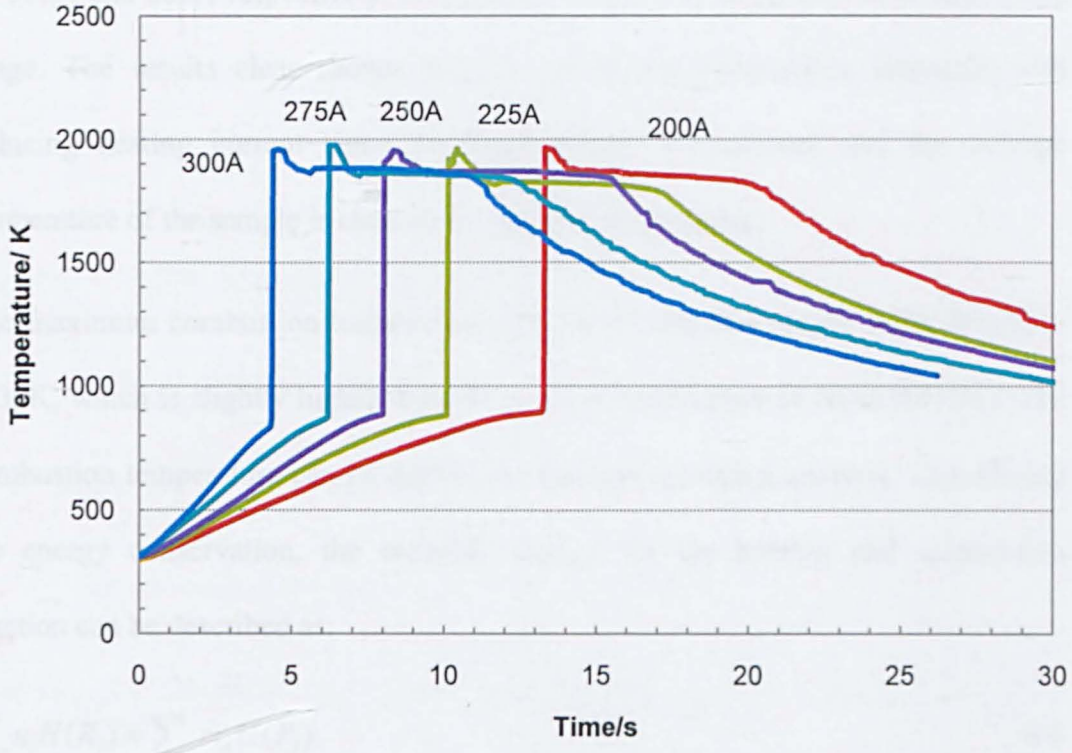

Figure 4-5 The effect of currents on the heating rates and ignition of Ni/Al compacts

To receive more details on the ignition and combustion propagation, the thermal image was recorded during synthesis. The thermal images during SHS reaction for the samples heated with 300A and 200A are shown in Figure 4-6. At the moment that ignition was about to commence, the temperature differences in the radius direction were approximately 70K and 40K under 300A and 200A respectively. Using the temperature profile recorded during combustion, the combustion propagation velocity can be determined, which is 0.2-0.3 m/s for the tested samples.

The small temperature gradient at inside the pellet during heating suggests that it was heated uniformly and the sample was preheated before ignition. The lowest temperature of pellet before ignition was determined as the preheating temperature. The recorded preheating temperatures were 833K and 890K for the samples heated by 300A and 200A respectively, and the rest samples in this group were within this range. The results clear shown that the preheating temperature increases with reducing heating current since the heating time is increased and the average temperature of the sample is close to the ignition temperature.

The maximum combustion temperature (T_c) for all samples ranged from 1910K to 1930K, which is slightly higher than the melting temperature of NiAl (1911K). The combustion temperature can be derived by thermal dynamics analysis. Considering the energy conservation, the enthalpy change for the heating and combustion reaction can be described as:

$$\sum_i n_i H(R_i) = \sum_j m_j H(P_j) \qquad \textbf{4-1}$$

where R_i, P_j refer to the appropriate reactants and products respectively, and n_i, m_j are the stochiometric coefficients of the reactants and products.

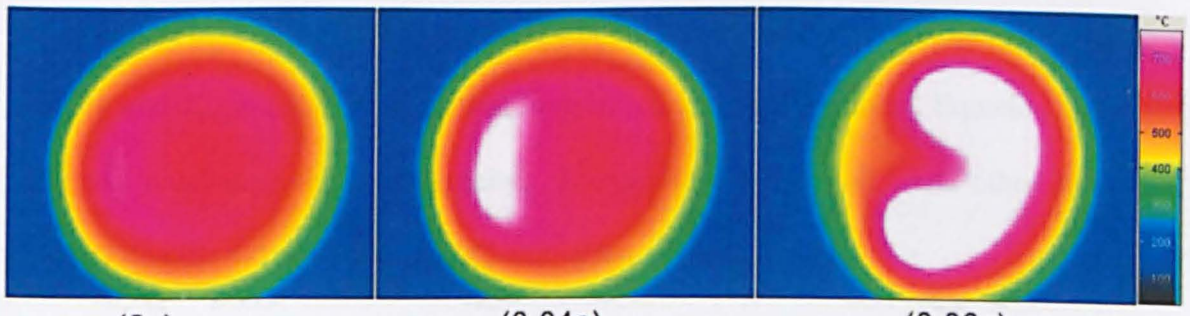

(a)

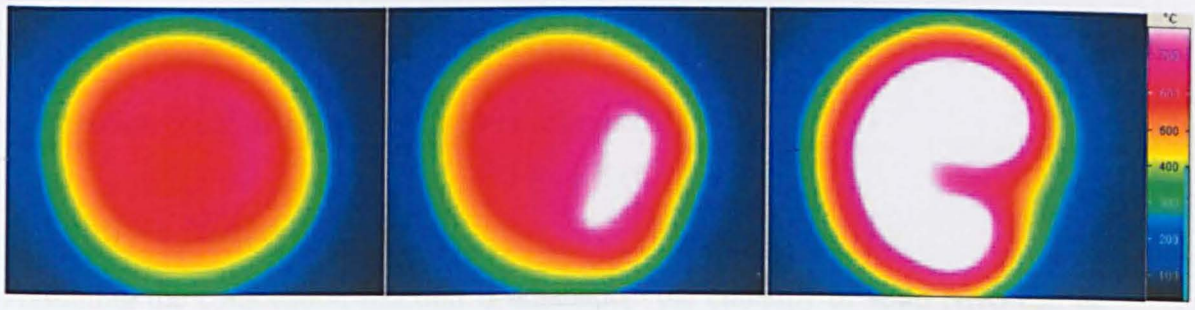

(b)

Figure 4-6 Thermal image during combustion synthesis using (a) 300A; (b) 200A

Three assumptions were made in the calculation:

1) All the raw materials were consumed and the product contained NiAl only;

2) Adiabatic condition was applied due to the fast reaction velocity;

3) Samples were preheated to a uniform temperature.

Therefore the adiabatic combustion temperature (T_{ad}) can be determined from Equation 4-1 as:

$$\sum n_i \Delta H_{298} + \int_{298}^{T_{Pre}} \sum n_i C_p(R_i) dT = \int_{298}^{T_{ad}} \sum m_j C_p(P_j) dT \qquad \textbf{4-2}$$

where ΔH_{298} is enthalpy of formation, T_{pre} is the preheating temperature, C_p is heat capacity and T_{ad} is combustion temperature in adiabatic environment. Equation 4-3 was used to calculate the heat capacity. The constant a, b, c and d and other data used in Equation 4-3 are given in Table 4-3 (Data reference[149]).

$$C_p = a + (b \times 10^{-3})T + (c \times 10^{-6})T^2 + \frac{d \times 10^5}{T^2} \qquad \textbf{4-3}$$

In this case, since final products contain single NiAl phase, the reaction of combustion could be simplified as (data reference[149]):

$$Ni + Al \rightarrow NiAl + 118.5kJ \qquad \textbf{4-4}$$

Assuming the combustion reaction is adiabatic, the enthalpy of solid NiAl can be calculated with the following equation [150] :

$$H_{NiAl}(solid) = -131488.5 + 4184T + 6.905 \times 10^{-2} T^2 \qquad \textbf{4-5}$$

At 1911K, the NiAl starts to melt, and the phase transition enthalpy 57.6 KJ/mole was used in the calculation.

Table 4-3 Thermal properties of Al and Ni element[150]

Element	Phase	Temperature of Transition (K)	Heat of Transition (kJ/mole)	a (J/mole)	b (J/mole)	c (J/mole)	d (J/mole)
Al	Solid	931.7	10.753	20.669	12.384	--	--
	liquid	2600	284.09	29.288	--	--	--
Ni	Solid α	626	0.385	16.987	29.45	--	--
	Solid β	1728	17.614	25.104	7.5312	--	--

The flow chart of reaction temperature calculation was presented in Figure 4-7. The symbols H in the chart standards the enthalpy, C_p standards the heat capacity and T_{ad} is the calculated reaction temperature.

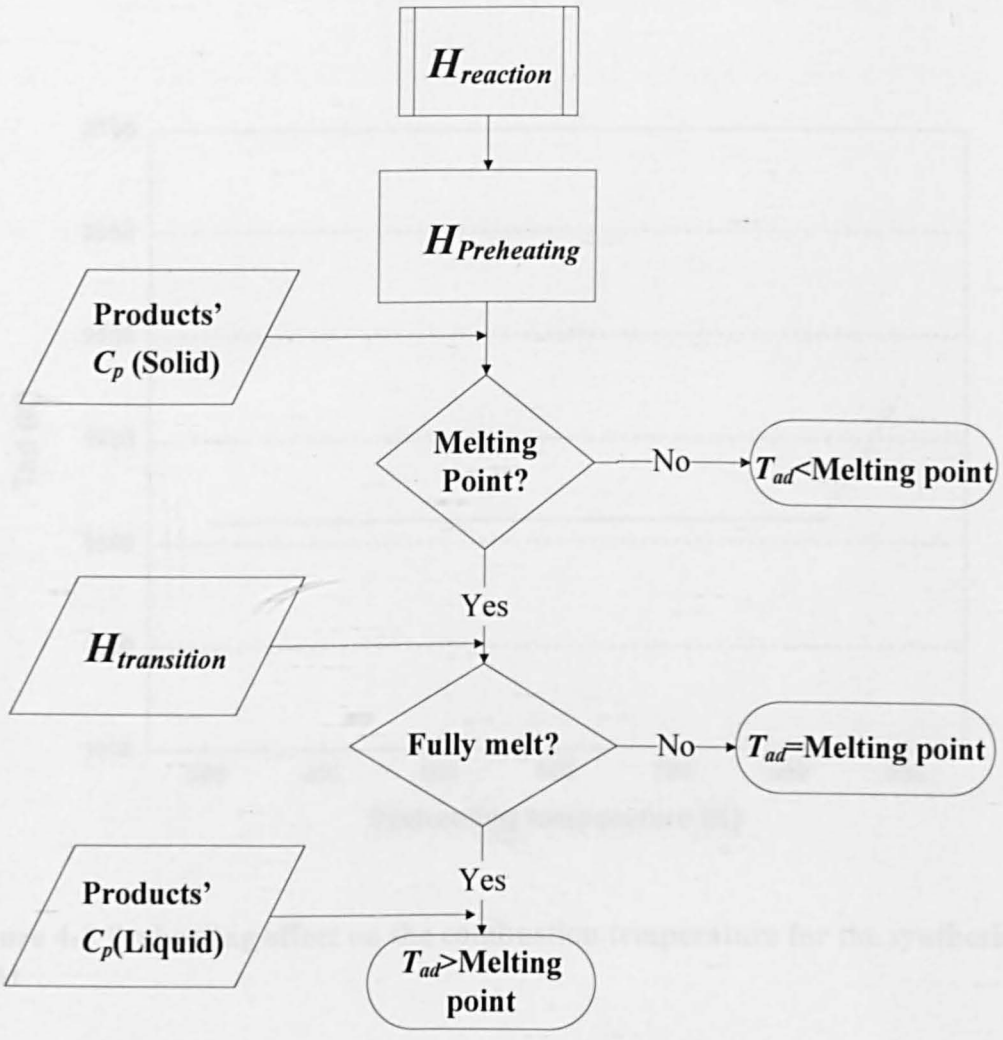

Figure 4-7 The flow chart of reaction temperature calculation

Figure 4-8 shows the calculated T_{ad} as a function of preheating temperature. The results show that when the preheating temperature is below 800K the T_{ad} remained at 1911K, since the temperature is controlled by the melting of NiAl and the solid to

liquid transition of NiAl was not complete. When the preheating temperature is above approximately 830K the T_{ad} start to increase, which indicates the NiAl product was fully melted during synthesis. Since all the reacted samples were preheated to above 833K as shown in Figure 4-5, it is expected that the NiAl product was fully melted during synthesis.

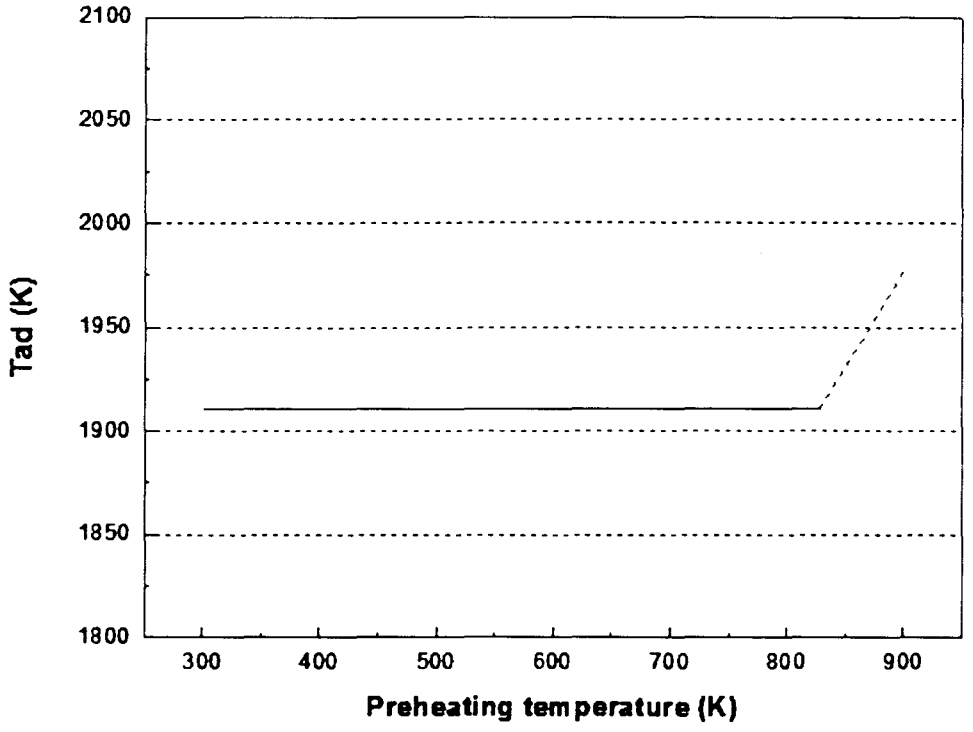

Figure 4-8 Preheating effect on the combustion temperature for the synthesis NiAl

After reaching to the peak, the temperature declined to approximately 1850K and remained at this temperature for about 7seconds. Considering the existence of liquid NiAl in synthesis, this plateau is supposed to represent the exothermal reaction of NiAl during solidification. The solidification temperature was slightly lower than the equilibrium solidification temperature of NiAl (1911 K) owing to the under cooling

effect. The time of solidification was controlled by the cooling condition and the amount of liquid phase. Since the size of sample and the composition are same, consistence time of 7 seconds was observed for all the samples.

Both Ni and Al are metallic materials which can be heated by induction heating. However, since the specimens were prepared as compressed pellets, green density will have a significant effect on both heating and combustion reaction. Figure 4-9 shows the heating profile of specimens with different green densities. The compression pressure and green density of each sample are given in Table 4-2.

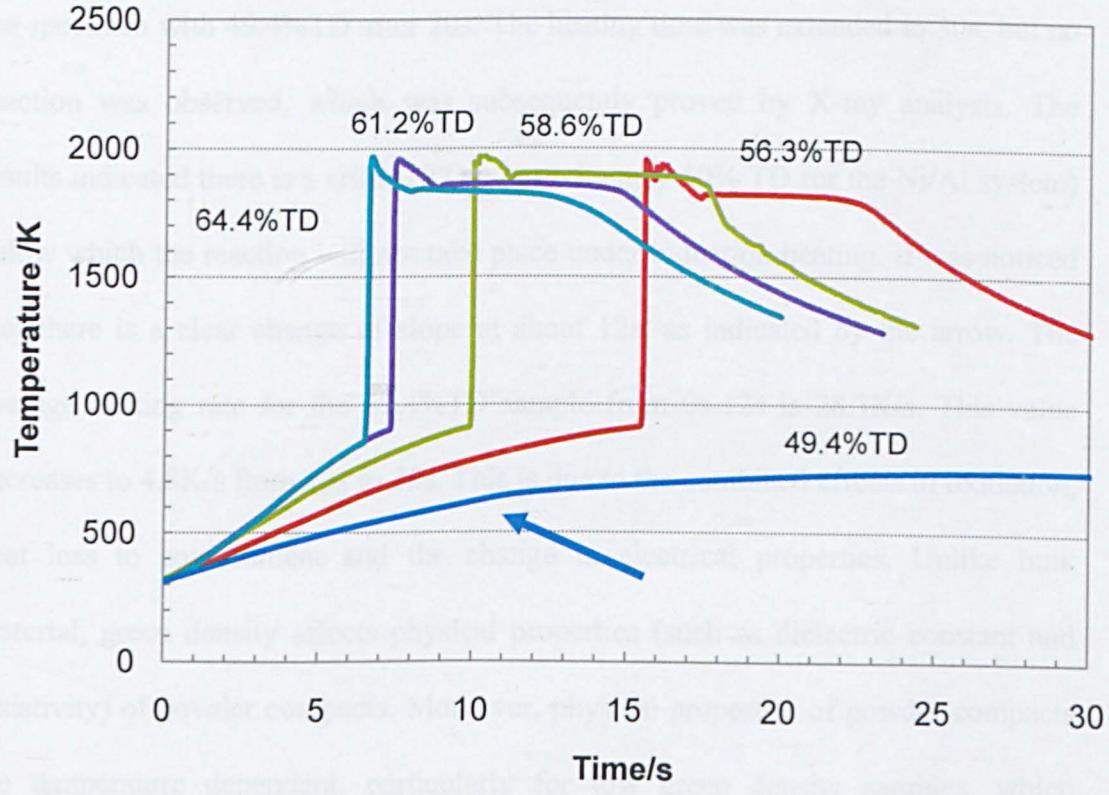

Figure 4-9 The effect of green density on the heating rates and ignition of Ni/Al compacts

Although the heating rates for specimens of 64.4%TD and 61.2%TD are similar, the one with 61.2%TD had a longer ignition time and a higher ignition temperature (T_{ig}). This is because that the sample with the higher green density has more particle contacts, lower resistance and higher thermal conductivity. The 58.6%TD specimen ignited at about 10s and the 56.3%TD one required approximately 16s. For the reacted samples, the cooling period contained a plateau at approximately 1800K for 7s, which is similar to the results for the samples heated at different currents. This is because the mass of all the samples was constant and after combustion all samples were converted to NiAl and fully melted. No combustion reaction was detected for the specimen with 49.4%TD after 20s. The heating time was extended to 30s, but no reaction was observed, which was subsequently proved by X-ray analysis. The results indicated there is a critical TD (approximately 50% TD for the Ni/Al system) below which the reaction will not take place under induction heating. It was noticed that there is a clear change of slope at about 12s, as indicated by the arrow. The average heating rate for the 49.4%TD sample from 0s-12s is 28.3K/s. This value decreases to 4.8K/s from 12s to 25s. This is due to the combined effects of oxidation, heat loss to environment and the change in electrical properties. Unlike bulk material, green density affects physical properties (such as dielectric constant and resistivity) of powder compacts. Moreover, physical properties of powder compacts are temperature dependent, particularly for low green density samples, which increases the difficulties for quantitative analysis.

4.4 Microstructure of the synthesised products

4.4.1 The crystalline structure of synthesized product

Figure 4-10 shows the 300A sample before and after 15 second etching. Before etching the sample is dense with traces of visible pores of around 2 micron in size. After 15s etching, except the emergence of dendritic crystals and grain boundary, some facetted crystals appeared as shown in Figure 4-10 b. The facetted crystals exist in the grain boundary and within the grain. In the stereo mode of SEM observation the crystals are ledges on surface. The facetted crystals within grain and at the boundary are shown at higher magnification in Figure 4-10c and Figure 4-10d respectively. The overall size of multi-layer crystal ranges from 4 μm to 10 μm.

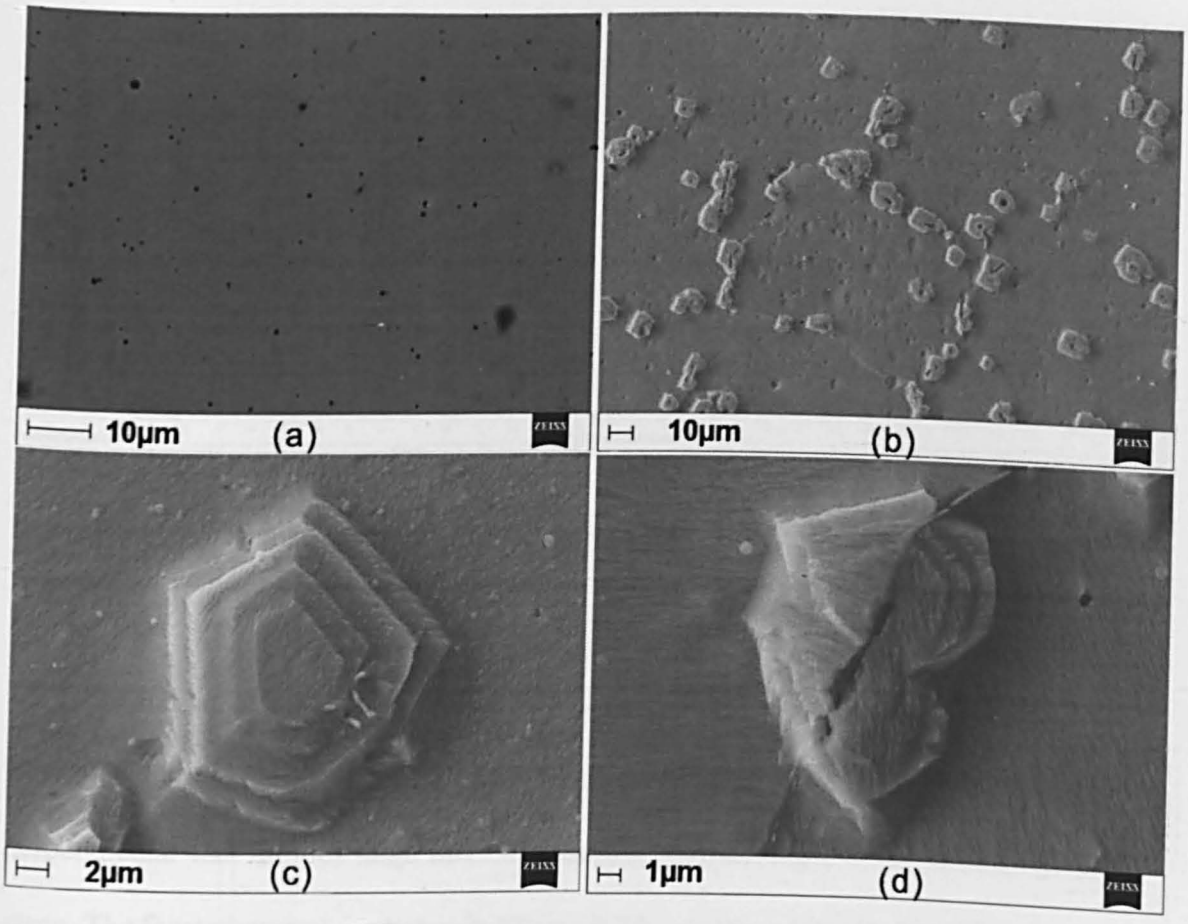

Figure 4-10 Microstructure of synthesized NiAl using 300A. (a)non-etched; (b)etched 15s; (c) individual faceted crystal in a large grain; (d) faceted crystal at grain boundary

By EDX analysis, as shown in Figure 4-11, the facetted crystal has the same atom composition to that of the dendritc crystals. As the EDX analysis has the minimum detection limit of 0.5atom% for Ni and Al element, it can be confirmed that the facetted crystal has same composition to matrix.

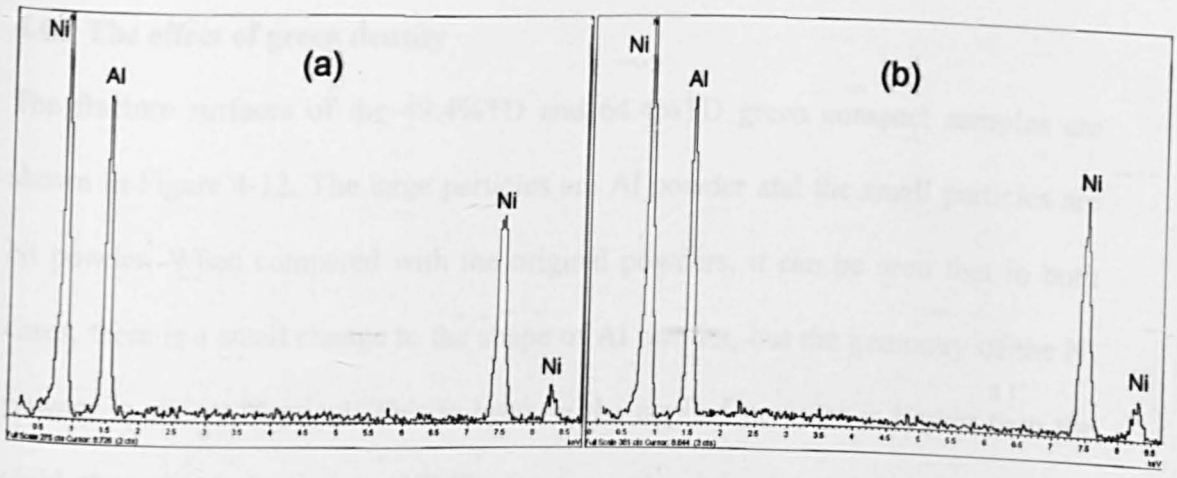

Figure 4-11 EDX analysis result; a) the facetted crystal; b)the matrix of sample

The appearance of crystals provides information about the product synthesis. As shown in Figure 4-10d, the dendrtic crystals in two neighbour grains are almost perpendicular that implies large thermal gradient within sample at the solidification stage. The faceted crystal as shown in Figure 4-10c contains 4 layers from the matrix and has a shape similar to a pentagon. The step distance between layers is about 1.5 microns and the grain size is around 16 microns. The crystal at the boundary shows 3 steps and the size is around 15 microns. Other than spiral growth of crystal, the multi-layer crystal suggests a 2D nucleation from the melts. Generally the appearance of 2D nucleation implies supersaturation of the melt during synthesis [151]. Since the samples used in this study were all in flat disc shape, the heat transfer during cooling was mostly one directional, being perpendicular to the surface of the disc thus favouring the 2D nucleation[151]. It is affirmed that both dendrtic crystals growth and facetted crystals growth are involved at the solidification, but quantitative analysis for these crystal growths requires further fundamental experimental work.

4.4.2 The effect of green density

The fracture surfaces of the 49.4%TD and 64.4%TD green compact samples are shown in Figure 4-12. The large particles are Al powder and the small particles are Ni powder. When compared with the original powders, it can be seen that in both cases, there is a small change to the shape of Al powder, but the geometry of the Ni powder is almost identical. This is because the applied pressure is higher than the yield strength of aluminium (17MPa for pure Aluminium) but lower than that of nickel (138MPa for pure nickel). As expected, the size of the pores in the high density sample (64.4%TD) was much smaller than that in the low density sample (49.4%TD).

The synthesised products for the samples with different green densities are shown in Figure 4-13 in backscatter mode (etching time 25s). There was no combustion reaction for the sample with 49.4%TD and the microstructure was similar to the original sample shown in Figure 4-10 (a). For the compacts with green densities 56.3% to 64.4%TD, NiAl was the only synthesised product, this was proved with X-ray diffraction. The grain size of the NiAl products were much larger than the original Al powder (15 μm) and Ni powder (4.5 μm), ranging from 30 to 80 μm. Figure 4-13 also shows that the green density has a significant effect on the size of the pores and the grain size of NiAl. When the green density increased from 56.3% to 64.4%TD, the size of the pore reduced from 15 μm down to less than 5 μm and the grain size of NiAl reduced from 80 μm to 30 μm. The pores are concentrated at the grain boundary since the cooling rate is high and there was insufficient time at high temperature to achieve full densification for the synthesised NiAl. However, the

samples synthesized with 61.2% and 64.4% TD were nearly full densified with a density over 95% of TD.

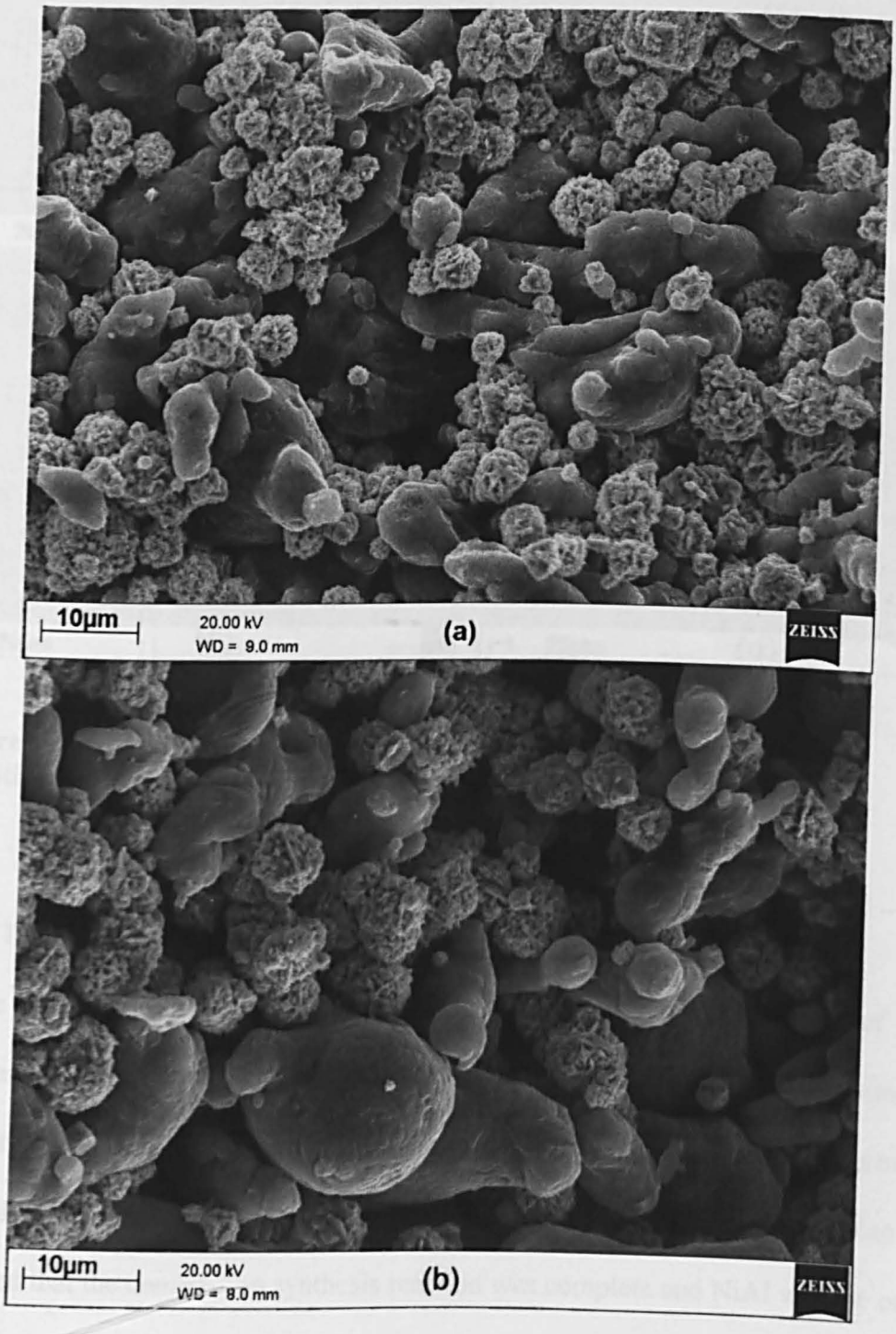

Figure 4-12 Fracture surface of green compacts: (a) 49.4%TD; (b) 64.4%TD

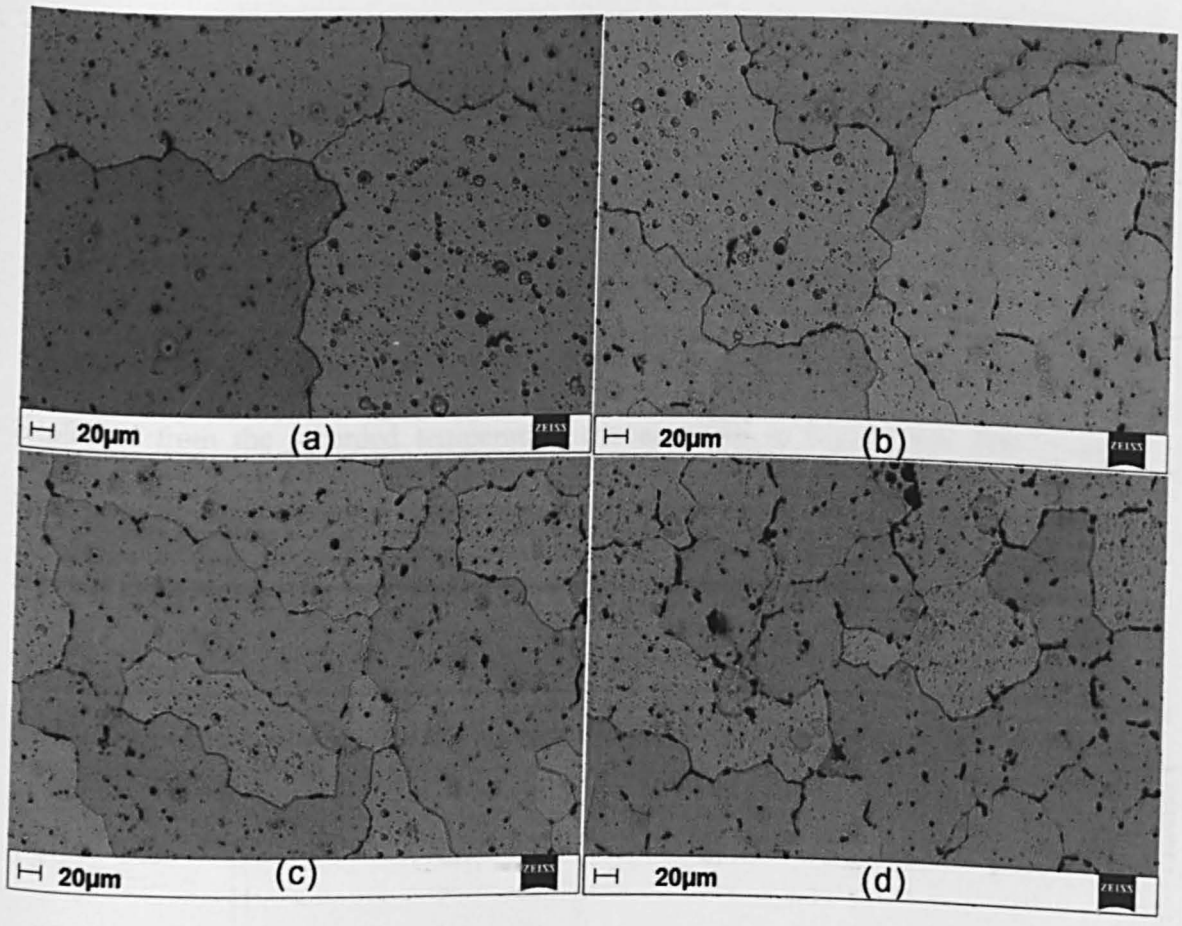

Figure 4-13 Microstructure of synthesised products with different green densities: (a) 56.3%TD; (b) 58.6%TD; (c) 61.2%TD; (d) 64.4%TD.

4.4.3 The effect of heating rates

Figure 4-14 shows the effects of heating rates on the microstructures of the synthesised products in backscatter mode (etching 25s). Due to the pronounced porosity of the green compacts and fast cooling rate defects in the form of pores exist in all the samples. However, confirmed by XRD pattern and EDX analysis it can be assumed that the combustion synthesis reaction was complete and NiAl was the only phase in the products under all the heating rates applied. This result differs from some previous investigations. For example, Fan and Ozdemir [94, 152] studied the reaction of CS of NiAl utilizing the quenching method and found residual Ni in the

synthesised products. The discrepancy is attributed to the different synthesis processing. In the current study, induction heating provides preheating and ignition which generate a much more homogeneous environment for the SHS synthesis.

The results also show that heating rates have a significant effect on the size of the synthesised NiAl. With increased heating rates, the grain size is reduced. This can be explained from the recorded temperature curves given in Figure 4-6. For lower heating rates, the time required to reach the ignition temperature is increased. The thermal images also supported that at ignition the temperature inside the compacts is more uniform and the average temperature is higher. Consequently, the synthesised products will be maintained at a higher temperature for a longer time.

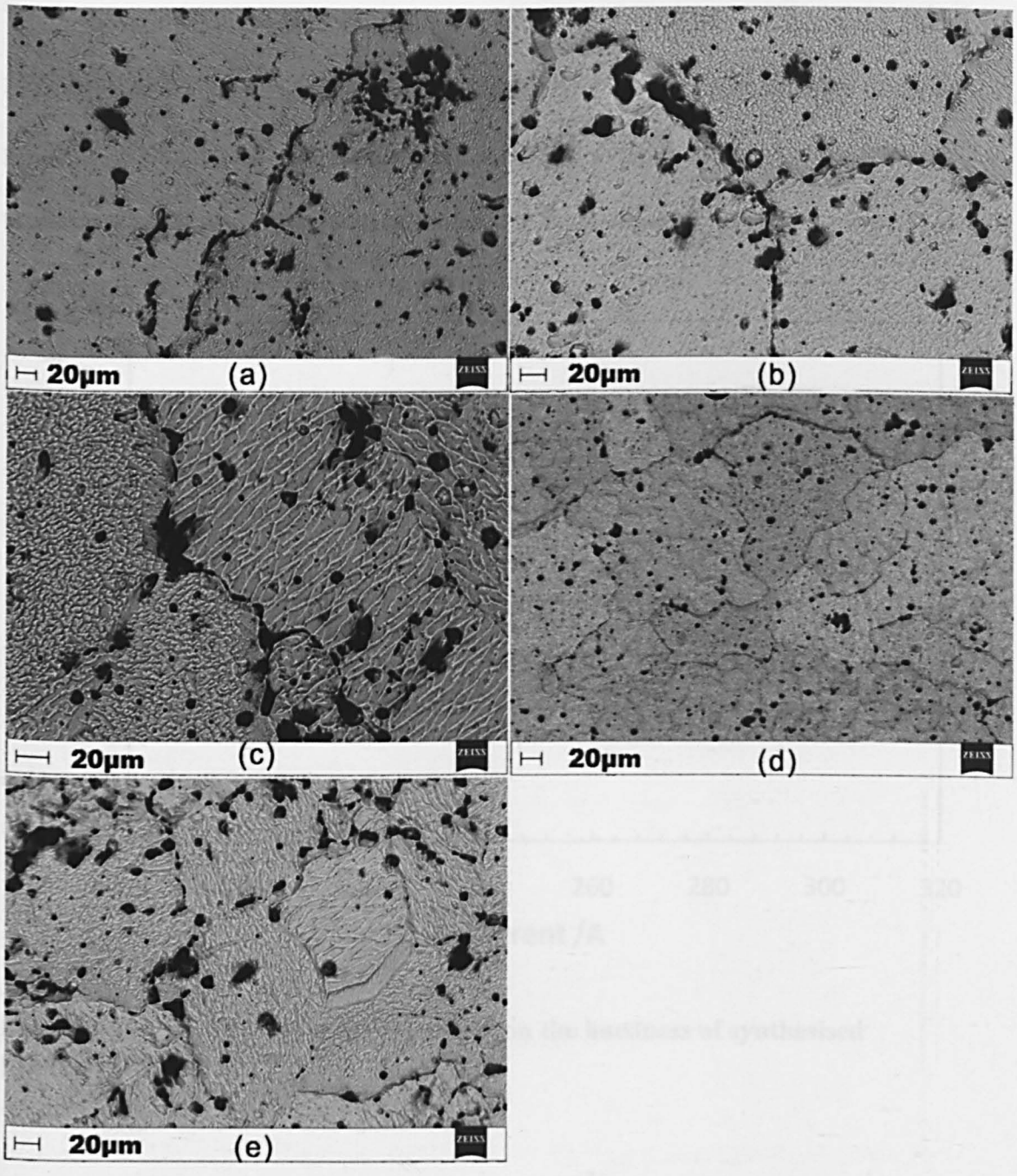

Figure 4-14 Microstructure of synthesised products with different heating power: (a) 200A; (b) 225A; (c) 250A ;(d) 275A; (e) 300A

4.4.4 Mechanical properties of synthesized products

The hardness of synthesised product as a function of heating rates is given in Figure 4-15, which shows a tendency for hardness to increase with increasing heating rate.

When the current increased from 200 A to 300 A, the hardness increased from 297±3.1H_v to 331±6.4 H_v. This result is consistent with the microstructure analysis given in Section 3.3. As the heating rate increases, the grain size of the synthesised products reduces which results in an increase in the hardness.

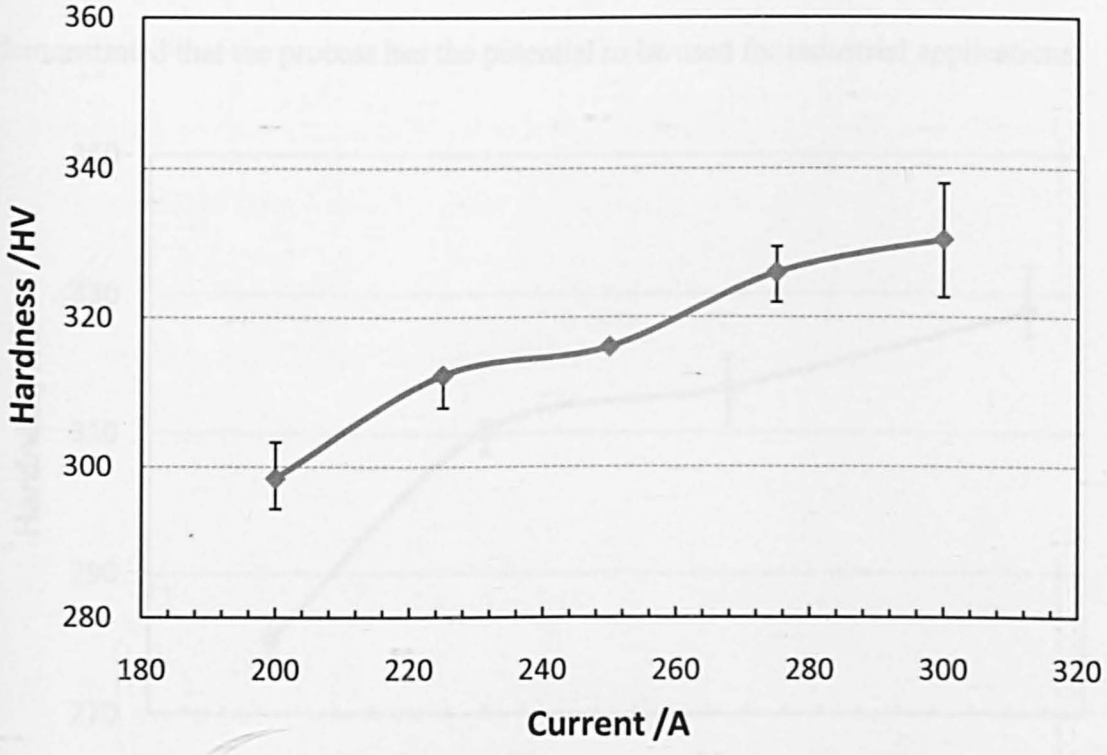

Figure 4-15 The effects to heating current on the hardness of synthesised products

The effects of green density on the hardness of synthesised products are shown in Figure 4-16. The 64.4% TD sample has the highest value of 327.3±7.2H_v and the lowest one is 283.8±3.6H_v for the 56.1% TD sample. This can also be explained by the microstructure analysis as given in Section 3.3. The increase of green density results in a product with higher density and smaller grain size which contribute to the increase in hardness.

The hardness of the synthesised products range from 327.3H_v to 283.3 H_v, which is comparable to that the synthesised NiAl under consistent pressure of 150MPa (hardness of 367±17$H_{v1.0}$) [134]. Considering the simplicity of the process, the results obtained in this study through the use of induction heating without pressure assistance compare favourably with those obtained in previous study and demonstrated that the process has the potential to be used for industrial applications.

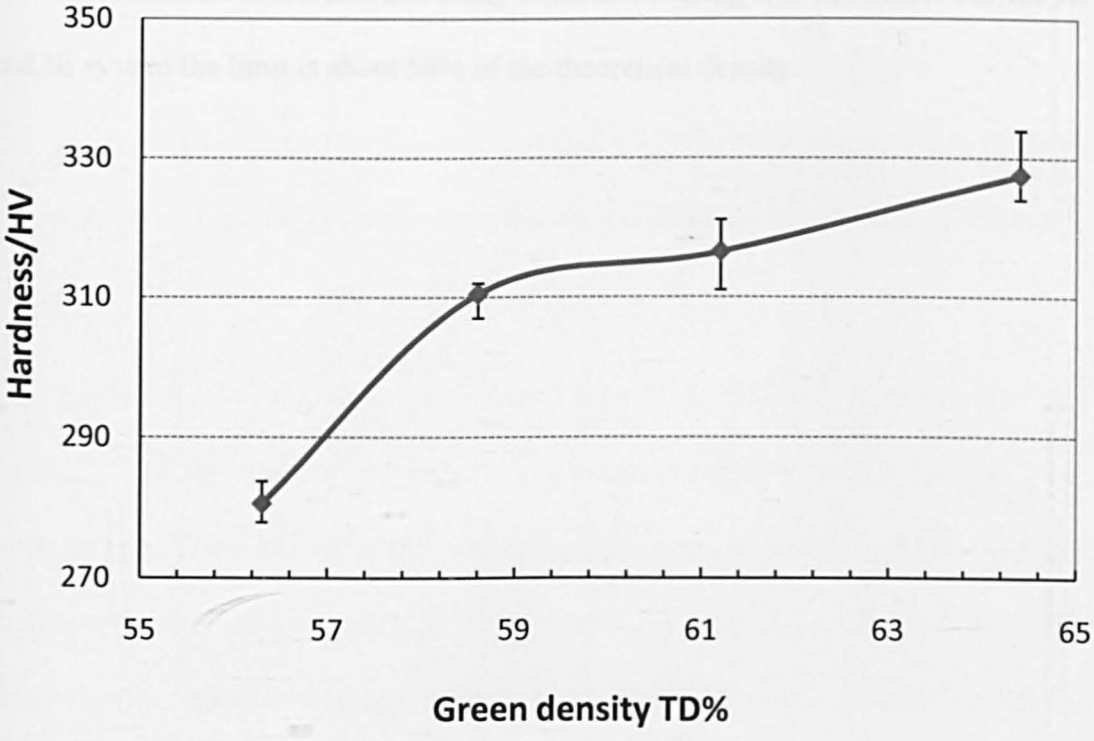

Figure 4-16 The effect of green density on the hardness of synthesised products

4.5 Summary

NiAl was successfully synthesised using induction heating. The heating behaviour of induction heating and ignition process were studied. The effects of heating rates and the green densities of compacts were investigated. The results show that NiAl was the only phase in the synthesised product under a high heating rate. The heating

currents and green density have significant effects on the heating rates, microstructures and the hardness of the synthesised products. Increasing induction current and green density results in an increase in the heating rates and a reduction in the grain size of the synthesised NiAl, this leads to a higher hardness. The hardness of the synthesised products is compatible to the products synthesised under high pressure. The experiments have also shown that there is a limit on green density below which combustion reaction using induction heating will not occur. For the Al and Ni system the limit is about 50% of the theoretical density.

Chapter 5 Combustion synthesis of $NiAl/Al_2O_3$ composites by induction heating

5.1 Introduction

The Al_2O_3 particle is a proven reinforcement since it has low density and high modulus [153]. In the case of NiAl SHS synthesis, D.Tingaurd et al. claimed that the non-reactive particles improve the NiAl matrix properties due to the modification of fracture mode from intergranular to transgranular [154]. Particularly, Al_2O_3 particles strengthen mechanical properties regardless of degradation through combustion [136, 155-156].

Thermodynamically, the addition of Al_2O_3 acts as a "dilution" agent to the NiAl synthesis. The dilution not only affects the exothermicity but also influences other parameters of SHS. The influence on exothermicity can be divided into two aspects: (a) the reduction of total enthalpy of synthesis for equivalent weight and (b) the absorption of heat throughout combustion propagation and product synthesis. Furthermore, the dilution affects the ignition and the combustion behaviour owing to the changes in thermal conductivity and porosity.

In Chapter 4 the feasibility of utilizing induction heating to ignite Ni/Al SHS was confirmed. In this chapter, research was focused on investigate the effects of Al_2O_3. The amount of Al_2O_3 affects the induction heating efficiency since it is an electromagnetic insulation material. In this study Al_2O_3 was added to the samples in varying amounts to determine the optimum limit. The microstructure and mechanical properties of the synthesized composites were examined and tested in this chapter.

5.2 Experimental procedures

Ni and Al were weighed at a stoichiometric mole ratio 1:1 and mixed with Al_2O_3 at 3%, 7%, 10%, 12% and 15% weight percentage (wt%). The powder mixture was compressed in a steel die of 16 mm diameter with compression pressure fixed at 100MPa.

The experimental details of set up and products' characterisation were the same as those described in Chapters 3 and 4.

5.3 Results and discussion

5.3.1 Chemical phase characteristics

The results of X-ray diffraction tests are given in Figure 5-1. X-ray pattern for the 3wt% to 7wt% samples show little evidence of Al_2O_3 since the quantities of Al_2O_3 are small and the diffraction intensity of Al_2O_3 is much weaker than that of NiAl. Figure 5-1 shows two chemical phases, NiAl and Al_2O_3, in the 10wt% sample and three phases, NiAl, Al_2O_3 and trace Ni_2Al_3 in the 12wt% sample. The Al_2O_3 phase is α-Al_2O_3 which is the same as in the original sample. No nickel or aluminium can be detected in the X-ray pattern which indicates that the combustion reaction was completed for these samples. Hence the Al_2O_3 was acting as a dilution and did not take part in the reaction. The reason for the formation of Ni_2Al_3 is discussed in section 5.3.7.

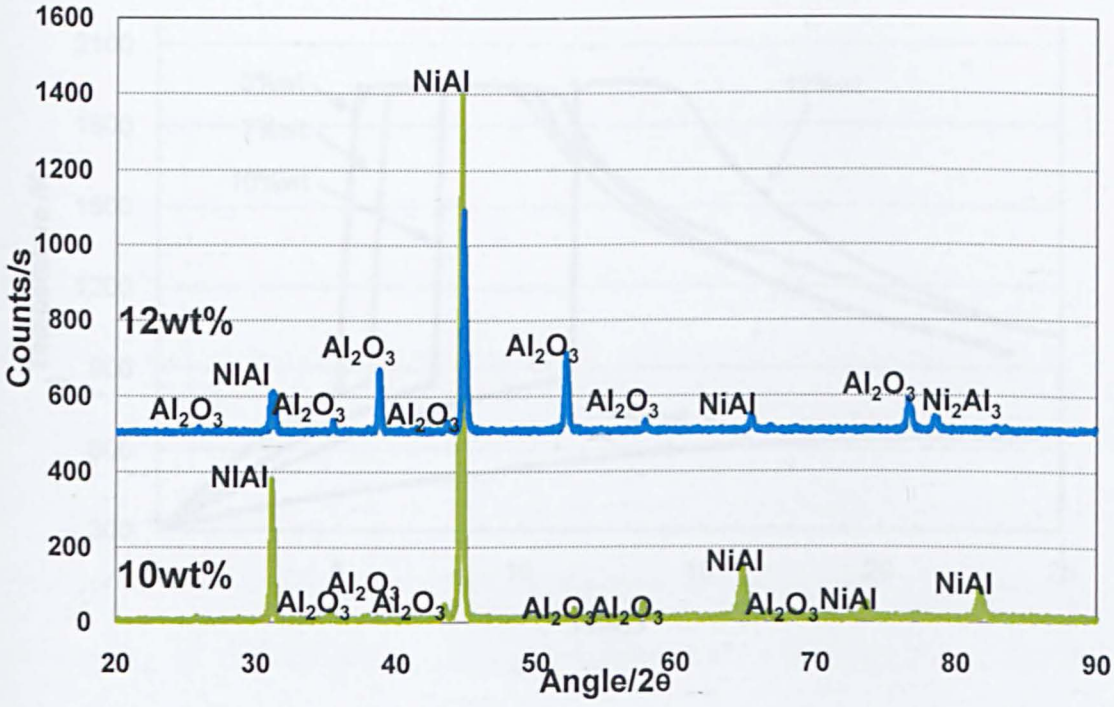

Figure 5-1 X-ray diffraction pattern for 10% and 12% Al_2O_3 addition products

5.3.2 The effect Al_2O_3 content on the combustion temperature

To investigate the effects of Al_2O_3 on ignition behaviour and combustion temperature, the temperature profiles for all the samples were recorded during synthesis and are shown in Figure 5-2. The 3wt%, 7wt%, 10wt% and 12wt% sample curves have sharp temperature increases at approximately 820 K, indicating the occurrence of combustion. In contrast, no combustion can be observed in the 15%wt sample even after 25 seconds heating. The temperature profiles for the reacted samples can be divided into four stages: Heating, Ignition and combustion, High temperature plateau and Cooling. In the following discussion each stage will be considered separately.

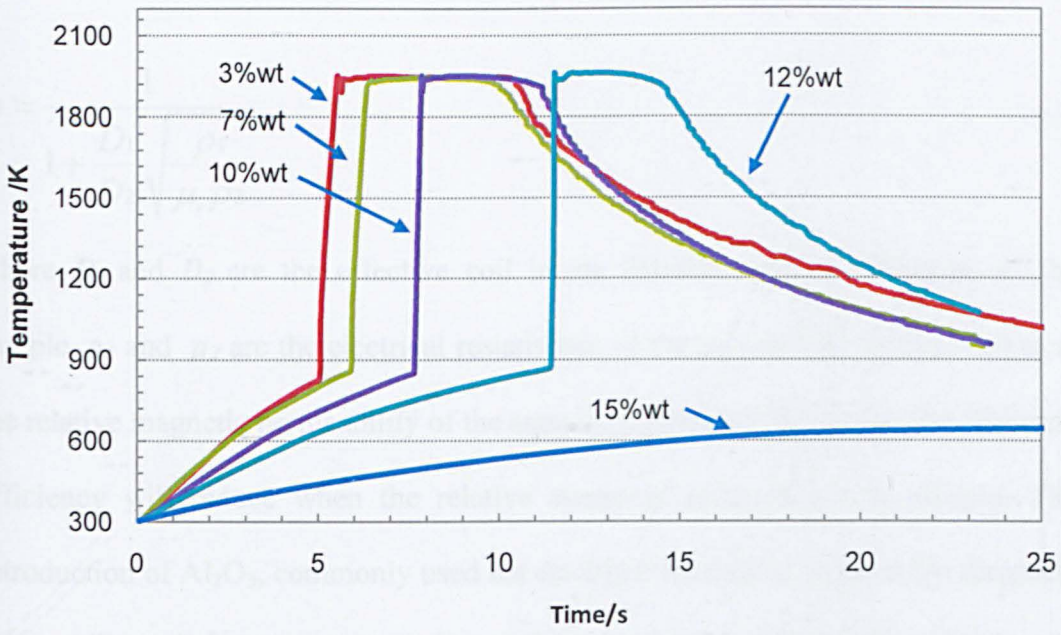

Figure 5-2 Measured temperature during process for the samples with different Al_2O_3 contents

5.3.3 Heating behaviour

The average heating rates of the specimens can be derived from Figure 5-2 and the results are given in Table 5-1, which shows the heating rate decreasing sharply with increasing Al_2O_3 content, i.e. the addition of Al_2O_3 slowed the heating process induced via induction heating. This is because the heating rate of the samples relies on both the efficiency of the heating process and samples' heat capacity. The effect of Al_2O_3 on these parameters is discussed below.

Table 5-1 Average heating rate as a function of Al_2O_3 content

Al_2O_3 content (wt%)	3	7	10	12	15
Average heating rate (K/s)	114.2	94.7	71.8	49.6	19.6

The electrical efficiency under induction heating η can be described by [157]:

$$\eta = \frac{1}{1 + \frac{D_1}{D_2}\sqrt{\frac{\rho_1}{\mu_r \rho_2}}} \qquad \textbf{5-1}$$

where D_1 and D_2 are the effective coil inside diameter and the diameter of the sample, ρ_1 and ρ_2 are the electrical resistivities of the coil and the sample and μ_r is the relative magnetic permeability of the sample. Equation 1 shows that the electrical efficiency will reduce when the relative magnetic permeability is reduced. The introduction of Al_2O_3, commonly used for electrical insulation, reduces the magnetic permeability of the compact mixture and consequently results in a reduction of heating rate.

The heat capacity of a material can be calculated using equation 2 below [149]:

$$C_p = a + (b \times 10^{-3})T + (c \times 10^{-6})T^2 + \frac{d \times 10^5}{T^2} \qquad \textbf{5-2}$$

where a, b, c and d are constants which are listed in Table 5-2 for the materials used in this study. Using equation 2 together with the data in Table 5-2, the energy required to heat from ambient temperature (298 K) to 800K is estimated as 344.5J/g for Al_2O_3 and as 524.6J/g for the Ni/Al mixture. The equivalent energy required for the 3wt%, 7wt%, 10wt% samples is estimated as 519.2J/g, 511.9J/g and 506.6J/g respectively. Hence the change in heat capacity is not the main reason for the decrease in the heating rate. Experimental results show a critical value for Al_2O_3 content above which the sample cannot be ignited by induction heating. The value is 15 wt% Al_2O_3 under these experimental conditions.

Table 5-2 Thermal capacity of materials (date reference [149])

Element	Phase	Temperature of Transition /K	Heat of Transition/ kJ/mol	a / J/mol	b / J/mol	c / J/mol	d / J/mol
Al	Solid	931.7	10.7477	20.659	12.379	--	--
	liquid	2600	283.958	29.274		--	--
Ni	Solid α	626	0.38474	16.978	29.441	--	--
	Solid β	1728	17.6062	25.092	7.5276	--	--
Al_2O_3	Solid	2300	108.732	109.23	18.350	--	-30.39

5.3.4 Ignition process

The ignition and combustion propagation were monitored using a thermal imaging technique, and the results are shown in Figure 5-3. Detailed information, shown in Figure 5-4, was extracted at 5 points positioned in the direction of combustion propagation. The points were labelled in numerical order with the ignition start point set as point 1. The distance between each point was set at 4 mm so that these points covered the centre and the edge of the sample. The combination of these two figures provides the temperature distributions from ignition to combustion and allows the combustion propagation rate to be estimated. The thermal images in Figure 5-3 show that prior to ignition, the temperature at the edge of the sample was slightly higher

than at the central area. This is a typical characteristic of high frequency induction heating known as the "edge effect" which implies the magnetic field strength at the edge is higher than that in centre area. The temperature difference between the edge and the central area was approximately 80K, as indicated in Figure 5-4. This is due to the edge being closer to the coil rings and thus in a region of higher induced current density. The temperature difference also showed that ignition commenced at the edge and propagated to the centre of the sample. However, the ignition zone was not circular because the magnetic field generated by the coil is not a perfect circle. Small differences in the magnetic field will result in large differences in induction heating.

Figure 5-4a and Figure 5-4b show a reduction in temperature between point 1 and point 2 after ignition. This is because during combustion propagation the sample shape changed such that point 1 and point 2 were no longer within the sample, which can be clearly seen in Figure 5-3. With increasing Al_2O_3 content the shape change becomes less obvious, the shape change for the 12wt% sample being insignificant as shown in Figure 5-3d.

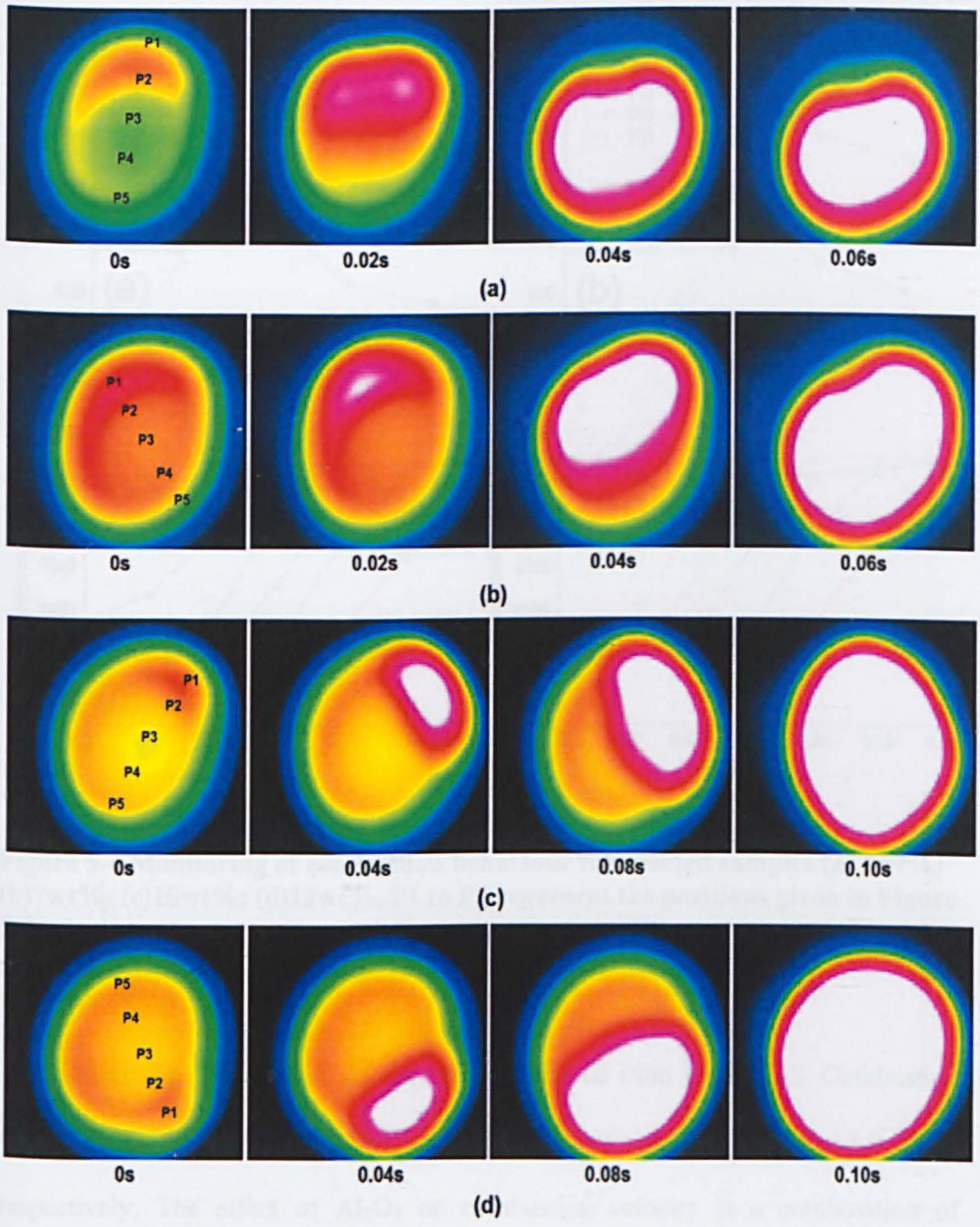

Figure 5-3 Ignition and combustion propagation (a)3wt%; (b)7wt%; (c)10wt%; (d)12wt%

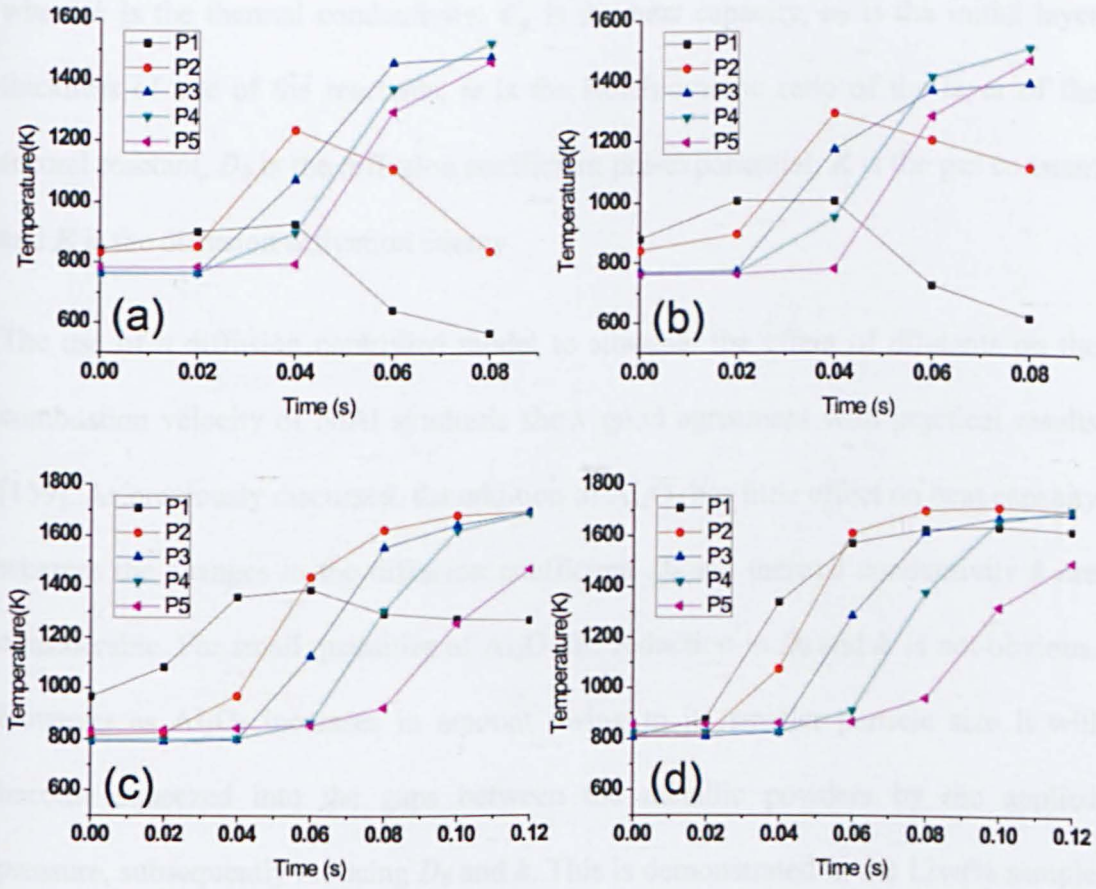

Figure 5-4 Monitoring of combustion behaviour for reacted samples (a) 3wt%; (b)7wt%; (c)10wt%; (d)12wt%. P1 to P5 represent the positions given in Figure 5-3

The combustion propagation velocity can be derived from Figure 5-3. Combustion velocities for the 3wt% and 12wt% sample were estimated at 0.3m/s and 0.15m/s respectively. The effect of Al_2O_3 on combustion velocity is a combination of changes in sample properties such as thermal conductivity, thermal capacity etc. In accordance with Fourier's law for heat transport, the combustion velocity for diffusion controlled SHS processes can be described using Equation 5-3[158]:

$$v^2 = \frac{2k}{a_0^2 w C_p \rho} D_0 \exp(-\frac{E}{RT}) \qquad \textbf{5-3}$$

where k is the thermal conductivity, C_p is the heat capacity, a_0 is the initial layer thickness of one of the reactants, w is the stoichiometric ratio of the layer of the second reactant, D_0 is the diffusion coefficient pre-exponential, R is the gas constant and E is the diffusion activation energy.

The use of a diffusion controlled model to simulate the effect of dilutants on the combustion velocity of NiAl synthesis show good agreement with practical results [159]. As previously discussed, the addition of Al_2O_3 has little effect on heat capacity whereas the changes in the diffusion coefficient D_0 and thermal conductivity k are considerable. For small quantities of Al_2O_3 the reduction in D_0 and k is not obvious. However as Al_2O_3 increases in amount owing to its smaller particle size it will become squeezed into the gaps between the metallic powders by the applied pressure, subsequently reducing D_0 and k. This is demonstrated in the 12wt% sample (approximate 15 volume percentage) where the Al_2O_3 powder is located between the Al and Ni powders as shown in Figure 5-5. The lower combustion velocities of the samples with higher Al_2O_3 content can therefore be attributed to the lessening of direct contact between the Al and Ni powders.

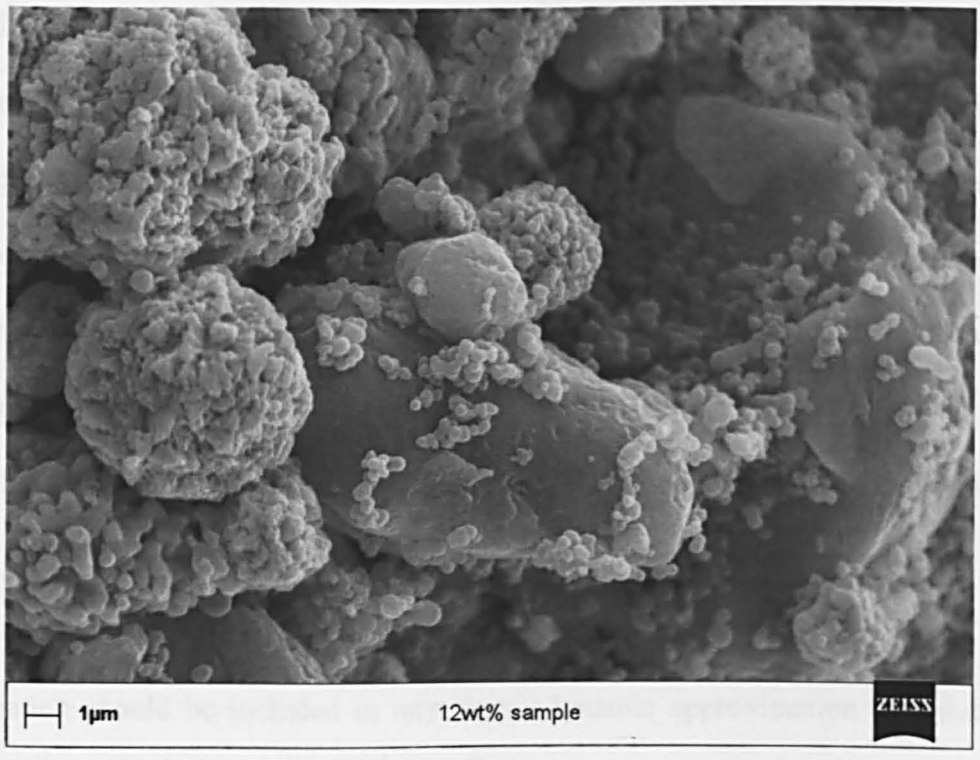

Figure 5-5 Fracture surface of compressed sample with 12wt% Al_2O_3.

5.3.5 Combustion and solidification

The recorded maximum temperatures of the reacted samples were almost identical (≈ 1950K) as is shown in Figure 5-2. After reaching the maximum temperature, each temperature profile shows a dip followed by a plateau at about 1900K. This plateau is assumed to represent the solidification stage of NiAl following the existence of liquid phase NiAl and is 11 K lower than the equilibrium solidification temperature of NiAl due to the under cooling effect. The length of the plateau shortens with the increase in the content of Al_2O_3. For example, the plateau length of the 3%wt sample was more than 5 seconds whilst for the 12%wt sample it was approximately 2 seconds. The reduction of the plateau period implies that the Al_2O_3 affects the amount of liquid phase present in the synthesized product.

In NiAl combustion synthesis, the maximum combustion temperature in an adiabatic system (T_{ad}) is 1911K i.e. its melting point. The melting point of Al_2O_3 is 2300K [160]. In the composite system, Al_2O_3 is assumed to consume the energy released by the reaction to maintain a solid phase. However, in this study the amount of Al_2O_3 content did not appear to affect the maximum temperature. Thermodynamic theory is introduced to explain this result. Previous research has shown that NiAl appears together with molten Al and during combustion the product contains both liquid and solid NiAl phases [161-162]. Figure 5-4 shows that each sample was heated as a whole and the temperature prior to ignition was above 700K. This suggests that preheating should be included in any thermodynamic approximation of induction heating. Figure 5-3 and Figure 5-4 show that the reactions were very fast (less than 0.1 second). Therefore, it is reasonable to assume the reaction is adiabatic.

Disregarding the reaction sequence and assuming that at maximum temperature the synthesis process is fully completed, the reaction could be simplified as: (data reference [149]):

$$Ni + Al \rightarrow NiAl + 118.5kJ \qquad \textbf{5-4}$$

Assuming the adiabatic environment and taking energy conservation, the equation 6-3 in chapter 6 can be modified as:

$$\sum n_i \Delta H_{298} + \int_{298}^{T_{Ini}} \sum n_i C_p(R_i) dT = \int_{298}^{T_{melt}} \sum m_j C_p(P_j) dT + \Delta H_{melt} + \int_{T_{melt}}^{T_{ad}} \sum m_j C_p(P_j) dT \qquad \textbf{5-5}$$

where T_{melt} is the melting point of product, T_{ad} is the reaction temperature in adiabatic condition and ΔH_{melt} is the melting enthalpy of the product. The solid to liquid phase transition enthalpy of NiAl compounds is 57.6 kJ mol^{-1} [149].

The calculation of C_p is given in Equation 5-2 and using relevant data found in Table 5-2, the required heating enthalpy of solid phase NiAl is determined by [161]:

$$H_{NiAl}(solid) = -131488.5 + 4184T + 6.905\times10^{-2}T^2 \qquad \textbf{5-6}$$

The percentage of liquid phase NiAl has a great influence on the combustion behaviour and product properties, which can be calculated using equations 5-2 to 5-6. Figure 5-6 shows the calculated liquid content of NiAl during synthesis as a function of Al_2O_3 content for different preheating conditions. It can be seen that the preheating parameter affects the liquid phase significantly. For example, the 12wt% Al_2O_3 sample, when preheated to 700K contains more than 60% liquid phase NiAl, but with no preheating contains only 6% liquid NiAl. Due to inevitable heat losses the liquid phase of the product during experiment will be less than that shown in Figure 5-6.

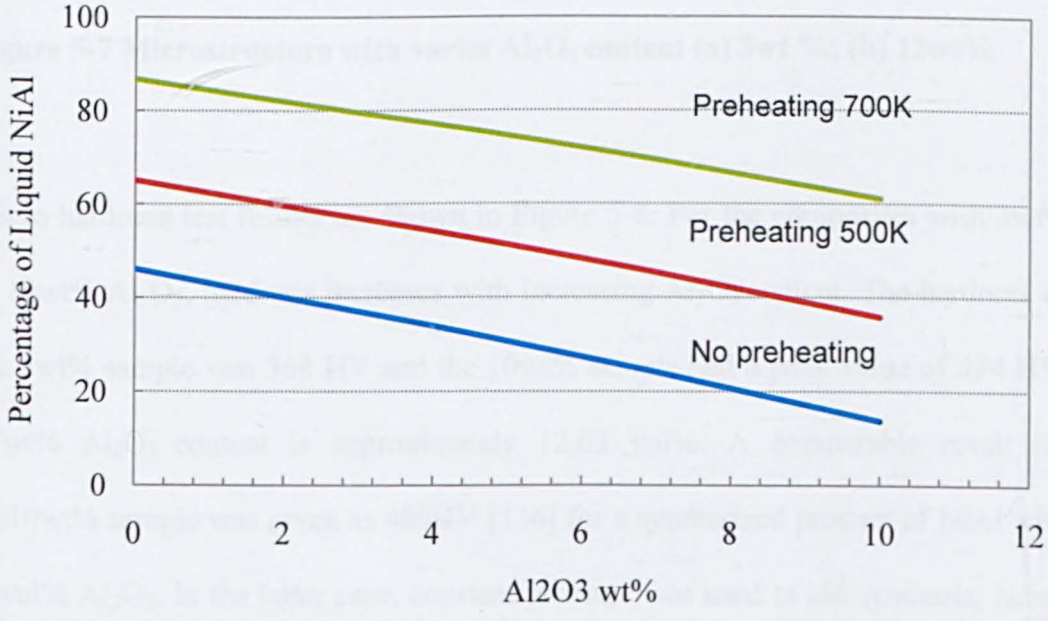

Figure 5-6 The effects of preheating and Al_2O_3 wt% on the liquid content of NiAl

5.3.6 Microstructure and properties

Figure 5-7 shows the microstructure of the 3wt% and 12wt% Al_2O_3 samples. The products were synthesised without pressure but have low porosity. This is because a large amount of liquid phase NiAl was formed during synthesis as shown in Figure 5-6. However, as shown in Figure 5-7b for the samples with high Al_2O_3 content, the fine agglomerated Al_2O_3 cannot be fully absorbed by the molten NiAl and appears as defects in the composite.

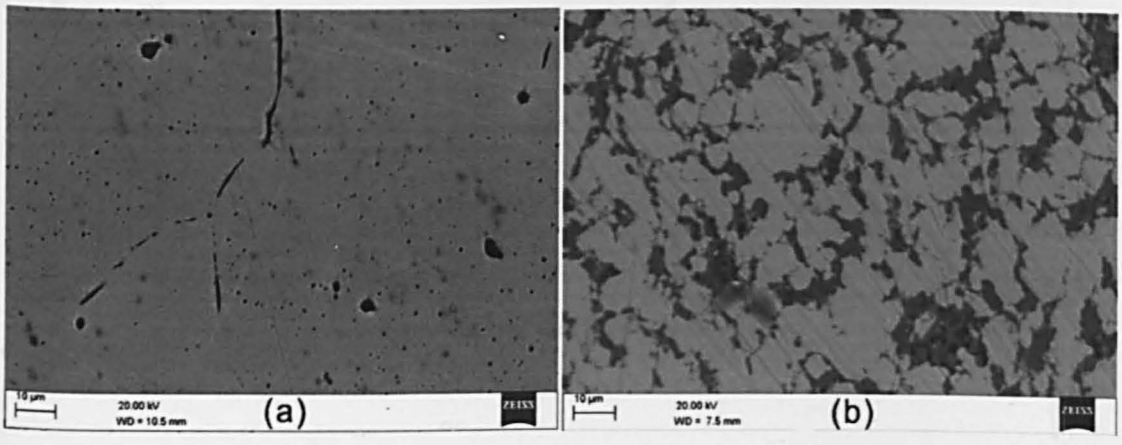

Figure 5-7 Microstructure with varies Al_2O_3 content (a) 3wt %; (b) 12wt%

Micro hardness test results are shown in Figure 5-8. For the composites with 3wt% to 10wt% Al_2O_3, hardness increases with increasing Al_2O_3 content. The hardness of the 3wt% sample was 368 HV and the 10wt% sample had a peak value of 474 HV. 10wt% Al_2O_3 content is approximately 12.63 vol%. A comparable result for the10wt% sample was given as 480HV [136] for a synthesized product of NiAl with 13vol% Al_2O_3. In the latter case, constant pressure was used to aid synthesis, hence the result of 474HV determined in this study is promising since no pressure assistance was used. Figure 5-8 also shows a decline of 52 HV in hardness occurring

between the 10wt% sample and the 12wt% one. This is owing to the existence of agglomerated Al_2O_3 and the fragile phase Ni_2Al_3 which have affected the hardness.

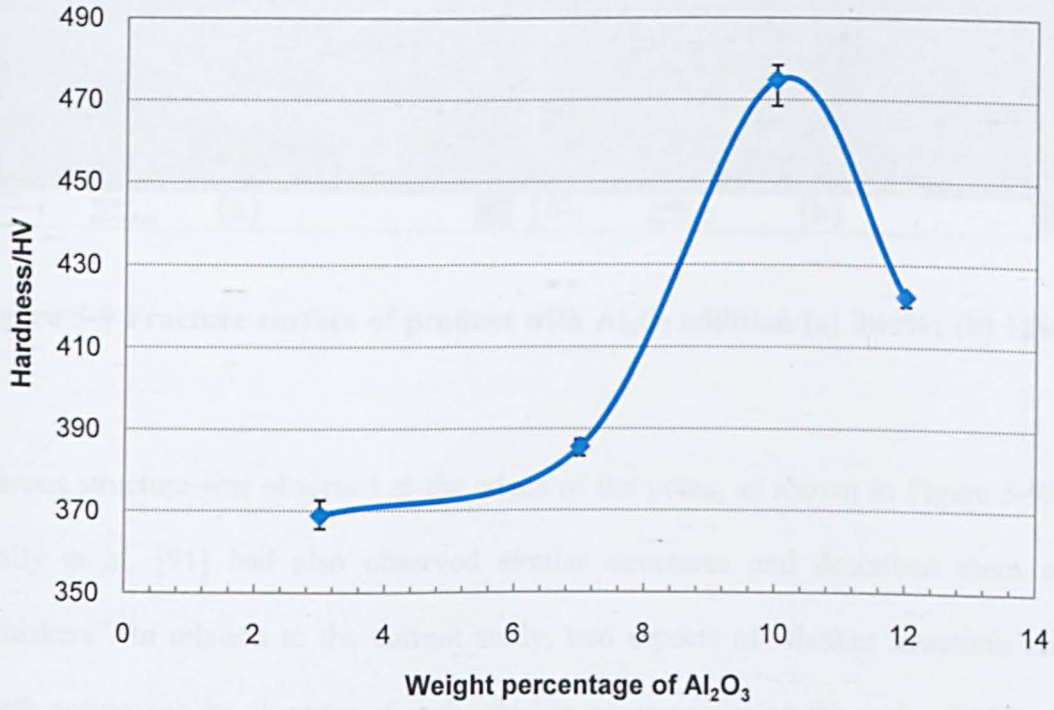

Figure 5-8 Effect of Al_2O_3 addition to hardness of product

To study the strengthening effect of Al_2O_3 on NiAl, the fracture surface of the samples was examined and results for the 3 wt % and 12 wt % are shown in Figure 5-9. For the 3wt% product, the fracture surface shows that NiAl transgranular fracture is the dominant fracture mechanism. Most of the Al_2O_3 particles located within the NiAl grains, which indicates that Al_2O_3 was fully absorbed by the molten NiAl. For the 10wt% and 12wt% samples, owing to the reduction of the liquid phase and the shorter solidification time, pores on a scale of over 10 microns were observed.

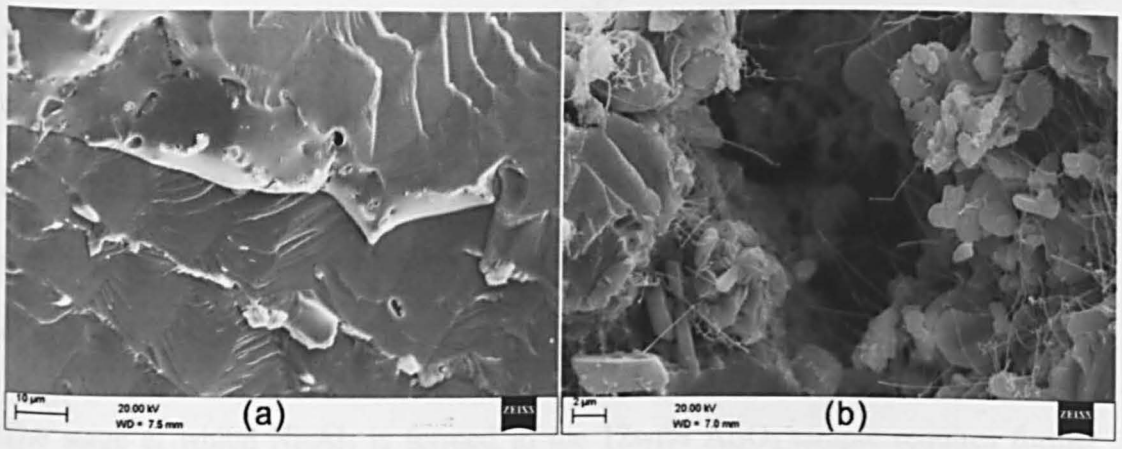

Figure 5-9 Fracture surface of product with Al_2O_3 addition (a) 3wt%; (b) 12wt%

Fibrous structure was observed at the edges of the pores, as shown in Figure 5-9b. Emily et al. [91] had also observed similar structures and described them as "whiskers". In relation to the current study, two aspects of whisker structures are worth noting: (a) the diameter of each whisker structure was on the scale of 100nm, (b) the whiskers were only observed around pores. Since the vapour pressure of Al at 1898K is 40 mmHg [149], it is reasonable to assume that Al vapour should exist during synthesis. Based on the analysis in previous theoretical calculation, it can be reasonably assumed that the temperature at or near a pore will remain at or near to the melting temperature of NiAl (1911k) during combustion. Therefore, the formation of whiskers may due to vaporisation of liquid Al followed by subsequent condensation around the pores.

5.3.7 Formation of Ni_2Al_3

Previous work on NiAl combustion synthesis, has reported that the formation of Ni_2Al_3 could commence in the early stages of synthesis and during cooling. Ping Zhu et al. quenched samples at 854 °C and observed the existence of Ni_2Al_3, which

indicated that the formation of Ni_2Al_3 was in the early synthesis stage[123]. Biswas et al. also found the appearance of Ni_2Al_3 in quenched sample prior to combustion [117]. On the other hand, the appearance of Ni_2Al_3 during the cooling period was confirmed in a time-resolved X-ray diffraction (TRXRD) study[162] and in a study of quenching at the combustion front [92].

The stage at which Ni_2Al_3 is formed in the 12wt% Al_2O_3 sample requires further discussion. As described by A.Biswas et al, Ni_2Al_3 film forms on the Ni particles and further diffusion of Al and Ni atoms across this film leads to the crystallization of NiAl [93, 117]. This suggests the existence of Ni_2Al_3 prior to combustion must be accompanied by residual Ni particles. Thus, if the Ni_2Al_3 was formed at an early stage, it would remain in the final product and combustion would not be complete. In Figure 5-1, the XRD spectra for the 12wt% Al_2O_3 sample shows that NiAl, Al_2O_3 and Ni_2Al_3 are the only existing phases. There are no residual raw materials. From the backscattered image of product, the reaction was shown to be complete for the 12wt% Al_2O_3 sample. The decomposition temperature for Ni_2Al_3 is 1133 °C, and Ping believed that Ni_2Al_3 synthesised at an early stage will decompose completely with only Al (Ni) liquid solution and Ni solid remaining[123]. Therefore, it is reasonable to conclude that the formation of Ni_2Al_3 at the cooling stage in the sample with 12wt% Al_2O_3 is highly possible.

Curfs et al. [162] proposed that the formation of Ni_2Al_3 at the cooling stage is owing to the reaction of liquid Al and solid NiAl. This mechanism can be used to explain the results found in this study. For the 12wt% Al_2O_3 sample, the synthesis process was not completed during the combustion (sharp temperature rising) and solidification (plateau period) stages. Residual liquid phase Al remained at cooling

stage which reacted with NiAl to form Ni_2Al_3. This conclusion is supported by the temperature curves shown in Figure 5-2 where the 12wt% sample had the shortest plateau. Taking this result together with the thermodynamic analysis in this chapter, it could be concluded that in the 12wt% Al_2O_3 sample, the amount of liquid phase Al is much smaller than in the other samples. The fibrous structure shown in Figure 5-9b possibly formed at the cooling stage due to the residual Al liquid. Comparison with the other samples leads to two reasons for the incomplete synthesis of NiAl in the12wt% Al_2O_3 sample: the lowest system energy and the lowest thermal conductivity. The lower system energy results in a lower liquid content in the synthesized product while the reduction in thermal conductivity leads to a longer combustion time and increased the heat loss during combustion. For these reasons Ni_2Al_3 formed in the 12wt% Al_2O_3 sample but not in the other samples. Zhu et al. detected Ni_2Al_3 to be present with no addition of Al_2O_3[123]. However, this is due to the different ignition process used. In this study, the whole sample was heated by induction heating and thus a much higher liquid content achieved.

5.4 Summary

1. Intermetallic $NiAl/Al_2O_3$ composites have been synthesised by Self-propagating High-temperature Synthesis (SHS) using induction heating ignition. The limit of Al_2O_3 content is 12 wt%, above which combustion reaction will not occur.
2. Heating behaviour and combustion propagation were analyzed. During heating temperature differences on the surface of sample were found not to be significant in induction heating. This heating behaviour results in a preheating of the entire component. The average heating rate decreases from

114.2K/s to 49.6Ks with a corresponding increase of Al_2O_3 contents from 0 to 12 wt%. The decrease in combustion velocity was mainly caused by the decrease in the diffusion coefficient.

3. The liquid content of NiAl is a function of Al_2O_3 content and preheating temperature which can be predicted using thermodynamic data.
4. At lower Al_2O_3 content ($\leq$10wt %), the hardness increases with increasing Al_2O_3 content. At high Al_2O_3 content, porosity and brittle phase Ni_2Al_3 reduce hardness. The use of pressure as an aid to synthesis has great potential to enhance material properties.
5. The results indicate that the formation of Ni_2Al_3 in the 12wt% Al_2O_3 sample possible occurs at the cooling stage; using Induction heating is different from other ignition processes in that the combustion reaction with Al_2O_3 content less than 10 wt% is complete and NiAl is the only synthesized product.

Chapter 6 Combustion Synthesis of TiC-NiAl Composite by Induction Heating

6.1 Introduction

The high wear resistance and excellent anti-oxidation performance of TiC have attracted wide research interest and, as a result, have boosted its application in the creation of bulk components and coatings [160]. Self-propagating high-temperature synthesis (SHS) is considered to be an economic method for the synthesis of ceramics and intermetallics such as TiC, with the advantage of producing products of high purity owing to the inherently elevated temperature of the SHS process [163-166]. Yeh et al. had studied the effects of TiC particles on NiAl SHS combustion behaviour [167]. However, the porosity of TiC fabricated via the SHS process has restricted its application. In order to overcome this problem, Gao et al. investigated the possibility of increasing the density of TiC using a NiAl/TiC composite. The results showed that density can be significantly improved and four-point bending strength was as high as 670±80MPa [168].

Although positive results on utilising SHS for the production of dense NiAl/TiC composites have been obtained in the past, the densification mechanism was not clear and no detailed information on process control was available. The reaction sequence for the powder mixture is important since two separate exothermic reactions are needed to form NiAl and TiC. To obtain a comprehensive understanding of this issue, Curfs et al. conducted a series of studies relating to the synthesis of NiAl/TiC [135]. Results from the early studies showed that TiC and

NiAl were the only synthesised products and analysis of the results showed that the synthesis started with TiC and was followed by the slow formation of NiAl [135]. However this conclusion is contrary to evidence from the same author's later research into the combustion synthesis of NiAl, which showed that NiAl was formed with the disappearance of Ni [162]. This discrepancy was investigated further by Ren K et al. who found that the TiC was surrounded by solidified NiAl crystal but the sequence of the reaction could not be determined from the experimental results [169].

In previous chapters, the induction heating has been successfully employed for SHS NiAl and NiAl/Al_2O_3 composites. In this chapter, induction heating will be directly used to ignite the combustion reaction of Ni, Al, Ti and C powder compacts for the synthesis of NiAl/TiC composite. After that the Ni/Al mixture and Ti/C mixture will be compressed separately for two-layer composite synthesis. The synthesis mechanism of NiAl/TiC composite and two-layer NiAl/TiC will also be discussed.

6.2 Experimental details

The chemical compositions and particle sizes of the relevant raw materials and the morphologies of all powders were shown in Chapter 3. The experimental samples were organised into two groups: single-layer and two-layer. In the single-layer group all powders in the designated composition were fully mixed and compressed into one pellet. Ni and Al powder in the stoichiometric mole ratio 1:1 were wet mixed together with 5, 10, 15 and 20 wt% of Ti/C (1:1 mole ratio) in acetone. The mixture was placed in an oven at 80°C for 1 hour to vaporize the acetone. The powder mixtures were then cold compressed in a steel die of 16 mm diameter at a pressure of 100MPa. Each compacted pellet weighted approximately 1 g. In the two-layer group,

the same powder preparation method was used for the Ni/Al and Ti/C mixtures which were then compressed separately, each layer weighing approximately 0.5 g. The Ni/Al pellet was placed under the Ti/C mixture.

6.3 Results and discussion

6.3.1 Synthesis of NiAl and TiC composites

Intensive combustion was observed in the 5wt%, 10wt% and 15wt% samples, but no combustion reaction was observed for the mixture with 20wt% of Ti/C. To verify the reaction products X-ray diffraction tests were carried out on both the green compacts and the heated samples. The X-ray pattern for the 5 to 15 wt% of Ti/C samples are shown in Figure 6-1. The X-ray pattern revealed that NiAl and TiC were the only phases existing in the products with no raw materials being present in the pattern. For the sample with 20 wt% of Ti/C, the spectrum was the same as that of the raw material, indicating that no combustion reaction took place after heating. This result implies that only NiAl/TiC composites with a TiC content of less than 15 wt% can be successfully synthesized by induction heating.

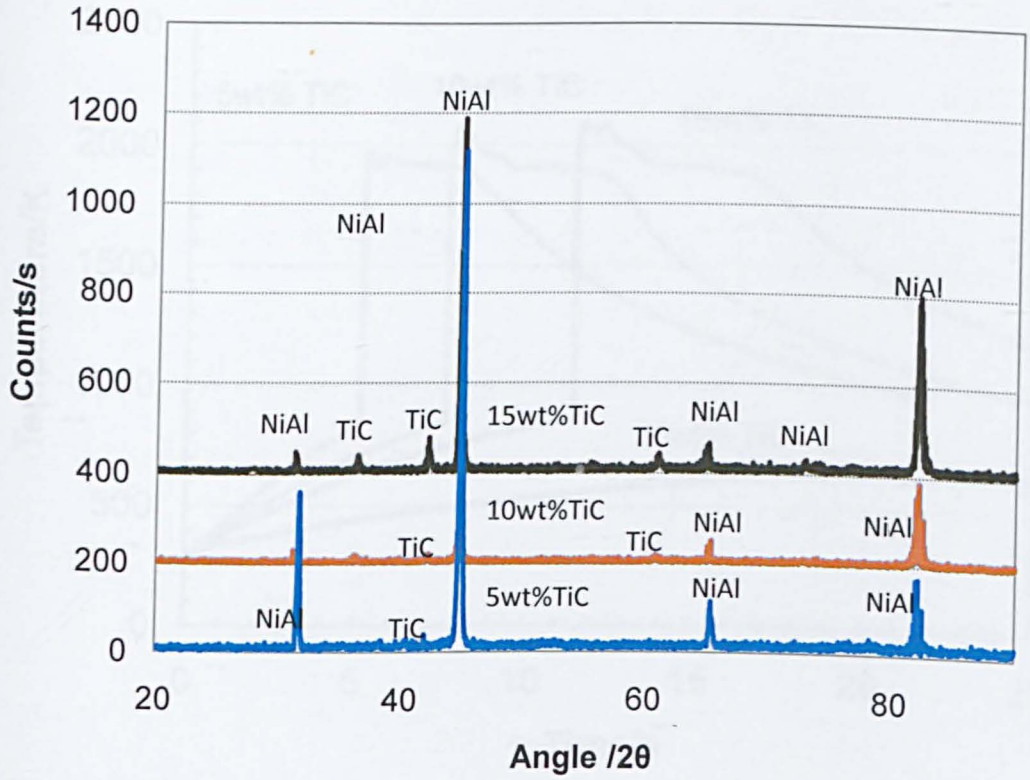

Figure 6-1 The X-ray pattern of synthesized products

6.3.2 Combustion reaction under induction heating

The full temperature profiles for the samples of Ni/Al and Ti/C mixtures are presented in Figure 6-2. The average heating rates before ignition commenced for the 5wt%, 10wt% and 15wt % samples were 109K/s, 72K/s and 51K/s respectively, indicating that heating rates decrease with increased Ti/C content. For the 20wt% sample there was no sharp increase in temperature, which is consistent with the XRD test result discussed previously.

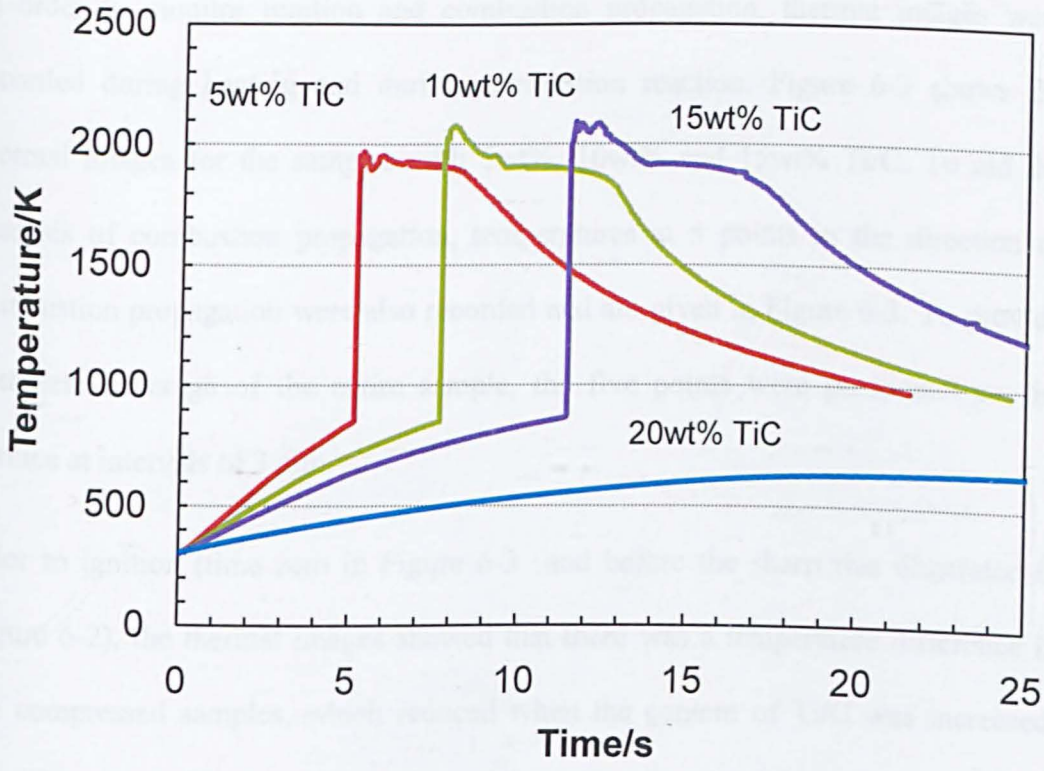

Figure 6-2 Temperature profile of samples during synthesis

The effect of Ti/C content on the heating rate can be explained by the mechanism of induction heating and the physical properties of the materials used. The equation 5-1 shows that the electrical efficiency reduces when the relative magnetic permeability is reduced. Since Ti and C powder are non-electromagnetic materials, the addition of Ti/C will reduce the relative magnetic permeability of the compacts. As a result, an increase in the quantity of Ti/C will decrease the electrical efficiency thus resulting in a reduction of the heating rate. However, due to a lack of data on the properties of the compressed compacts, the real efficiency values cannot be quantified. Further discussion on the combustion reaction will be given in Section 6.3.2.

In order to monitor ignition and combustion propagation, thermal images were recorded during heating and during combustion reaction. Figure 6-3 shows the thermal images for the samples with 5wt%, 10wt% and 15wt% Ti/C. To aid the analysis of combustion propagation, temperatures at 5 points in the direction of combustion propagation were also recorded and are given in Figure 6-3. To provide complete coverage of the entire sample, the five points were positioned on the surface at intervals of 3 mm.

Prior to ignition (time zero in Figure 6-3 and before the sharp rise illustrated in Figure 6-2), the thermal images showed that there was a temperature difference in the compressed samples, which reduced when the content of Ti/C was increased. When the Ti/C contents were increased from 5 wt% to 15 wt%, the temperature difference-reduced from 150 K to 30 K. As shown in Figure 6-2, the increase of Ti/C content reduces the heating rate of the components and hence a longer time will be required for heat to propagate within the sample. The temperature difference of 20K at the inner area (2 mm away from the outer ring) was not considered significant when compared with that of 700K for the whole area prior to the commencement of ignition. Meanwhile, the temperature at the ignition position (outer ring) was approximately 120K higher than that of the central area. It should be noted that the temperature distribution was not fully symmetrical about the axis of the disc because the magnetic field was not concentric owing to the shape of the coil.

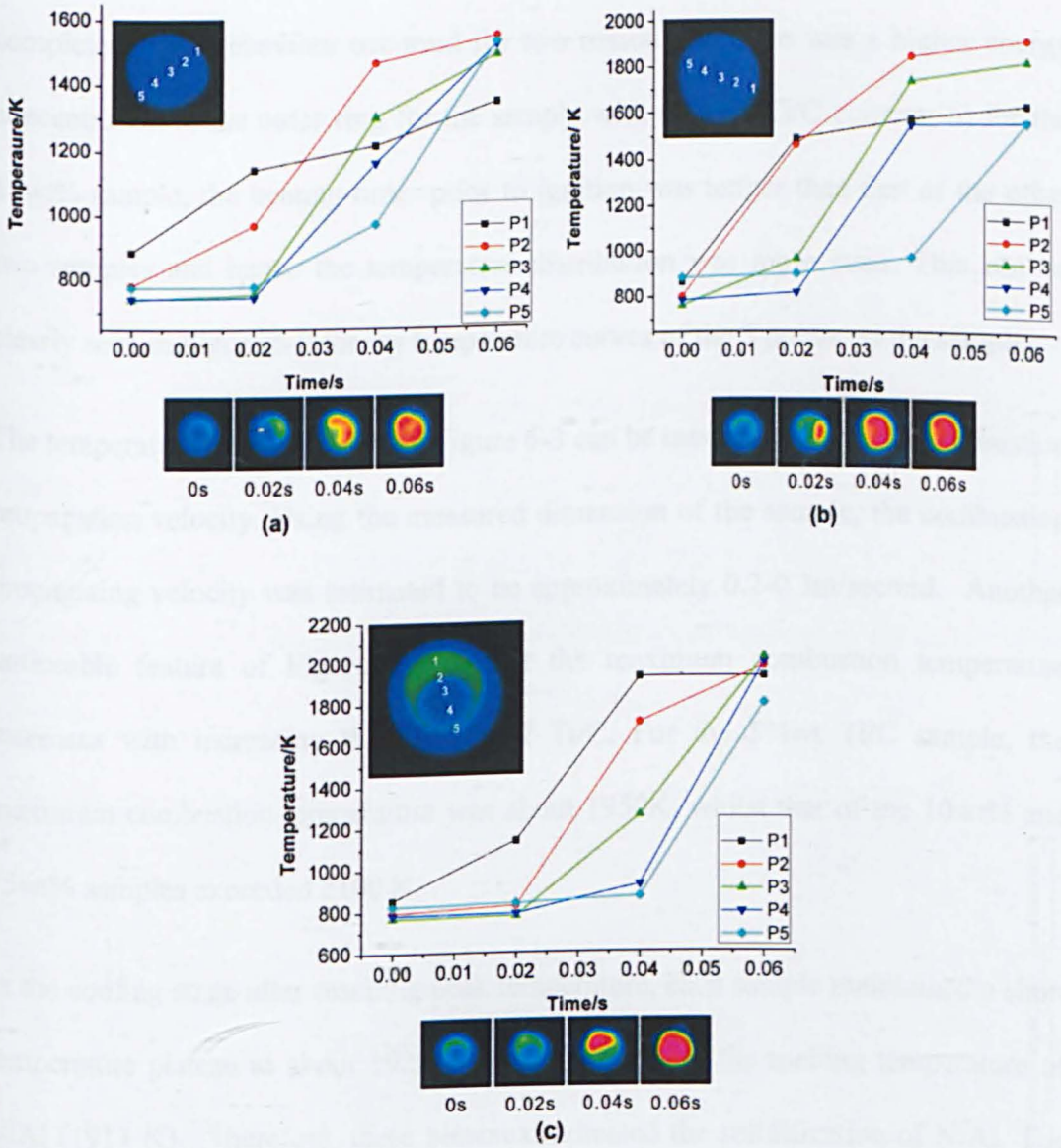

Figure 6-3 Thermal images and temperature profiles during synthesis. (a) 5wt% TiC ; (b) 10wt% TiC;(c) 15wt% TiC

For all of the reacted specimens the combustion wave propagation was completed within 0.06 s. The combustion propagation model, however, varied slightly with different Ti/C content. For the 5wt% and 10wt% samples, the combustion started at the outer position and then split into two wave fronts propagating around the periphery. The 15wt% sample also ignited at the edge, but continued with one

combustion front which spread into the entire sample until the propagation was completed. This behaviour occurred for two reasons: a) there was a higher energy concentration at the outer ring for the sample with a lower Ti/C content; b) for the 15wt% sample, the heating time prior to ignition was longer than that of the other two samples and hence the temperature distribution was more even. This can be clearly seen in Figure 6-2 for the temperature curves of the 5 points on the samples.

The temperature profiles shown in Figure 6-3 can be used to estimate the combustion propagation velocity. Using the measured dimension of the sample, the combustion propagating velocity was estimated to be approximately 0.2-0.3m/second. Another noticeable feature of Figure 6-2 is that the maximum combustion temperature increases with increasing the content of Ti/C. For the 5%wt Ti/C sample, the maximum combustion temperature was about 1950K, whilst that of the 10wt% and 15wt% samples exceeded 2100 K.

In the cooling stage after reaching peak temperature, each sample maintained a short temperature plateau at about 1920 K, which is close to the melting temperature of NiAl (1911 K). Therefore, these plateaux indicated the solidification of NiAl. The duration of the plateau increased from 3.5 seconds to 6 seconds as the Ti/C content increased from 5wt% to 15wt% as a result of the higher liquid content owing to the raised combustion temperature.

6.3.3 Microstructure and synthesis mechanism for TiC

The microstructure of the synthesized NiAl/TiC composites was observed using SEM in back scatter mode and presented in Figure 6-4. In back scatter mode, the matrix phase, NiAl, appears brighter than the TiC phase. At low Ti/C content the

distribution of TiC phase was heterogeneous, while at 15wt% Ti/C content the distribution are more scattered. Also, with the increase of Ti/C content, pore sizes were reduced. In the 5wt% Ti/C sample pores exist in the products whilst the 15wt% Ti/C sample was almost fully densified. These results can be explained by studying the thermal history during synthesis. As shown in Figure 6-2, by increasing the content of Ti/C from 5wt% to 15 wt%, the peak temperature increased from 1950 to 2100 K and the time during which the temperature remained above the melting point of NiAl (1911 K) increased from 3.5 seconds to 6.0 seconds. The consequence was to increase the liquid content, reduce the viscosity and provide a longer time for liquid flow. These joint effects contributed to the densification of the synthesised products.

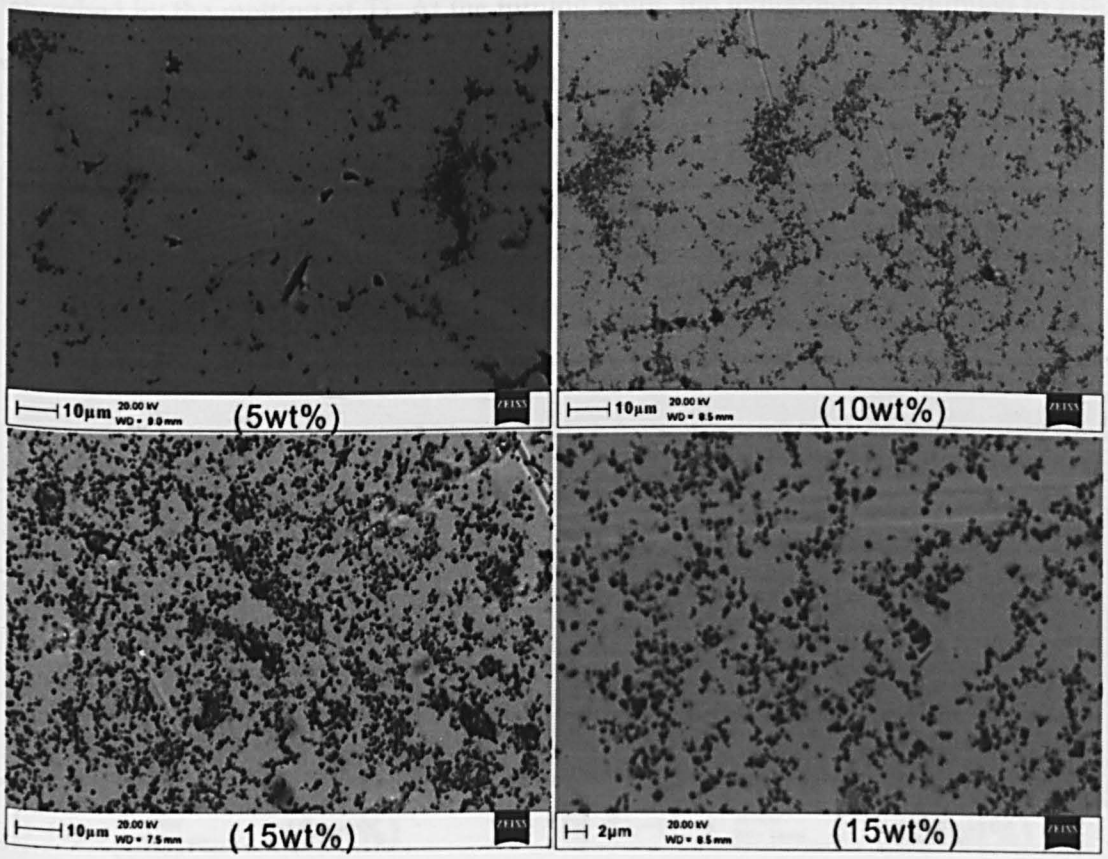

Figure 6-4 Microstructure of NiAl/TiC samples

By comparing the morphologies of TiC particles and the raw materials together with the temperature monitoring results (Figure 6-2), the synthesis mechanism of TiC by combustion can be derived. The average particle size of TiC, as shown in Figure 6-4 and Figure 6-5, was less than 1μm, which is close to the particle size of carbon powder (average 1μm) but is much smaller than the particle size of Ti (48 μm). In addition, the fracture surfaces of the 5wt% and 15wt% TiC sample in Figure 6-5 show that TiC particles were not only distributed at the NiAl boundary, but also embedded within the NiAl grains. The temperature monitoring results show that the Ti/C content increases leads to the temperature rise, above the melting point of Ti (1941 K). In addition there is a decrease in the heating rate at near to the melting temperature of Ti which indicates that the heat produced by the Ni/Al reaction was absorbed by the melting of Ti. At the turning point, the temperature continued to rise owing to the combustion reaction of Ti+C. Based on this analysis, the liquid synthesis mechanism should be the dominant synthesis route for TiC formation. The crystal morphology of each TiC particle was regular cubic and the size was increased slightly when the Ti/C content was increased.

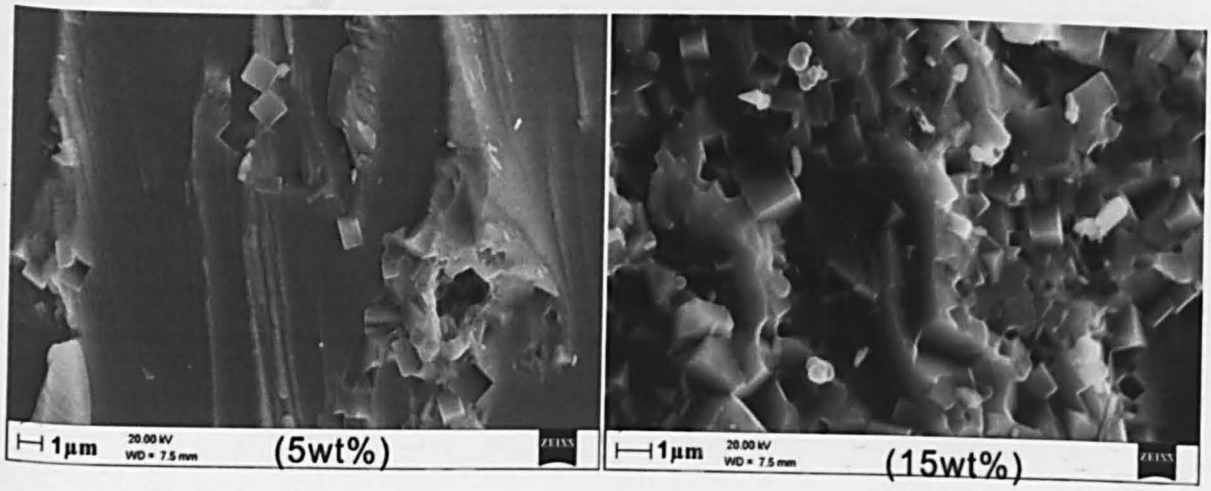

Figure 6-5 Fracture surface of 5wt%TiC and 15wt%TiC specimen

In the 5wt% Ti/C sample, the dominant fracture mechanism was NiAl transgranular fracture. Because of its average sub-micron particle size, the TiC obstructed the fracture propagation. In the 15wt% Ti/C specimen, although the NiAl transgranular fracture was the main fracture mechanism, cracks along the TiC boundary were also observed. This result suggests that, with increased TiC content, the mechanical properties of the composites should rise, however continued addition of TiC may result in reduced ductility.

Micro hardness testing was conducted on the samples, and the results are given in Figure 6-6. There is an obvious tendency that the increase of TiC content elevated the hardness of the synthesised NiAl/TiC composite. The hardness of NiAl synthesised under the same experimental conditions was approximately $324H_v$. Due to the non-homogeneous distribution of TiC phase, the hardness of 5wt% Ti/C and 10wt% Ti/C sample were slightly fluctuant, namely $459\pm37H_v$ and $511\pm29H_v$ respectively. Compare with the value of NiAl without Ti/C addition, the hardness of 5wt% Ti/C sample received an increase by approximately 50%. For the 15wt% Ti/C sample the hardness increased to $526\pm15H_v$ which is an increase of 62% to the pure NiAl sample.

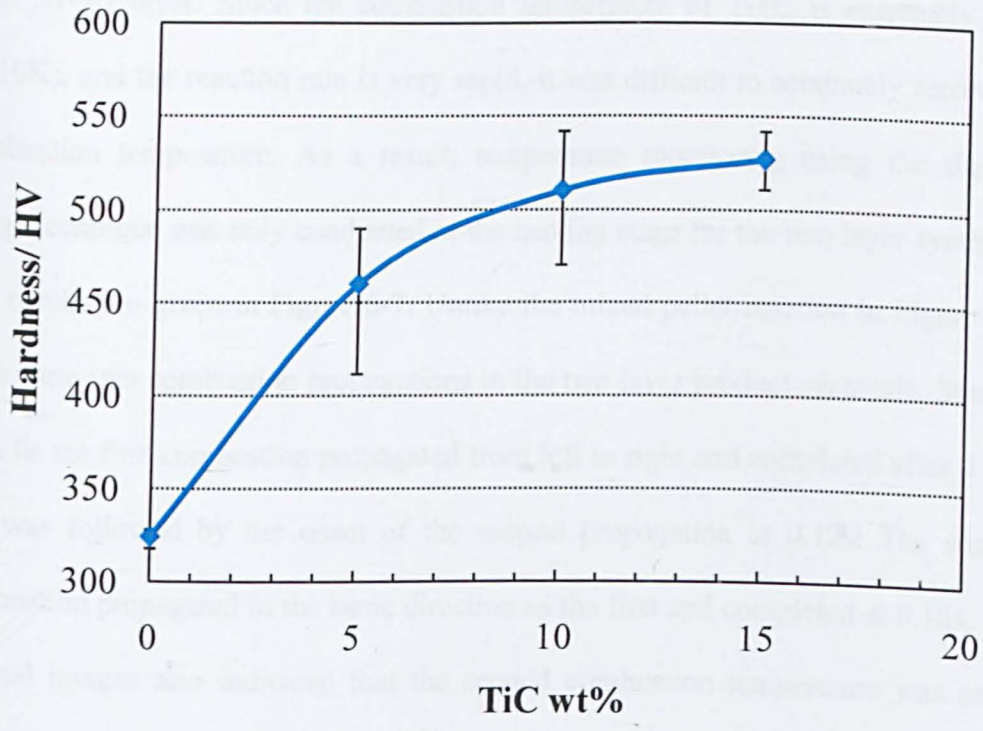

Figure 6-6 Effect of TiC on NiAl hardness

6.3.4 Synthesis of two-layer composite

Combustion reaction

The research work described early has shown that the combustion reaction of Ti+C ignited by the reaction of Ni+Al and TiC can be synthesized to form a NiAl/TiC composite provided that the content of TiC is limited to 15 wt% with this ignition system. To produce composites with a higher TiC content, a compressed Ti/C disc was placed on top of a compressed Ni/Al disc and then heated using the induction heating described in Section 6.2.

A preliminary test showed that the Ti/C mixture was insufficiently heated through induction heating indicating that, in the two-layer case, the upper layer receives heat

from Ni+Al layer. Since the combustion temperature of Ti+C is extremely high (3210K), and the reaction rate is very rapid, it was difficult to accurately record the combustion temperature. As a result, temperature monitoring using the thermal image technique was only conducted at the heating stage for the two layer synthesis. The results are given in Figure 6-7. Unlike the mixed pellet reaction in Figure 6-3, there were two combustion propagations in the two layer product synthesis. Starting from 0s the first combustion propagated from left to right and completed after 0.10s, this was followed by the onset of the second propagation at 0.12s. The second combustion propagated in the same direction as the first and completed at 0.16s. The thermal images also indicated that the second combustion temperature was much higher than the first one. Since the thermal image was taken on the surface of Ti/C compact, the temperature on the Ni/Al could not be recorded.

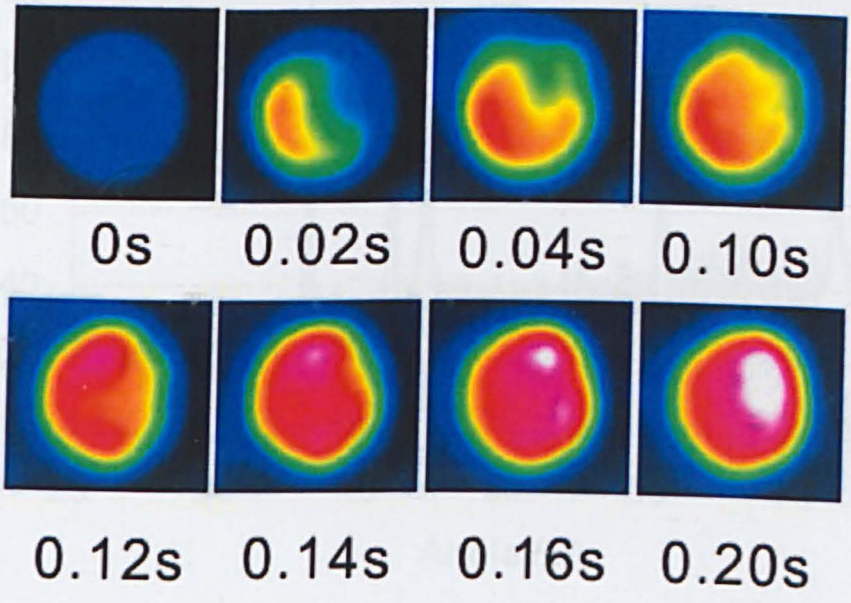

Figure 6-7 Thermal images of two layers sample during combustion reaction

The test showed that combustion reaction was successfully performed as expected. The combustion reaction of Ti+C was ignited by the combustion of Ni+Al. The reaction products cut and the cross section was examined using XRD. Figure 6-8 shows the XRD pattern of the two layer product. It shows that TiC and NiAl were successfully synthesised and no raw materials remained in the final product. However, TiC and NiAl existed at the same plane indicating that there was mixing between the two phases despite the Ti/C and Ni/Al discs having been placed separately.

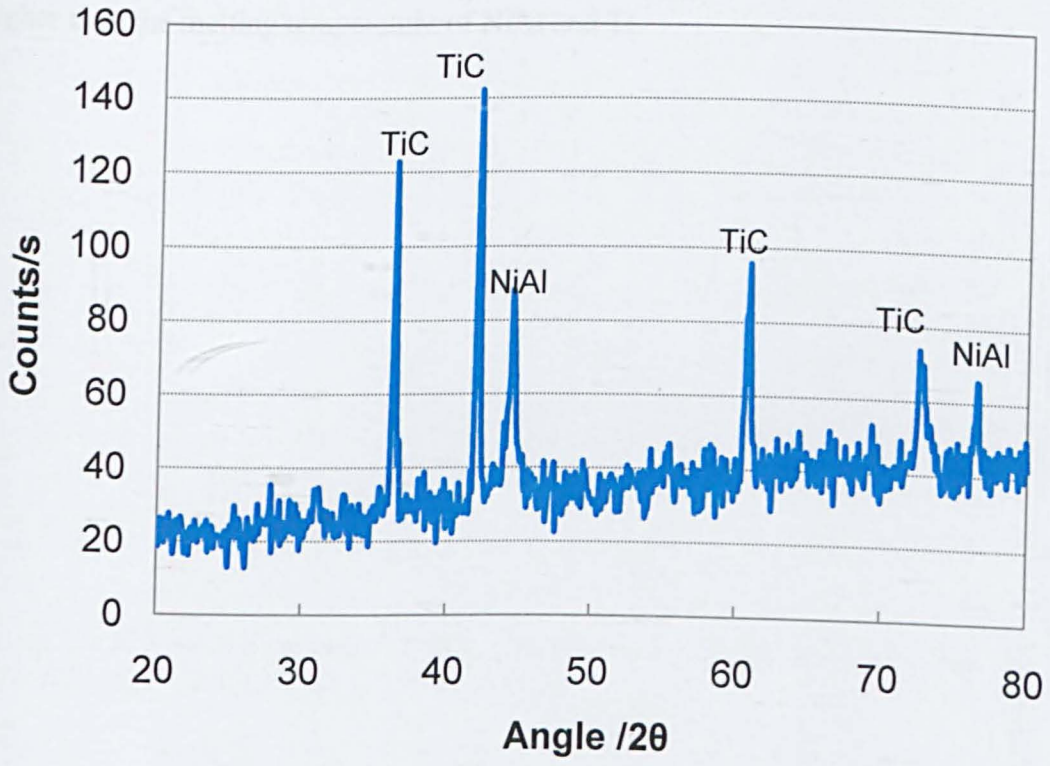

Figure 6-8 XRD pattern of two layer products

Microstructure

Figure 6-9a shows the back scatter microstructure of the two layer product. The upper layer comprised the Ti+C pellet and the base layer the Ni+Al mixture. The interface between the two layers was dense and no pores were observed. Both layers contain bright and dark areas, suggesting that there was a mixing between the two layers during the combustion reactions. Figure 6-9b and c show the microstructure of the upper and base layers respectively. EDX analysis (Figure 6-9d) shows the brighter area was NiAl and dark area contained TiC and NiAl, strengthening the conclusion. The mixing between NiAl and TiC was clearly due to the melting of NiAl and Ti since the combustion temperature of the second reaction was much higher than the melting temperature of NiAl and Ti.

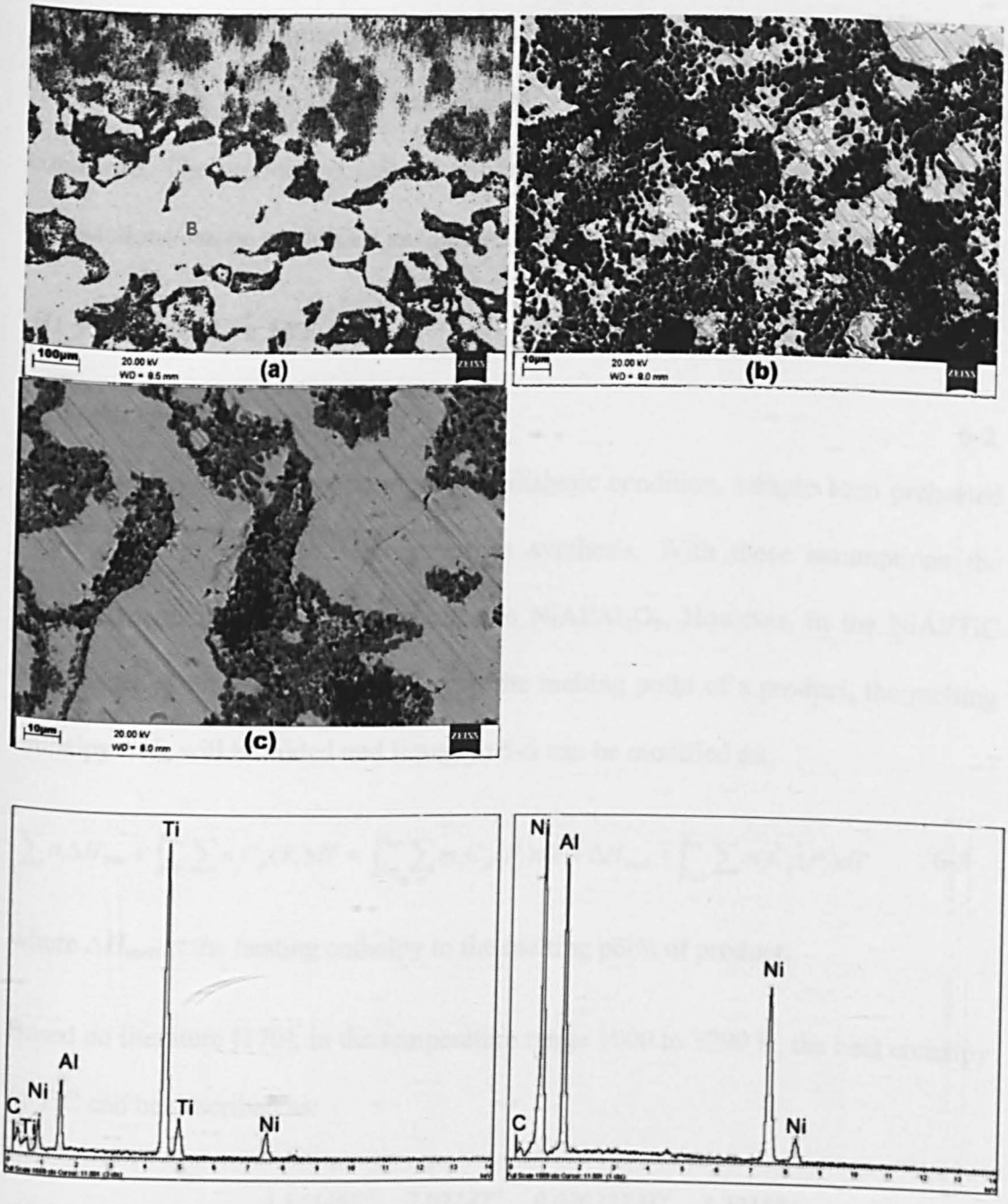

Figure 6-9 Microstructure of two layer product (a)two layer product;(b)TiC rich area; (c) NiAl rich area;(d) EDX results

6.3.5 Thermal dynamics analysis for the NiAl/TiC system

The temperature monitoring results given in Figure 6-2 show the reaction temperature for the NiAl/TiC system is a function of Ti/C content. This function can

be determined via thermal dynamic calculation. In the experiment, the X-ray pattern results showed the synthesis was complete and all the raw materials were fully consumed. The products contained only two compounds NiAl and TiC. Therefore, the reactions can be simplified as (data reference [149-150])

$$Ni + Al \rightarrow NiAl + 118.5kJ \qquad \textbf{6-1}$$

$$Ti + C \rightarrow TiC + 183.8kJ \qquad \textbf{6-2}$$

As Figure 6-3 suggests, assumptions of adiabatic condition, sample been preheated can be applied to NiAl/TiC composites synthesis. With these assumptions the thermodynamics principles is the same to NiAl/Al_2O_3. However, in the NiAl/TiC composites synthesis, if the T_{ad} exceeds the melting point of a product, the melting enthalpy ΔH_m will be added and Equation 5-5 can be modified as:

$$\sum n_i \Delta H_{298} + \int_{298}^{T_{Pre}} \sum n_i C_p(R_i) dT = \int_{298}^{T_{melt}} \sum m_j C_p(P_j) dT + \Delta H_{melt} + \int_{T_{melt}}^{T_{ad}} \sum m_j C_p(P_j) dT \qquad \textbf{6-3}$$

where ΔH_{melt} is the heating enthalpy to the melting point of product.

Based on literature [170], in the temperature range 1000 to 3290 K, the heat enthalpy of TiC can be described as:

$$H_{TiC}(solid) = 43.27T + \frac{4.54446T^2}{2} + \frac{2.0214T^3}{3} - \frac{0.0203272T^4}{4} - \frac{1.701881}{T} + 184.0960 \qquad \textbf{6-4}$$

where T = temperature (K)/1000.

The heat capacity Cp is determined by the following equation and the constant a, b, c and d and other data used are given in Table 6-1.

$$C_p = a + (b \times 10^{-3})T + (c \times 10^{-6})T^2 + \frac{d \times 10^5}{T^2} \qquad \textbf{6-5}$$

Table 6-1 Thermal properties of elements (Data reference [149])

Element	Phase	Temperature of Transition(K)	Heat of Transition(kcal/g mole)	a (cal/g mole)	b (cal/g mole)	c (cal/g mole)	d (cal/g mole)
Ti	Solid α	1155	0.950	21.955	10.539	--	--
C	Solid	--	--	17.146	4.2656	--	-2.10

Figure 6-10 shows the calculated T_{ad} as a function of Ti/C content and preheating conditions. Since there is no reliable data for the thermal properties of liquid NiAl above 1911K, Equation 6-6 for the solid state was used to continue the calculation. The curves above 1911 K are presented in the Figure 6-10 using a dashed line. The results show that the preheating has a significant effect on T_{ad}, when the addition of Ti/C is below 18 wt%. Without preheating, the combustion temperature of all the mixtures remained at 1911K until the Ti/C content was increased to approximately 18wt% since below this weight fraction NiAl will not fully melt. With preheating to 500K, the minimum requirement to fully melt NiAl is reduced to 13wt% Ti/C. Above this weight fraction T_{ad} will increase linearly with Ti/C content. If the preheating temperature was increased to 700K, the minimum requirement for Ti/C to fully melt NiAl was further reduced to 6.5wt%, which, in turn, could be further reduced to 0.9 wt% when preheated to 800K. The test results in Figure 6-2 show all pellets were heated to above 700K prior to ignition, therefore the reaction product NiAl should be fully melted in the samples with 10wt% and 15wt% Ti/C and the combustion temperature should be higher than 1911K. This calculated result correlates well to the measured temperatures given in Figure 6-2.

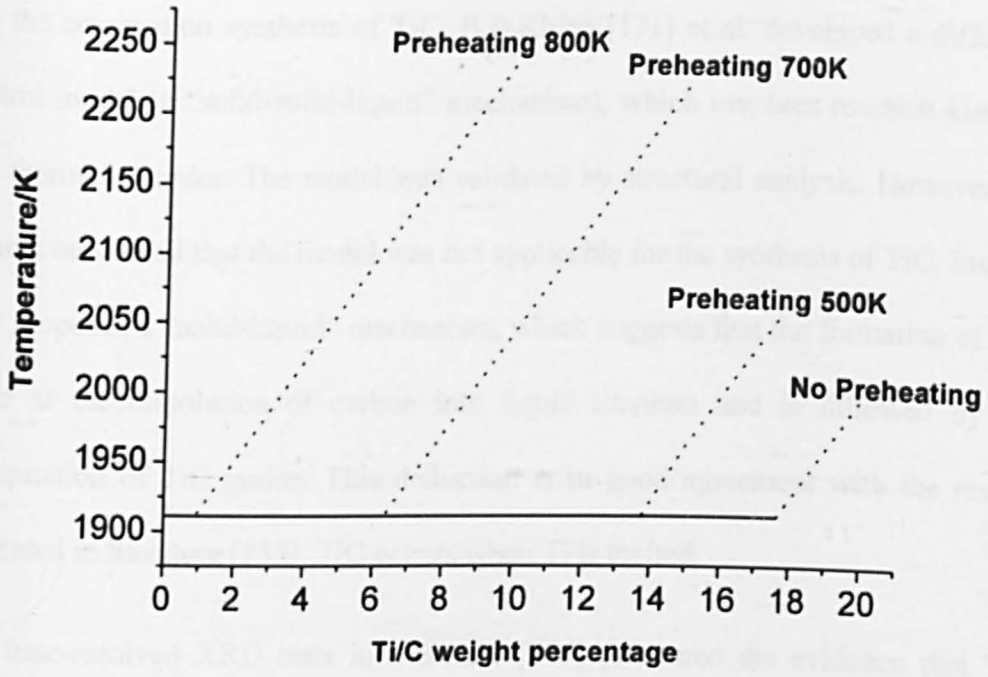

Figure 6-10 Calculated combustion temperature as a function of Ti/C content and preheating temperature.

6.3.6 Reaction mechanism of the combustion synthesis

The intrinsically fast reaction velocity and elevated temperature of the combustion synthesis limited the investigation on the reaction mechanism. Previously, time-resolved XRD techniques and "Quench" methods have been used to analyse the synthesis process. In literature [135], the author utilized a time-resolved XRD to investigate the combustion reaction for the Ni/Al/Ti/C system. The XRD pattern showed that the disappearance of elements started from Al, as it has the lowest melting point, followed by Ni, Ti and finally C. On the other hand, for the synthesised product the author claimed the TiC appeared simultaneously with the melting of Ti whereas the NiAl emerged in a later stage.

For the combustion synthesis of TiC, B.B.Khina [171] et al. developed a diffusion control model (a "solid-solid-liquid" mechanism), which involves reaction kinetics and thermodynamics. The model was validated by structural analysis. However the authors concluded that the model was not applicable for the synthesis of TiC. Instead they proposed a "solid-liquid" mechanism, which suggests that the formation of TiC starts at the dissolution of carbon into liquid titanium and is followed by the precipitation of TiC grains. This deduction is in good agreement with the results presented in literature [135], TiC occurs when Ti is melted.

The time-resolved XRD tests in literature [135] presented the evidence that TiC appeared at 1.4s while NiAl emerged at 4.2s, thus the author concluded NiAl formation was slower than that of TiC. This conclusion is questionable because it ignored the limitation of XRD technique that it can only detect crystalline phases. The later appearance of NiAl in XRD pattern may be owing to a solidification period after combustion. As Figure 6-10 implied, without preheating process the combustion temperature will exceed NiAl melting point when Ti/C content over 18wt%. In literature [135] the raw materials were mixed as molecular ratios 1:1:1:1, equal to 41.14wt% of Ti/C. With this amount of Ti/C the reaction temperature was certainly higher than the melting point of NiAl, regardless the missing details of ignition system in literature [135]. The fabricated NiAl would be fully melted and the liquid NiAl phase was not possibly be detected by XRD till the sample's temperature cooled down to its crystallization point. Hence the later appearance of NiAl in XRD test is not a convincible proof to determine the reaction sequence.

In the experimental work for the two-layer NiAl/TiC composite, two propagations were detected by the thermal images as shown in Figure 6-7. As previously stated,

the Ti/C layer cannot be adequately heated via induction heating so it may be concluded that the first combustion is the synthesis reaction of NiAl. The combustion temperature after the second reaction was above 2300K, which corresponds to the synthesis of TiC. Owing to the melting of NiAl and heat loss to the environment through conduction and radiation, the temperature detected was much lower than the theoretical temperature for the adiabatic synthesis of TiC. The microstructure in Figure 6-9 suggests that the product synthesized was a mutual infiltration of NiAl and TiC. The interface of the two layers was dense and no pores were observed. This is because NiAl had melted at the boundary and spread into the Ti/C layer during the formation of TiC. As shown in Figure 6-10, the heat generated by the formation of TiC should be able to provide sufficient heat to fully melt the synthesized NiAl. Hence the reaction sequence may be stated as: Ni/Al mixture was heated by induction heating and ignited; the released energy melted Ti and then initialized the combustion reaction of Ti/C, which is accompanied by the melting and flow of NiAl. The melting of Ti lead to the formation of fine TiC grains whereas the melting and flow of NiAl results in fully densified TiC/NiAl composites.

6.4 Conclusion

The combustion reaction of TiC was ignited using a high frequency induction heater. High density, multi layer TiC-NiAl composites were produced using this method. The results show:

a) With addition of Ti/C 1:1 weight percentage 5%, 10% and 15%, the reaction products were pure NiAl and TiC.

b) To ignite the combustion reaction by induction heating for the Ni/Al+Ti/C system, there is a limit for the content of Ti/C, above which the ignition will not start. The peak temperature during reaction increases with increasing Ti/C content.

c) NiAl can be fully melted in the NiAl/TiC composites during combustion reaction. As a result, fully densified NiAl/TiC composites can be produced. The hardness of synthesized NiAl can be significantly improved by the addition of Ti/C.

d) The microstructure analysis, temperature measurements and comparison with literature suggests the formation of TiC follows a liquid synthesis mechanism. The TiC was formed after the melting of Ti, so that nano structured TiC can be produced.

e) The reaction sequence for the Ni/Al/Ti/C system can be stated as: Ni/Al mixture was heated by induction heating and ignited its combustion; the energy released melted Ti and initialized the combustion reaction of Ti/C which led to the formation of TiC and it is accompanied by the melting of NiAl.

Chapter 7 Computer simulation for induction heating

7.1 Introduction

One of the innovations in this research is utilizing the induction heating technique for SHS ignition. The heating behaviour of this ignition system has been investigated experimentally in previous chapters using high resolution thermal image technique and infra-red pyrometers. The temperature profiles on the surface were measured but the temperatures inside the samples are difficult to measure. Computer simulation can provide deep understanding on the heating process, but no work has been reported for SHS synthesis. Moreover, it is known that the electromagnetic field coupling with compressed particles is different to bulk materials, but researches on this issue were rare.

Trace back to 1997 Chaboudez et al. attempted using finite element method to simulate induction heating of steel bar[172]. In his work the simulated temperatures were slightly higher but matched well to reality. Hiroki et al continued research in this direction and added analysis of magnetic field by employing 3 dimensional modelling [173]. Recent years, with the advance in computer technology as well as the fast development of commercial finite element simulation tools, the simulation on induction heating process became a powerful tool in industry design. Aiming to broaden the understanding on the ignition process for SHS reaction, finite element simulation was carried out in this study. Since the properties for powder compacts are not available and mild steel can be used as substrate for coatings, ASTM 1020

steel was used in the simulation to illustrate the effects of processing parameters during induction heating.

The research in previous chapters has also shown that the length of solidification time has a great influence on the crystallization, as subsequently to the mechanical properties of synthesized products. The measured temperature profiles show the solidification step for products is in the scale of seconds. The length of solidification varies with preheating conditions, the contents of samples and heat exchange with environment. A good understanding on the effects of these factors will provide a foundation for a better for the ignition and synthesis process.

In this work, all the simulation was conducted with commercial software ANSYS multiphysics 12.0. The communication with ANSYS program was implemented via APDL (ANSYS Parametric Design Language) commands and saved as mac format file. The codes for each simulation are listed Appendix A.

7.2 Simulation model setup for induction heating

7.2.1 Procedure and setting

The induction heating process contains two physical environment, namely transient thermal transfer environment and electromagnetic harmonic environment. The ANSYS provides the multi-physics package and enables it to generate a solution sequence alternating between these two environments.

The ferrous material has the "curie point" around 700 °C at which there is a sharp change in material property. It should be considered in the simulation. The solving sequence starts with electromagnetic analysis followed transient thermal analysis.

The results of thermal analysis are used to determine whether or not the electromagnetic environment should be updated. When the temperature of steel piece reaches the transition point the electromagnetic solution will start again to overwrite the previous solution. The flow diagram for the simulation is shown in Figure 7-1.

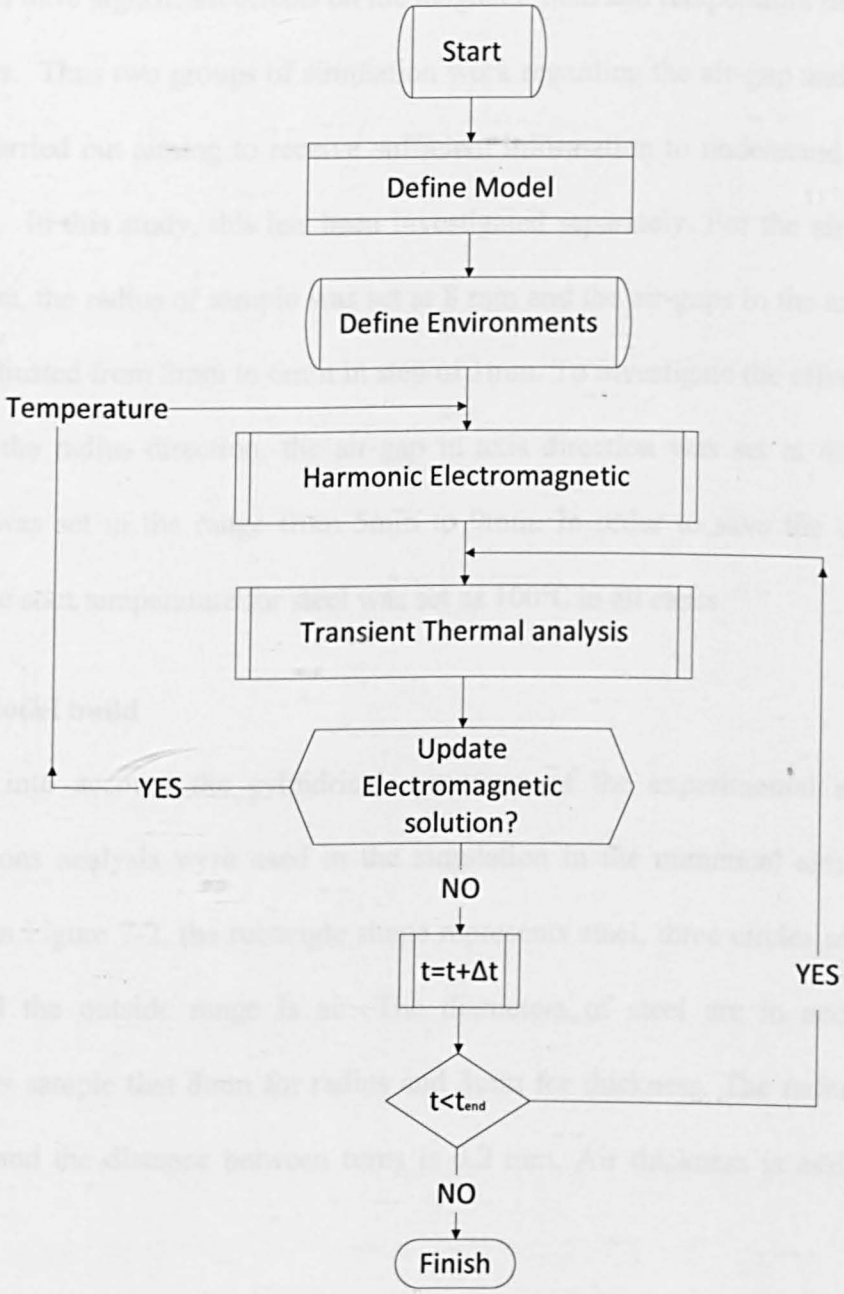

Figure 7-1 Flow diagram for induction heating simulation

The parameter of air-gap between coils affects the distribution of electromagnetic field, which needs to be carefully studied. The radial direction air-gap is defined as the distance between inner coil radius to out surface of sample. The axis direction air-gap is defined as the distance between sample surfaces to bottom of coil. Both air-gaps have significant effects on the magnetic field and temperature distribution of samples. Thus two groups of simulation work regarding the air-gap and steel radius were carried out aiming to receive sufficient information to understand the ignition system. In this study, this has been investigated separately. For the air-gap in axis direction, the radius of sample was set at 8 mm and the air-gaps in the axis direction were adjusted from 2mm to 6mm in step of 1mm. To investigate the effect of the air-gap in the radius direction, the air-gap in axis direction was set at 4mm and the radius was set in the range from 5mm to 9mm. In order to save the computation time, the start temperature for steel was set as 100°C in all cases.

7.2.2 Model build

Taking into account the cylindrical symmetry of the experimental setting, two dimensions analysis were used in the simulation in the numerical simulations, as shown in Figure 7-2, the rectangle shape represents steel, three circles represent the coil and the outside range is air. The diameters of steel are in accordance of compress sample that 8mm for radius and 3mm for thickness. The radius of coil is 1.5mm and the distance between turns is 0.2 mm. Air thickness is assigned to 20 mm.

The permeability of 1020 steel is listed in Table 7-1, and the resistivity of steel is listed in Table 7-2.

Table 7-1 Relative permeability of Steel at different temperature

Temperature/°C	25.5	160	291.5	477.6	635	698	709	720.3	742	761	1000
Relative permeability/ H/M	200	190	182	161	135	104	84	35	17	1	1

Table 7-2 Resistivity of Steel at different temperature

Temperature/ °C	125	250	375	500	625	750	875	1000
Resistivity/ Ω·m	0.272e-6	0.384e-6	0.512e-6	0.656e-6	0.824e-6	1.032e-6	1.152e-6	1.2e-6

7.2.3 Attributes assignment

Before meshing, the materials properties and the real constant must be assigned for each area the finite elements, which are called attributes setting in ANSYS. In this case, it requires individual setting for each physical environment. The setting results are listed in Table 7-3. For electromagnetic environment, element PLANE13 was selected due to its capability of nonlinear magnetic analysis. For the transient thermal environment element PLANE55 was introduced and for steel temperature analysis SURF151 was employed to estimate the radiation loss on surface. Details of each finite element can be found in Appendix B. The materials properties used in the simulation were obtained from references [149, 157, 160].

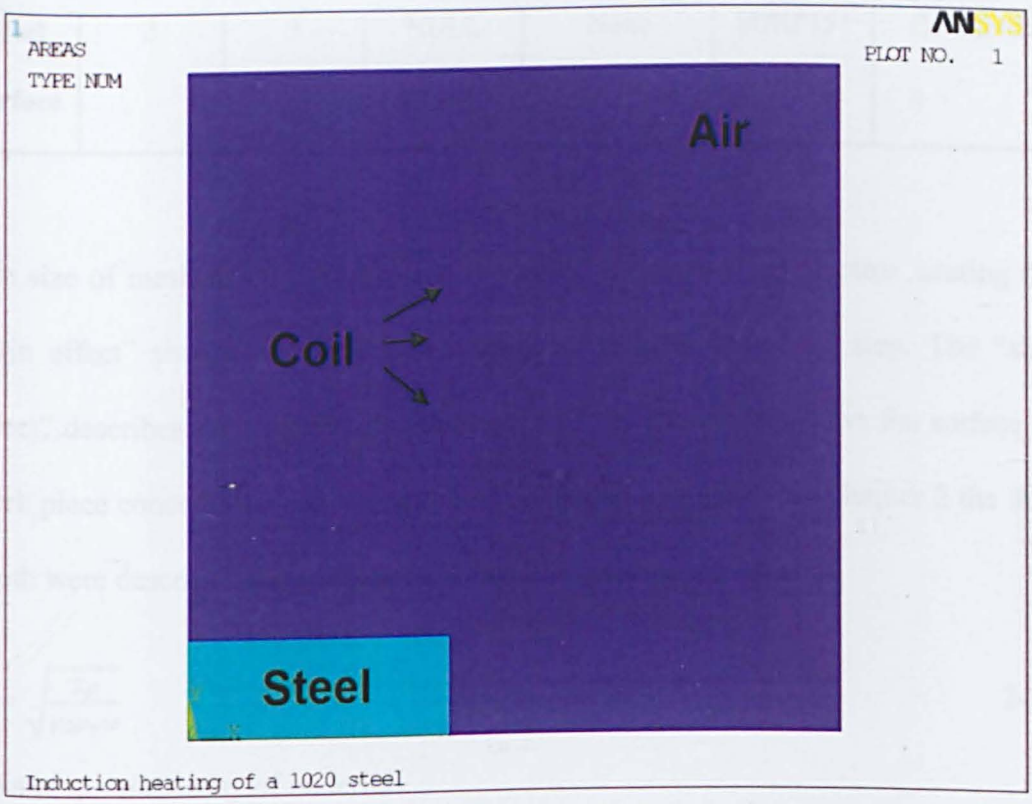

Figure 7-2 Model setting induction heating simulation

Table 7-3 Attributes setting for environments and modelling

Area	Element number	Real constant	Electromagnetic environment		Transient thermal environment	
			Element type	Materials properties	Element type	Materials properties
Steel	1	1	PLANE13	Resistivity, Permeability	PLANE55	Conductivity, Enthalpy
Coil	2	1	PLANE13	Permeability	NULL Type(0)	None
Air	2	1	PLANE13	Permeability	NULL Type(0)	None

Steel surface	3	3	NULL Type(0)	None	SURF151	Emissivity

The size of mesh determines the accuracy of simulation. For induction heating the "skin effect" should be taken into consideration at the meshing step. The "skin effect" describes the phenomenon during induction heating. It shows the surface of work piece concentrates most energy and be heated up quickly. In chapter 2 the skin depth were described as Equation 2-14 that

$$\delta = \sqrt{\frac{2\rho}{\mu_0 \mu_r \omega}} \qquad \textbf{2-14}$$

where: ρ= resistivity of materials
μ_0=permeability of the free space
μ_r=permeability of the materials relative to free space
ω= frequency

Based on the Equation 2-14, once the materials were selected the skin depth depends upon frequency. In this study, as recommended by ANSYS technical support centre at European, the mesh size was set as half of the skin depth at the steel surface. Also, in the ANSYS help file the mesh size was set at half of the skin depth.

The overall mesh result is presented in Figure 7-3. The mesh size around coil areas was refined to increase the accuracy. This is because the electromagnetic field starts around this region and electromagnetic field distribution is more complicated. Thus each circle of coil was divided by 40 divisions for finer meshing size.

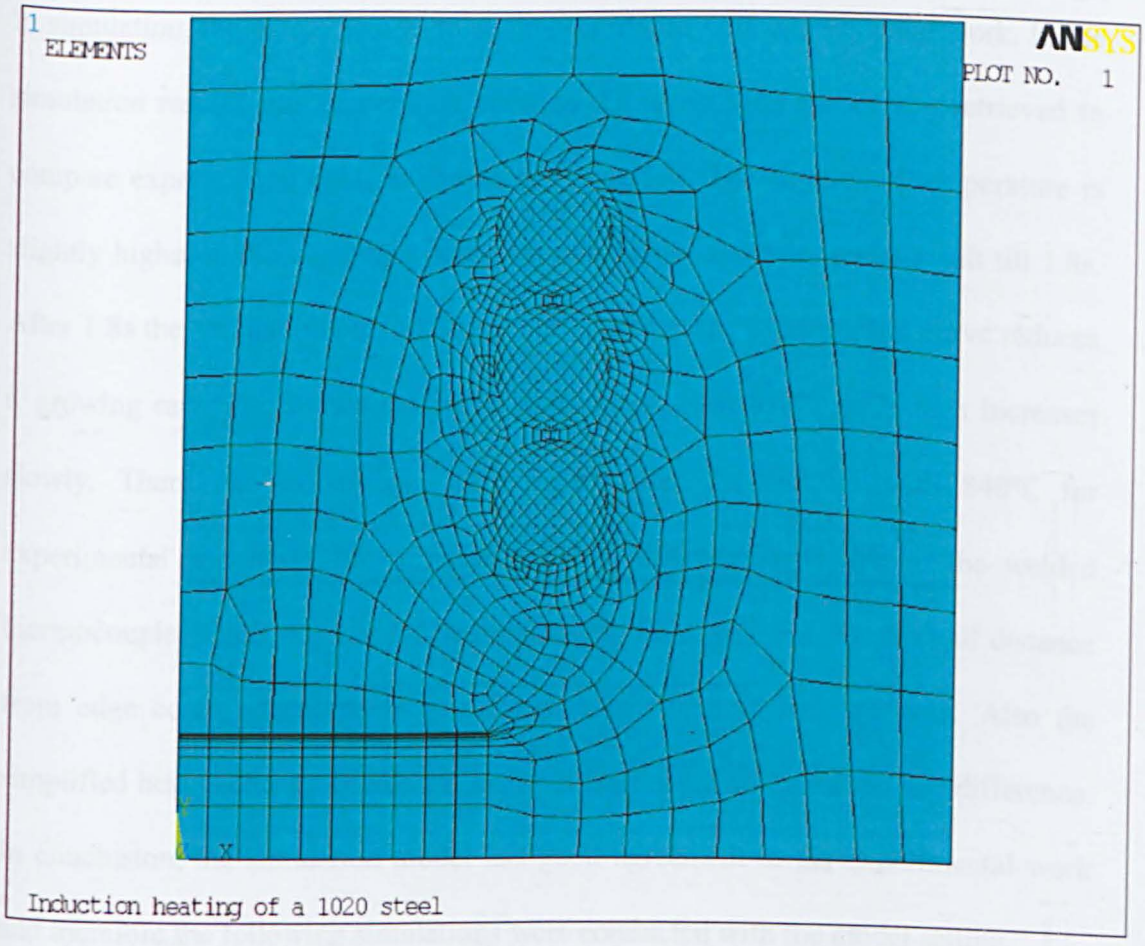

Figure 7-3 Mesh results for the induction heating simulation

7.2.4 Validation with experimental work

To validate the simulation model experimental testing was conducted. ASTM 1020 steel was machined to disk with radius of 8mm and thickness of 2mm. At the edge of steel bar a type K thermocouple was welded via sparking welding. The air-gap in axis direction was fixed at 4mm. The current in the coil was set at 300A and the frequency was 300MHz. The temperature recording was progressed with PICO® TC08 using compute recording.

In simulation, the parameters were set in accordance with experimental work. In the simulation results, the temperature curve at the upper right corner was retrieved to compare experimental data, as shown in Figure 7-4. The simulation temperature is slightly higher at the beginning, and then matches with experimental result till 1.8s. After 1.8s the simulation curve keeps its gradient but the experimental curve reduces it growing rate. The simulation curve rises up to about 810°C at 2s then increases slowly. There two curves get close again after 2s, end up with 840°C for experimental and 860°C for simulation. This difference may due to the welded thermocouple which was not located exactly at the edge point. Even small distance from edge could contribute large difference in magnetic field strength. Also the simplified heat exchange conditions in simulation could contribute to this difference. In conclusion, the simulation model has good agreement to the experimental work and therefore the following simulations were conducted with the model setting.

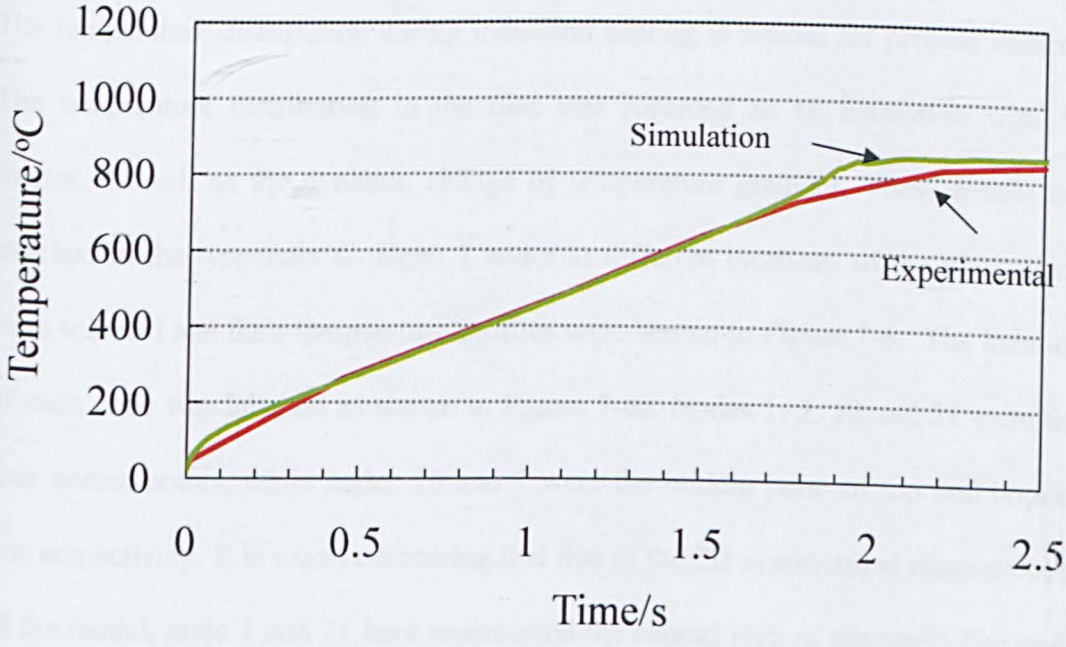

Figure 7-4 Measured steel temperature via induction heating

7.3 The effect of air-gap in axis direction

The temperature distribution results with various air-gap distances are shown in Figure 7-5. The end time for induction heating simulation was set as 4 seconds, allowed the steel to be heated to over 700 °C in all cases. At the end of heating all cases showed two similarities in the temperature distribution. The region close to the side surface had higher temperature than the inner area. The maximum temperature appeared at the right corner of surface and the minimum temperature points were located at the left corner at the bottom. The major difference of these scenarios was the value of maximum temperature, which showed smaller air-gap resulting in higher temperature. When the air-gap in axis direction was set as 2mm, the maximum temperature reached to 1508°C, which almost reached the melting point of pure iron. However for the 5mm air-gap sample the maximum temperature is only 834°C under the same heating condition.

The temperature distribution during induction heating is crucial for process control. The temperature distribution in the disc was recorded as an animation with 50 frames, as well as the dynamic change of temperature gradient. These results are attached in the Appendix C. Here, 7 nodes at different locations of the work piece were selected and their temperature profiles were shown in Figure 7-6. The location of each node was labelled as shown in Figure 7-6a, Nodes 1, 2, 12 and 21 were the four corner points, while nodes 26 and 7 were the middle point of top and bottom line respectively. It is worth addressing that due to the 2D symmetrical characteristic of the model, node 1 and 21 here represented the central area of the steel. The node 71 is in the vertical line of node 26 and 7. The Figure 7-6b, c, d, e and f represent the nodes' temperature in air-gap 2mm, 3mm, 4mm, 5mm and 6mm respectively.

In Figure 7-6b-f, the temperature curves in each graph showed same tendency. The node 12 had the highest temperature, followed by node 2. Generally the temperature of node 2 was approximately 100°C lower than that of node 12. Both of them had an obvious decline of heating rate due to the "curie effect". In comparison, there were no obvious change of heating rate in the nodes 7, 26 and 71. The temperature curves for these three nodes are very close to each other. Node 26 had slightly higher temperature than the other two. For the node 1 and 21, their curves are almost overlapped and can hardly be distinguished, which implies that vertical thermal gradient in the middle of sample was very small.

Even though the heat losses at the edge area are higher than that at the central part, the node 12 at the edge always had the highest temperature in heating despite the change of the air-gaps. This phenomenon is common in industrial applications, which normally referred as "Edge Effect"[157]. The edge effect is contributed by distortion of electromagnetic field. The graphs of magnetic field intensity (SI unit H) at the start of heating were given in Figure 7-7 individually. The graphs were arranged alphabetically to represent sample of air-gap 2mm, 3mm, 4mm, 5mm and 6mm respectively. There is a common point in these graphs that the magnetic field were distorted and concentrated on the upper right corner. At the corner the magnetic field penetrated both surface and side surface therefore be fast heated. In industry this "Edge Effect" usually occurs in the induction heating of steel, aluminium and other magnetic materials.

In realistic situation there can be some minor shifting of the Curie temperature, depending upon the heat intensity. Observing Figure 7-7 b-f this phenomenon appeared in the simulation as well. The node 12's temperature curves changed the

gradient at about 870°C in Figure 7-6b and c, afterwards stepped back to around 800°C in Figure 7-6d, e and f. The original setting of the Curie temperature of steel was 780°C in simulation. The Curie temperature shifting in this simulation is due to the fast heating rate.

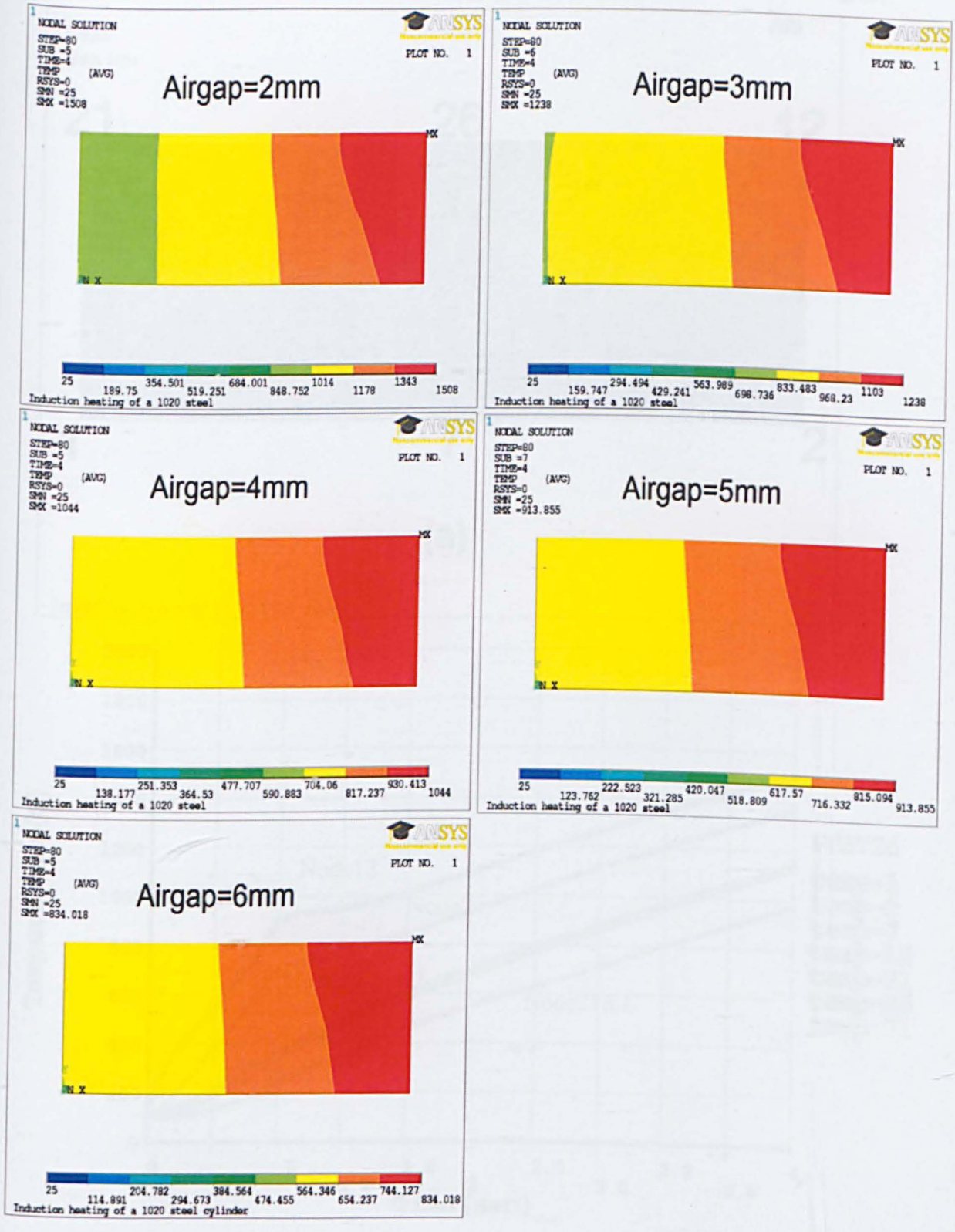

Figure 7-5 The effect of air-gaps in axis direction on the temperature distribution at the end of heating of 4 s.

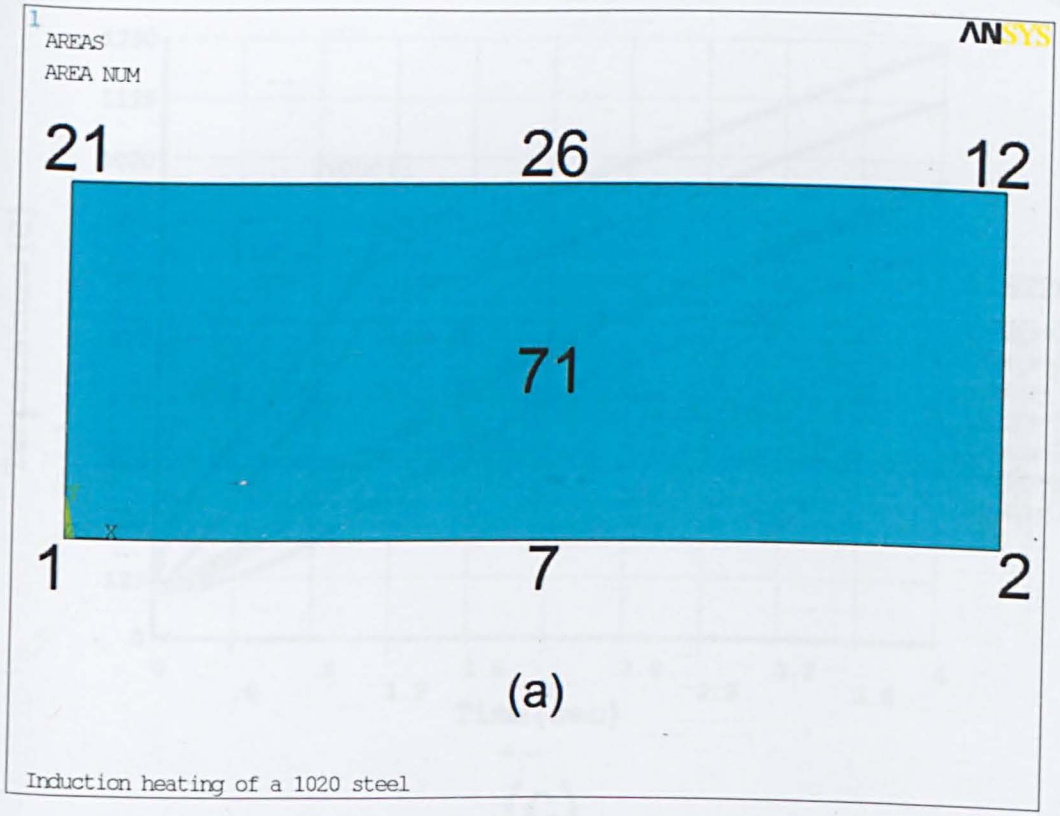
AREAS
AREA NUM
ANSYS
21
26
12
71
1
7
2
(a)
Induction heating of a 1020 steel

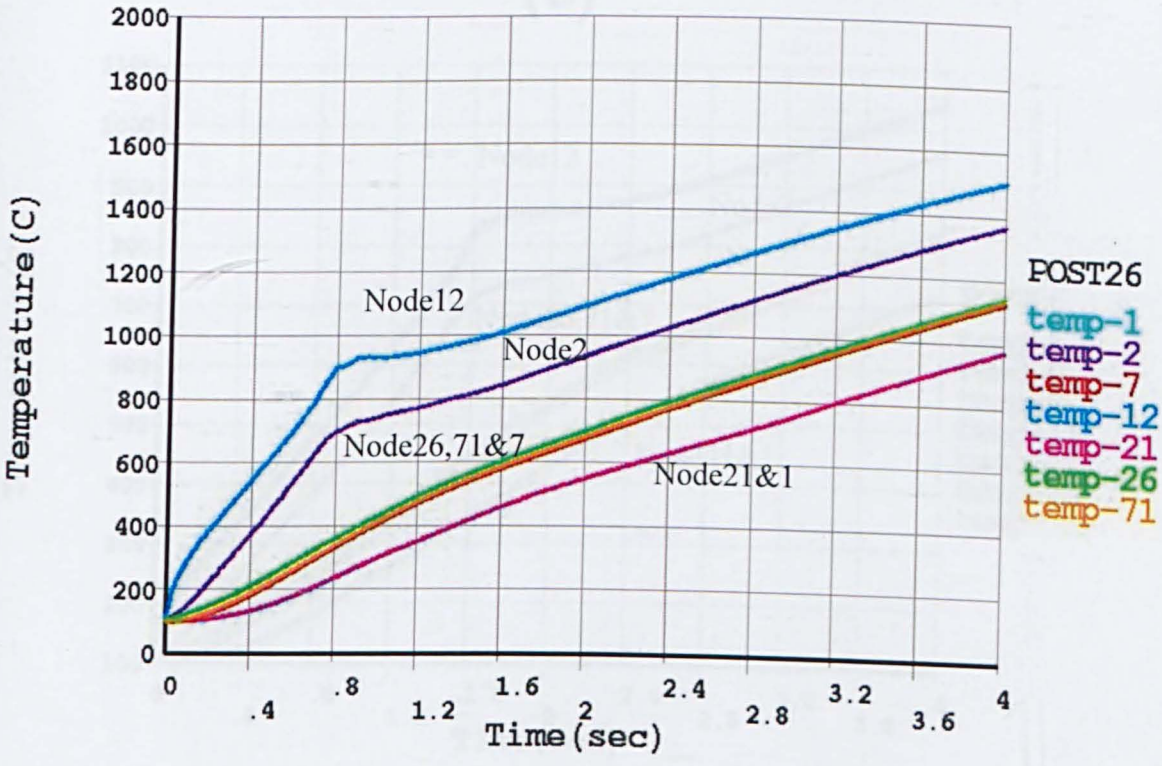
Temperature (C)
2000
1800
1600
1400
1200
1000
800
600
400
200
0
Node12
Node2
Node26,71&7
Node21&1
0
.4
.8
1.2
1.6
2
2.4
2.8
3.2
3.6
4
Time (sec)
POST26
temp-1
temp-2
temp-7
temp-12
temp-21
temp-26
temp-71

(b)

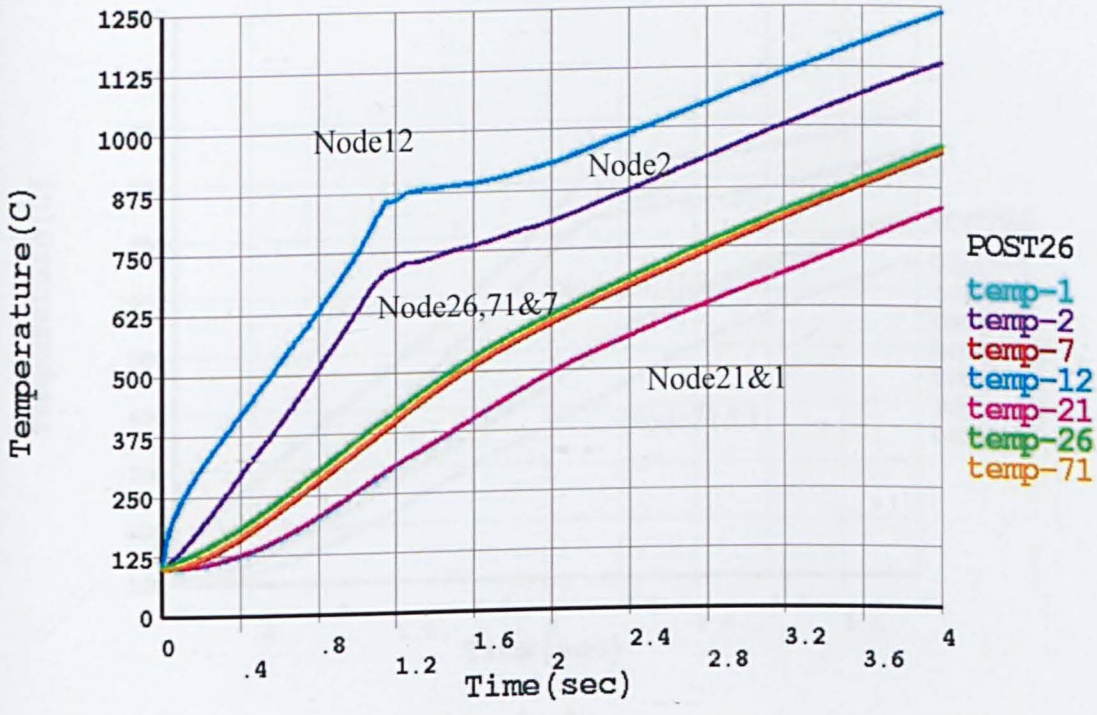
Temperature (C)
1250
1125
1000
875
750
625
500
375
250
125
0
Node12
Node2
Node26,71&7
Node21&1
0
.4
.8
1.2
1.6
2
2.4
2.8
3.2
3.6
4
Time (sec)
POST26
temp-1
temp-2
temp-7
temp-12
temp-21
temp-26
temp-71

(c)

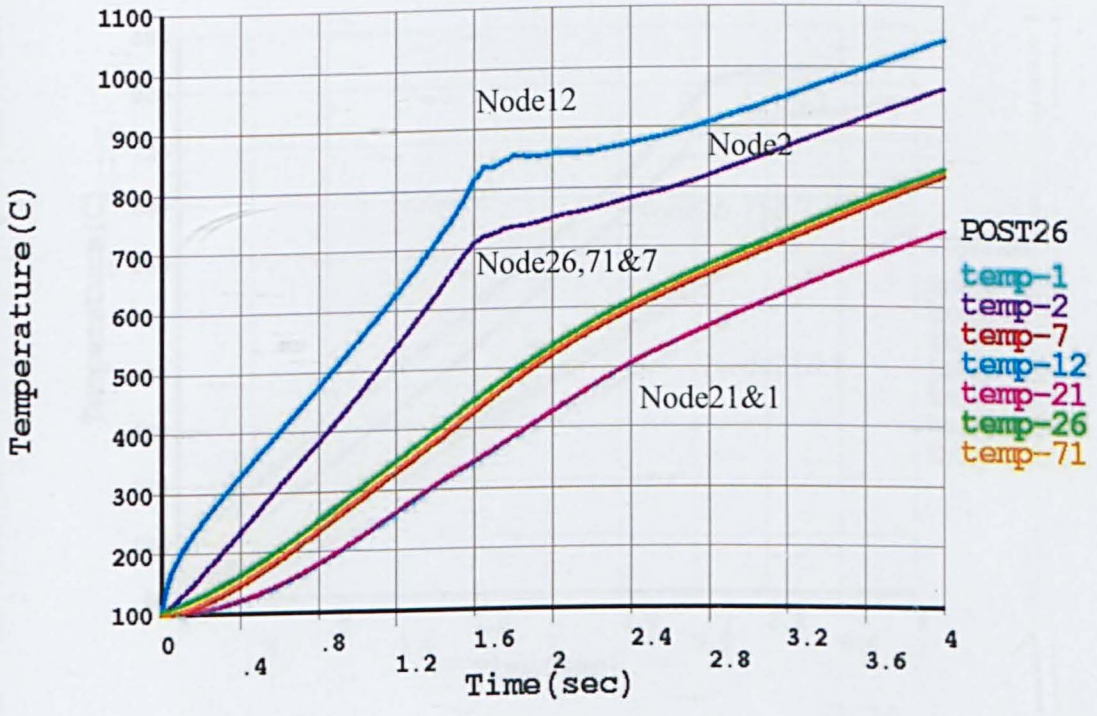
Temperature (C)
1100
1000
900
800
700
600
500
400
300
200
100
0
Node12
Node2
Node26,71&7
Node21&1
0
.4
.8
1.2
1.6
2
2.4
2.8
3.2
3.6
4
Time (sec)
POST26
temp-1
temp-2
temp-7
temp-12
temp-21
temp-26
temp-71

(d)

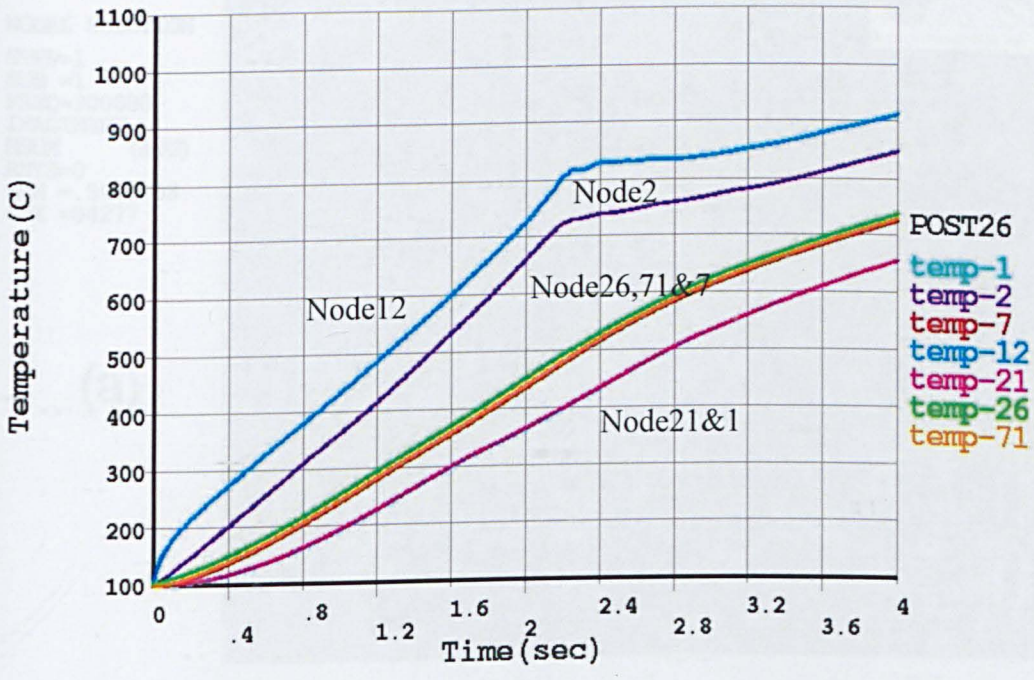

(e)

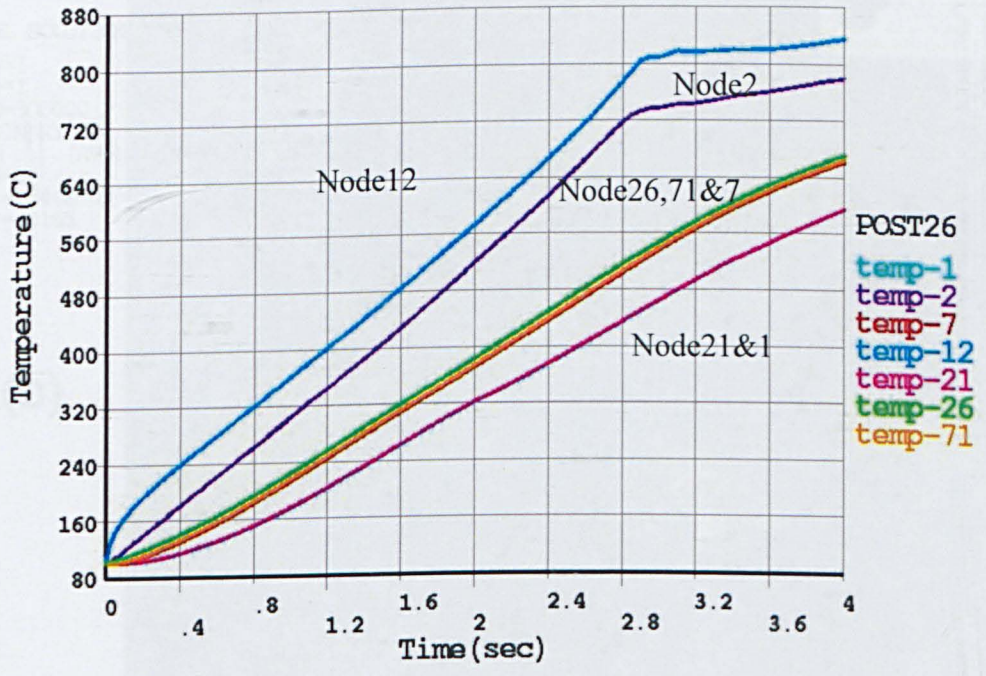

(f)

Figure 7-6 Heating of samples with various air-gap (a) nodes position ; (b) 2mm; (c) 3mm; (d) 4mm; (e) 5mm; (f) 6mm

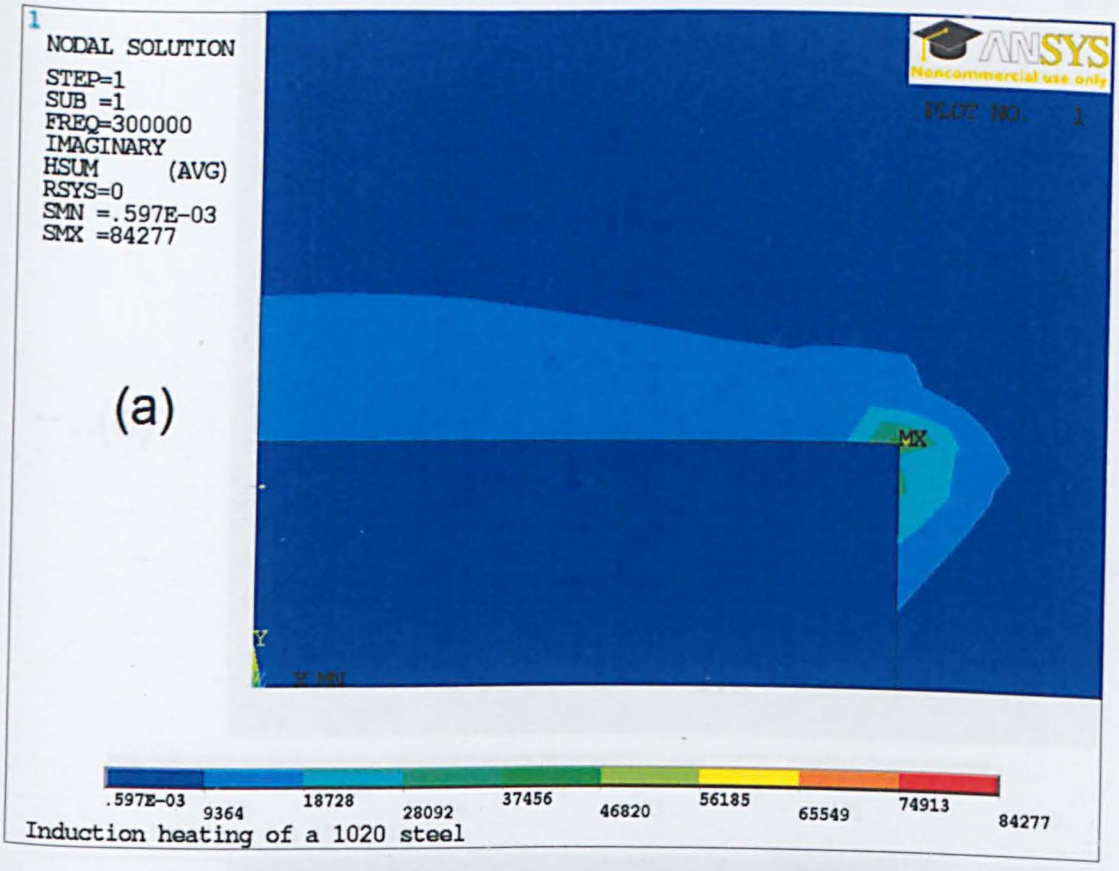
1
NODAL SOLUTION
STEP=1
SUB =1
FREQ=300000
IMAGINARY
HSUM (AVG)
RSYS=0
SMN =.597E-03
SMX =84277
(a)
ANSYS
Noncommercial use only
MX
.597E-03
9364
18728
28092
37456
46820
56185
65549
74913
84277
Induction heating of a 1020 steel

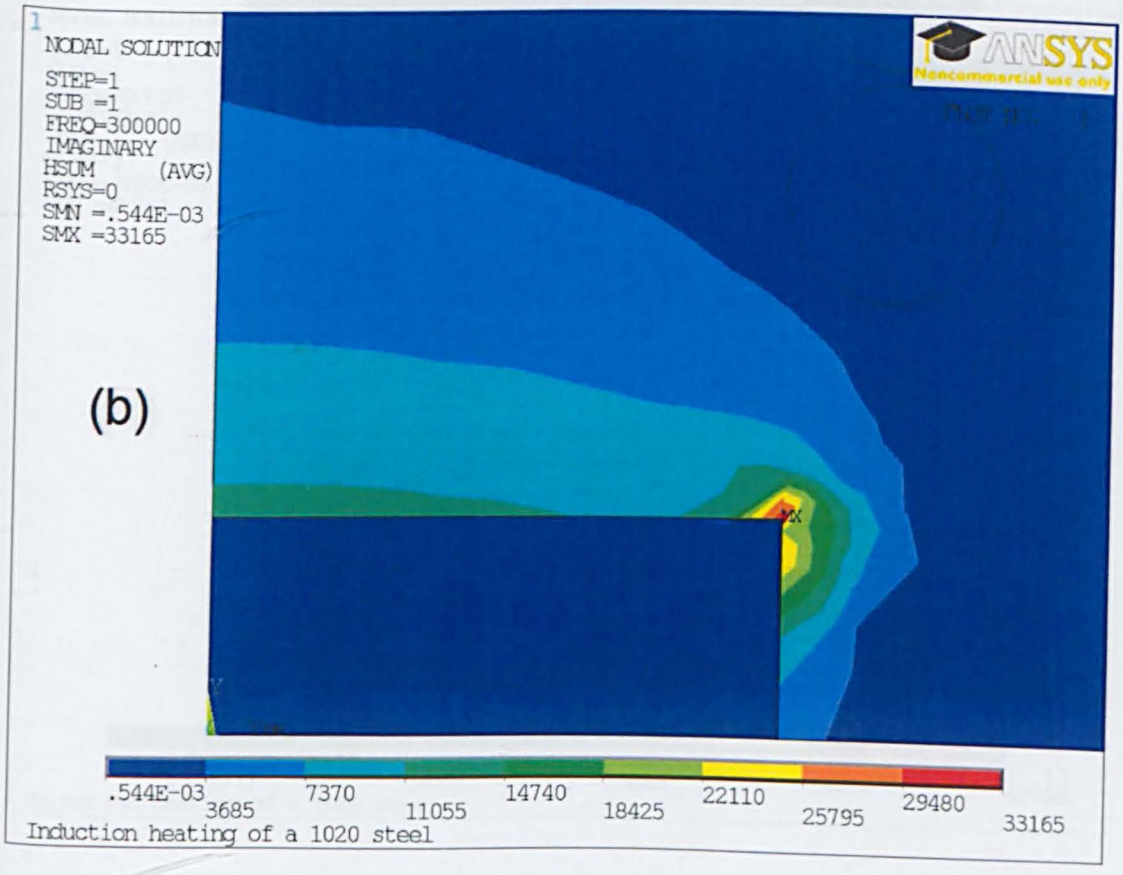
1
NODAL SOLUTION
STEP=1
SUB =1
FREQ=300000
IMAGINARY
HSUM (AVG)
RSYS=0
SMN =.544E-03
SMX =33165
(b)
ANSYS
Noncommercial use only
MX
.544E-03
3685
7370
11055
14740
18425
22110
25795
29480
33165
Induction heating of a 1020 steel

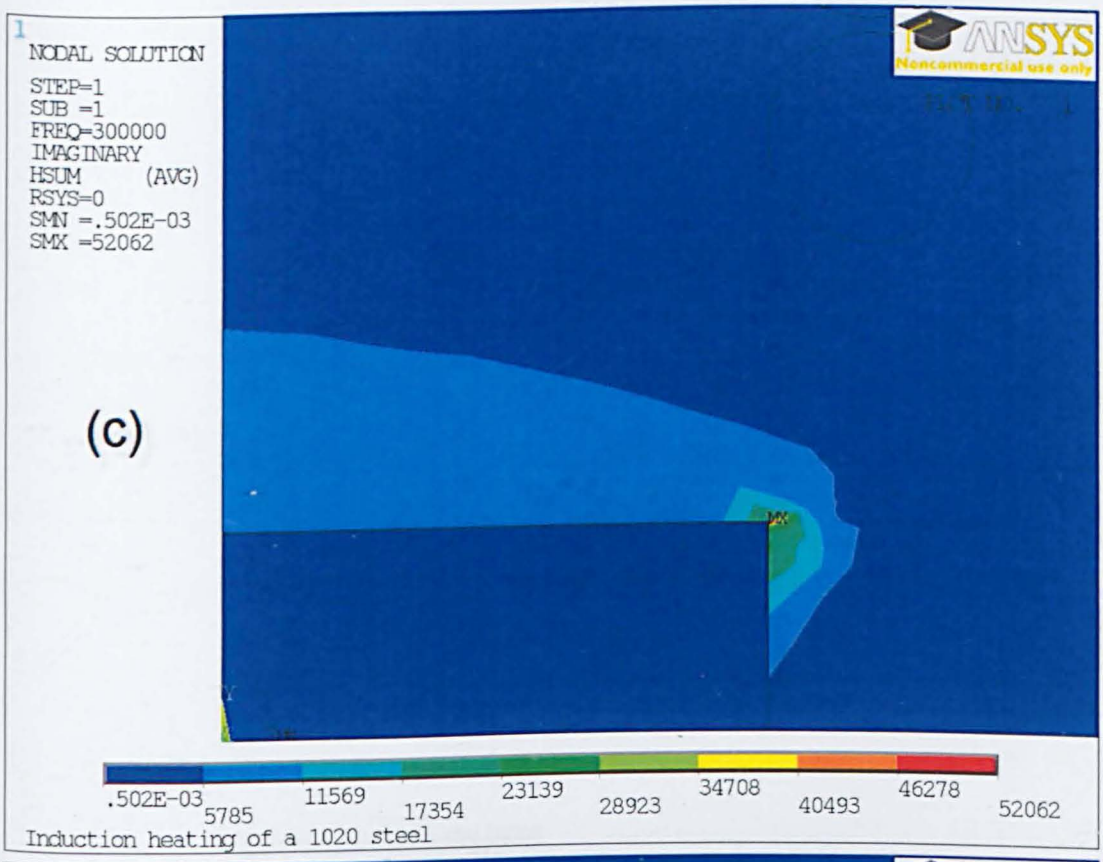
1
NODAL SOLUTION
STEP=1
SUB =1
FREQ=300000
IMAGINARY
HSUM (AVG)
RSYS=0
SMN =.502E-03
SMX =52062
(c)
ANSYS
Noncommercial use only
.502E-03
5785
11569
17354
23139
28923
34708
40493
46278
52062
Induction heating of a 1020 steel

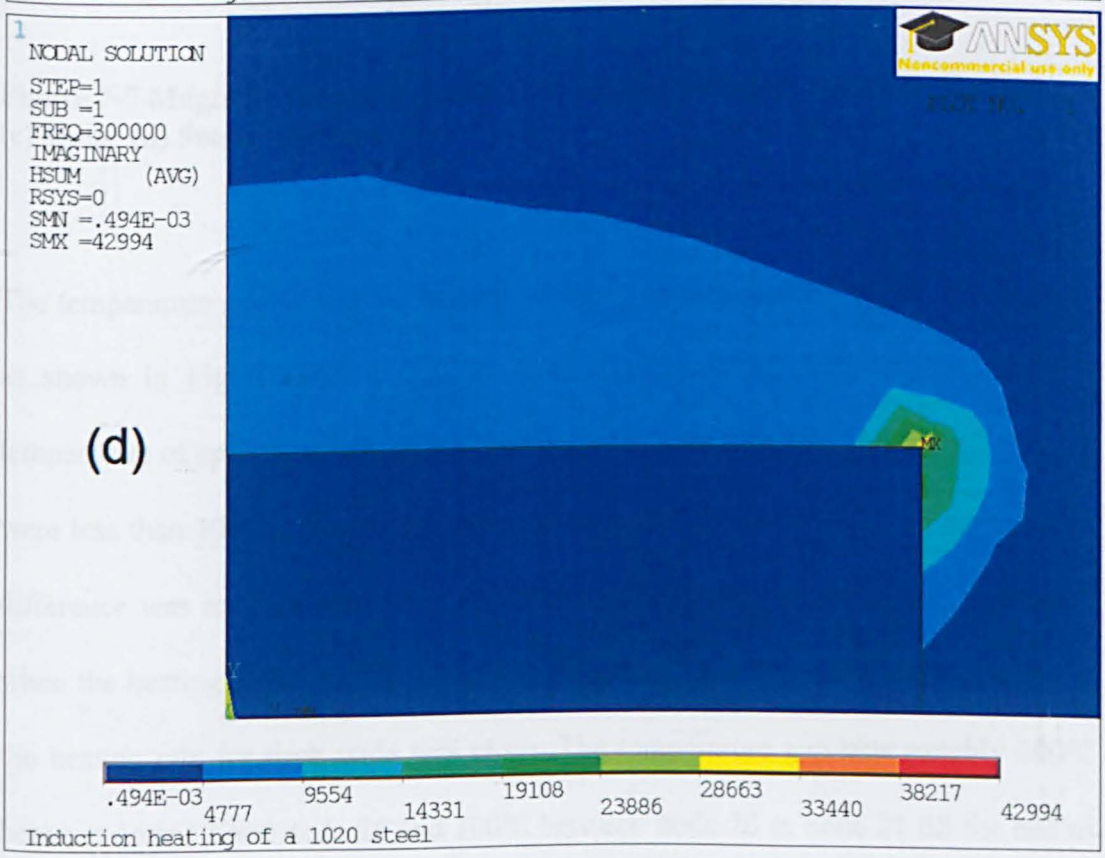
1
NODAL SOLUTION
STEP=1
SUB =1
FREQ=300000
IMAGINARY
HSUM (AVG)
RSYS=0
SMN =.494E-03
SMX =42994
(d)
ANSYS
Noncommercial use only
.494E-03
4777
9554
14331
19108
23886
28663
33440
38217
42994
Induction heating of a 1020 steel

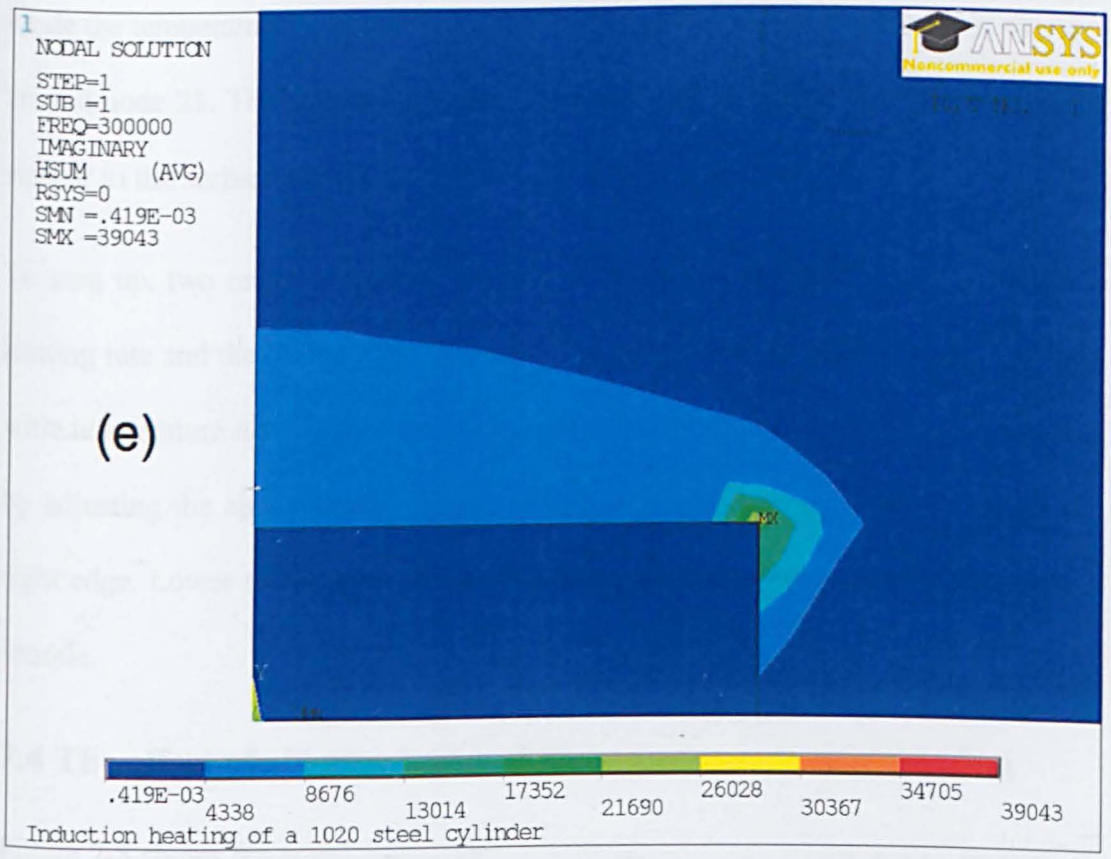

Figure 7-7 Magnetic field distribution at different air-gap: (a) 2mm; (b) 3mm; (c) 4mm; (d) 5mm; (e) 6mm

The temperature gradient in the horizontal direction was significant. On the surface, as shown in Figure 7-6b to Figure 7-6e when node 12 reached the transition temperature of approximately 800 °C, the node 26 were less than 500 °C and node 21 were less than 400 °C. Due to the lower heating rate in Figure 7-7 f the temperature difference was reduced that for node 26 and node 21were about 550°C and 450°C when the heating rate for node 12 became smaller. After the transition temperature, the heating rate for each node was close. The temperature gap was roughly 200°C between node 12 and node 26 and 100°C between node 26 to node 21 till the end of heating. At the bottom the node 2 temperature was 100°C less than that of node 12,

while the temperature at node 7 and node 1 were almost identical to the value at node 26 and node 21. Thus the temperature distribution at the bottom of pellet was quite similar to the surface except the highest temperature was lower.

To sum up, two major influences of air-gap on heating behaviour are the effect of heating rate and the "Edge Effect". Small air-gap will lead to higher heating rate but wide temperature distribution. Uniform heating in this setting can hardly be achieved by adjusting the air-gap, due to the distortion of electromagnetic field at the upper right edge. Lower the heating rate may reduce the temperature difference inside the sample.

7.4 The effect of air-gap in radial direction on induction heating

Figure 7-8 shows the nodal temperature results for all cases by the end of heating of 4 seconds. The radius given in the diagram represents radius of work piece. Each sample showed the maximum temperature at the right up corner and the minimum temperature point was at the bottom of central axis. The maximum temperature increased from 834°C to 1126°C when the radiuses were increased from 5 mm to 9 mm which corresponding to a reduction of air-gap from 5 mm to 1 mm in radial direction. In addition, the broadened radius leads to larger internal temperature gradient under the same air-gap in axis direction (4 mm).

Same as the analysis for the effects of air-gap in axis direction as shown in Section 7.2, temperature monitoring was carried out on selected 7 nodes at different positions. The nodes' numbers and positions were listed in Figure 7-9 a. Figure 7-9 b to f presents the nodes' temperature of 5mm, 6mm, 7mm, 8mm and 9mm radius case respectively.

There are a few similarities between the air-gaps in the axis direction and in the radial direction. In Figure 7-9 b to f, the node 12 had the maximum temperature showing the "Edge Effect" occurred in all cases including the 5mm one and 9mm case. Regardless the change of sample size the temperature of node 26, 71 and 7 were very close, and the curves for node 1 and 21 overlapped. Also the shifting of Curie point was observed in Figure 7-9 d to f.

Figure 7-8 Temperature distribution at the end of heating for samples heated at different air-gaps (=10- the radius of sample) in radial direction

In Figure 7-8 the temperature distribution was broadened with the increase of radius, but the temperature at central axis was not compared. At the end of heating, the temperature of node 1 and node 2 were 750°C in Figure 7-9 b to e, and in Figure 7-9 f their temperature was 720°C. It reveals the horizontal radius could be the major reason for the broadened temperature distribution.

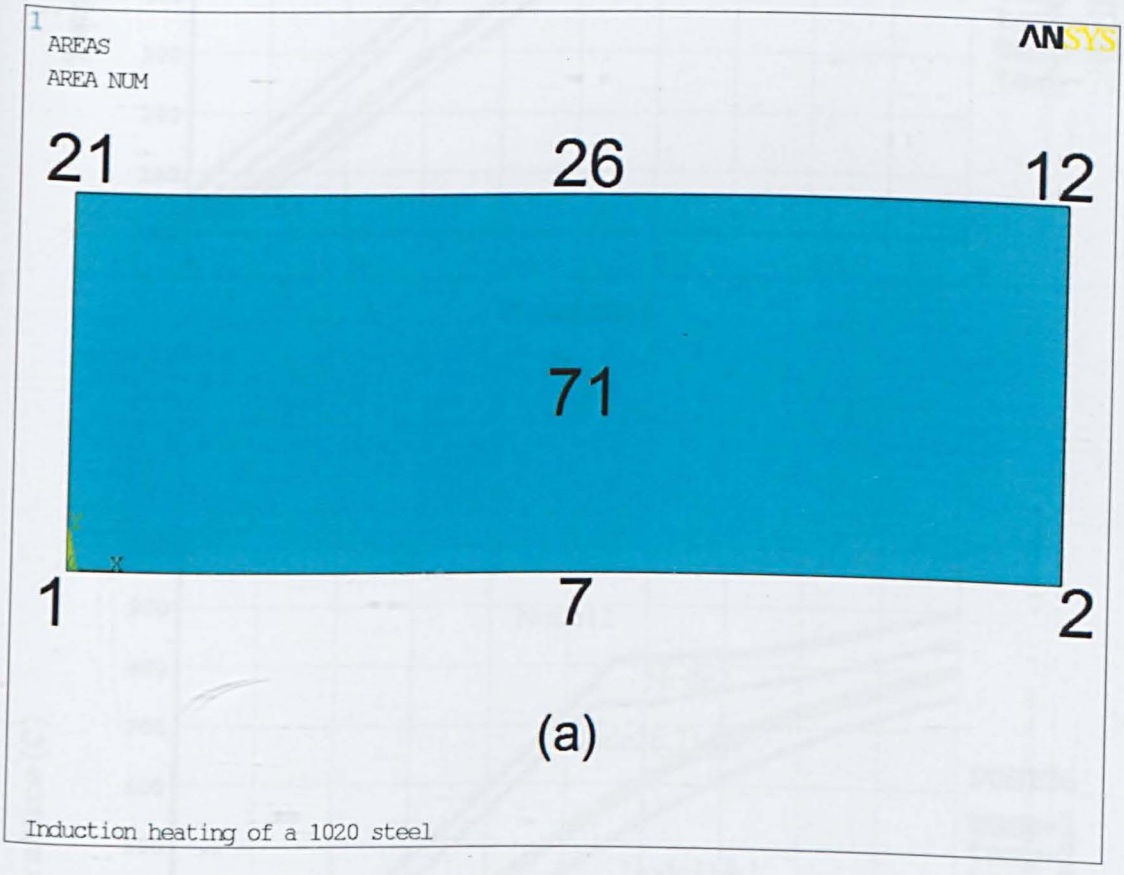

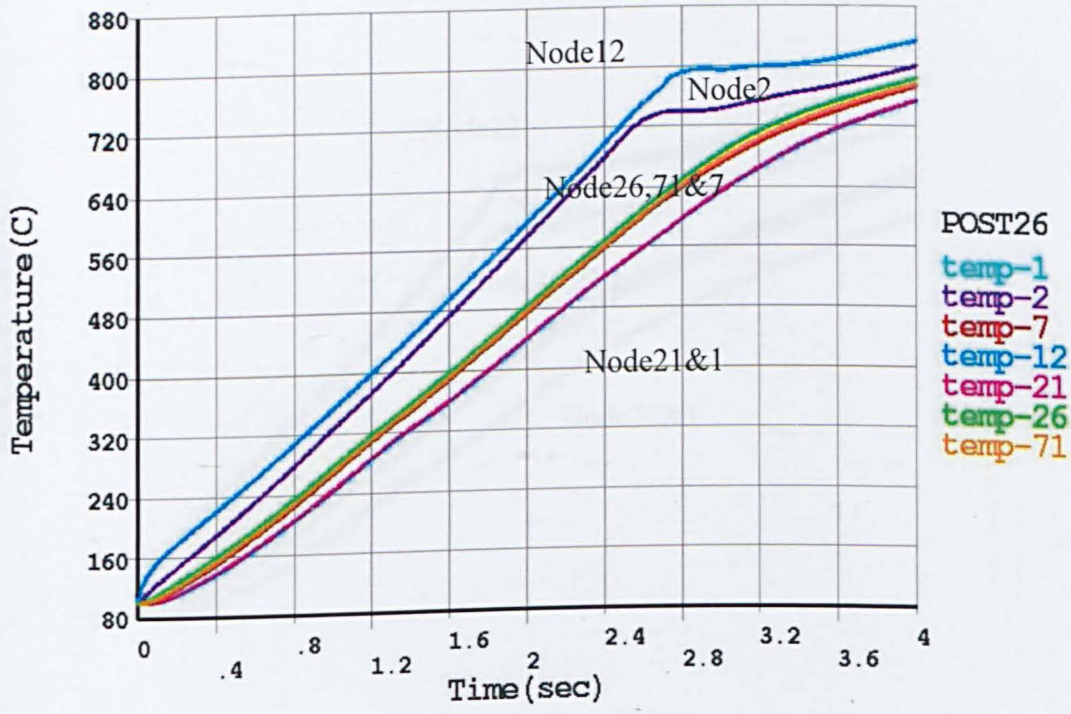
Node12
Node2
Node26,71&7
Node21&1
Temperature (C)
Time (sec)
880
800
720
640
560
480
400
320
240
160
80
0
.4
.8
1.2
1.6
2
2.4
2.8
3.2
3.6
4
POST26
temp-1
temp-2
temp-7
temp-12
temp-21
temp-26
temp-71

(b)

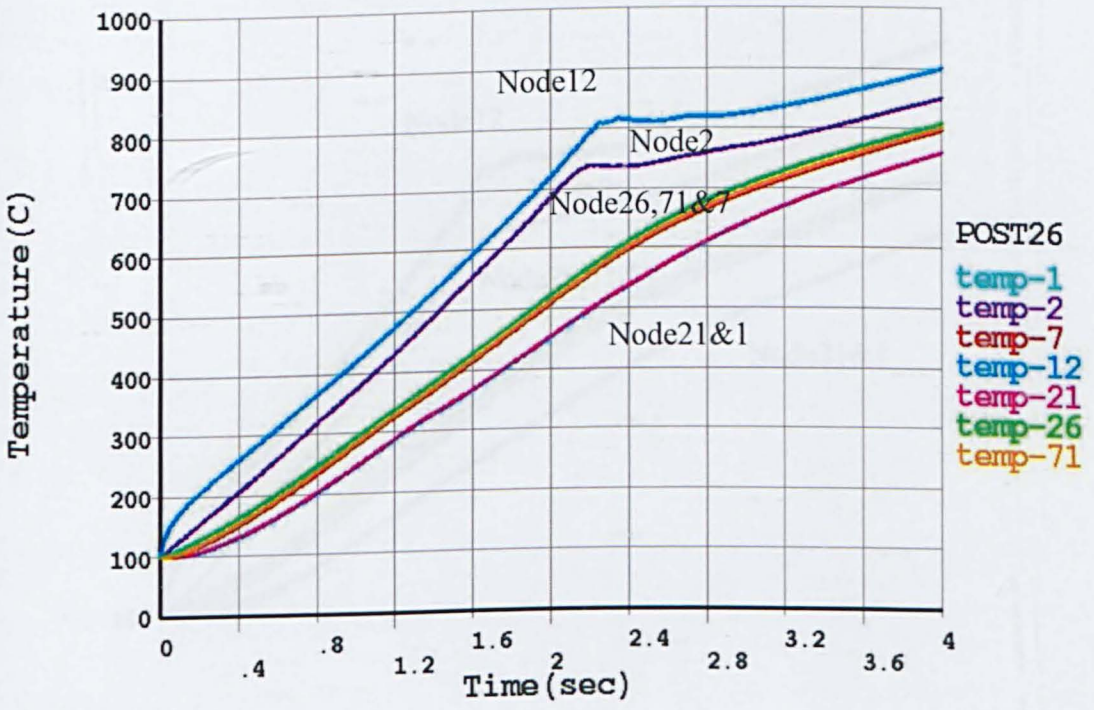
Node12
Node2
Node26,71&7
Node21&1
Temperature (C)
Time (sec)
1000
900
800
700
600
500
400
300
200
100
0
0
.4
.8
1.2
1.6
2
2.4
2.8
3.2
3.6
4
POST26
temp-1
temp-2
temp-7
temp-12
temp-21
temp-26
temp-71

(c)

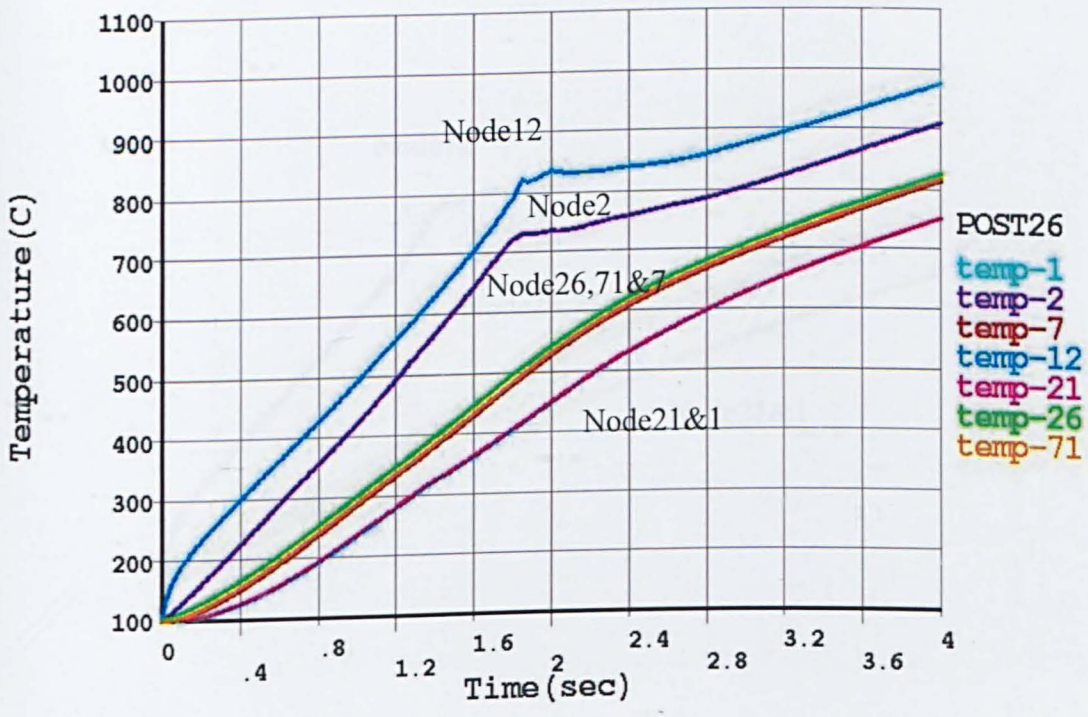
Temperature (C)
1100
1000
900
800
700
600
500
400
300
200
100
0
.4
.8
1.2
1.6
2
2.4
2.8
3.2
3.6
4
Time (sec)
Node12
Node2
Node26,71&7
Node21&1
POST26
temp-1
temp-2
temp-7
temp-12
temp-21
temp-26
temp-71

(d)

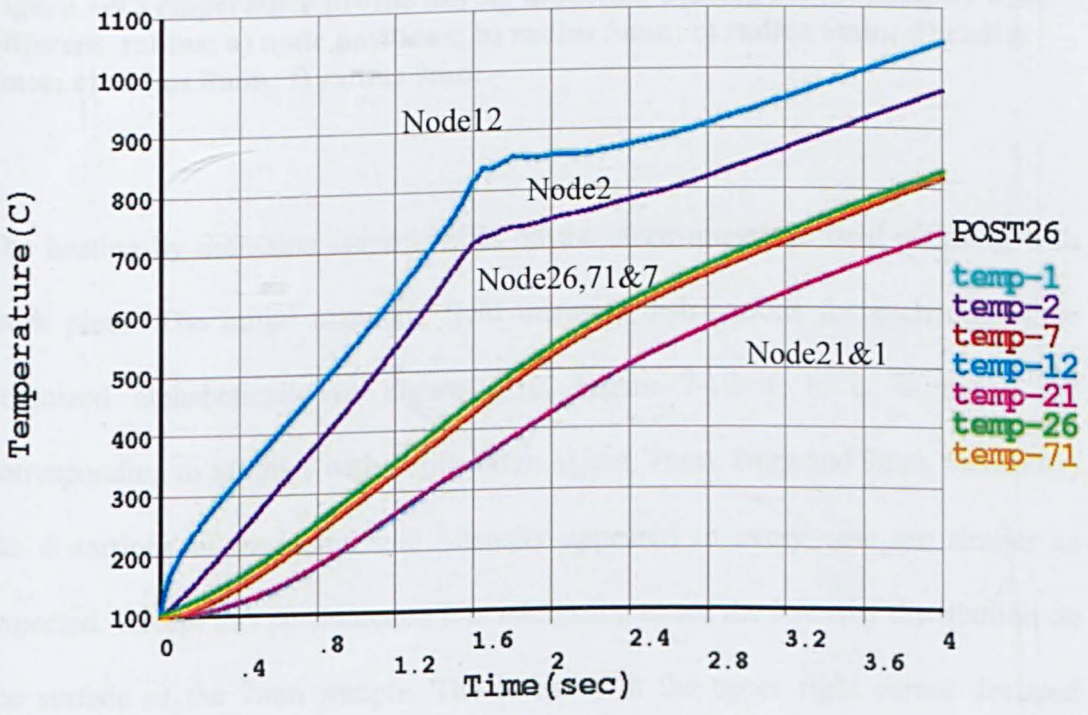
Temperature (C)
1100
1000
900
800
700
600
500
400
300
200
100
0
.4
.8
1.2
1.6
2
2.4
2.8
3.2
3.6
4
Time (sec)
Node12
Node2
Node26,71&7
Node21&1
POST26
temp-1
temp-2
temp-7
temp-12
temp-21
temp-26
temp-71

(e)

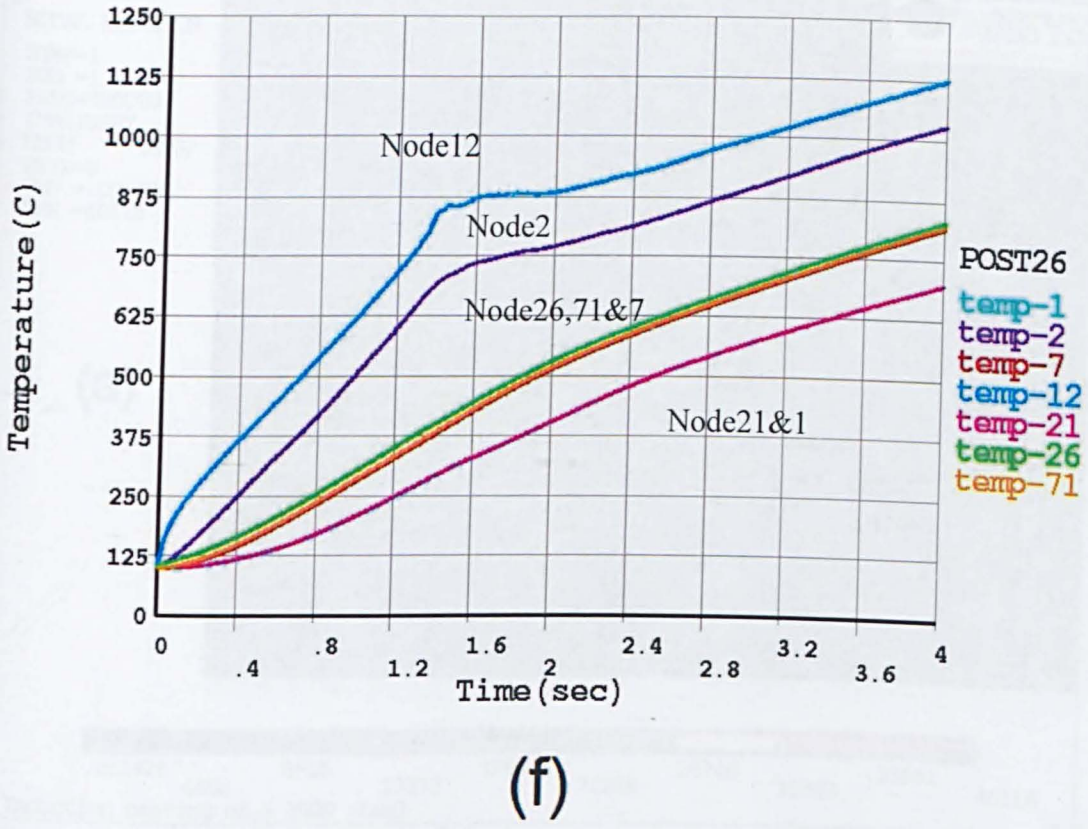

(f)

Figure 7-9 Temperature profile during induction heating for the samples with different radius; a) node positions; b) radius 5mm; c) radius 6mm; d) radius 7mm; e) radius 8mm; f) radius 9mm

The heating by induction current relies on the electromagnetic field coupling with work piece. The initial magnetic field intensity distributions for each case were organized alphabetically in Figure 7-10. Figure 7-10 a, b, c, d and e are corresponding to samples with radius 5mm, 6,mm, 7mm, 8mm and 9mm. Generally, the distortions of magnetic field intensity appeared in every case are similar as expected. Except this phenomenon it is interesting to see the intensity distribution on the surface of the 7mm sample. The intensity at the upper right corner declined sharply and climbed up along radius direction. This fluctuation implies that after the distortion at the corner the intensity was not evenly distributed.

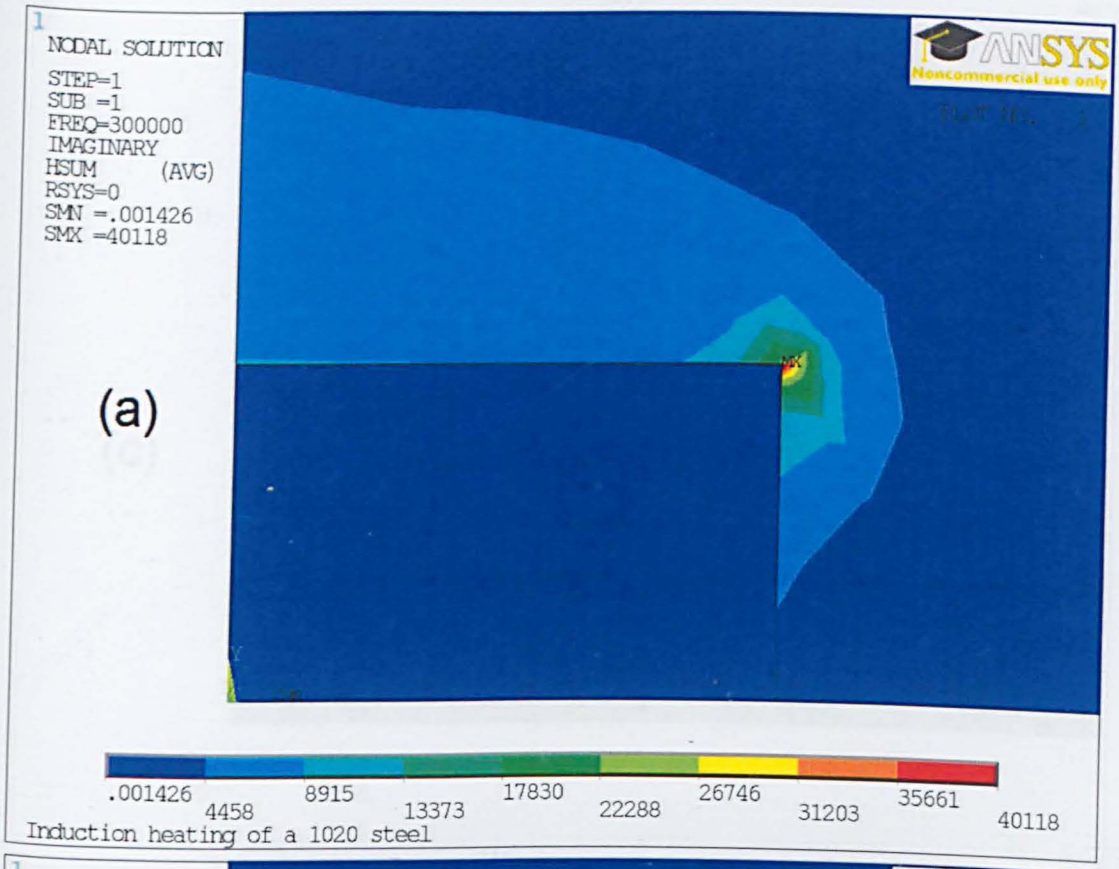
1
NODAL SOLUTION
STEP=1
SUB =1
FREQ=300000
IMAGINARY
HSUM (AVG)
RSYS=0
SMN =.001426
SMX =40118
(a)
ANSYS
Noncommercial use only
.001426
4458
8915
13373
17830
22288
26746
31203
35661
40118
Induction heating of a 1020 steel

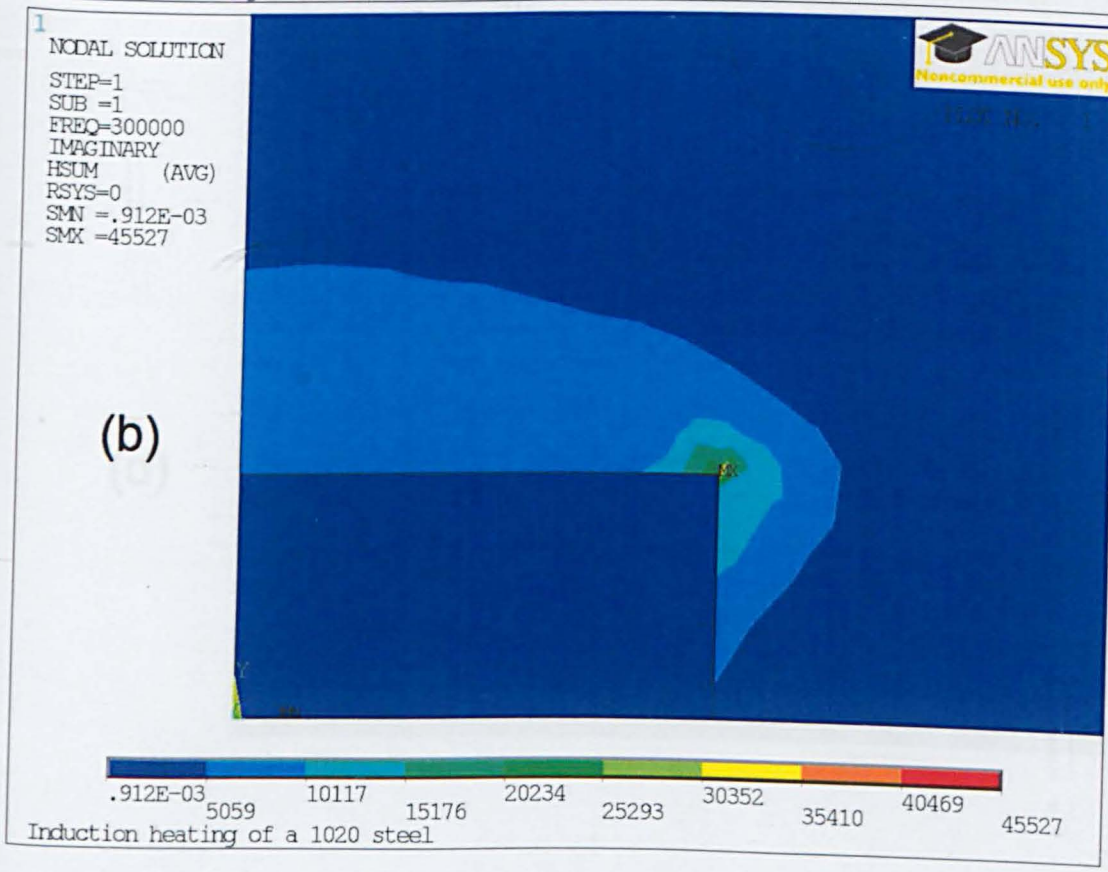
1
NODAL SOLUTION
STEP=1
SUB =1
FREQ=300000
IMAGINARY
HSUM (AVG)
RSYS=0
SMN =.912E-03
SMX =45527
(b)
ANSYS
Noncommercial use only
.912E-03
5059
10117
15176
20234
25293
30352
35410
40469
45527
Induction heating of a 1020 steel

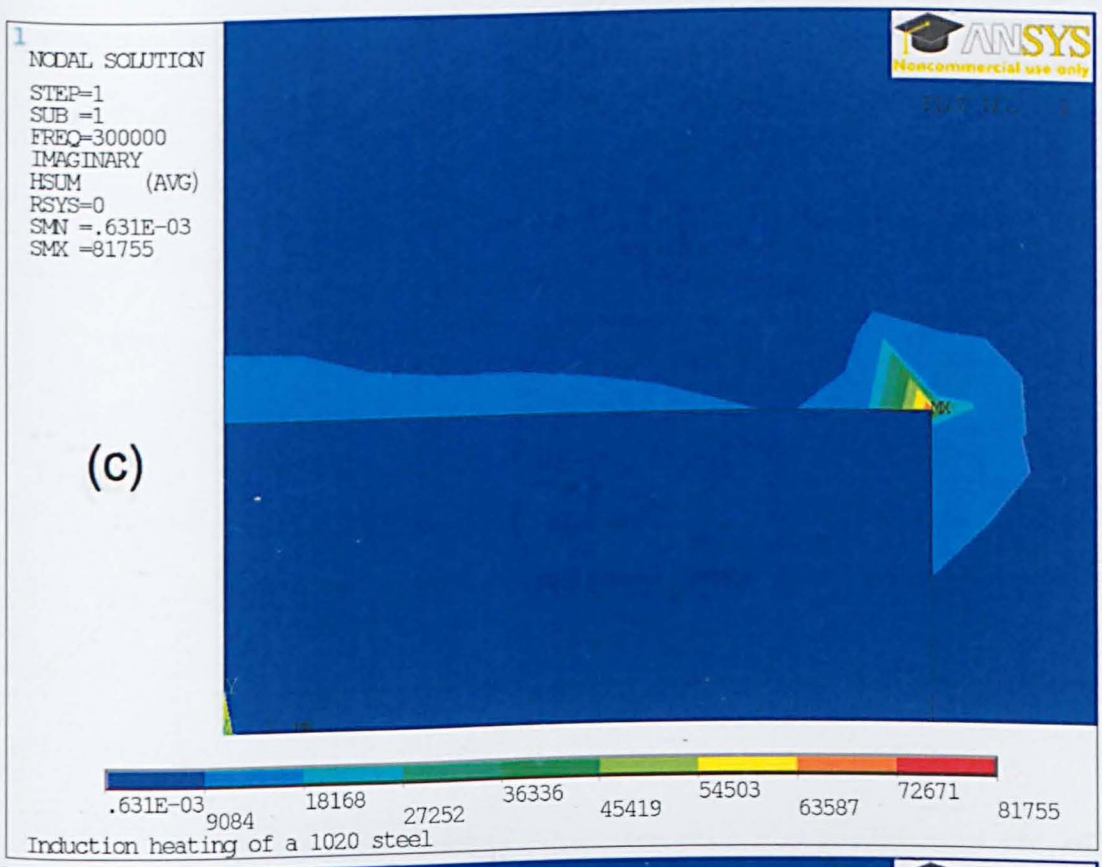
1
NODAL SOLUTION
STEP=1
SUB =1
FREQ=300000
IMAGINARY
HSUM (AVG)
RSYS=0
SMN =.631E-03
SMX =81755
(c)
ANSYS
Noncommercial use only
.631E-03
9084
18168
27252
36336
45419
54503
63587
72671
81755
Induction heating of a 1020 steel

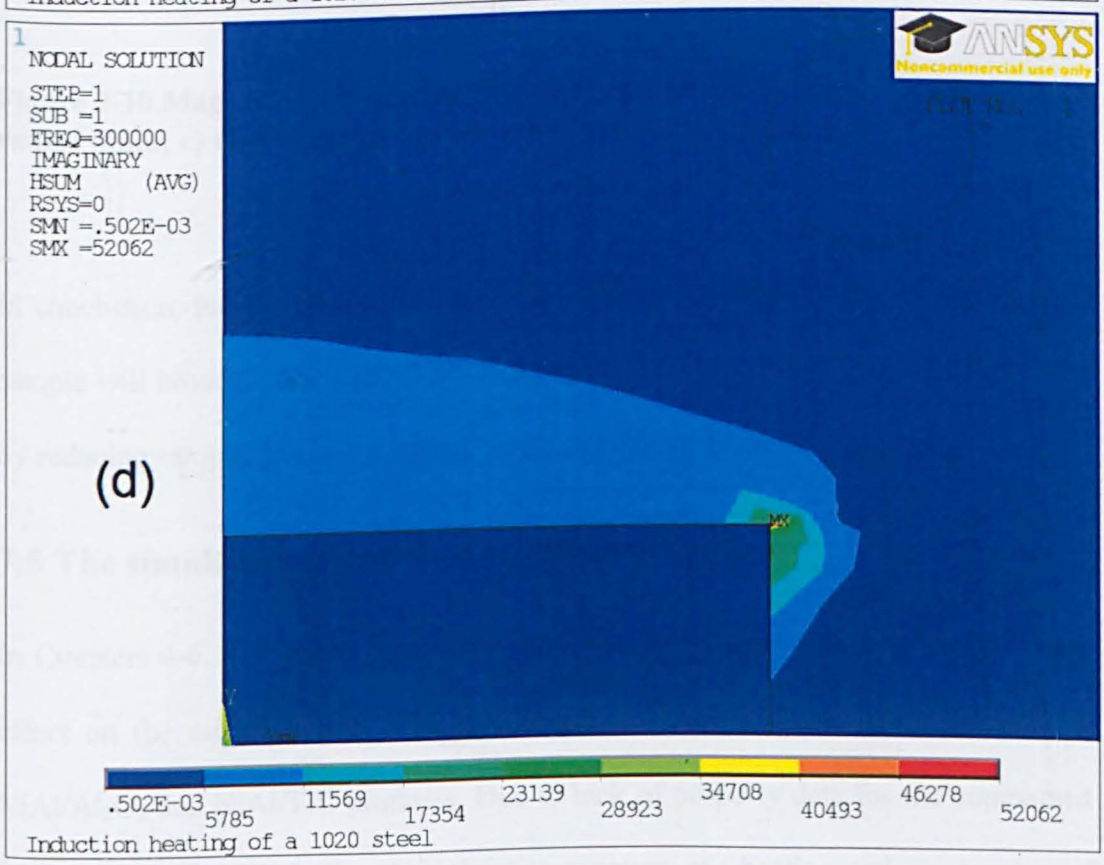
1
NODAL SOLUTION
STEP=1
SUB =1
FREQ=300000
IMAGINARY
HSUM (AVG)
RSYS=0
SMN =.502E-03
SMX =52062
(d)
ANSYS
Noncommercial use only
.502E-03
5785
11569
17354
23139
28923
34708
40493
46278
52062
Induction heating of a 1020 steel

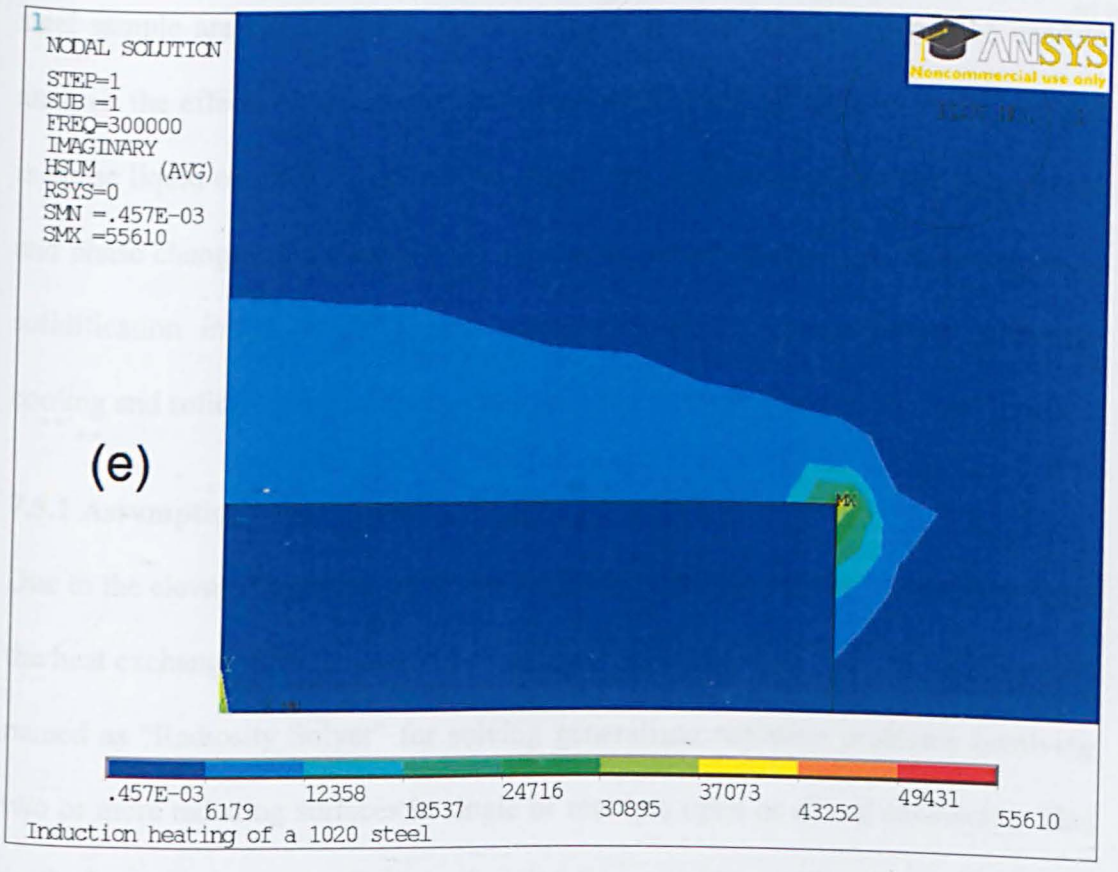

Figure 7-10 Magnetic field distribution in radius group a) radius 5mm; b) radius 6mm; c) radius 7mm; d) radius 8mm; e) radius 9mm

In conclusion, increasing the radius (reduce air-gap in radial direction) of the steel sample will broaden the distribution lead to more serious "Edge Effect". In contrast, by reducing sample's radius could generate narrow temperature distribution.

7.5 The simulation of product solidification

In Chapters 4-6, the results have shown the heating and cooling have a significant effect on the microstructure and mechanical properties of the synthesized NiAl, $NiAl/Al_2O_3$ and NiAl/TiC products. Due to lack of property data for the compacted product and the complexity of combustion reaction, the heating and combustion of SHS cannot be simulated. However a similar heating behaviours as shown for the

steel sample are expected and the results described in Section 7.3 can be used to analysis the effects of processing parameter. At the cooling stage, since the product is dense liquid or solid, computer simulation can be done to predict the temperature and phase changes in the sample during cooling. As discussed before, the length of solidification influence the crystallization and mechanical properties. Thus the cooling and solidification of the synthesized products was simulated in this section.

7.5.1 Assumptions and settings

Due to the elevated temperature in synthesis, the radiation plays an important role in the heat exchange with the open environment. The ANSYS 12.0 provides a package named as "Radiosity Solver" for solving generalized radiation problems involving two or more radiating surfaces in single or multiple open or closed enclosures. This method provides accuracy for complex situation so in this section all the simulation work was conducted with this method.

The nature of highly non-linear process of solidification requires careful considerations in simulation. For example, although the end of combustion reaction can be estimated using thermal images when the combustion propagation terminates, it remains unclear when the products synthesis is complete. Also, the lack of reliable thermal properties is another challenge. The following assumptions were used in this study to make the simulation feasible:

- The synthesis is completed at the solidification
- No thermal contact resistance at the interface
- The shape of the sample is fixed during cooling
- The heat loss via convection is ignored

- The surrounding air is at fixed temperature

The setup for the simulation was shown in Figure 7-11. In agreement with the compact pellet size as studied in Chapters 4-6, the radius of product is set as 8mm and the thickness is set as 1.4 mm. To reduce the computation time the size of substrate is reduced. The height and radius of substrate are both 50mm. This size of substrate provides enough accuracy and convenience of meshing. The air enclosure is set as a 100mm high cylinder with 200mm diameter.

The attribute settings for the simulation are listed in

Table 7-4. The element PLANE55 was employed because it supports 2-D asymmetrical model and can be used in "Radiosity Solver". More details of this element are enclosed in Appendix D. The properties of the products are referenced from and manufacturer [149-150, 160], as listed in Table 7-5. Unfortunately the heat capacity and conductivity of materials should be functions of temperature. In this case, lack of data is the biggest challenge which should be addressed here. For the substrate the heat capacity and conductivity data were consulted from manufacture. The mesh result is presented in Figure 7-12. Fine meshing was applied in the products area to improve the accuracy.

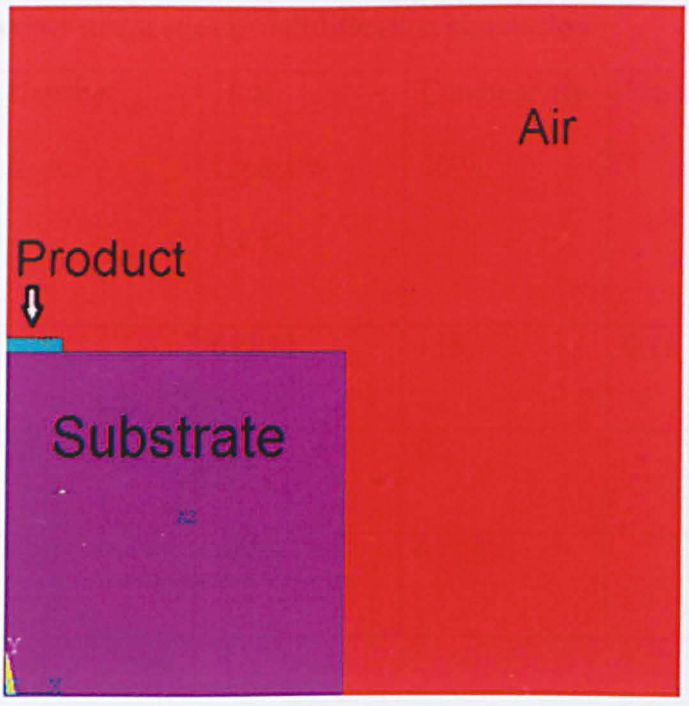

Figure 7-11 Model of product cooling cases

Table 7-4 Attributes setting for modelling in product solidification case

Area	Element number	Real constant	Element type	Materials properties
Product	1	1	PLANE55	Density, Capacity, Conductivity, Enthalpy, Emissivity
Substrate	1	1	PLANE55	Density, Capacity, Conductivity
Air	2	1	PLANE55	Density, Capacity, Conductivity

Table 7-5 Materials properties in solidification simulation

	Density/ Kg/m^3	Heat capacity/ 300K	Conductivity/ 300K	Emissivity
NiAl	5838	617.13	118	0.72
Substrate	3850	880	0.2	
Air	1.205	1.005	0.0257	

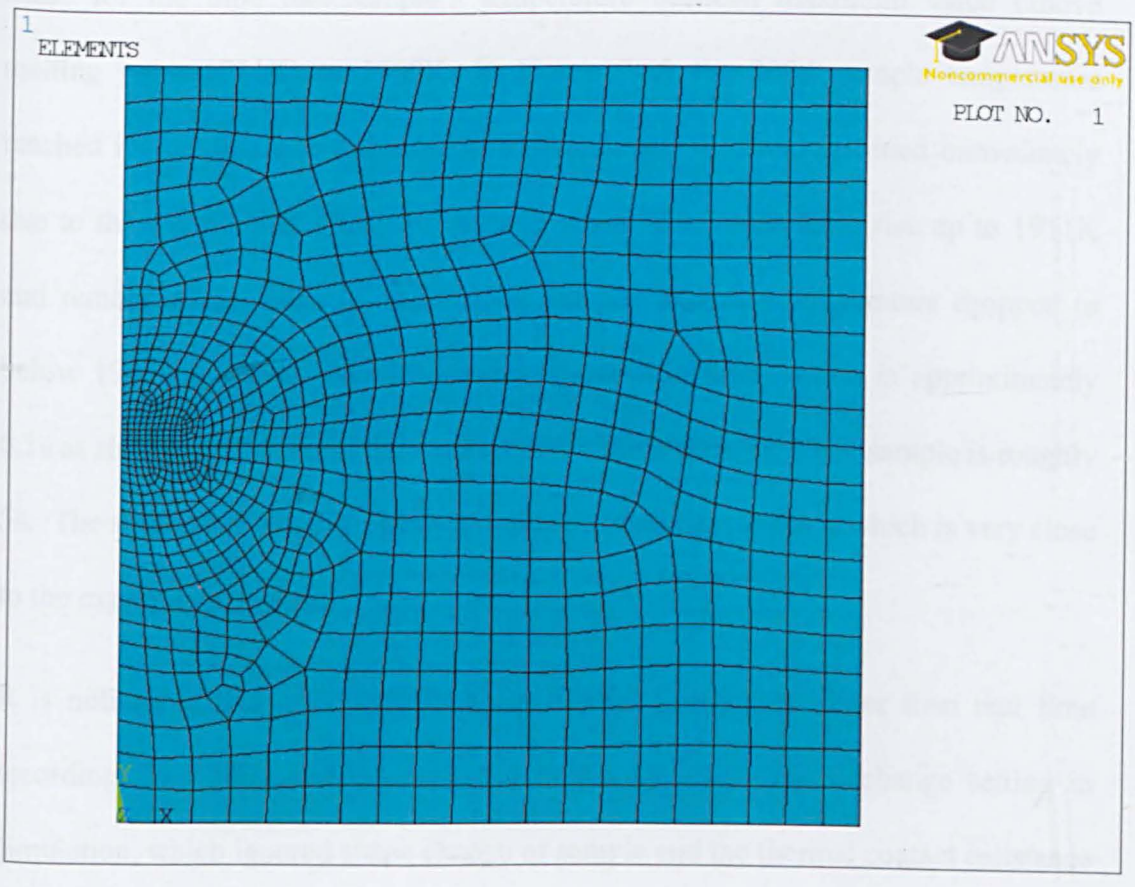

Figure 7-12 Meshing for the solidification simulation

7.5.2 Validation of the mode

As stated in previous chapters, in this experimental setting the ignition system preheats the pellet before ignition. Therefore the solidification process with preheating condition is more practical to be computed. In ANSYS APDL, simply adjusting the enthalpy of products enables the computation for various preheating conditions. To compare with 300A sample as discussed in Chapter 4, the preheating temperature for simulation was set at 800 K. In Figure 7-13 the 300A sample temperature profile was presented with simulation result.

The simulation was aiming to estimate the solidification period so attention was made for the time that sample's temperature between maximum value (above melting point 1911K) to 1900K. In Figure 7-13 the 300A sample temperature reached its maximum temperature at approximately 4.5s and declined immediately due to the overcooling effect for crystallization. The temperature rise up to 1911K and remain at the value till 9.5s. After that the sample's temperature dropped to below 1900K. Despite the combustion propagation time, which is approximately 0.1s as shown in Chapter 4, the whole solidification time for 300A sample is roughly 5s. The simulation result suggests the solidification time is 4.85s which is very close to the experimental work.

It is noticeable that after 1900K the simulation curve falls faster than real time recording. The quick decline may due to the idealized heat exchange setting in simulation, which ignored shape change of sample and the thermal contact resistance at interface. Also, the value of preheating condition in simulation setting (800K) could be lower than practical work.

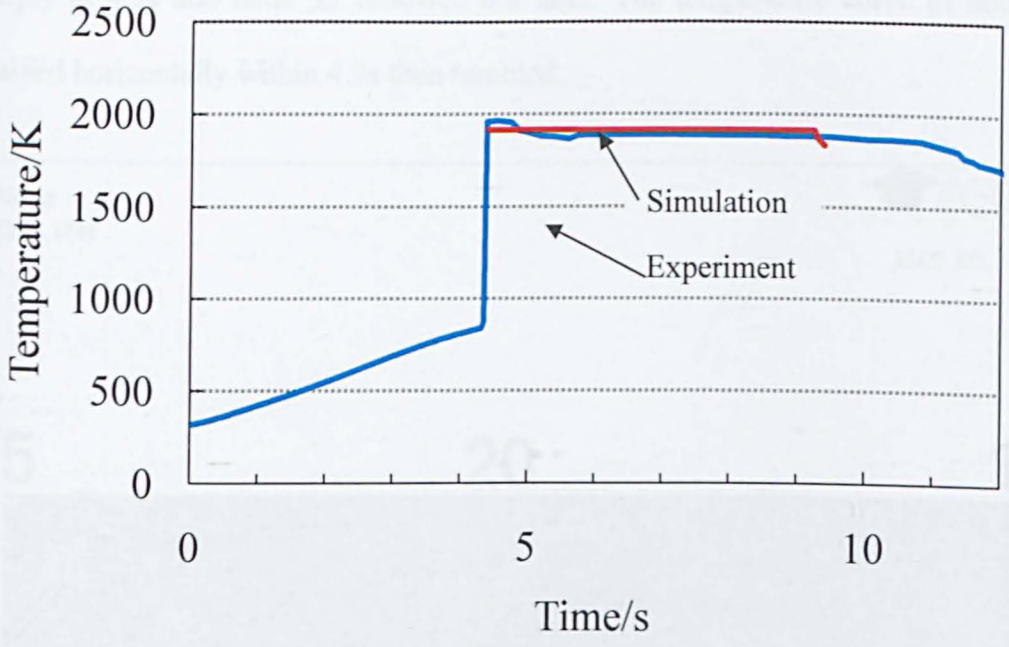

Figure 7-13 Temperature profile of 300A sample

7.5.3 NiAl solidification with preheating

To obtain more details of the solidification, similar to the analysis in induction heating, 7 nodes as shown in Figure 7-14 at different positions were selected to monitor the temperature decline during cooling. Node 2 and 12 were at the outer surface and node 1 and 15 were located at the axis.

The temperature curves of these 7 nodes were listed in Figure 7-15. Generally the node at edge cooled earlier than the inner nodes but the difference in vertical direction was not significant. Node 2 fell down in the first place, at the time about 1.7s. Node 12 started cooling down immediately afterwards. At approximately 1.4s node 15 and node 20 dropped about 5°C. Node 15 and 20 declined about 5°C at 3.2s, remained at that temperature for another 1.6s and 1s respectively. Node 7 dropped

sharply at 4.5s and node 33 followed 0.2 later. The temperature curve of node 1 retained horizontally within 4.9s then tumbled.

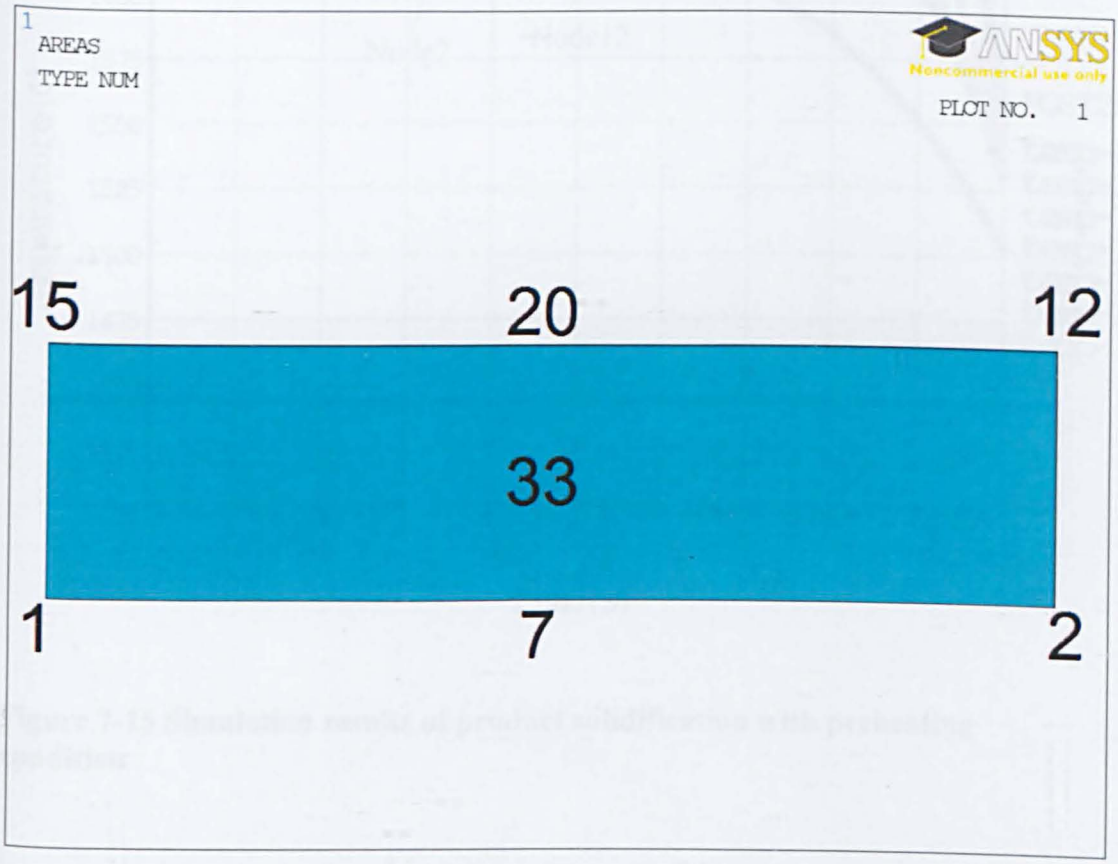

Figure 7-14 Nodes' position of product

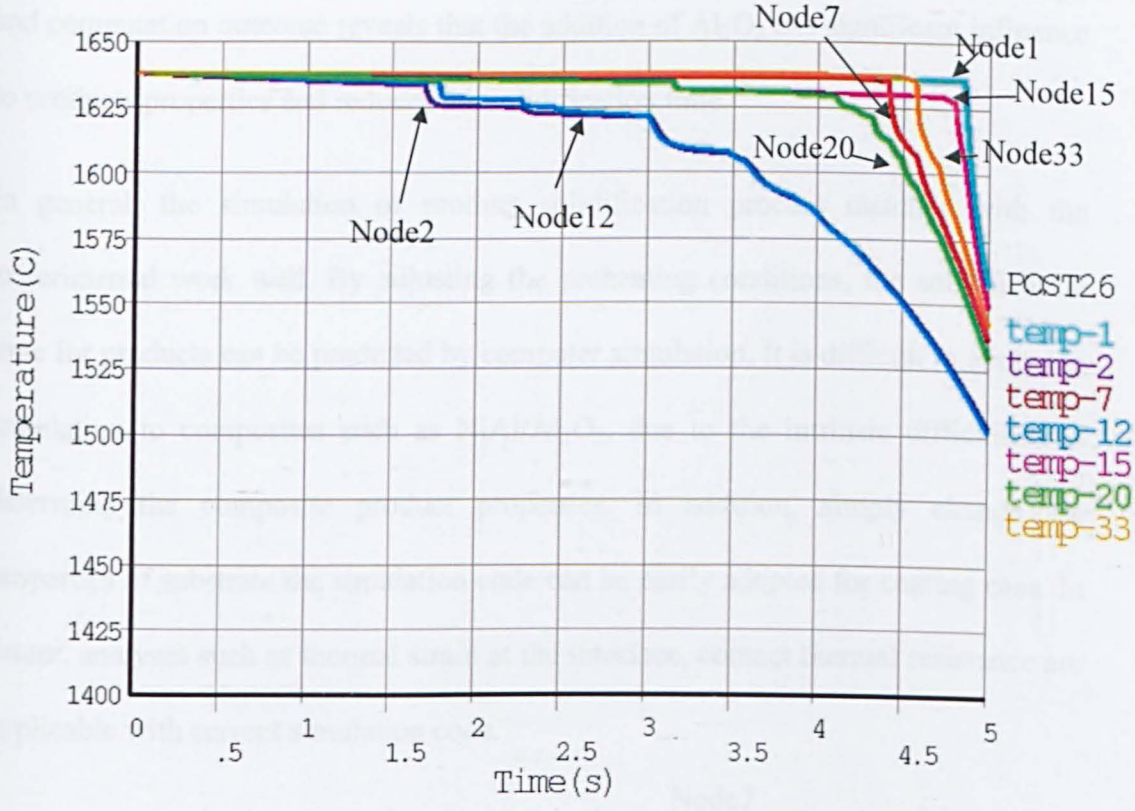

Figure 7-15 Simulation results of product solidification with preheating condition

7.5.4 The effect of Al_2O_3 as additive

The addition of Al_2O_3 changes the density, conductivity, specific heat as well as enthalpy. With small amount of addition the change of products properties could be omitted. However, due to the lack of enough thermal data to the composite products, the computation for large amount of addition may be not reliable. For example, attempt of 10% Al_2O_3 addition simulation was carried out and the results are given in Figure 7-16. In this attempt only the variation of enthalpy was taken into consideration. The effect of Al_2O_3 on other properties was ignored. The solidification time suggested by Figure 7-16 is roughly 4s but the recorded result was less than 3s, as shown in Figure 7-17. The discrepancy between experimental work

and computation outcome reveals that the addition of Al_2O_3 has significant influence to products properties and reduces the solidification time.

In general, the simulation of product solidification process matches with the experimental work well. By adjusting the preheating conditions, the solidification time for products can be predicted by computer simulation. It is difficult to apply the simulation to composites such as $NiAl/Al_2O_3$, due to the intrinsic difficulties in determine the composite product properties. In addition, simply change the properties of substrate the simulation code can be easily adopted for coating case. In future, analyses such as thermal strain at the interface, contact thermal resistance are applicable with current simulation code.

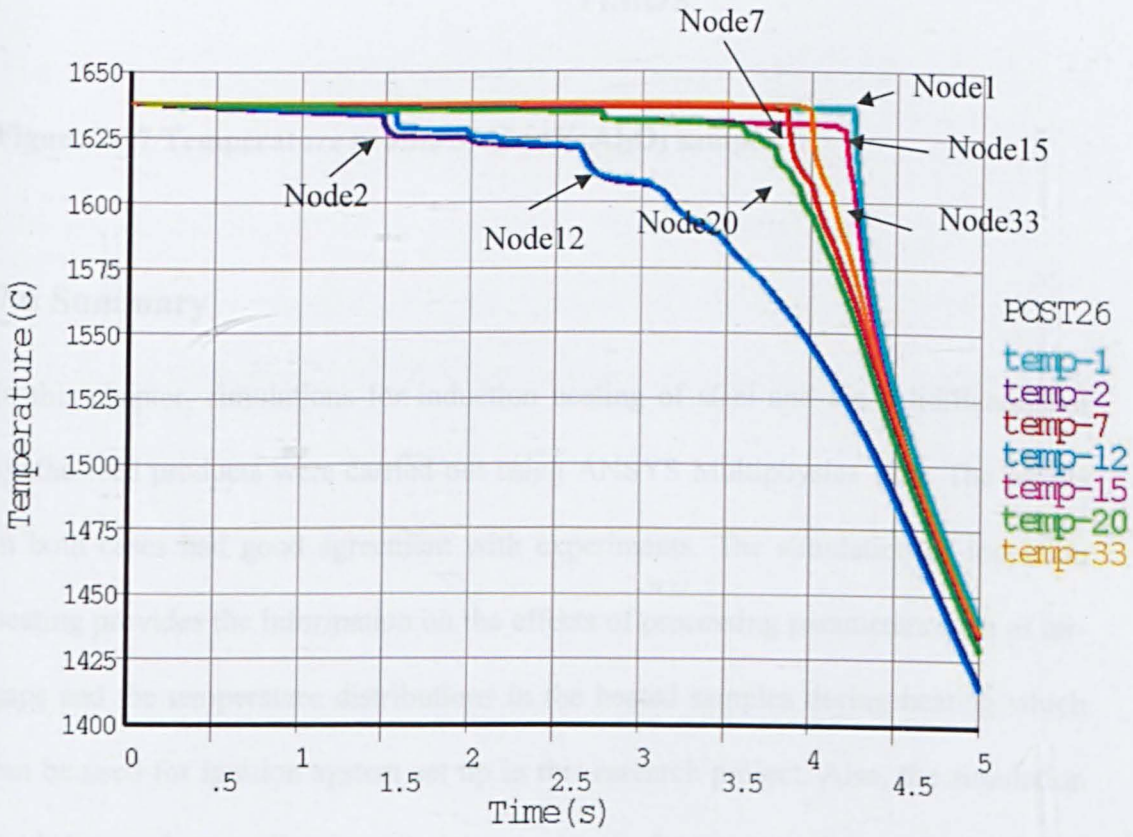

Figure 7-16 Simulation results for synthesized NiAl with 10wt% Al_2O_3 during solidification.

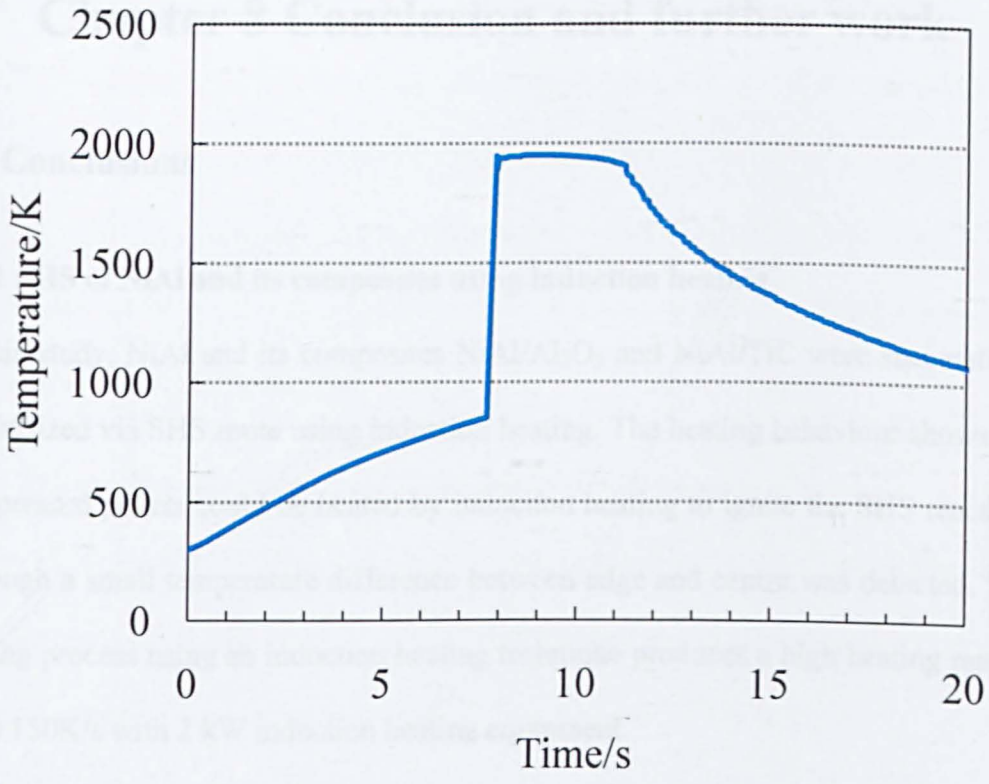

Figure 7-17 Temperature profile of 10wt% Al_2O_3 sample

7.6 Summary

In this chapter, simulations for induction heating of steel and the solidification of synthesized products were carried out using ANSYS Multiphysics 12.0. The results in both cases had good agreement with experiments. The simulation of induction heating provides the information on the effects of processing parameters such as air-gaps and the temperature distributions in the heated samples during heating which can be used for ignition system set up in this research project. Also, the simulation work for product cooling is quite encouraging in future attempts on coating. More details of simulation process and results are attached at appendix.

Chapter 8 Conclusion and further work

8.1 Conclusions

8.1.1 SHS of NiAl and its composites using induction heating

In this study, NiAl and its composites NiAl/Al_2O_3 and NiAl/TiC were successfully synthesized via SHS route using induction heating. The heating behaviour shows the compressed pellets could be heated by induction heating to ignite the SHS reaction, although a small temperature difference between edge and centre was detected. The heating process using an induction heating technique produces a high heating rate of up to 150K/s with 2 kW induction heating equipment.

The effects of heating rate on the synthesis of NiAl products were studied. The results show that a fast heating rate leads to smaller grain size and higher micro hardness. On the other hand, the study on the effect of green density shows that the porosity of the compressed product has significant effects on the heating rate and the properties of synthesized products. The experiments have also shown that there is a limit on green density below which combustion reaction using induction heating will not occur. For the Al and Ni system the limit is about 50% of the theoretical density.

NiAl/Al_2O_3 and NiAl/TiC composites could by ignited by induction heating and synthesized using SHS technique, but in both cases, there is a limit on the additions of Al_2O_3 and TiC above which the SHS reaction cannot be ignited and the composites cannot be synthesized. Under this experimental setting the limits for Ni/Al-Al_2O_3 and Ni/Al-Ti/C system are 12% wt% and 15 wt% respectively.

At a lower Al_2O_3 content (≤10wt %), the hardness increases with increasing Al_2O_3 content. At a high Al_2O_3 content, porosity and brittle phase Ni_2Al reduce hardness. The hard phase TiC has a significant effect on the hardness of NiAl. The hardness of the 5wt% Ti/C sample was increased by approximately 50%. For the 15wt% Ti/C sample the hardness increased to 526±15HV which is an increase of 62% compared to the non-Ti/C addition sample.

8.1.2 The temperature recording and combustion monitoring

Temperature monitoring plays an essential role in the synthesis process and provides a useful tool for process control. Two infra-red thermometers combined with a high revolution thermal image camera were used in this study.

For the heating behaviour monitoring the thermal image pictures proved that under this experimental setting the temperature of pellets' outer ring was slightly higher than that of its core. This is due to the electromagnetic field generated by the coil being even, and the coupling of compressed powders with electromagnetic field is rather complicated.

The full temperature profiles showed that there are four stages in the synthesis process, heating, combustion, solidification (plateau) and cooling. Combined with thermodynamic analysis, the temperature profiles implied the existence of a liquid phase in NiAl synthesis. The shortened solidification in $NiAl/Al_2O_3$ is due the "thermal dilution" effect of Al_2O_3. In the NiAl/TiC system, the full temperature profiles can be used to analyze the reaction sequence.

8.1.3 Synthesis mechanism of NiAl and NiAl based composite.

Two crystalline morphologies were detected in the NiAl products, despite XRD analysis showing that there was only one chemical phase, the NiAl, in the products. The facetted crystalline structure indicates a 2D nucleation process, which is normally a sign of super saturation in the liquid phase during combustion.

In NiAl/Al_2O_3 system, the addition of Al_2O_3 at small amounts (less than 10wt %) does not affect the density of the synthesized products. But with higher amounts, the Al_2O_3 will consume more of the heat released by the reaction; consequently causing pores. In particular, due to the high vapour pressure of Al at high temperature, "whisker" structures were found with high concentrations of Al_2O_3.

The microstructure analysis, temperature measurements and comparison with literature suggests the formation of TiC follows a liquid synthesis mechanism. The TiC was formed after the melting of Ti, so that nano structured TiC can be produced. The reaction sequence for the Ni/Al/Ti/C system can be stated as: Ni/Al mixture was heated by induction heating which ignited its combustion; the energy released melted Ti and initialized the combustion reaction of Ti/C leading to the formation of TiC accompanied by the melting of NiAl.

8.2 Recommend future work

The thermodynamic calculations in this study were focused on enthalpy conservation. Based on those results the adiabatic temperature of reaction was computed. However, due to lack of data, calculations for NiAl/TiC may need further work once the relevant data is available.

In Chapter 4, the crystalline orientation of NiAl XRD result is an interesting issue that deserves more attention. By studying this phenomenon more details of the synthesis mechanism can be expected. In this study, limited access to testing facilities restricted further analysis. Also, the facetted crystalline required more work. Further research on the orientation of facetted crystalline NiAl, the height of each layer and the chemical resistance of facetted crystalline NiAl are recommended.

Induction heating with SHS has been successfully applied for both NiAl and NiAl based composite fabrications. By this route the products are dense and the mechanical properties are comparable to those derived from the hot compressed SHS method. Thus there is potential for this route to be applied to coating applications. By selecting proper proportions of reactants and optimizing heating parameters, NiAl and NiAl composite coating of metallic materials is feasible. In the solidification simulation presented in Chapter 7, by simply replacing the substrate data the thermal strain at the interface can be estimated.

Appendix A Simulation codes

Simulation code for induction heating (axial direction air-gap 4mm, sample radius 8mm)

```
/batch

/filnam,induc

/config,nres,100000

/prep7

shpp,off

/title, Induction heating of a 1020 steel

/com,

et,1,13,,,1          ! PLANE13, axisymmetric, AZ dof

et,2,13,,,1

et,3,151,,,1,1,1      ! SURF151, thermal, radiation

r,3,0                 ! Real constant set for SURF151

row=.008              ! outer radius of workpiece

ro=.02                ! outer radius of model

gap=.004              ! distance of gap

t=.003                ! model thickness
```

```
doc=.0032            !distance between coil turns

roc=0.0015           !radius of coil

toa=.02              !thickness of air


freq=300000          ! frequency (Hz.)

pi=4*atan(1)         ! pi

cond=.392e7          ! maximum conductivity

muzero=4e-7*pi       ! free-space permeability

mur=200              ! maximum relative permeability

skind=sqrt(1/(pi*freq*cond*muzero*mur)) ! skin depth


ftime=4          ! final time

tinc=.05             ! time increment for harmonic analysis

time=0               ! initialize time

delt=.01             ! maximum delta time step


!Electromagnetic model

emunit,mks     ! set magnetic units
```

```
mp,murx,1,1              ! air relative permeability

mp,murx,3,1              ! coil relative permeability

mptemp,1,25.5,160,291.5,477.6,635,698      ! temps for relative permeability

mptemp,7,709,720.3,742,761,1000

mpdata,murx,2,1,200,190,182,161,135,104    ! steel relative permeability

mpdata,murx,2,7,84,35,17,1,1

mptemp

mptemp,1,0,125,250,375,500,625         ! temps for resistivity

mptemp,7,750,875,1000

mpdata,rsvx,2,1,.184e-6,.272e-6,.384e-6,.512e-6,.656e-6,.824e-6

mpdata,rsvx,2,7,1.032e-6,1.152e-6,1.2e-6 ! steel resistivity

rectng,0,row,0,t                        ! billet

cyl4,row+roc,t+gap+roc,roc          ! coil 1st turn

cyl4,row+roc,t+gap+roc+doc, roc  !coil 2nd turn

cyl4,row+roc,t+gap+roc+doc+doc,roc  !coil 3rd turn

rectng,0,ro,0,toa                       !outer air

aovlap,all                !glue all area

numcmp,area           !compress numbers of area
```

```
numcmp,line            !compress numbers of lines

numcmp,kp              !compress number of keypoints


ksel,s,loc,y,t         ! select keypoints at outer radius of workpiece

kesize,all,skind/2     ! set meshing size to 1/2 skin depth

ksel,s,loc,y,0         ! select keypoints at center

kesize,all,40*skind    ! set meshing size

lsel,s,,,1             !select lines

lsel,a,,,3

lesize, all,,,10       ! set 10 division through thickness

lsel,s,,,5,20

lesize,all,,,10

lsel,all


ksel,s,loc,y,t         ! select keypoints at outer radius of workpiece

kesize,all,skind/2     ! set meshing size to 1/2 skin depth

ksel,s,loc,y,0         ! select keypoints at center

kesize,all,40*skind    ! set meshing size
```

```
lsel,s,,,1                !select lines

lsel,a,,,3

lesize, all,,,10          ! set 10 division through thickness

lsel,s,,,5,12

lesize,all,,,10

lsel,all



asel,s,area,,1        !select area 1 billet

aatt,2,1,1              !set attributes for billet region materials 2, real 1, element type
1

asel,s,,,2,4        ! select area 2 coil

aatt,3,1,2              ! set attributes for coil materials 3 real1 element type 2

asel,s,area,,5          ! select area 3 air

aatt,1,1,2              ! set attributes for coil materials 1 real 1 element type 2

asel,all              ! select all area

mshape,0,2d           ! set element shape as quadrilateral 2d mode

mshk,2                !short for mshkey, specifies to use mapped meshing but for area
3 since it's irregular shape it's setted as free meshing

amesh,1               !mesh billet area
```

```
lesize,all,10          !specifies the divisions on unmeshed lines

lsel,all

amesh, all             !mesh remaining areas



n                      ! create space node for SURF151

*get,nmax,node,,num,max

lsel,s,,,2,3     ! select the top of billet

type,3

real,3

mat,2

lmesh,all          ! mesh billet outer radius with SURF151

*get,emax,elem,,num,max

esel,s,,,emax-18,emax          !select the surface elements for radiation

emodif,all,3,nmax          ! modify element to add space node for radiation

et,3,0                     ! reset type 3 to null element

nsel,s,loc,x

d,all,az,0                 ! apply flux-normal b.c.

nsel,all
```

```
esel,s,mat,,3                !select the coil by material's type

bfe,all,js,,,,56.6e6          ! apply current density to coil

esel,all

finish



/solu

antyp,harm

harfrq,300000

physics,write,emag      ! write emag physics file

finish



/prep7

lsclear,all           ! clear all b.c.'s and options

et,1,55,,,1           ! PLANE55 thermal element, axisymmetric

et,2,0               ! null element type for coil and air region

et,3,151,,,1,1,1       ! SURF151 element for radiation

keyopt,3,9,1
```

```
r,3,1,5.67e-8          ! form factor, Stefan-Boltzmann constant
mptemp
mptemp,1,0,730,930,1000        ! temps for conductivity
mpdata,kxx,2,1,60.64,29.5,28,28
mptemp                         ! temps for enthalpy
mptemp,1,0,27,127,327,527,727
mptemp,7,765,765.001,927
mpdata,enth,2,1,0,91609056,453285756,1.2748e9,2.2519e9,3.3396e9
mpdata,enth,2,7,3.548547e9,3.548556e9,4.3520e9
mp,emis,2,.75                  ! emissivity
finish
/solu
antype,trans
toffst,273
tunif,100                      ! initial uniform temperature
d,nmax,temp,25                 ! ambient temperature
cnvtol,heat,1e-6               ! convergence tolerance
kbc,1                          ! step loads
```

```
 trnopt,full
 autos,on                    ! auto time-stepping
 deltim,1e-5,1e-6,delt,on    ! time step control
 outres,basic,all            ! save all load step information
 physics,write,thermal       ! write thermal physics file
 finish
 *do,i,1,ftime/tinc  ! solution *do loop
 time=time+tinc                          ! increment time
 physics,read,emag   ! read emag physics file
 /solu
 *if,i,eq,1,then
  tunif,100              ! initial temperature
 *else
  ldread,temp,last,,,,,rth   ! read thermal analysis temperatures
 *endif
 solve                  ! solve harmonic analysis
 finish
 physics,read,thermal       ! read thermal physics file
```

```
/assign,esav,therm,esav       ! redirect files for use in thermal restart
/assign,emat,therm,emat
/solu
parsav,scalar,parameter,sav   !save parameters before multiframe restart
*if,i,gt,1,then
 antype,trans,rest            ! thermal restart
*endif
parres,new,parameter,sav      !restore parameters after multiframe restart
time,time                     ! time at end of thermal run
esel,s,mat,,2                 ! select billet region
ldread,hgen,,,,2,,rmg         ! apply coupled joule heating load from emag
esel,all
solve
finish
/assign,esav                  ! reassign files to default
/assign,emat
*enddo                        ! end of solution looping
finish
```

```
save

/post26

/axlab,x,Time(sec)

/axlab,y,Temperature(C)

nsol,2,1,temp,,temp-1

nsol,3,2,temp,,temp-2

nsol,4,12,temp,,temp-12

nsol,5,21,temp,,temp-21

nsol,6,7,temp,,temp-7

nsol,7,26,temp,,temp-26

nsol,8,71,temp,,temp-71
```

Simulation code for solidification with preheating

```
/batch

/config,nres,10000

/filnam,Phase transition

/prep7

et,1,55,,,1          !type plane 55 for NiAl and substrate

et,2,55,,,1          !Type plane 55 for Air
```

```
mp,dens,1,5830          !NiAl density

mp,dens,2,3850          !Substrate density

mp,dens,3,1.205         !Air density at 20 ℃

mp,c,1,617.13           !NiAl heat capacity

mp,c,2,680              !Substrate capacity

mp,c,3,1.005            !Air capacity at 20 ℃

mp,kxx,3,0.0257         !Air conductivity

mp,kxx,2,0.1            !Substrate conductivity


mptemp,1,25,1636,1638                                   !temp setting for materials
properties

mpdata,enth,1,1,0,6.25853e9,1.0487e10           !enthalpy of NiAl

mpdata,kxx,1,1,118,118,118              !heat conductivity coefficient of NiAl

mp,emis,1,.68                           ! emissivity


mpdata,kxx,2,1,.5,.2,.2                         !heat conductivity coefficient of
substrate
```

```
ton=0.0014                          !thickness of nial

tos=0.05                            !thickness of substrate

ron=0.008                           !radius of NiAl

ros=0.05                            !radius of substrate

toe=0.1                             !environment size

divs=10                             !division of NiAl surface


emunit,mks                          !set units

rectng,0,ros,0,tos                  !substrate

rectng,0,ron,tos,tos+ton            !NiAl

rectng,0,toe,0,toe                  !environment

aovlap,all                          !glue all area

numcmp,area                         !compress numbers of area

numcmp,line                         !compress numbers of lines

numcmp,kp                           !compress number of keypoints


esize,0.005                         !element size
```

```
asel,s,area,,1                    !select area 1 NiAl

aatt,1,1,1                        !set attributes for NiAl region materials 1,
real, element type1

asel,s,area,,2                    !select area 2 substrate

aatt,2,1,1                        !set attributes for substrate materials
2,real1,element 1

asel,s,area,,3                    !select area 3 air

aatt,3,1,2                        !set attributes for Air region materials 3,
real1, element 2

asel,all                          !select all area

ksel,s,,,4,7                      !select the keypoints for NiAl

kesize,all,ron/divs               !set element size

ksel,all                          !select all keypoints

mshape,0,2d                       !set element shape as quadrilateral 2d mode

mshk2,                            !short for mshkey, specifies to use mapped
meshing but for area 3 since it's irregular shape it's setted as free meshing

amesh,all

allsel
```

```
/solu

antype,trans

toffst,273

timint,on                    !transient effect

cnvtol,heat,1e-3             ! convergence tolerance

kbc,1                        ! step loads

trnopt,full

autos,on                     ! auto time-stepping

deltim,1e-3,1e-4,1e-3,on     ! time step control

outres,basic,all             ! save all load step information

time,8



asel,s,,,2,

nsla,s,1

ic,all,temp,20

allsel
```

```
asel,s,,,3

nsla,s,1

ic,all,temp,25

allsel



asel,s,,,1

nsla,s,1

ic,all,temp,1638

allsel

stef,5.67e-8

v2dopt,1                    !define geometry axisymmetric

spctemp,,25

lsel,s,,,3

lsel,s,,,2

radiat

solve

/post26
```

```
nsol,2,1,temp,,temp-1

nsol,3,2,temp,,temp-2

nsol,4,15,temp,,temp-15

nsol,5,12,temp,,temp-12

nsol,6,7,temp,,temp-7

nsol,7,20,temp,,temp-20

nsol,8,33,temp,,temp-33

/axlab,x,Time(s)

/axlab,y,Temperature(C)
```

Appendix B Element used in induction heating simulation

Element description (From ANSYS 12.0 help file)

PLANE13

2-D Coupled-Field Solid

PLANE13 Element Description

PLANE13 has a 2-D magnetic, thermal, electrical, piezoelectric, and structural field capability with limited coupling between the fields. PLANE13 is defined by four nodes with up to four ℃s of freedom per node. The element has nonlinear magnetic capability for modeling B-H curves or permanent magnet demagnetization curves. PLANE13 has large deflection and stress stiffening capabilities. When used in purely structural analyses, PLANE13 also has large strain capabilities.

SURF151

2-D Thermal Surface Effect

SURF151 may be used for various load and surface effect applications. It may be overlaid onto a face of any 2-D thermal solid element (except axisymmetric harmonic elements PLANE75 and PLANE78). The element is applicable to 2-D thermal analyses. Various loads and surface effects may exist simultaneously.

The element is defined by two to four node points and the material properties. An extra node (away from the base element) may be used for convection or radiation effects. Convections or heat fluxes may be input as surface loads on the element.

Appendix C Animation of simulation for induction and solidification

The animation of simulation results are given in a CD

- Animation of induction heating steel bar with various thicknesses
- Animation of induction heating steel bar with various heights
- Animation of NiAl solidification
- Animation of NiAl/Al_2O_3(10%wt) solidification

Appendix D (Data source: ANSYS 12.0 help file)

PLANE55

2-D Thermal Solid

PLANE55 can be used as a plane element or as an axisymmetric ring element with a 2-D thermal conduction capability. The element has four nodes with a single degree of freedom, temperature, at each node.

The element is applicable to a 2-D, steady-state or transient thermal analysis. The element can also compensate for mass transport heat flow from a constant velocity field. If the model containing the temperature element is also to be analyzed structurally, the element should be replaced by an equivalent structural element (such as PLANE42). A similar element with midside node capability is PLANE77. A similar axisymmetric element which accepts nonaxisymmetric loading is PLANE75.

An option exists that allows the element to model nonlinear steady-state fluid flow through a porous medium. With this option the thermal parameters are interpreted as analogous fluid flow parameters

Using the Radiosity Solver Method

Offered in the ANSYS Multiphysics, ANSYS Mechanical, and ANSYS Professional programs only, this method also works for generalized radiation problems involving

two or more surfaces receiving and emitting radiation. The method is supported by all 3-D/2-D elements having a temperature degree of freedom.

Elements supported for the radiosity method include:

FLOTRAN.

FLUID141

FLUID142

ANSYS 2-D.

PLANE13

PLANE35

PLANE55

PLANE67

PLANE77

The following radiosity topics are available:

Procedure

Further Options for Static Analysis

Procedure

The Radiosity Solver method consists of five steps:

Define the radiating surfaces.

Define Solution options.

Define View Factor options.

Calculate and query view factors.

Define load options.

Defining the Radiating Surfaces

You define the radiating surfaces by performing the following tasks:

Build the thermal model in the preprocessor (PREP7). Radiating surfaces support symmetry conditions in some cases; see Advanced Radiosity Options for information on modeling symmetry for radiating surfaces. Symmetry conditions are not supported for FLOTRAN analyses using the radiosity method. For the Radiosity Solution Method radiating surfaces are faces of a 3-D model or sides of a 2-D model. In the Radiosity Solver Method, you can have up to ten enclosures, with surfaces radiating to each other.

Flag the radiation surfaces for a given emissivity and enclosure number using the **SF**, **SFA**, **SFE**, or **SFL** command. For all surface or line facets radiating to each other, issue the same enclosure number.

To specify temperature dependent emissivity, issue the **SF**, **SFA**, **SFE**, or **SFL** command with VALUE = -N. Emissivity values are from the EMIS property table for material N [**MP**]. Negative value of enclosure number is required for FLUID141 and FLUID142 elements to model radiation occurring between surfaces inside the fluid

domain. Positive value of enclosure number corresponds to radiation between surfaces in the solid domain.

Since radiation can pass through a fluid region and impact on a solid, you can apply the surface-to-surface radiation load on a fluid/solid interface, as well as on external model boundaries. In this case, you should apply the RDSF load to either the fluid or solid element faces, or the solid entity defining the interface. If you apply the load to more than one face, FLOTRAN applies the boundary conditions on only one face and issues a message that it skipped duplicate boundary conditions.

Verify the flagged radiation surfaces for properly specified emissivity, enclosure number and direction of radiation:

Command(s): /PSF

GUI: Utility Menu> PlotCtrls> Symbols

To apply radiation surface loads on the SHELL57 or SHELL157 elements, you must specify the face number with the exterior or interior orientation to properly flag it. You can use the **SF**, **SFA**, or **SFE** commands to apply these loads. The **SF** and **SFA** commands apply the radiation surface loads only on face 1 of the shell element. To apply radiation surface loads on face 2 or on both faces of the shell elements, use the **SFE** command. See SHELL57 and SHELL157 in the Elements Reference for information on face orientation and numbering.

Defining Solution Options

For radiation problems, you must also define the Stefan-Boltzmann constant in the appropriate units:

Command(s): STEF

GUI: **Main Menu> Preprocessor> Radiation Opts> Solution Opt**

Main Menu> Radiation Opt> Radiosity Meth> Solution Opt

Main Menu> Solution> Radiation Opts> Solution Opt

If you define your model data in terms of degrees Fahrenheit or degrees Celsius, you must specify a temperature offset:

Command(s): TOFFST

GUI: **Main Menu> Preprocessor> Radiation Opts> Solution Opt**

Main Menu> Radiation Opt> Radiosity Meth> Solution Opt

Main Menu> Solution> Radiation Opts> Solution Opt

Next, select the Radiosity Solver and choose a direct solver or an iterative solver (default). You can also specify a relaxation factor and convergence tolerance for the heat flux:

Command(s): RADOPT

GUI: **Main Menu> Preprocessor> Radiation Opts> Solution Opt**

Main Menu> Radiation Opt> Radiosity Meth> Solution Opt

Main Menu> Solution> Radiation Opts> Solution Opt

If you are analyzing an open enclosure problem, you must specify the ambient temperature or the ambient node for each enclosure.

Specify the space temperature for the ambient radiation:

Command(s): SPCTEMP

GUI: **Main Menu> Preprocessor> Radiation Opts> Solution Opt**

Main Menu> Radiation Opt> Radiosity Meth> Solution Opt

Main Menu> Solution> Radiation Opts> Solution Opt

The **SPCTEMP** command specifies a space temperature for each enclosure. You can also list or delete all specified space temperatures using this command.

To specify a space node for each enclosure, use one of the following:

Command(s): SPCNOD

GUI: **Main Menu> Preprocessor> Radiation Opts> Solution Opt**

Main Menu> Radiation Opt> Radiosity Meth> Solution Opt

Main Menu> Solution> Radiation Opts> Solution Opt

If the ambient is another body in the model, you must specify the space node for the ambient radiation using the **SPCNOD** command for each enclosure. The **SPCNOD** command specifies a space node for each enclosure. The Radiosity Solver retrieves the nodal temperature for the specified node as the ambient temperature. You can also list or delete all specified space nodes using this command.

Note

In FLOTRAN in an axisymmetric radiosity analysis, you need to specify a space node even if the enclosure is closed.

To specify debug level for radiosity convergence output for FLOTRAN, use one of the following.

Command(s): FLDATA5, OUTP, DRAD

GUI: **Main Menu> Preprocessor> FLOTRAN Set Up> Additional Out> Print Controls**

The debug level defaults to 0 (none). A level of 1 (standard) provides final convergence information. A level of 2 (full) provides complete information for each global iteration.

Defining View Factor Options

To calculate new view factors for either 3-D or 2-D geometry, you can specify various options:

Command(s): HEMIOPT

GUI: **Main Menu> Preprocessor> Radiation Opts> View Factor**
Main Menu> Radiation Opt> Radiosity Meth> View Factor
Main Menu> Solution> Radiation Opts> View Factor

HEMIOPT allows you to set the resolution for 3-D view factor calculation using the Hemicube method. The default resolution is 10. Increasing the value increases the accuracy of the view factor calculation.

Command(s): V2DOPT

GUI: **Main Menu> Preprocessor> Radiation Opts> View Factor**
Main Menu> Radiation Opt> Radiosity Meth> View Factor

Main Menu> Solution> Radiation Opts> View Factor

V2DOPT allows you to select options for 2-D view factor calculation. The geometry type can be set to either 2-D plane or axisymmetric (defaults to plane). You can also define the number of divisions (defaults to 20) for an axisymmetric geometry.

ANSYS uses different algorithms to calculate the form factors for 2-D and 3-D models respectively. It assumes a 3-D model by default. The 2-D models may be either planar (NDIV value = 0), or axisymmetric (NDIV value > 0), with planar as the default. Axisymmetric models are expanded internally to a 3-D model, with NDIV representing the number of axisymmetric sections. For example, setting NDIV to 10 indicates ten sections, each spanning 36 °Cs. This expansion is done only for view factor calculation, and not for the thermal solution.

The **V2DOPT** command also allows you to select hidden or non-hidden viewing option (defaults to hidden).

The non-hidden method calculates the form factors from every element to every other element regardless of any blocking elements.

The hidden method (default) first uses a hidden-line algorithm to determine which elements are "visible" to every other element. (A "target" element is visible to a "viewing" element if their normals point toward each other and there are no blocking elements.) Then, form factors are calculated as follows:

Each radiating or "viewing" element is enclosed with a unit hemisphere (or a semicircle in 2-D).

All target or "receiving" elements are projected onto the hemisphere or semicircle.

To calculate the form factor, a predetermined number of rays are projected from the viewing element to the hemisphere or semicircle. Thus, the form factor is the ratio of the number of rays incident on the projected surface to the number of rays emitted by the viewing element. In general, accuracy of the form factors increases with the number of rays. You can increase the number of rays via the NZONE field on the **V2DOPT** command.

For more information, see the discussion on hidden and non-hidden options and axisymmetric geometry in Using the AUX12 Radiation Matrix Method earlier in this chapter andRadiation Matrix Method in the Theory Reference for ANSYS and ANSYS Workbench

You can specify whether new view factors should be computed or if existing values should be used:

Command(s): VFOPT

GUI: **Main Menu> Preprocessor> Radiation Opts> View Factor**
Main Menu> Radiation Opt> Radiosity Meth> View Factor
Main Menu> Solution> Radiation Opts> View Factor

VFOPT, Opt allows you to compute view factors and write them to a file (Opt = NEW). If view factors already exist in the database, this command also allows you to deactivate the view factor computation (Opt = OFF). OFF is the default upon encountering the second and subsequent **SOLVE** commands in **/SOLU**. After the first SOLVE command, ANSYS uses view factors existing in the database, unless they are overwritten by the **VFOPT** command.

VFOPT allows you to output view factors in ASCII or binary file format. Binary is the default.

Calculating and Querying View Factors

Next, you calculate the view factors. You can also query the view factor database and calculate an average view factor.

Compute and store the view factors:

Command(s): VFCALC

GUI: Main Menu> Radiation Opt> Radiosity Meth> Compute

List the calculated view factors for the selected source and target elements by querying the view factor database and calculate the average view factor:

Command(s): VFQUERY

GUI: Main Menu> Radiation Opt> Radiosity Meth> Query

You can retrieve the calculated average view factor using ***GET**,`Par`,RAD,,VFAVG. For FLOTRAN, you can retrieve the net heat rate lost by an enclosure using ***GET**,`Par`,RAD,n,NETHF.

Defining Load Options

Next, you specify an initial temperature if your model starts at a uniform temperature. You then specify the number or size of the time steps and specify a ramped boundary condition.

To assign a uniform temperature to all nodes, use one of the following:

Command(s): **TUNIF**

GUI: **Main Menu> Solution> Define Loads> Settings> Uniform Temp**

Solution accuracy is governed by the time step size you use and the convergence criterion you chose. When using auto-time stepping, review the transient results carefully. The radiosity method works best when there are other forms of heat transfer besides radiation determining the temperature of a body.

Set the number or size of time steps, using one of the following:

Command(s): **NSUBST** or **DELTIM**

GUI: **Main Menu> Preprocessor> Loads> Load Step Opts> Time/Frequenc> Freq and Substps or Time and Substps**

Main Menu> Preprocessor> Loads> Load Step Opts> Time/Frequenc> Time-Time Step

Due to the highly nonlinear nature of radiation, you should specify ramped boundary conditions:

Command(s): **KBC**

GUI: **Main Menu> Preprocessor> Loads> Load Step Opts> Time/Frequenc> Time-Time Step**

Reference

[1] Du XH, Guo JT, Zhou BD. Superplasticity of stoichiometric NiAl with large grains. Scripta Materialia (2001);45:69-74.

[2] Guo JT, Chen RS, Li GS. Superplasticity and cavity stringers in a multiphase NiAl-based intermetallic alloy. Journal of Materials Processing Technology (2003);139:337-340.

[3] Lin D, Hu J, Jiang D. Superplasticity of Ni-rich single phase NiAl intermetallics with large grains. Intermetallics(2005) ;13:343-349.

[4] Zhang G-y, Zhang H, Zhang H-a, Wu X-m, Guo J-t. Superplasticity of Directionally Solidified NiAl-15Cr Alloy at High Temperature. Journal of Iron and Steel Research, International (2006);13:44-48.

[5] Albiter A, Salazar M, Bedolla E, Drew RAL, Perez R. Improvement of the mechanical properties in a nanocrystalline NiAl intermetallic alloy with Fe, Ga and Mo additions. Materials Science and Engineering A (2003);347:154-164.

[6] Enayati MH, Karimzadeh F, Anvari SZ. Synthesis of nanocrystalline NiAl by mechanical alloying. Journal of Materials Processing Technology (2008);200:312-315.

[7] Joardar J, Pabi SK, Murty BS. Milling criteria for the synthesis of nanocrystalline NiAl by mechanical alloying. Journal of Alloys and Compounds (2007);429:204-210.

[8] Yazdanmehr M, Anijdan SHM, Samadi A, Bahrami A. Mechanical behavior modeling of nanocrystalline NiAl compound by a feed-forward back-propagation multi-layer perceptron ANN. Computational Materials Science (2009);44:1231-1235.

[9] Zhou LZ, Guo JT, Li GS, Xiong LY, Wang SH, Li CG. Investigation of annealing behavior of nanocrystalline NiAl. Materials and Design (1997);18:373-377.

[10] Kaya M, Orhan N, Tosun G. The effect of the combustion channels on the compressive strength of porous NiTi shape memory alloy fabricated by SHS as implant material. Current Opinion in Solid State and Materials Science (2010);14:21-25.

[11] Li B-Y, Rong L-J, Li Y-Y, Gjunter VE. Electric resistance phenomena in porous Ni-Ti shape-memory alloys produced by SHS. Scripta Materialia (2001);44:823-827.

[12] Kaya M, Orhan N, Kurt B, Khan TI. The effect of solution treatment under loading on the microstructure and phase transformation behavior of porous NiTi shape memory alloy fabricated by SHS. Journal of Alloys and Compounds (2009);475:378-382.

[13] Wisutmethangoon S, Denmud N, Sikong L. Characteristics and compressive properties of porous NiTi alloy synthesized by SHS technique. Materials Science and Engineering: A (2009);515:93-97.

[14] Ferretti M, Ciccarelli C, Magnone E, Rubino S, Parodi N, Martinelli A. Application of the SHS technique in the synthesis of the perovskite-type MgxCyNi$_3$ compound. Materials Research Bulletin (2004);39:647-654.

[15] Kodera Y, Yamasaki N, Yamamoto T, Kawasaki T, Ohyanagi M, Munir ZA. Hydrogen storage Mg_2Ni alloy produced by induction field activated combustion synthesis. Journal of Alloys and Compounds (2007);446-447:138-141.

[16] Chen X-J, Xia T-D, Liu X-L, Liu T-Z, Zhao W-J. Mechanism of combustion synthesis of Mg_2Ni. Journal of Alloys and Compounds (2006);426:123-130.

[17] Saita I, Li L, Saito K, Akiyama T. Hydriding combustion synthesis of Mg_2NiH_4. Journal of Alloys and Compounds (2003);356-357:490-493.

[18] Li L, Akiyama T, Yagi J-i. Hydrogen storage alloy of Mg_2NiH_4 hydride produced by hydriding combustion synthesis from powder of mixture metal. Journal of Alloys and Compounds (2000);308:98-103.

[19] John J.Moore HJF. Combustion synthesis of advanced materials Part 1. Progress in Materials Science (1995);39:243-273.

[20] John J.Moore HJ. Combustion synthesis of advanced materials, Part 2. Progress in Materials Science (1995);39:275-316.

[21] Bosc-Rouessac F, Marin-Ayral RM, Haidoux A, Massoni N, Bart F. Combustion synthesis of ceramic matrices for immobilization of 14C. Journal of Alloys and Compounds (2008);466:551-557.

[22] Ge Z, Chen K, Guo J, Zhou H, Ferreira JMF. Combustion synthesis of ternary carbide Ti_3AlC_2 in Ti-Al-C system. Journal of the European Ceramic Society (2003);23:567-574.

[23] Guojian J, Jiayue X, Hanrui Z, Wenlan L. Combustion of Na2B4O7 + Mg + C to synthesis B_4C powders. Journal of Nuclear Materials (2009);393:487-491.

[24] Kata D, Lis J, Pampuch R. Combustion synthesis of multiphase powders in the Si---C---N system. Solid State Ionics (1997);101-103:65-70.

[25] Khoptiar Y, Gotman I. Ti2AlC ternary carbide synthesized by thermal explosion. Materials Letters (2002);57:72-76.

[26] Kunrath AO, Reimanis IE, Moore JJ. Combustion synthesis of TiC-Cr_3C_2 composites. Journal of Alloys and Compounds (2001);329:131-135.

[27] Mas-Guindal MJ, Contreras L, Turrillas X, Vaughan GBM, Kvick Å, Rodríguez MA. Self-propagating high-temperature synthesis of TiC-WC composite materials. Journal of Alloys and Compounds (2006);419:227-233.

[28] Nersisyan HH, Hou YB, Won CW. Synthesis of [alpha]-SiC(6H) using 6H polytype SiC diluent by the seeding technique. Powder Technology (2009);189:48-51.

[29] Nersisyan HH, Won HI, Won CW. Combustion synthesis of WC powder in the presence of alkali salts. Materials Letters (2005);59:3950-3954.

[30] Pampuch R, Lis J, Stobierski L, Tymkiewicz M. Solid combustion synthesis of Ti_3SiC_2. Journal of the European Ceramic Society (1989);5:283-287.

[31] Tsuchida T, Kan T. Synthesis of Al3BC in air from mechanically activated Al/B/C powder mixtures. Journal of the European Ceramic Society (1999);19:1795-1799.

[32] Yang S, Sun ZM, Hashimoto H, Abe T. Synthesis of single-phase Ti_3SiC_2 powder. Journal of the European Ceramic Society (2003);23:3147-3152.

[33] Yeh CL, Chen YD. Synthesis of niobium carbonitride by self-propagating combustion of Nb-C system in nitrogen. Ceramics International (2005);31:1031-1039.

[34] Yeh CL, Liu EW. Combustion synthesis of tantalum carbides TaC and Ta_2C. Journal of Alloys and Compounds (2006);415:66-72.

[35] Yeh CL, Shen YG. Effects of using Al_4C_3 as a reactant on formation of Ti_3AlC_2 by combustion synthesis in SHS mode. Journal of Alloys and Compounds (2009);473:408-413.

[36] Yeh CL, Shen YG. Effects of TiC and Al_4C_3 addition on combustion synthesis of Ti_2AlC. Journal of Alloys and Compounds (2009);470:424-428.

[37] Huang X, Zhong J, Dou L, Wang K. Combustion synthesis of CaB_6 powder from calcium hexaborate and Mg. International Journal of Refractory Metals and Hard Materials;In Press, Corrected Proof.

[38] Kudaka K, Iizumi K, Sasaki T, Okada S. Mechanochemical synthesis of MoB_2 and Mo_2B_5. Journal of Alloys and Compounds (2001);315:104-107.

[39] Radev DD, Marinov M, Tumbalev V, Radev I, Konstantinov L. Mechanically activated self-propagated high-temperature synthesis of nanometer-structured MgB_2. Physica C: Superconductivity (2005);418:53-58.

[40] Shibuya M, Ohyanagi M. Effect of nickel boride additive on simultaneous densification and phase decomposition of TiB_2-WB_2 solid solutions by pressureless sintering using induction heating. Journal of the European Ceramic Society (2007);27:301-306.

[41] Yeh CL, Chen WH. Preparation of niobium borides NbB and NbB2 by self-propagating combustion synthesis. Journal of Alloys and Compounds (2006);420:111-116.

[42] Yeh CL, Chen WH. A comparative study on combustion synthesis of Nb-B compounds. Journal of Alloys and Compounds (2006);422:78-85.

[43] Zlotnikov I, Gotman I, Gutmanas EY. Processing of dense bulk MgB_2 superconductor via pressure-assisted thermal explosion mode of SHS. Journal of the European Ceramic Society (2005);25:3517-3522.

[44] Jokisaari JR, Bhaduri S, Bhaduri SB. Processing of single phase Mo_5Si_3 by microwave activated combustion synthesis. Materials Science and Engineering A (2002);323:478-483.

[45] Jokisaari JR, Bhaduri S, Bhaduri SB. Microwave activated combustion synthesis of bulk cobalt silicides. Journal of Alloys and Compounds (2005);394:160-167.

[46] Li L, Akiyama T, Yagi J-i. Activation behaviors of Mg_2NiH_4 at different hydrogen pressures in hydriding combustion synthesis. International Journal of Hydrogen Energy (2001);26:1035-1040.

[47] Manukyan KV, Kharatyan SL, Blugan G, Kuebler J. Combustion synthesis and compaction of Si3N4-TiN composite powder. Ceramics International (2007);33:379-383.

[48] Nartowski AM, Parkin IP. Solid state metathesis synthesis of metal silicides; reactions of calcium and magnesium silicide with metal oxides. Polyhedron (2002);21:187-191.

[49] Park H-K, Park J-H, Yoon J-K, Ko I-Y, Doh J-M, Shon I-J. Simultaneous synthesis and consolidation of nanostructured $TaSi_2$-Si_3N4 composite by pulsed current activated combustion. Ceramics International (2009);35:99-104.

[50] Riley DP, Oliver CP, Kisi EH. In-situ neutron diffraction of titanium silicide, Ti_5Si_3, during self-propagating high-temperature synthesis (SHS). Intermetallics (2006);14:33-38.

[51] Shon IJ, Kim HC, Rho DH, Munir ZA. Simultaneous synthesis and densification of Ti_5Si_3 and Ti_5Si_3-20 vol% ZrO_2 composites by field-activated and pressure-assisted combustion. Materials Science and Engineering: A (1999);269:129-135.

[52] Shon I-J, Park J-H, Yoon J-K, Park H-K. Consolidation of nanostructured ZrSi2-Si3N4 synthesized from mechanically activated (4ZrN + 11Si) powders by high frequency induction heated combustion synthesis. Materials Research Bulletin (2009);44:1462-1467.

[53] Yeh CL, Chen CY. Combustion synthesis of TiN-Ti silicide and TiN-Si_3N_4 composites from Ti-Si_3N4 powder compacts in Ar and N2. Journal of Alloys and Compounds;In Press, Corrected Proof.

[54] Yeh CL, Chen WH. An experimental investigation on combustion synthesis of transition metal silicides V_5Si_3, Nb_5Si_3, and Ta_5Si_3. Journal of Alloys and Compounds (2007);439:59-66.

[55] Yeh CL, Wang HJ. A comparative study on combustion synthesis of Ta-Si compounds. Intermetallics (2007);15:1277-1284.

[56] Anselmi-Tamburini U, Spinolo G, Flor G, Munir ZA. Combustion synthesis of Zr---Al intermetallic compounds. Journal of Alloys and Compounds (1997);247:190-194.

[57] Bertolino N, Anselmi-Tamburini U, Maglia F, Spinolo G, Munir ZA. Combustion synthesis of Zr-Si intermetallic compounds. Journal of Alloys and Compounds (1999);288:238-248.

[58] Cao WB, Kirihara S, Miyamoto Y, Matsuura K, Kudoh M. Development of freeform fabrication method for Ti-Al-Ni intermetallics. Intermetallics (2002);10:879-885.

[59] Gao H, He Y, Shen P, Zou J, Xu N, Jiang Y, Huang B, Liu CT. Porous FeAl intermetallics fabricated by elemental powder reactive synthesis. Intermetallics (2009);17:1041-1046.

[60] Li L, Akiyama T, Yagi J-i. Reaction mechanism of hydriding combustion synthesis of Mg2NiH4. Intermetallics (1999);7:671-677.

[61] Maglia F, Milanese C, Anselmi-Tamburini U, Doppiu S, Cocco G, Munir ZA. Combustion synthesis of mechanically activated powders in the Ta-Si system. Journal of Alloys and Compounds (2004);385:269-275.

[62] Milanese C, Maglia F, Tacca A, Anselmi-Tamburini U, Zanotti C, Giuliani P. Ignition and reaction mechanism of Co-Al and Nb-Al intermetallic compounds prepared by combustion synthesis. Journal of Alloys and Compounds (2006);421:156-162.

[63] Murali S, Sritharan T, Hing P. Self-propagating high temperature synthesis of AlFeSi intermetallic compound. Intermetallics (2003);11:279-281.

[64] Sritharan T, Murali S, Hing P. Synthesis of aluminium-iron-silicon intermetallics by reaction of elemental powders. Materials Science and Engineering A (2000);286:209-217.

[65] Yeh CL, Shen YG. Formation of TiAl-Ti_2AlC in situ composites by combustion synthesis. Intermetallics (2009);17:169-173.

[66] Zanotti C, Giuliani P, Terrosu A, Gennari S, Maglia F. Porous Ni-Ti ignition and combustion synthesis. Intermetallics (2007);15:404-412.

[67] Sheng Y. Combustion Synthesis (In Chinese). Beijing: Metallurgical Industry Press, 1999.

[68] Cecilia Bartuli RWS, Emil Shtessel. SHS Powders for Thermal Spray Applications,. Ceramics International 23:61-63.

[69] Xuejun Zhang YZ, Jiecai Han. Low-pressure injection molding and SHS-HIP without envelope of AlN–TiB_2 ceramic slender tube with blind hole. Materials and Design (2005);26:413.

[70] Bautista CS, Ferriere A, Rodriguez GP, Lopez-Almodovar M, Barba A, Sierra C, Vazquez AJ. NiAl intermetallic coatings elaborated by a solar assisted SHS process. Intermetallics (2006);14:1270-1275.

[71] De Jouvancourt H, Record MC, Marin-Ayral RM. Effects of platinum concentration on combustion synthesis of NiAl: application in repairing Ni based superalloys. Materials Science and Technology (2007);23:593-599.

[72] Hu W, Li M, Fukumoto M. Preparation and properties of HVOF NiAl nanostructured coatings. Materials Science and Engineering: A (2008);478:1-8.

[73] Li Y, Liu Y, Geng H, Nie D. Synthesis and cladding of Ni_3Al intermetallic on steel substrate by laser controlled reactive synthesis. Journal of Materials Processing Technology (2006);171:405-410.

[74] Man HC, Yang YQ, Lee WB. Laser induced reaction synthesis of TiC+WC reinforced metal matrix composites coatings on Al 6061. Surface and Coatings Technology (2004);185:74-80.

[75] Matsuura K, Kudoh M, Kirihara S, Miyamoto Y. Use of SHS reaction between powder and droplets for coating, welding and freeform fabrication of intermetallics. Thermec'2003, Pts 1-5 (2003);426-4:4271-4276.

[76] Peiqing La MB, Qunji Xue, Weimin Liu. A study of Ni3Al coating on carbon steel surface via the SHS casting route. Surface and Coating Techonology 133:44-51.

[77] Peiqing La QX, Weimin Liu,. A study of $MoSi_2$-MoS_2 coatings fabricated by SHS casting route. Materials Science and Engineering A 277 (2000) 266-273.

[78] S.Q. Wang XXL, K.M. Chen, H.J. Jin. TiC/Ni_3Al coating on steel via combustion synthesis during casting. Materials Letters 2006.

[79] Sierra C, Vazquez A. NiAl coatings on carbon steel by self-propagating high-temperature synthesis assisted with concentrated solar energy: mass influence on adherence and porosity. Solar Energy Materials and Solar Cells (2005);86:33-42.

[80] Sierra C, Vazquez AJ. NiAl coating on carbon steel with an intermediate Ni gradient layer. Surface & Coatings Technology (2006);200:4383-4388.

[81] Zhong D, Moore JJ, Disam J, Thiel S, Dahan I. Deposition of NiAl thin films from NiAl compound target fabricated via combustion synthesis. Surface and Coatings Technology (1999);120-121:22-27.

[82] Matsuura K, Jinmon H, Hirashima Y, Khan TI, Kudoh M. Reactive casting of Ni-Al-Fe ternary intermetallic alloys. Isij International (2000);40:161-166.

[83] Ruizhu Z. Self-propagation High-temperature synthesis for Radiocative Waste Immobilization. School of Materials Science and Engineering, vol. Doctor. Beijing University of Science and Technology Beijing, 2005. p.117.

[84] Peiqing La MB, Qunji Xue, Weimin Liu. A study of Ni_3Al coating on carbon steel surface via the SHS casting route. Surface and Coating Techonology (2007):133.

[85] Peiqing La QX, Weimin Liu. A study of $MoSi_2$-MoS_2 coatings fabricated by SHS casting route. Materials Science and Engineering A 277 (2000):266-273.

[86] C. Sa´nchez Bautista AF, G.P. Rodrı´guez , M. Lo´pez-Almodovar , A. Barba , C. Sierra , A.J. Va´zquez,. NiAl intermetallic coatings elaborated by a solar assisted SHS process. intermetallic (2006):1370-1375.

[87] S.Q. Wang XXL, K.M. Chen, H.J. Jin. TiC/Ni_3Al coating on steel via combustion synthesis during casting. Materials Letters (2006).

[88] Mossino P. Some aspects in self-propagating high-temperature synthesis. Ceramics International (2004);30:313–332.

[89] Merzhanov AG. History and recent developments in SHS. Ceramics International (2006);21:371-3713.

[90] Dong SS, Hou P, Cheng HY, Yang HB, Zou GT. Fabrication of intermetallic NiAl by self-propagating high-temperature synthesis reaction using aluminium nanopowder under high pressure. Journal of Physics-Condensed Matter (2002);14:11023-11030.

[91] Hunt EM, Plantier KB, Pantoya ML. Nano-scale reactants in the self-propagating high-temperature synthesis of nickel aluminide. Acta Materialia (2004);52:3183-3191.

[92] Fan Q, Chai H, Jin Z. Dissolution-precipitation mechanism of self-propagating high-temperature synthesis of mononickel aluminide. Intermetallics (2001);9:609-619.

[93] Biswas A, Roy SK, Gurumurthy KR, Prabhu N, Banerjee S. A study of self-propagating high-temperature synthesis of NiAl in thermal explosion mode. Acta Materialia (2002);50:757-773.

[94] Ozdemir O, Zeytin S, Bindal C. A study on NiAl produced by pressure-assisted combustion synthesis. Vacuum;In Press, Corrected Proof.

[95] C.L. Yeh SHS. In situ formation of TiAl–TiB2 composite by SHS. Journal of Alloys and Compounds (2005).

[96] J.H. Lee SKK, C.W. Won. Sintering behavior of Al_2O_3-TiC composite powder prepared by SHS process. Materials Research Bulletin (2001);36:989–996.

[97] Slocombe A, Li L. Selective laser sintering of TiC-Al_2O_3 composite with self-propagating high-temperature synthesis. Journal of Materials Processing Technology (2001);118:173-178.

[98] Wang Y, Wang C, Pan X, Dong C. Laser-induced combustion synthesis of Zr-Ti-Al-Ni amorphous-based alloys. Materials Letters (2005);59:2574-2578.

[99] Maffi S, Cignoli F, Bellomunno C, De Iuliis S, Zizak G. Spectral effects in laser induced incandescence application to flame-made titania nanoparticles. Spectrochimica Acta Part B: Atomic Spectroscopy (2008);63:202-209.

[100] Belyaev VV, Kovalev OB. Simulation of one method of laser welding of metal plates involving an SHS-reacting powder mixture. International Journal of Heat and Mass Transfer (2009);52:173-180.

[101] Li Y, Hu J, Liu Y, Guo Z, Tosto S. Effect of process parameter on the combustion temperature of laser-induced self-propagating high-temperature synthesized Al/TiC composites. Journal of Materials Processing Technology (2009);209:2564-2569.

[102] Duangduen Atong DEC. Ignition behavior and characteristics of microwave-combustion synthesized Al_2O_3–TiC powders. Ceramics International 2004.

[103] Poli G, Sola R, Veronesi P. Microwave-assisted combustion synthesis of NiAl intermetallics in a single mode applicator: Modeling and optimisation. Materials Science and Engineering a-Structural Materials Properties Microstructure and Processing (2006);441:149-156.

[104] Veronesi P, Leonelli C, Poli G, Casagrande A. Enhanced reactive NiAl coatings by microwave-assisted SHS. Compel-the International Journal for Computation and Mathematics in Electrical and Electronic Engineering (2008);27:491-499.

[105] Rogriguez GP, Garcia I, Vazquez AJ. Coating processing by self-propagating high-temperature synthesis (SHS) using a Fresnel lens. Journal De Physique Iv (1999);9:411-416.

[106] Gu H, Zhu Y, Li L. Catalytic mechanism of Nb_2O_5 and NbF_5 on the dehydriding property of Mg95Ni5 prepared by hydriding combustion synthesis and mechanical milling. International Journal of Hydrogen Energy (2009);34:7707-7713.

[107] Mingliang M, Xinkuan L, Shengqi X, Donglang C, Jing'en Z. Effect of material characteristics on the ignition of the combustion reactions induced by ball milling. Journal of Materials Processing Technology (2001);116:124-127.

[108] Xiao G, Fan Q, Gu M, Jin Z. Microstructural evolution during the combustion synthesis of TiC-Al cermet with larger metallic particles. Materials Science and Engineering: A (2006);425:318-325.

[109] Yang C, Jin SZ, Liang BY, Liu GJ, Jia SS. Synthesis of Ti_3AlC_2 ceramic by high-energy ball milling of elemental powders of Ti, Al and C. Journal of Materials Processing Technology (2009);209:871-875.

[110] Zhu Y, Wang Y, Li L. Electrochemical properties of Mg-based hydrogen storage alloys prepared by hydriding combustion synthesis and subsequent mechanical milling (HCS+MM). International Journal of Hydrogen Energy (2008);33:2965-2969.

[111] Eckert J, Bner I. Nanostructure formation and properties of ball-milled NiAl intermetallic compound. Materials Science and Engineering A (1997);239-240:619-624.
[112] Moshksar MM, Mirzaee M. Formation of NiAl intermetallic by gradual and explosive exothermic reaction mechanism during ball milling. Intermetallics (2004);12:1361-1366.
[113] Liu KW, Mücklich F, Birringer R. Synthesis of nano-RuAl by mechanical alloying. Intermetallics (2001);9:81-88.
[114] P.R.Soni. Mechanical Alloying: Fundamentals and Applications Cambridge International Science Pubilishing, 1999.
[115] Alexander S. Mukasyan ASR, Arvind Varma. Mechanisms of reaction wave propagation during combustion synthesis of advanced materials. Chemical Engineering Science (1999);54:3357-3367.
[116] al MSe. Fabrication of Al_2O_3–ZrB_2 in situ composite by SHS. Composite Science Technoly (2007).
[117] Biswas A, Roy SK. Comparison between the microstructural evolutions of two modes of SHS of NiAl: key to a common reaction mechanism. Acta Materialia (2004);52:257-270.
[118] Essmann U, Henes R, Holzwarth U, Klopfer F, Buchler E. Containerless growth and annealing behaviour of NiAl single crystals. Physica Status Solidi a-Applied Research (1997);160:487-497.
[119] Shteinberg AS, Shcherbakov VA, Munir ZA. Kinetics of combustion in the layered Ni-Al system. Combustion Science and Technology (2001);169:1-24.
[120] Guoqing Xiao QF, Meizhuan Gu, Zihong Wang, Zhihao Jin. Dissolution-precipitation mechanism of self-propagating high-temperature synthesis of TiC-Ni cermet. Materials Science and Engineering A (2004).
[121] Quncheng F. A study on mechanism of self-propagating high-temperature synthesis by combustion front quenching thechnique. Materials Science and Engineering, vol. Doctor. Xi'An, PRChina: Xi'An Jiaotong University 2000.
[122] Guoqing Xiao QF, Meizhuan Gu, Zihong Wang, Zhihao Jin. Dissolution-precipitation mechanism of self-propagating high-temperature synthesis of TiC-Ni cermet. Materials Science and Engineering A (2004).
[123] Zhu P, Li JCM, Liu CT. Reaction mechanism of combustion synthesis of NiAl. Materials Science and Engineering A (2002);329-331:57-68.
[124] R.C Juang CJL, C.C Chen. Combustion synthesis of hexagonal aluminum nitride powders under low nitrogen pressure. Materials Science and Engineering A357 (2003):219-227.
[125] al. DCe. Investigation of the SHS mechanisms of titanium nitride by in situ time-resolved diffraction and infrared thermography. Journal of Alloys and Compounds (2006).
[126] C. Curfs XT, G.B.M. Vaughan , A.E. Terry , A° . Kvick , M.A. Rodrı´guez. Al-Ni intermetallics obtained by SHS; A time-resolved X-ray diffraction study. Intermetallic (2007);15:1163-1171.
[127] John Davies PS. Induction heating handbook: McGraw-Hill press, 1979.
[128] T.J. Ahmed DS, H.E.N. Bersee and A. Beukers. Induction welding of thermoplastic composites—an overview Composites Part A. Applied Science and Manufacturing (2006);37:1638-1651.

[129] Pitchumani RJJaR. Flow control using localized induction heating in a VARTM process. Composites Science and Technology (March 2007);67:669-684.

[130] W. Suwanwatana SYaJ, J.W. Gillespie. Influence of particle size on hysteresis heating behavior of nickel particulate polymer films. Composites Science and Technology (2006);66:2825-2836.

[131] Wang Zhenting CHzG. Wear Resistance of Micro-nanostructured WC composite coating fabricated by induced heating sintering. Materials for mechanical engineering (Mar 2004);28.

[132] Shibuya M, Kawata, M, Ohyanagi, M, Munir, Z.A. Titanium diboride-tungsten diboride solid solutions formed by induction-field-activated combustion synthesis. Journal of the American Ceramic Society (2003);86:706-710

[133] Lee HY, Ikenaga A, Kim SH, Kim KB. The effects of induction heating rate on properties of Ni-Al based intermetallic compound layer coated on ductile cast iron by combustion synthesis. Intermetallics (2007);15:1050-1056.

[134] Ozdemir O, Zeytin S, Bindal C. Tribological properties of NiAl produced by pressure-assisted combustion synthesis. Wear (2008);265:979-985.

[135] Curfs C, Cano IG, Vaughan GBM, Turrillas X, Kvick A, Rodriguez MA. TiC-NiAl composites obtained by SHS: a time-resolved XRD study. Journal of the European Ceramic Society (2002);22:1039-1044.

[136] Michalski A, Jaroszewicz J, Rosinski M, Siemiaszko D. NiAl-Al_2O_3 composites produced by pulse plasma sintering with the participation of the SHS reaction. Intermetallics (2006);14:603-606.

[137] G.S.Upadhyaya. Powder metallurgy technology: Cambridge Int Science Publishing 1997.

[138] T. Sakurai OY, Y.Miyamoto. Combustion synthesis of fine AlN powder and its reaction control. Materials Science and Engineering A 416 (2006):40-14.

[139] Dumez MC, Marin-Ayral RM, Tedenac JC. The role of experimental parameters in combustion synthesis of NiAl under high gas pressure. Journal of Alloys and Compounds (1998);268:141-151.

[140] Marin-Ayral RM, Dumez MC, Tedenac JC. Influence of high gas pressure on combustion synthesis of the solid-solid reaction of NiAl compound. Materials Research Bulletin (2000);35:233-243.

[141] Chen Y, Wang HM. Laser melted TiC reinforced nickel aluminide matrix in situ composites. Journal of Alloys and Compounds (2005);391:49-54.

[142] Guo H, Sun L, Li H, Gong S. High temperature oxidation behavior of hafnium modified NiAl bond coat in EB-PVD thermal barrier coating system. Thin Solid Films (2008);516:5732-5735.

[143] Haynes JA, Pint BA, Zhang Y, Wright IG. Comparison of the cyclic oxidation behavior of [beta]-NiAl, [beta]-NiPtAl and [gamma]-[gamma]' NiPtAl coatings on various superalloys. Surface and Coatings Technology (2007);202:730-734.

[144] Bartuli C, Smith RW, Shtessel E. SHS powders for thermal spray applications. Ceramics International (1997);23:61-68.

[145] Wang YL, Smallman RE, Jones IP. Effect of ternary iron addition on the creep behaviour of NiAl. Materials Science and Engineering A (2002);329-331:847-851.

[146] Wang YL, Jones IP, Smallman RE. The effects of iron on the creep properties of NiAl. Intermetallics (2006);14:800-810.
[147] Jiang C, Sordelet DJ, Gleeson B. Effects of Pt on the elastic properties of B2 NiAl: A combined first-principles and experimental study. Acta Materialia (2006);54:2361-2369.
[148] H.Okamoto. Al-Ni (aluminum-nickel). Journal of Phase Equilibria and Diffusion (2004);25:394.
[149] Weast. CRC Handbook of Chemistry and Physics 68th: CRC Press, 1987-1988.
[150] Colin J. Smithells EAB. Metals Reference Book: Butterworths London&Boston, 1976.
[151] Markov IV. Crystal Growth for Beginners: Fundamentals of Nucleation, Crystal Growth and Epitaxy: World Scientific Publishing Co Pte Ltd, Aug 2003.
[152] Fan Q, Chai H, Jin Z. Dissolution-precipitation-substitution mechanism of self-propagating high-temperature synthesis of [beta]-NiAl(Cu)/[alpha](Cu,Ni) composite. Intermetallics (2002);10:541-554.
[153] Udhayabanu V, Ravi KR, Vinod V, Murty BS. Synthesis of in-situ NiAl-Al_2O_3 nanocomposite by reactive milling and subsequent heat treatment. Intermetallics;In Press, Corrected Proof.
[154] Tingaud D, Nardou F. Influence of non-reactive particles on the microstructure of NiAl and NiAl-ZrO2 processed by thermal explosion. Intermetallics (2008);16:732-737.
[155] Matsuura K, Kudoh M. Grain refinement of combustion-synthesized NiAl by addition of ceramic particles. Materials Science and Engineering A (1997);239-240:625-632.
[156] Moshksar MM, Doty H, Abbaschian R. Grain growth in NiAl---Al_2O_3 in situ composites. Intermetallics (1997);5:393-399.
[157] Valery Rudnev DL, Raymond Cook, Micah Black. Handbook of Induction Heating, 2003.
[158] Mossino P. Some aspects in self-propagating high-temperature synthesis. Ceramics International 30 (2004):313–332.
[159] Gennari S, Tamburini UA, Maglia F, Spinolo G, Munir ZA. A new approach to the modeling of SHS reactions: Combustion synthesis of transition metal aluminides. Acta Materialia (2006);54:2343-2351.
[160] CRC Handbook of Chemistry and Physics CRC Press 2007-2008.
[161] Zhu P, Li JCM, Liu CT. Adiabatic temperature of combustion synthesis of Al-Ni systems. Materials Science and Engineering A (2003);357:248-257.
[162] Curfs C, Tun-As X, Vaughan GBM, Terr AE, Kvick A, Rodriguez MA. Al-Ni intermetallics obtained by SHS; A time-resolved X-ray diffraction study. Intermetallics (2007);15:1163-1171.
[163] Moreno B, Chinarro E, Jurado JR. Combustion synthesis of the cermet LaCrO3-Ru. Journal of the European Ceramic Society (2008);28:2563-2566.
[164] Kexin C, Haibo J, Heping Z, Ferreira JMF. Combustion synthesis of AlN-SiC solid solution particles. Journal of the European Ceramic Society (2000);20:2601-2606.

[165] Marin-Ayral RM, Pascal C, Martinez F, Tedenac JC. Simultaneous synthesis and densification of titanium nitride by high pressure combustion synthesis. Journal of the European Ceramic Society (2000);20:2679-2684.

[166] Munir ZA, Anselmi-Tamburini U. Self-propagating exothermic reactions: The synthesis of high-temperature materials by combustion. Materials Science Reports (1989);3:279-365.

[167] Yeh CL, Su SH, Chang HY. Effects of TiC addition on combustion synthesis of NiAl in SHS mode. Journal of Alloys and Compounds (2005);398:85-93.

[168] Gao MX, Pan Y, Oliveira FJ, Baptista JL, Vieira JM. Interpenetrating microstructure and fracture mechanism of NiAl/TiC composites by pressureless melt infiltration. Materials Letters (2004);58:1761-1765.

[169] Ren KG, Chen KX, Zhou HP, Ning XS, Jin HB. Combustion synthesis of NiAl/TiC multiphase composites and their related microstructure. Rare Metal Materials and Engineering (2007);36:848-851.

[170] Chase MW. NIST-JANAF thermochemical tables: Washington, DC American Chemical Society ; New York : American Institute of Physics for the National Institute of Standards and Technology 1998.

[171] Khina BB, Formanek B, Solpan I. Limits of applicability of the "diffusion-controlled product growth" kinetic approach to modeling SHS. Physica B: Condensed Matter (2005);355:14-31.

[172] C. Chaboudez SC, R. Glardon , D. Mari , J. Rappaz, and M . Swierkosz. Numerical Modeling in Induction Heating for Axisymmetric Geometries. IEEE TRANSACTIONS ON MAGNETICS (1997);33:739-745.

[173] Hiroki Kawaguchi ME, Takashi Todaka. Thermal and magnetic field analysis of induction heating problems. Journal of Materials Processing Technology (2005);161:193-198.